MAGNESIUM ISOTOPES AS A PROBE OF THE MILKY WAY CHEMICAL EVOLUTION

ANDERS OVERAA THYGESEN

SUPERVISOR:
PROF. DR. NORBERT CHRISTLIEB

REFEREES:
PROF. DR. NORBERT CHRISTLIEB
PROF. DR. EVA GREBEL

AUGUST 3, 2015

DISSERTATION

SUBMITTED TO THE

COMBINED FACULTIES FOR THE NATURAL SCIENCES AND FOR MATHEMATICS

OF THE RUPERTO-CAROLA-UNIVERSITY OF HEIDELBERG, GERMANY

FOR THE DEGREE OF

DOCTOR OF NATURAL SCIENCES

PUT FORWARD BY:

ANDERS OVERAA THYGESEN

BORN IN RANDERS, DENMARK

ORAL EXAMINATION: OCTOBER 14, 2015

ABSTRACT

The study of elemental abundance ratios from spectroscopy of stars has for a long time been used to investigate the structure and the chemical evolution history of the Milky Way. However, even with the ever-increasing number of stars with detailed abundances, many details about the Milky Way evolution are still not understood. While elemental abundance measurements already provide a lot of information, nucleosynthesis models predict not only bulk abundances of an element, but also its isotopic composition. When these can be measured, additional details about the nucleosynthesis can be obtained. The isotopic composition of elements in stars has only been measured for the lightest elements and even for these, observations of the highest quality are needed. In addition, detailed modeling of the line-formation in the stellar atmospheres is needed to correctly interpret the data.

The purpose of this thesis is to:

- Investigate the chemical evolution history of the massive, high-metallicity globular cluster 47 Tucanae, by performing an extensive study of a range of elements in cool giants.
- Perform the first study of Mg isotopes in this cluster, to further constrain its chemical evolution history. In addition, this work represents the *first study ever* of the effects of using 3D stellar atmospheric models to derive the Mg isotopic mixture.
- Perform the first study of Mg isotopes in stars in the inner disk of the Milky Way and the Milky Way bulge, including stars in the globular cluster NGC 6522.
- Demonstrate that this type of study is feasible for stars in the bulge, and show how the Mg isotopic ratios can be used to constrain chemical evolution models for this part of the Galaxy.

The Mg isotopic ratios were successfully measured in all 21 observed stars and provided additional constraints on the chemical evolution history of 47 Tucanae. In addition, the first results for Mg isotopes with 3D stellar atmospheres gave improved fits to the MgH molecular features, compared to 1D. This also resulted in an increase of the measured fraction of ^{25}Mg, improving the agreement with chemical evolution models. For the inner disk and the bulge, we reached a level of accuracy on the Mg isotopic ratios that will allow us to distinguish between different chemical evolution models. For the one field star in the bulge, we see

an indication of more efficient star formation compared to the disk, but a larger sample of stars is needed before firm claims can be made.

ZUSAMMENFASSUNG

Messungen von chemischen Elementhäufigkeitsverhältnissen aus Sternspektren sind seit langer Zeit verwendet worden, um die Struktur und die chemische Entwicklungsgeschichte der Milchstraße zu untersuchen. Doch selbst mit der ständig steigenden Anzahl der Sterne mit detaillierten Häufigkeiten sind viele Details über die Entwicklung der Milchstraße noch immer nicht verstanden. Während solche Häufigkeitsmessungen bereits eine Vielzahl von Informationen enthalten, prognostizieren Nukleosynthesemodelle nicht nur die pauschale Häufigkeit eines Elements, sondern auch dessen Isotopenzusammensetzung. Wenn diese gemessen werden kann, lassen sich zusätzliche Informationen über Kernprozesse gewinnen. Bisher konnten Isotopenzusammensetzungen in Sternen nur für die leichtesten Elemente gemessen werden und selbst für diese sind Beobachtungen von höchster Qualität erforderlich. Zusätzlich ist eine detaillierte Modellierung der Linienbildung in den Sternatmosphären nötig, um die Daten richtig interpretieren zu können.

Das Ziel dieser Arbeit ist:

- die chemische Entwicklungsgeschichte des massereichen, metallreichen Kugelsternhaufens 47 Tucanae durch eine umfassende Studie eines breiten Bereichs an Elementen in kühlen Riesensternen zu untersuchen;
- erste Messungen von Mg-Isotopen in diesem Haufen durchzuführen, um seine chemische Entwicklung weiter einzuschränken. Darüber hinaus stellt diese Arbeit die erste Studie über die Auswirkungen von dreidimensionalen Sternatmosphärenmodellen auf das abgeleitete Mg-Isotopengemisch dar.
- Die erste Untersuchung von Mg-Isotopen in Sternen der inneren Scheibe der Milchstraße sowie ihrer zentralen Verdickung – dem "Bulge";
- eine Demonstration, daß diese Art von Studie für Sterne im Bulge machbar ist, und somit zu zeigen, wie die Mg-Isotopenverhältnisse Modelle der chemischen Entwicklung für diesen Teil der Galaxie einschränken können.

Die Isotopenverhältnisse für Mg wurden erfolgreich in allen Sternen dieses Projekts gemessen und erlauben zusätzliche Einschränkungen über die chemische Entwicklung von 47 Tucanae. Weiterhin konnten

die ersten Ergebnisse der MgIsotope aus dreidimensionalen Modellatmosphären Molekülbanden von MgH weitaus besser repräsentieren als die gängigen eindimensionalen Modelle. Dies führte auch zu einem Anstieg des gemessenen Anteils von ^{25}Mg, wodurch die Übereinstimmung mit den chemischen Modellen verbessert wurde. Für die innere Scheibe und den Bulge erreichten wir ein Maß an Genauigkeit auf die Mg-Isotopenverhältnisse, das uns erlaubt, zwischen verschiedenen chemischen Entwicklungsmodellen zu unterscheiden. Für den Stern im Bulge sehen wir einen Hinweis auf effizientere Sternentstehung im Vergleich zur Scheibe, jedoch sind Messungen in einer größeren Anzahl von Sternen notwendig, bevor festere Aussagen getroffen werden können.

"I'll keep this wisdom in my flesh / I leave here believing more than I had /
And there's a reason I'll be / A reason I'll be back."

— Eddie Vedder, No Ceiling, 2007

First and foremost I want to express my gratitude to my two supervisors, Prof. Norbert Christlieb and Dr. Luca Sbordone. You, and the rest of the group made me feel extremely welcome at the Landessternwarte from day one, and continued to contribute to make the LSW a pleasant and inspiring place for me to work throughout my studies. Thanks for giving me the freedom to pursue my project as independently as I wanted, and for your willingness to guide and teach me when I was in need of advice. A very special thanks to Luca for your seemingly infinite patience with me, for always taking time for discussions, and for your support throughout my time as a PhD student. It made a world of difference, both on a scientific and personal level. Your ability to always rekindle my enthusiasm for my research never ceases to amaze me.

I would also like to extend my thanks to Hans Ludwig for your help with CO^{5}BOLD, countless useful discussions, valuable input, and your willingness to explain things to me three, four, five times if needed. You always make me think more about my science. Thanks to my many collaborators who have been involved in my research, in particular Dr. David Yong, Dr. Amanda Karakas and Dr. Melissa Ness for many useful discussions and constructive feedback on my work (and more than one epic karaoke session). Thanks also to Dr. Andreas Koch for his help with the German translation of my abstract, and many interesting discussions.

It has been a pleasure to be a member of the Zentrum für Astronomie in Heidelberg, and I wish to acknowledge the generous funding from the SFB 881 "The Milky Way Galaxy", as well as a Distinguished Doctoral Fellowship from the Heidelberg Graduate School for Fundamental Physics. This allowed me to accomplish my PhD, and made it possible for me to attend numerous meetings and conferences around the world, which have been invaluable experiences. It has also been a pleasure to be a member of the International Max Planck Research School and I want to thank Dr. Christian Fendt, whose engagement has contributed greatly to the well-being of all the students at IMPRS, as well as provided useful support on several occasions.

I also want to thank all the wonderful people in Heidelberg, and elsewhere, who made the last three years an amazing journey. In no particular order: Andrew, Tobias, Michael, Taisiya, Emer, Melanie, Ben,

Richard, Paolo, Sonia, Ilya, Dave, László, Wieńczysław, Joanna, Camille, Eric, Kathrin, Amelia, Paulina, Sundar, Liz, Roger, Ioana, Nikolay, all the swing dancing people and all the remaining people that I have unintentionally left out. You have all helped make my time as a graduate student better and full of fond memories. A special thanks to Catarina and Anastasia for helping me keep my sanity through the last few months of my PhD, getting my mind off science, help keeping my cool and preventing my brain from exploding for the last month of my thesis writing.

Til sidst, men ikke mindst, tak til jer derhjemme. Ude er godt, men hjemme bedst. Tak, mor og far, for at støtte mig på alle måder og for jeres utallige besøg, også når jeg indimellem har for travlt til at være fuldt til stede. Tak, Sigrid, for at være verdens sejeste søster og altid være der for mig. Det betyder alverden at jeg har jer at læne mig op af, selvom jeg er langt væk. Tak til Jakob, Rune, Lise, Bo, Jeppe, Cecilie, Gudmund og resten af flokken. Der er længe imellem vi ses, men jeg værdsætter det virkeligt at I bevarer kontakten, det gør en verden til forskel.

CONTENTS

List of Figures i
List of Tables viii
1 INTRODUCTION 1
1.1 The chemical evolution of the Milky Way 1
1.2 Observing magnesium isotopes 3
1.3 The production of magnesium isotopes 7
1.3.1 Massive stars 7
1.3.2 The AGB channel 9
1.4 The role of globular clusters 13
1.4.1 The globular cluster 47 Tucanae 19
1.5 The Milky Way Bulge 21
1.6 Structure of dissertation 24
2 STELLAR ATMOSPHERIC MODELS 27
2.0.1 CO^{5}BOLD 3D hydrodynamic models 30
2.1 Spectral synthesis 33
2.1.1 Synthesis with `Linfor3D` 33
3 THE ABUNDANCE PATTERN OF GIANTS IN 47TUC 45
3.1 Introduction 45
3.2 Observations and data reduction 45
3.3 Abundance analysis 48
3.3.1 Fundamental stellar parameters 48
3.3.2 Element abundances 55
3.4 Results 68
3.4.1 The abundance pattern 69
3.5 Discussion 80
3.5.1 NLTE effects for Al 81
3.5.2 Comparison with M71 83
4 MAGNESIUM ISOTOPES AND THE POLLUTION HISTORY OF 47TUC 85
4.1 Introduction 85
4.2 Analysis 85
4.2.1 Line selection 85
4.2.2 Mg isotopes with `MOOG` 89
4.2.3 Mg isotopes with CO^{5}BOLD/Linfor3D 91
4.2.4 Estimating uncertainties 102
4.3 Results 103
4.3.1 Results from 3D 104
4.4 Discussion 108
4.4.1 Star 10237 112

4.4.2 Comparison with earlier works 113
4.4.3 Pollution scenarios 116
4.4.4 Isotopes in 3D. A potential solution to the ^{25}Mg problem 125
4.5 Conclusions 129
5 MAGNESIUM ISOTOPES IN BULGE RED GIANTS 133
5.1 Introduction 133
5.2 Observations and data reduction 133
5.2.1 Data reduction 135
5.3 Analysis 136
5.3.1 Elemental abundance measurements 138
5.3.2 Magnesium isotope measurement 142
5.3.3 Determining uncertainties 144
5.4 Results 148
5.4.1 Elemental abundances 152
5.4.2 Magnesium isotopes 154
5.5 Discussion 154
5.5.1 NGC 6522 154
5.5.2 Field stars 159
5.5.3 Comparison with previous work 161
5.5.4 Chemical evolution models 163
5.6 Conclusions 165
6 SUMMARY AND FUTURE PROSPECTS 169
6.1 Summary 169
6.2 Future prospects 172
6.2.1 Magnesium isotopes in halo sub-dwarfs 172
6.2.2 Magnesium isotopes in post-AGB stars 175
6.2.3 Detailed abundances of giants in the Globular Clusters NGC 288 and NGC 362 176
A APPENDIX 179
A.1 Tables 179
A.2 Light element correlations 208
A.3 Kurucz molecular line format 209
BIBLIOGRAPHY 211

LIST OF FIGURES

Figure 1.1 Three examples of the observed MgH feature at 5134 Å in red giant stars, with the central wavelength of the three isotopic transitions indicated by vertical, dashed lines. Even by eye, the difference in line asymmetry is evident. The spectra have been shifted vertically for clarity. The S/N in these spectra is ~ 150. 6

Figure 1.2 A schematic illustration of the NeNa and MgAl burning chains in AGB stars. The dashed circles indicate unstable isotopes. Adopted from Karakas & Lattanzio (2003). 11

Figure 2.1 An example of an intensity observation of the solar surface, as seen by the Swedish Solar Telescope. The convective pattern is evident. Image credit: the Institute for Solar Physics, Sweden and Vasco Henriques. 29

Figure 2.2 The emergent bolometric intensity for the 20 snapshots used in the spectral syntheses from our low metallicity model. Each snapshot has a size of 4600 Mm $\times$ 4600 Mm and $\Delta t = 60$ h of stellar time between each snapshot. 32

Figure 2.3 Syntheses of the MgH feature at 5138 Å for each individual snapshot of the low metallicity model 35

Figure 2.4 Normalized syntheses of the MgH feature at 5138 Å for each individual snapshot of the low metallicity model 35

Figure 2.5 Left: The continuum intensity map of a single model snapshot. Bright areas indicate warm, outflowing gas. Indicated are two points for which we compute a spectral syntheses of the two MgH features shown to the right. In each syntheses, the red diamonds are a synthesis from the intergranular lanes, whereas the black syntheses are from the hot granule. Vertical lines show the laboratory wavelengths for the MgH transitions, where the bottom synthesis is a blend of two different MgH transisions (solid and dashed lines). 37

Figure 2.6 The correlation of the continuum intensity (divided by the mean intensity) and the EW of the MgH feature at 5135 Å for all horizontal positions and all snapshots of the low metallicity model 39
Figure 2.7 Syntheses of the four MgH regions of interest, including all blending lines, for the low metallicity model. Shown are the full 3D (solid), <3D> (red dashed) and 1D LHD (blue dot dashed) syntheses. 39
Figure 2.8 Contribution functions of the flux equivalent width (EW) for MgH for each of the four features used, as a function of optical depth. Shown for the full 3D (solid), <3D> (dashed) and $1D_{LHD}$ (triple-dot dashed) models. 40
Figure 2.9 Top: Full 3D, <3D> and 1D LHD syntheses of the four MgH features, not including blends from other species. Bottom: As above, but with the 1D syntheses scaled to the same core strength as the full 3D synthesis. In the bottom right corner is shown $T_{\rm eff}/\log g/[{\rm Fe/H}]$ for the model. 41
Figure 2.10 Syntheses of each of the four MgH regions, but only including the blending lines. Shown for the low metallicity model. 43
Figure 3.1 Color-magnitude diagram of 47 Tucanae with observed targets indicated. Blue circles and red triangles are used for the pristine and polluted population of stars respectively. See Sect. 3.4.1.1 for population selection criteria. 46
Figure 3.2 Fractional contribution of free electrons for the top five electron donors as a function of optical depth. The solid, gray line shows the total contribution from the 5 species. Top: 10237, which is the most Mg-depleted star. Bottom: 38916, the most Mg-enhanced star. 52
Figure 3.3 Electron pressure as a function of temperature for three different models of the star 10237. The solid black line shows the ATLAS12 model with tailored abundance pattern, and the red dashed line shows the interpolated, scaled solar ATLAS9 model. Finally, the α-enhanced ATLAS9 model is shown as the blue dot-dashed line. 53
Figure 3.4 Difference in electron pressure as a function of temperature between star 10237 and star 38916. 53

Figure 3.5 Example of the oxygen synthesis for the two lines used to derive the O abundance in this work, shown here for star 10237. Solid red line shows the optimal fit and the dotted blue lines changing the O abundance by ±0.07 dex. The black, dashed line show a synthesis without oxygen. 59
Figure 3.6 NLTE corrections ($A(Na)_{NLTE}$-$A(Na)_{LTE}$) as a function of T_{eff}, $\log g$, EW, and ξ_t. The red points shows the actual values for the star 6798. 60
Figure 3.7 Example of the NLTE line profile fitting of the three Ba lines used here. Shown is the star 10237. In each panel, we give the abundance used in the fit. 63
Figure 3.8 [Ba/Fe] vs. T_{eff} for both LTE (black) and NLTE (red). Taking non-local thermodynamic equilibrium (NLTE) into account removes the correlation between abundance and T_{eff}. 63
Figure 3.9 Size of the NLTE corrections for Al vs. T_{eff}. 64
Figure 3.10 As Fig 3.8 but for the measured [Al/Fe] ratios. 64
Figure 3.11 Correlations between the light elements. Top left: [Na/Fe] vs. [O/Fe], top right: [Mg/Fe] vs. [Al/Fe], bottom left: [Al/Fe] vs. [O/Fe], bottom right: [Na/Fe] vs. [Al/Fe]. The dashed line indicates the adopted cut between the pristine (black circles) and polluted (red triangles) population of stars. The red arrows indicate lower limits on the [O/Fe] abundance. 74
Figure 3.12 Distribution of [Na/Fe] vs. [O/Fe] from our bootstrapping exercise, shown as a density plot. Binsize is 0.01. The measurements are shown in red. The two targets with no oxygen errorbars only got lower limits, so were excluded from the bootstrapping calculations. 75
Figure 3.13 Abundance pattern for our sample stars. Shown are the interquartile ranges. The most extreme outliers are indicated with open circles. 77
Figure 3.14 [Mg/Fe] vs. [Al/Fe] in LTE (left) and NLTE (right). The observed range in [Al/Fe] decreases when NLTE is taken into account. 83

Figure 4.1 Synthesis of the four MgH features used to derive the isotopic fractions of Mg in star 5265. The red line shows the synthesis using the best-fitting [C/Fe], whereas the dashed lines show the change of the line shape when the [C/Fe] is changed by ±0.3 dex around this value. 88

Figure 4.2 Synthesis of the four MgH features used to derive the isotopic fractions of Mg in star 5265. The red line shows the synthesis using a scaled Solar value for [N/Fe] whereas the dashed lines show the change of the line shape when the [N/Fe] is changed by ±0.5 dex. 89

Figure 4.3 1D syntheses of the 5135.07 Å MgH feature for different isotopic components. 90

Figure 4.4 Line fits and χ^2 distributions for the fitted isotopic ratios for all MgH features in star 4794. Vertical, magenta lines show best-fitting values. The red dashed lines indicate 1σ fitting precision. 92

Figure 4.5 Average thermal structure of the 3D models (solid line) as well as an equivalent 1D ATLAS12 (triple dot-dash) and LHD (dash) model. The red lines indicate the RMS variation of the temperature in the 3D models. Top panel: HiMet, bottom: LoMet. 94

Figure 4.6 The auto-correlation of the horizontal grey intensity for the HiMet model. The blue, dashed line, shows the value for the time step between two consecutive snapshots. 95

Figure 4.7 Comparison of the syntheses of the 5138 Å feature for ^{24}MgH. Note the line asymmetry in the red wing. The syntheses have been scaled to have the same overall strength. 98

Figure 4.8 Syntheses of the MgH feature at 5135.07 Å. Shown is the full 3D synthesis (solid), the <3D> synthesis (dashed) and the 1D LHD synthesis (dot-dashed). Indicated is also the central position of each of the MgH components. Top: LoMet, bottom: HiMet. 99

Figure 4.9 As Fig. 4.8, but for the MgH feature at 5138.71 Å. This feature is a blend of two MgH transitions, indicated with solid and dashed vertical lines. 100

Figure 4.10 Percentage of ^{24}Mg vs. [Na/Fe] (top), ^{25}Mg vs. [Na/Fe] (middle) and ^{26}Mg vs. [Na/Fe] (bottom). Black triangles indicate the pristine populations and red triangles the polluted population. 105

Figure 4.11 Best-fitting synthesis from 3D (red, solid line) and 1D (blue, triple-dot dash line) for the star 4794. Also shown are the residuals of the two fits, as well as the central positions of the MgH features. 109
Figure 4.12 Percentage abundances of the Mg isotopes vs. $T_{\rm eff}$. 110
Figure 4.13 Percentage of ^{24}Mg vs. [Al/Fe] (top), ^{25}Mg vs. [Al/Fe] (middle) and ^{26}Mg vs. [Al/Fe] (bottom). Black triangles indicate the pristine populations and red triangles the polluted population. Also shown are the results from Meléndez & Cohen (2009) for M71. In the M71 sample, the polluted population is indicated with green, open squares. Blue open diamonds show the pristine population. Typical uncertainties of the isotope measurements for M71 is also shown. 115
Figure 4.14 Linear fraction of ^{24}Mg vs. [Al/Fe]. Our results are shown as black and red triangles. For comparison the results from Da Costa et al. 2009 (green squares), Meléndez & Cohen 2009 (blue diamonds), Yong et al. 2003a (black crosses) and Yong et al. 2006 (pink asterisks) are shown. 116
Figure 4.15 Same as in Fig. 4.14, but for ^{25}Mg. 117
Figure 4.16 Same as in Fig 4.14, but for ^{26}Mg. 117
Figure 4.17 ^{26}Mg/^{24}Mg vs. ^{25}Mg/^{24}Mg measured in our sample. Shown are also isotopic ratios from the supernova yields of Nomoto et al. (2006) ($Z = 0$, blue diamonds; $Z = 0.004$, green triangles; $Z = 0.004$ IMF weighted value, red triangle), Tominaga et al. (2007) ($Z = 0$, black squares) and from the chemical evolution model of Kobayashi et al. (2011) (black X). Shown is also the dilution curve for the isotopes using the model form Ventura et al. (2014). The Solar position is shown with a black cross. 119
Figure 4.18 Isotopic fractions vs. [Al/Fe]. The solid blue lines is the predicted composition of the stars from Ventura et al. (2014). The dashed lines shows the dilution curve, when shifted by +0.12 dex in [Al/Fe]. 122
Figure 4.19 Isotopic ratios of magnesium from 1D (gray, open squares) and 3D (black, filled circles), together with the dilution curve for AGB star ejecta. Results are shown for stars 4794, 13396 and 29861. 126

Figure 4.20 Isotopic fractions vs. [Al/Fe] for the stars with 3D results. The solid blue lines is the predicted composition of the stars from Ventura et al. (2014). The dashed lines shows the dilution curve, when shifted by +0.12 dex in [Al/Fe]. Symbols have the same meaning as in Fig. 4.19. 128
Figure 5.1 Comparison between our EW measurements and the measurements of Fulbright et al. (2006). Black circles is Fe I lines and blue triangles Fe II. The red lines show the mean difference and black lines ± the standard deviation. 137
Figure 5.2 Syntheses of the two forbidden [OI] lines in the star J192058957. Only a lower limit on the O abundance can be derived. 139
Figure 5.3 Syntheses of the Na lines at 6154 Å and 6160 Å, with and without inclusion of the TiO blends in the syntheses, for the star J15040305. 140
Figure 5.4 Syntheses with (red, solid) and without (black, dashed) TiO bands in the star J142728406 of the Al features at 6696.02 Å, and 6698.67 Å, together with the observed spectrum. The syntheses are computed with identical Al abundances. Note that no artificial shift has been applied to any of the syntheses. 141
Figure 5.5 NLTE synthesis of the three Ba II lines in the bulge star IV-203. Some residual sky emission is also visible in the spectra. 142
Figure 5.6 Syntheses of the four MgH bands, with and without the inclusion of TiO blends. 143
Figure 5.7 Best-fitting MgH syntheses and χ^2-distributions for $^{25}Mg/^{24}Mg$ and $^{26}Mg/^{24}Mg$ for each feature in IV-203. The MgH transitions are indicated. Grey dot-dashed and blue dashed line shows syntheses with ±5% ^{25}Mg and ^{26}Mg respectively. Red dashed lines show the 1σ uncertainty. Vertical magenta lines: Best-fitting values. 145
Figure 5.8 As Fig. 5.7 but for the metal-rich field giant J14574719. Grey dot-dashed and blue dashed line shows syntheses with ±3% ^{25}Mg and ^{26}Mg respectively. 146

Figure 5.9 Abundance ratios [O/Fe], [Mg/Fe], [Ti/Fe] and [α/Fe] vs. [Fe/H]. Filled black symbols: disk targets, open, red triangles: bulge field star, red circles: NGC 6522 stars. The disk star with an arrow only has a lower limit on the oxygen abundance. The dashed line shows the solar value. Shown is also abundance measurements from Venn et al. (2004); Bensby et al. (2014) and Hinkel et al. (2014) for comparison purposes. 155

Figure 5.10 [Na/Fe], [Al/Fe], and [Ni/Fe] vs. [Fe/H]. Symbols have the same meaning as in Fig. 5.9. Note the different scaling of the abscissas. 155

Figure 5.11 Mg isotopic ratios for our sample of stars. Symbols have the same meaning as in Fig 5.9. The dashed line indicate the solar isotopic fractions. Open, grey circles show the results from Yong et al. (2003b) 160

Figure 5.12 Comparison between our measured isotopic ratios and the predictions from Kobayashi et al. (2011) for the bulge (solid, blue line) and Solar neighborhood (dashed red line). 165

Figure 6.1 1D synthesis of the MgH band of the Galactic halo star NLTT51106 ([Fe/H] $= -1.9$ dex) from our already obtained data. Shown is the best-fitting synthesis, as well as a pure ^{24}MgH and a solar mixture. Magnesium isotopic fractions are given as percentages [^{24}Mg:^{25}Mg:^{26}Mg]. Small variations in the heavy isotopes can easily be detected. 173

Figure 6.2 Left: Magnesium isotope measurements and model predictions from Fenner et al. (2003). The solid line includes AGB contribution whereas the dotted does not. Yellow diamonds from Yong et al. (2003b), blue dots from Gay & Lambert (2000). Right: Similar figure from Meléndez & Cohen (2007). 174

Figure A.1 [X/Fe] vs. [Na/Fe] from O to Ti. In each plot is shown representative uncertainties. Symbols the same as in Fig. 3.11 208

Figure A.2 [X/Fe] vs. [Na/Fe] from V to Zr. In each plot is shown representative uncertainties. Symbols the same as in Fig. 3.11 208

Figure A.3 [X/Fe] vs. [Na/Fe] from Mo to Dy. In each plot is shown representative uncertainties. Symbols the same as in Fig. 3.11 209

LIST OF TABLES

Table 2.1 Model parameters for our CO^{5}BOLD 3D models. 31

Table 3.1 Properties of the observed targets. Boldface numbers indicate polluted targets. The uncertainties on the magnitudes are at the 3% level. 48

Table 3.2 Photometric $T_{\rm eff}$'s for each sample star. Subscripts "R" and "G" refer to the calibrations of Ramírez & Meléndez (2005) and González Hernández & Bonifacio (2009), respectively. 50

Table 3.3 Changes to the fundamental parameters when perturbing a typical star (6798) by the estimated uncertainties. Changes given as best fit minus perturbed. 56

Table 3.4 Changes to derived abundances relative to best-fitting model, when perturbed by the uncertainties on the fundamental stellar parameters. Shown for the star 6798. 67

Table 3.5 Changes to derived abundances, relative to a tailored ATLAS12 model when using ATLAS9 scaled Solar model and an ATLAS9 model with +0.4 dex α-enhancement. Both models have the same fundamental parameters. Shown here for star 1062. 68

Table 3.6 Fundamental atmospheric parameters for our stars. 70

Table 3.7 IQR, median value, and median uncertainty ($\bar{\sigma}$) for all measured elements. 72

Table 3.8 [Y/Fe], [Zr/Fe], and [Ba/Fe] as reported by several other studies, as well as what is found in this work. 81

Table 4.1 Model parameters for our CO^{5}BOLD 3D models. 93

Table 4.2 The change in mean value of the isotopic percentages of Mg due to atmospheric uncertainties, relative to the best fit. Shown here for star 6798. 103

Table 4.3 Median value, interquartile ranges and σ_{IQR} for all three isotopes. Shown for the total sample and split in populations. 104
Table 4.4 Mg isotopic fractions for individual features, given as percentage [^{24}Mg:^{25}Mg:^{26}Mg]. Also shown are the weighted means and associated uncertainties. Boldface IDs indicate polluted stars. 106
Table 4.5 Summary of the mean Mg isotopic fractions, as well as stellar parameters and light element abundances. Boldface IDs indicate polluted stars. 107
Table 4.6 Mg isotopic ratios [^{24}Mg:^{25}Mg ^{26}Mg] derived from 1D and 3D syntheses respectively. 108
Table 5.1 Observing log of all targets in the sample. Boldface indicate bulge star and italic the GC stars. Exp. time is the individual exposure time. The number of sub-exposures are provided in the last column. 134
Table 5.2 Changes of the Mg isotopic ratios, relative to the best fitting value, when perturbed with the atmospheric parameter uncertainties. Shown for three representative stars. 149
Table 5.3 Fundamental parameters for the bulge and disk stars and their uncertainties. 151
Table 5.4 The measured values of [Fe I/H], [Fe II/H] and [C/Fe], uncertainties, and number of lines used, for all stars in the sample. [C/Fe] is an upper limit. 152
Table 5.5 As Table. 5.4 but for [O/Fe], [Na/Fe] and [Mg/Fe]. [Al/Fe] has been derived using NLTE. 153
Table 5.6 As Table. 5.4 but for [Al/Fe], [Ti/Fe] and [Ni/Fe]. 153
Table 5.7 [Ba/Fe]$_{NLTE}$ measurements for the two GC stars. Measured relative to Fe II. 153
Table 5.8 Individual Mg isotopic fractions, weighted mean and total uncertainty given as percentage ^{24}Mg:^{25}Mg:^{26}Mg. 156
Table 5.9 Comparison between the Mg isotopic fractions from our analysis of three dwarfs from Yong et al. (2003b), and the original values. Included are also preliminary results for HIP34608 (Yong, priv. comm. 2015). The resolution of the observations, R, is given in the last row. 162

Table A.1 The full line list for the elements without reported HFS. XX.0 refers to neutral species and XX.1 to the first ionization stage. All wavelengths are given in Å. The table is also available online through CDS. 179

Table A.2 Line list of HFS-elements measured. XX.0 and XX.1 indicate neutral and ionized species respectively. The full table is also available online. With the exception of barium, all lines have been split into individual HFS components in this list. Oscillator strength given as reduced $\log(gf)$. All wavelengths given in Å. 184

Table A.3 Abundance ratios for red giants in 47 Tucanae. Boldface IDs indicate the polluted population. Fe to Mg. 202

Table A.4 Abundance ratios for red giants in 47 Tucanae. Boldface IDs indicate the polluted population. Al to Sc. 203

Table A.5 Abundance ratios for red giants in 47 Tucanae. Boldface IDs indicate the polluted population. Ti to Mn. 204

Table A.6 Abundance ratios for red giants in 47 Tucanae. Boldface IDs indicate the polluted population. Co to Y. 205

Table A.7 Abundance ratios for red giants in 47 Tucanae. Boldface IDs indicate the polluted population. Zr to La. 206

Table A.8 Abundance ratios for red giants in 47 Tucanae. Boldface IDs indicate the polluted population. Ce to Dy. 207

Table A.9 Kurucz molecular line list input format. 209

ACRONYMS

4MOST 4-metre Multi-Object Spectroscopic Telescope

AGB asymptotic giant branch

APOGEE Apache Point Observatory Galaxy Evolution Experiment

ARGOS Abundances and Radial velocity Galactic Origins Survey

CCF cross-correlation function

CMD color-magnitude diagram

CO^{5}BOLD COnservative COde for the COmputation of COmpressible COnvection in a BOx of L Dimensions, L=2,3

EP excitation potential

EW equivalent width

FRMS fast rotating massive stars

FST full spectrum of turbulence

GALAH GALactic Archaeology with HERMES

GC globular cluster

GES Gaia-ESO Survey

HB horizontal branch

HBB hot bottom burning

HFS hyperfine splitting

IMF initial mass function

IQR interquartile range

IS image slicer

ISM interstellar medium

LTE local thermodynamic equilibrium

MDF metallicity distribution function

MLT mixing-length theory

MS main sequence

MW Milky Way

NIR near infrared

NLTE non-local thermodynamic equilibrium

RGB red giant branch

RV radial velocity

S/N signal-to-noise

SN supernova

SGB subgiant branch

TDU third dredge-up

TO turn-off

UVES Ultraviolet and Visible light Echelle Spectrograph

VALD Vienna Atomic Line Database

VLT Very Large Telescope

WEAVE WHT Enhanced Area Velocity Explorer

1 INTRODUCTION

"But that means everything is made up of everything else," said Ridcully.
"Yes. Isn't it amazing?"

— Terry Pratchett, Reaper Man, 1991

1.1 THE CHEMICAL EVOLUTION OF THE MILKY WAY

Since ancient times mankind has looked up at the shining points of light in the sky and marveled at the sight, trying to explain and understand how it all came to be. In today's modern world, this has not changed much, although our understanding and ability to explore the universe around us has improved dramatically. This is largely due to the observing power of modern-day telescopes like the Very Large Telescope (VLT), the Keck Telescopes and the Magellan Telescopes on Earth, as well as several space-borne observatories like the Hubble Space Telescope and the Herschel satellite. All of these impressive instruments have provided a tremendous insight into the conditions of both the near and far reaches of space, constantly improving our knowledge of the Universe.

One of the key areas in contemporary astrophysics is to gain a better understanding of the history of our home galaxy, the Milky Way (MW). Understanding the evolution of the MW in detail is crucial for understanding the overall behaviour of similar galaxies elsewhere in the local Universe. It is the most fundamental yardstick we have for comparison with other spiral galaxies, as the MW is the system we can study in the most detail, due to the Earth being embedded in it. On the other hand, this also poses some challenges as to the overall structure of the MW as we cannot observe it from the outside.

A powerful tool for investigating the evolution of the MW is the study of elemental and isotopic abundances in stars. Stars are generally believed to be time capsules, where the abundances we can observe today usually reflect the chemical composition of the gas cloud from which the stars were formed. However, some exceptions exist, where evolutionary effects may alter the abundance of certain elements through dredge-up of processed material, diffusion of heavy elements or destruction of light elements at the bottom of the convective envelope (in particular for Li).

Using optical and near-infrared spectroscopy of stars, we can infer the composition of the stellar atmospheres by inspecting emission and absorption lines from different elements. The abundances that are observed this way can then be used to infer information about the stellar generations preceding the current one. The stars belonging to these earlier generations we can no longer observe, which is also why this research area is referred to as "galactic archaeology" (Freeman & Bland-Hawthorn 2002). This area has provided some tremendous results over the last decade, with the rise of both high- and low-resolution multi-object spectroscopy, allowing for spectroscopy of hundreds of stars in a relatively short period of time. This has helped the hunt for the rare, extremely metal-poor stars in the MW, which are believed to hold the fossil record of the supernova (SN) yields from the first generation of stars and signatures of early nucleosynthesis (e. g. (Cayrel et al. 2004; François et al. 2007; Caffau et al. 2013a) and Howes et al. 2014). These opportunities have also helped to provide evidence for both the thin and thick disk components of the MW (e. g. Casagrande et al. 2011; Haywood et al. 2013; Bensby et al. 2014), originally proposed by Gilmore & Reid (1983), the presence of both an inner and outer halo (Carollo et al. 2007) not previously recognized, as well as detailed information about the structure and multi-population nature of the MW bulge (more on this in Sect. 1.5) as well as the multiple population phenomenon in Globular Clusters (Sect. 1.4).

The field of galactic archaeology has the promise to provide us with a wealth of new information in the next 5-10 years with the advent of several large-scale spectroscopic surveys like the Gaia-ESO survey (Gilmore et al. 2012), the Apache Point Observatory Galaxy Evolution Experiment (APOGEE) survey (Allende Prieto et al. 2008), and the GALactic Archaeology with HERMES (GALAH) program (Zucker et al. 2012), as well as the proposed WHT Enhanced Area Velocity Explorer (WEAVE) instrument (Dalton et al. 2012), and 4-metre Multi-Object Spectroscopic Telescope (4MOST) project (de Jong et al. 2014) among others. These projects will provide detailed elemental abundances for millions of stars. Since stars should have a chemical fingerprint that is characteristic for their birth nebula, the hope is that stars which are now situated in different parts of the Galaxy can be associated through chemical tagging. Combined with the proper motion and distance measurements for millions of stars provided by the Gaia satellite, this will allow us to associate stars through their chemistry, but also to reconstruct their orbits and potentially discover their birthplace. Similar efforts have already been undertaken with existing facilities with the works of Meléndez et al. (2006) and Melendez & Ramirez (2007), who try to identify solar twins, to find other stars that were previously associated with the proto-solar nebula.

Chemical tagging and association of stars are not the only interesting aspects that can be probed from abundance measurements. Since different elements are produced by different processes that happen on different timescales (e.g. supernovae of type II and Ia, spin-stars, asymptotic giant branch (AGB) stars), certain abundance patterns allow to place the stars in the evolutionary path of its population of origin, adding a time dimension. The combination of such information has helped to construct and constrain theoretical models for the MW chemo-dynamical evolution (e. g. Lacey & Fall 1985; Matteucci & Francois 1989; Prantzos & Silk 1998; Chiappini et al. 2001; Kobayashi & Nakasato 2011 and Minchev et al. 2013). These models are now reaching a level of complexity where predictions can be made for the average behaviour of the elements in different MW components, as well as location-dependent elemental distributions. These chemical evolution models have had success in reproducing the average abundance patterns of the major elements in the Solar neighborhood, as well as other parts of the Galaxy.

Whereas the chemical abundance patterns from elemental abundances already provide significant insight into the overall chemo-dynamical evolution of the MW, most theoretical models that provide nucleosynthesis yields predict not only the bulk abundances of a given element, but also its isotopic abundance distribution. The isotopic mixture depends on details of the nucleosynthesis in the models, and the conditions in the burning sites. Thus, in cases where not only bulk abundances, but also the isotopic abundances of an element can be measured in stars, one has a window to inspect in detail the conditions in the progenitor(s) that provided the elements in the stars we observe today. Such analyses have only been done for a few elements, including Li (e. g. Smith et al. 1998 but see also the discussion of ^{6}Li detection of Asplund et al. 2006a; Cayrel et al. 2007; Steffen et al. 2012 and Lind et al. 2013), C (e. g. Sneden et al. 1986; Suntzeff & Smith 1991; Gratton et al. 2000; Keller et al. 2001 and Carretta et al. 2005), N (Hedrosa et al. 2013), O (Harris et al. 1988; García-Hernández et al. 2010), Mg (e. g. Yong et al. 2003a,b), Ti (Chavez & Lambert 2009), Ba (Gallagher et al. 2010), Sm (Lundqvist et al. 2007), and Eu (Sneden et al. 2002).

1.2 OBSERVING MAGNESIUM ISOTOPES

Measuring isotopic ratios of elements from spectroscopy is exceedingly difficult for anything but the lightest atoms, and in most cases not possible. To understand why, lets consider the frequency shift of an electronic transition in an atom, when the mass is changed. The change in energy levels arises due to a change in the center-of-mass of the system, and

the fractional shift of the transistion frequencies can be approximated from the Bohr formula as (e. g. Drake 2006):

$$\frac{\nu_H - \nu_L}{\nu_L} = \frac{m_e(M_H - M_L)}{M_L(M_H + m_e)} = \frac{\mu_H - \mu_L}{\mu_L}. \tag{1.1}$$

Here, ν_H and ν_L are the frequencies of the transition for the heavy isotope, H and the light isotope, L, m_e is the electron mass, M_H, M_L the atomic masses of the two isotopes and $\mu H, L$ the reduced masses of the atoms. From the above formula is is clear that an isotope of higher mass will have a transition frequency that is higher, compared to the lighter isotope, which implies a blueshift of the spectral line. Since isotopes of various elements only differ by a few neutron masses it is evident that the isotopic shifts of the transition frequencies due to the mass effect become vanishingly small for anything but the lightest atoms, as it is proportional to the fractional change of the reduced mass. The addition of a neutron to the atom does not change the electronic field appreciably, and thus only has a small effect on the electron configuration. The largest shift is observed between lines of hydrogen and deuterium, where the H-α line of deuterium has a blueshift of ~ 1.7 Å compared to the line of hydrogen. Even for Li, the isotopic line shift of ^{6}Li of the doublet line at 6707 Å is only 0.13 Å, or $\sim 6\,\mathrm{km\,s^{-1}}$, compared to the wavelength of the dominant ^{7}Li line. These values should be compared to the resolving power of modern day spectrographs, which is about 0.05 Å or roughly $3\,\mathrm{km\,s^{-1}}$. Considering that in cool stars, the thermal line broadening alone often amounts to several $\mathrm{km\,s^{-1}}$, one sees that even for the lightest atoms (with the exception of H and He), we cannot resolve the isotopic shifts of the atomic lines. Even when there is an appreciable shift, it will often only manifest as an asymmetry in the line shape (see Caffau et al. (2014) for an overview of some recent results for light elements).

For slightly heavier atoms (C, N, O, Mg), the atomic line shifts due to the differences in isotopic masses are negligible, e. g. the Mg line at 6318.7 Å shifts only 0.007 Å between ^{24}Mg and ^{26}Mg. In these cases, the isotopic composition is often derived from the analysis of molecular lines of diatomic molecules. The change in the electron configuration of the molecules is small, as for the atoms, but the energy levels of the nuclear motion in the molecule will change appreciably since the vibrational and rotational structure is more strongly affected by the added neutron(s) (Herzberg & Mrozowski 1951). Indeed, if one views the diatomic molecule as a linear harmonic oscillator, the vibrational frequency is given as $\nu = (1/2\pi)\sqrt{k/\mu}$, with k being the force constant, and μ being the reduced mass *of the molecule*. This corresponds to a vibrational energy of $E_v = h\nu(v + 1/2)$, with $v = 0, 1, 2, ...$ being the

vibrational quantum number. Since k is determined by the electronic structure, which is essentially the same for two isotopic molecules, the relative change of oscillation frequency between two isotopic molecules will be:

$$\frac{\nu_{osc.,H}}{\nu_{osc.,L}} = \sqrt{\frac{\mu_{osc.,L}}{\mu_{osc.,H}}} \tag{1.2}$$

with the subscripts having the same meaning as in Eqn. 1.1. Since the difference in reduced mass of two isotopic molecules is significantly larger than for two isotopic atoms, the change to the vibrational energy levels will change appreciably. Further, it is clear from Eqn. 1.2 that the frequencies of the heavier isotope will be lower, and hence the transitions of the heavier isotope will appear redshifted, opposed to the atoms, where the heavy isotope will have blueshifted lines. In addition, also the rotational structure will change when the isotopes are changing, due to the rotational constant being inversely proportional to the reduced mass, but this shift is much smaller than the shifts arising from the vibrational levels.

Even with the larger spectral line shifts present in molecules, in many cases the line shifts are still small, making the analysis challenging. The detection of these subtle features associated with different isotopes require observations of the highest quality, both in terms of signal-to-noise (S/N), as well as spectral resolution, in combination with detailed modeling of the stellar atmosphere.

Magnesium belongs to the so-called α-elements, which refers to the main formation channel, namely through α-captures during nuclear burning. It is an important element in stellar abundance studies for several reasons. Not only does it have strong resonance lines that can be detected over a large range of metallicities, but it is also one of the most important electron donors in the atmospheres of cool stars. Magnesium has three stable isotopes, ^{24}Mg, ^{25}Mg, and ^{26}Mg, with the vast majority of Mg being in the form of ^{24}Mg, when one looks at field stars in the Solar neighborhood (Yong et al. 2003b). This is particularly evident at metallicities below $[\mathrm{Fe/H}] = -1.0$ dex[1], where at least 90% of the Mg is in the form of ^{24}Mg. When going to higher metallicities, a sharp upturn of the heavy isotopes is seen for reasons that will be discussed more in Section 1.3 For the Sun, the percentage distribution of [^{24}Mg:^{25}Mg:^{26}Mg

1 Throughout this thesis, we adopt the customary base-10 logarithmic astronomical scale for abundances, where H is defined to be $\log \epsilon_{\mathrm{H}} = 12$ and $\log \epsilon_{\mathrm{X}} = \log(N_{\mathrm{X}}/N_{\mathrm{H}}) + 12$, with N_{X} and N_{H} being the number densities of element X and hydrogen, respectively. The 'bracket notation', [X/H], indicates the abundance of element X measured relative to the abundance of the same element in the Sun, i. e. $[\mathrm{X/H}] = \log \epsilon_{\mathrm{X}} - \log \epsilon_{\mathrm{X},\odot}$.

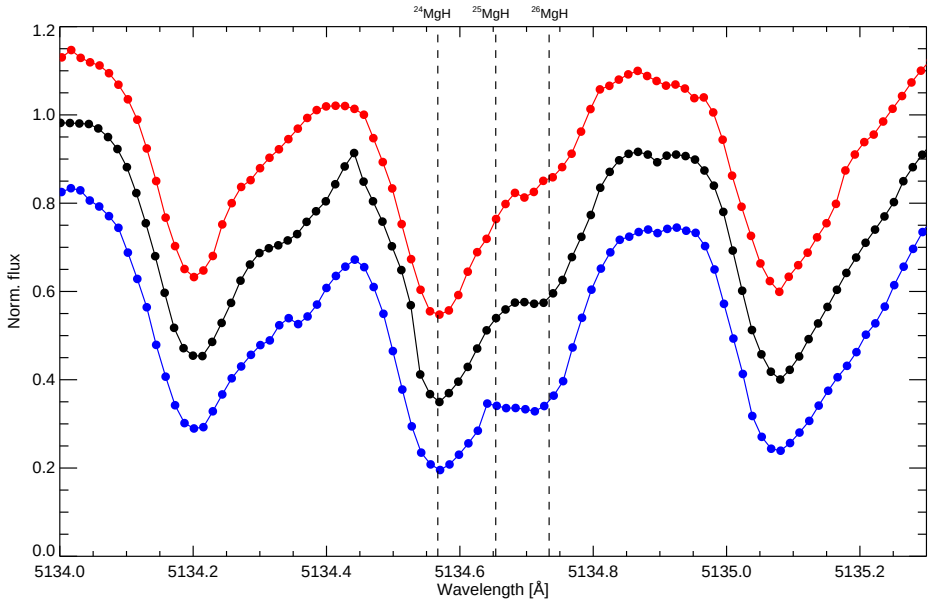

Figure 1.1: Three examples of the observed MgH feature at 5134 Å in red giant stars, with the central wavelength of the three isotopic transitions indicated by vertical, dashed lines. Even by eye, the difference in line asymmetry is evident. The spectra have been shifted vertically for clarity. The S/N in these spectra is $\sim$ 150.

] is [79:10:11], so even at high metallicity, most Mg is in the form of ^{24}Mg. In some special cases, however, the fraction of the heavy isotopes is observed to be as high as [60:20:20] (Yong et al. 2003b).

As discussed above, the isotopic shifts of the atomic Mg lines are too small to be resolved by current spectrographs, and even if we were able to reach high enough spectral resolution, the shift is significantly smaller than the line broadening already present in stellar absorption lines. The isotopes of Mg can instead be inferred from measurements of the molecular MgH features in the optical region around 5135 Å, where the isotopic shifts are larger ($\sim$ 0.09 Å and $\sim$ 0.17 Å shifts of ^{25}MgH and ^{26}MgH respectively, relative to the ^{24}MgH transitions). In Fig. 1.1 we show examples of one of the observed MgH features in three of the stars analyzed in this work. Even at spectral resolving powers $R > 100\,000$, the signatures of the heavy isotopes only show up as asymmetries in the red wings of the MgH lines, and it is clear that both high S/N and high resolution are needed simultaneously, if one wants to derive precise isotopic ratios. However, it is also evident, that with the resolution and S/N of the spectra shown in the figure, even small differences in the line asymmetries can be seen.

Since only MgH features can be used for the derivation of the Mg isotopic mixture in stars, this means that observations are restricted to cool stars, with effective temperatures, $T_{\rm eff} \lesssim 5200$ K. Above these tempera-

tures, the stellar atmospheres are too hot for any observable amount of MgH to form. On the other hand, it is also adviceable to avoid stars of too low $T_{\rm eff}$, as the spectra then become dominated by other molecular features, making continuum placement extremely difficult, so one tries to stay above $\approx 3700\,\mathrm{K}$. This limits MgH studies to either nearby dwarf stars, or red giants, in order to reach the necessary S/N (> 80, but preferably > 150) in a reasonable amount of observing time. On the other hand, the low gravity in giants also serves to weaken the MgH features, meaning that below metallicities of $[\mathrm{Fe/H}] \sim -1.5\,\mathrm{dex}$ the MgH features become so weak that they are not practically observable, whereas they can readily be observed in dwarfs down to $[\mathrm{Fe/H}] \sim -2.5\,\mathrm{dex}$.

Mg isotope ratios have previously been measured in cool stars in the Solar neighborhood (Barbuy et al. 1987; Gay & Lambert 2000; Yong et al. 2003b; Meléndez & Cohen 2007). Such measurements have been used to constrain the metallicity at which AGB stars become an important source of enrichment in the MW halo, although the two groups investigating this reached different conclusions (Yong et al. 2003b; Meléndez & Cohen 2007). Measurements of Mg isotopes have also been used, in a few cases, to investigate the multiple population phenomenon in globular cluster (GC)s (Shetrone 1996; Yong et al. 2003a, 2006; Meléndez & Cohen 2009 and Da Costa et al. 2009), providing complementary information to what bulk Mg abundances can deliver (see Gratton et al. 2012 for an excellent review of the multiple population phenomenon). This has helped to put additional constraints on the internal evolution of the clusters.

1.3 THE PRODUCTION OF MAGNESIUM ISOTOPES

Isotopes of magnesium are particularly interesting in the context of Galactic chemical evolution, as they have the potential to provide a unique probe of the chemical enrichment timescale of a stellar population, due to the different production channels for the different isotopes, which will be discussed in the following.

1.3.1 *Massive stars*

At different stages in the evolution of massive stars ($> 10\,\mathrm{M}_\odot$), it is possible for these stars to produce both ^{24}Mg, as well as the heavy isotopes, ^{25}Mg and ^{26}Mg.

Core-collapse supernovae, in particular, are strong producers of ^{24}Mg. Here, ^{24}Mg is produced as a primary element through hydrostatic burning of carbon (Arnett & Thielemann 1985) or neon (Thielemann & Arnett 1985), and subsequently dispersed during the SN explosion (Woosley

& Weaver 1995). Here, a primary element refers to an element that is produced directly from fusion products in the star, starting from the fusion of H and He, where the preceding nuclear burning provides all the needed material to produce the element in question. Opposed to this are secondary elements, where the production depends on metals already present in the star at birth, like for instance the production of N in the CNO cycle. These elements need an initial metallicity seed to be produced, and an increase in secondary elements is expected when the metallicity of the supernovae increases. With ^{24}Mg being a primary species in massive stars, the production is independent of metallicity, and one expects ^{24}Mg to be present in all stellar populations, except Population III stars, which are entirely metal-free.

The two heavier Mg isotopes can be produced in core-collapse SNe through α-captures on ^{22}Ne, through the $^{22}\mathrm{Ne}(\alpha, n)^{25}\mathrm{Mg}$ and $^{22}\mathrm{Ne}(\alpha, \gamma)^{26}\mathrm{Mg}$ processes. Here it is worth noting that the production of ^{24}Mg through Ne burning is from α-captures on ^{20}Ne, which is a primary species, whereas ^{22}Ne is a secondary species and typically 90 % of the Ne is in the form of ^{20}Ne. Thus, these processes are dependent on an initial metallicity seed. Only when the metallicity reaches values larger than $[\mathrm{Fe/H}] \geq -1.0$ dex does one begin to see a significant contribution to the heavy Mg isotopes from this production channel (Alibés et al. 2001; Prantzos & Goswami 2001; Kobayashi et al. 2011). Below these metallicities, only trace amounts of the heavy Mg isotopes are produced in SNe, and any amount of the heavy isotopes observed in metal-poor stars have to have another origin than SNe. For more details on core-collapse SNe, we refer to the recent review of Nomoto et al. (2013).

Pre-supernova production of Mg isotopes is also possible in massive stars in a couple of cases. The first is fast rotating massive stars (FRMS) (or, spin-stars), which have been proposed as sources of chemical enrichment in the MW (e. g. Meynet & Maeder 2002; Hirschi et al. 2005; Cescutti & Chiappini 2010; Chiappini et al. 2011; Cescutti et al. 2013 and Cescutti & Chiappini 2014 to name a few). Here, rotationally induced mixing transports processed material from the deeper layers to the surface of the star, where it is lost to the interstellar medium (ISM) through an, initially slow, stellar wind. The study of Decressin et al. (2007) suggests that these stars can modify the isotopic abundances of Mg during their hydrostatic burning, but only at the very end of the main sequence (MS), and even at this point, only a slight production of the heavy isotopes occurs. At this point, the stellar wind releasing the material to the ISM is expected to have reached high velocities, as the star is approaching the Wolf-Rayet stage. On the other hand, FRMS can produce ^{24}Mg from proton capture on ^{23}Na, so these enrichment sources could still impact the isotopic distribution of Mg. It is worth

noting that the models of Decressin et al. (2007) are only concerned with a single metallicity, and it would be most interesting to see how the behaviour of the Mg isotopes changes with the metallicity of the star.

Interestingly, rotation also impacts the SNe models of Chieffi & Limongi (2013) that included rotation (at solar metallicity), predict a significant increase in the yields of the heavy Mg isotopes, compared to the non-rotating models. In addition, their rotating models typically predict a yield of ^{26}Mg that is twice that of ^{25}Mg. Heger & Langer (2000) also investigated the effect of rotation in massive stars and showed that they show a stronger radial gradient in their ^{26}Al abundance, relative to their non-rotating models. Since ^{26}Al decays to ^{26}Mg, introducing rotation does affect the final yields. Most other studies of spin-stars are mainly concerned with neutron-capture elements, and even though they cover a range in metallicities, the published studies provide no predictions for the Mg isotopes (e. g. Hirschi et al. 2005; Frischknecht et al. 2012 and Cescutti et al. 2013).

An additional production channel in massive stars has recently been put forward by Denissenkov & Hartwick (2014), who proposed super-massive (a few $10^4\,M_\odot$) stars as a source of light elements and Mg isotopes. These stars reach conditions that can activate the Mg-Al burning chain (more on this below) and should also be considered as an enrichment source. Their models are fully convective, so processed material can efficiently be transported to the surface of the star where it is lost to the ISM either through a stellar wind or through instabilities. By the end of their life, they are thought to collapse directly to a black hole, and no supernova is expected. These models were constructed to explain the anomalous abundance patterns observed in GCs and rely on some very specific assumptions (see Section 1.4). However, if such stars are active in GCs, they could also be present elsewhere.

1.3.2 *The AGB channel*

When low- to intermediate-mass stars ($\leq 10\,M_\odot$) reach the AGB phase, they become a source of many different elements, created in different regions, which can be released to the ISM through thermal pulses. Briefly, the evolution of an AGB star is as follows: The AGB stars are no longer burning material in their core, but are generating energy from H-shell burning below the convective envelope, as well as burning in a He-shell outside the degenerate core. The He shell is very thin and will eventually become unstable and go through a shell flash burning, producing a huge amount of energy. This, in turn, will power convection in the region between the He shell and the H shell (the intershell), mixing the products from the He shell burning into the intershell region (flash-

driven convection). In addition, the energy input from the He shell flash will serve to expand the star (a thermal pulse), shutting off the burning in the H shell, as it expands and cools. This cooling will also increase the opacity in this region, allowing the base of the outer convective envelope to move inwards. If the envelope extends deep enough, it will reach the intershell region and transport material that has been exposed to He burning, to the surface of the star, a so-called third dredge-up (TDU). Following this, the star will contract until the H shell is reignited. The nuclear ashes left behind by the H shell will gradually increase the pressure and temperature at the bottom of the intershell region, until the He shell reignites and the star undergoes another thermal pulse (see Karakas & Lattanzio 2014 for more details). In this way, it is possible for AGB stars to tap into the deep layers of the star and enrich the ISM in processed material.

Models of stellar nucleosynthesis predict that an important source of especially the heavy Mg isotopes are AGB stars. However, the temperatures ($> 300 \times 10^6$ K) required to activate the nuclear burning responsible for the production of heavy Mg isotopes mean that only intermediate to massive AGB stars with masses $4\,M_\odot \geq M \geq 10\,M_\odot$, are viable sources (with small mass changes, depending on the metallicity of the stars). Lower-mass AGB models simply do not reach hot enough temperatures to activate the nuclear burning reactions producing Mg, except the $3\,M_\odot$ models, which can have one or two thermal pulses reaching the required temperatures in some cases. However, a larger number of thermal pulses is required for any significant Mg production. Throughout the rest of this thesis, unless otherwise stated, by "AGB stars" I refer to intermediate mass AGB stars with $M \geq 4\,M_\odot$. If concerned with lower-mass AGB stars, this will be stated explicitly.

Although not an important source of the main magnesium isotope, ^{24}Mg, AGB stars are still able to produce some amount of ^{24}Mg through proton captures on ^{23}Na (Wallerstein et al. 1997). This process requires an initial seed of ^{22}Ne to create ^{23}Na, so the efficiency of this process is somewhat dependent on the initial metallicity of the star, where the lowest metallicity AGB stars will have less ^{22}Ne available. However, some primary production of ^{22}Ne can also occur through the chain $^{14}\mathrm{N}(\alpha,\gamma)^{18}\mathrm{O}(\alpha,\gamma)^{22}\mathrm{Ne}$, if ^{14}N is created through primary carbon burning. This, in turn, can result in a small ^{24}Mg production, irrespective of the initial Ne seed.

The heavy Mg isotopes, ^{25}Mg and ^{26}Mg, on the other hand, are efficiently produced in AGB stars, according to current models. This can occur at two main nuclear burning sites, making the model yield computations rather complex, as they depend on e. g. temperature, mixing prescription, metallicity and mass-loss, and often all possible produc-

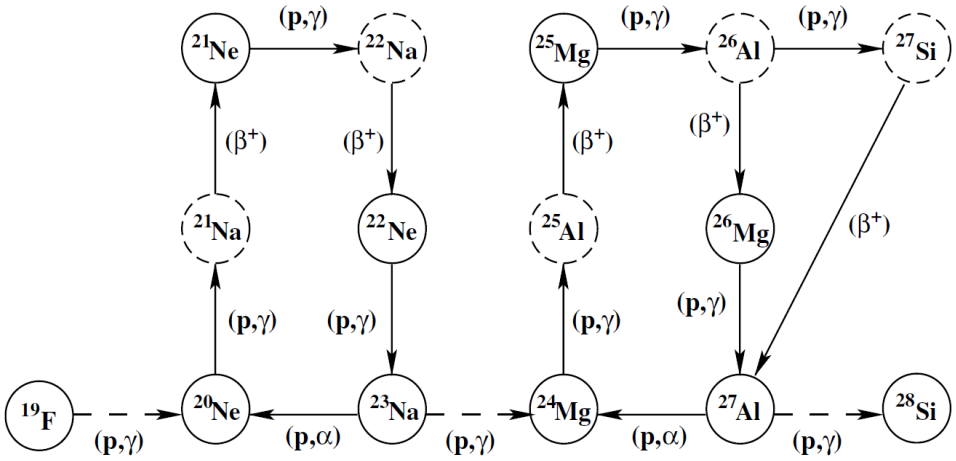

Figure 1.2: A schematic illustration of the NeNa and MgAl burning chains in AGB stars. The dashed circles indicate unstable isotopes. Adopted from Karakas & Lattanzio (2003).

tion sites will be active at some point during the AGB phase, so one cannot exclusively look at a single process.

^{25}Mg and ^{26}Mg can be produced in the helium burning shell, through the same α-capture process as described for the supernova channel. This occurs at a temperature of 300×10^6 K, and is a metallicity-dependent process, as it requires an initial ^{22}Ne seed (Karakas & Lattanzio 2003). However, as noted above, some primary production of Ne may occur, especially at low metallicities, but the production depends on the uncertain details of the TDU, without which no production occurs.

If the temperatures in the H-burning regions of the AGB stars are sufficiently high, it is possible to activate the Mg-Al chain, as will be explained further below. Here, a series of proton captures and β^+ decays will transform ^{24}Mg to ^{25}Mg and ^{26}Mg, as well as ^{27}Al (Eqn. 1.3 and Fig. 1.2):

$$^{24}\mathrm{Mg}(p,\gamma)^{25}\mathrm{Al}(\beta^+)^{25}\mathrm{Mg}(p,\gamma)^{26}\mathrm{Al}(\beta^+)^{26}\mathrm{Mg}(p,\gamma)^{27}\mathrm{Al} \tag{1.3}$$

This happens in the H-burning shell at temperatures of approximately 30×10^6 K.

If the stars are massive enough, they will also undergo hot bottom burning (HBB) at the bottom of the convective envelope. HBB occurs when the base of the convective envelope reaches temperatures high enough to sustain proton-capture nucleosynthesis. The lower density here, compared to the H-burning shell, means that temperatures of at least 60×10^6 K are required to activate the Mg-Al chain, with some dependence on the metallicity. A low- metallicity star has a higher density, because it is more compact than an equivalent high-metallicity star, so a

lower temperature is required for proton-capture nucleosynthesis, compared to a higher-metallicity star. Only the most massive AGB stars are expected to reach temperatures high enough to activate HBB. In addition, high metallicities tend to lower the temperatures at the bottom of the convective envelope (e.g. Ventura & D'Antona 2008; Fishlock et al. 2014) making HBB less efficient than at low metallicity.

Many uncertainties are still associated with the yields, and predictions coming from different modeling groups show a lot of variation (see e.g. Denissenkov & Herwig 2003; Karakas 2010; Doherty et al. 2014; Ventura et al. 2014; Fishlock et al. 2014). Different nuclear reaction rates, different treatments of convection (mixing-length theory (MLT) Kippenhahn & Weigert 1990 vs. full spectrum of turbulence (FST) Canuto & Mazzitelli 1991), as well as different assumptions about mass loss, all influence the final yields of the ^{25}Mg and ^{26}Mg isotopes. In particular, the two latter points are of importance, as they control the number of thermal pulses an AGB star goes through, before having lost its entire envelope to the ISM. When the star undergoes a thermal pulse, a TDU episode may occur if the convective envelope extends deep enough to reach the He-intershell. If this happens, processed material is brought from the intershell region to the surface. Thus, stars with a large number of TDUs will release material that has undergone a larger degree of processing through nuclear burning. This affects not only the Mg isotopes, but all abundances associated with AGB star nucleosynthesis. However, the models that experience HBB have no need for TDU to transport processed material to the surface, as this happens naturally through convection, since HBB takes place at the bottom of the convective envelope.

The AGB models that employ the FST prescription of convection tend to have higher temperatures at the base of the convective envelope, which leads to a more efficient processing of ^{24}Mg compared to the models using the MLT formulation. Also, the FST models undergo fewer and shallower TDU episodes, because of the choice of mass loss prescription in these particular AGB models. This also affects the final model yields, since each TDU enriches the outer stellar envelope in processed material, that can subsequently be lost to the surrounding ISM. Another difference in the yields between the two types of models is, that the MLT models predict a net *increase* in the overall Mg abundance. This originates from the production of the heavy isotopes in the He burning shell, discussed above (Karakas et al. 2006; Fishlock et al. 2014). The FST models, on the other hand, are so efficient at destroying ^{24}Mg during HBB, that an overall decrease in the Mg abundance is found. This is a consequence of the few TDU episodes that these models experience, as material from the inter-shell region is not brought to the surface of the star, so the convective envelope is essentially a closed box. The different convection prescriptions will naturally also influence the yields of other

elements associated with TDU, but since Mg isotopes are the focus of this thesis, the behaviour of the other elements will not be considered here, and I will refer the interested reader to the review by Karakas & Lattanzio (2014) and the remaining modeling papers cited above.

Common for all the AGB models is that they predict a depletion of ^{24}Mg, a significant increase in ^{25}Mg, often by more than an order of magnitude, and additionally some production of ^{26}Mg, typically less than ^{25}Mg. Furthermore, the ^{26}Mg that is produced will often be processed to the end of the Mg-Al chain, which results in an increase in aluminum and reduces the yield of ^{26}Mg to the ISM. This is also the process that is believed to be responsible for the Mg-Al anti-correlation observed in several GCs in the MW, which will be discussed in more detail in Sect. 1.4.

In summary, the Mg-Al chain is largely providing a re-distribution of the Mg isotopes, together with some production of Al, whereas the He-burning shell provides a production of ^{25}Mg and ^{26}Mg, which may increase the overall Mg content in the star, depending on the exact stellar model being used, and the assumptions used to treat the physics in the stellar interiors.

1.4 THE ROLE OF GLOBULAR CLUSTERS

It is well established that disk galaxies like the Milky Way form their stellar halos at least partly through accretion of satellite galaxies (e. g. McCarthy et al. 2012). Some of the GC systems that may have been present in these satellite galaxies have likely survived to the present day, although a large amount of stars may have been lost from the cluster itself. Some clusters may also have been completely disrupted. Even today, we observe clusters in the process of being dissolved (Odenkirchen et al. 2001), and such events have likely also occurred in the past. Globular clusters are believed to play an important role in the formation history of the MW, in particular in the formation of the MW halo. As illustrated by Leaman et al. (2013), two GC families exist in the MW, with one family likely having been formed in situ, whereas the other is more likely to have an accretion origin. Depending on the adopted theory for the enrichment history of GCs, these stellar aggregates may have lost up to 90% of their initial stellar population (D'Ercole et al. 2008), meaning that they can potentially have contributed with a large amount of stars to the oldest MW populations. This is further supported by the works of Martell & Grebel (2010); Martell et al. (2011) and Carollo et al. (2013), who have searched the halo for stars with the chemical signatures of GC stars, and estimated a lower limit of 17% of the MW halo stars could have originated in GCs. Thus, a good understanding of the properties and formation histories of GCs are crucial for understanding the chem-

ical evolution history of the MW, as their influence may be substantial, at least in certain parts of our galaxy.

Over the past few decades it has been realized that most, if not all, GCs host at least two populations of stars, removing their previous status as single stellar populations. This has spawned a renewed interest in GC studies, that aim to understand the underlying cause of the multiple populations observed. These populations reveal themselves through a number of different observational facts, that all need to be explained by models:

- Separate sequences of stars in GC color-magnitude diagrams on the MS, turn-off (TO), subgiant branch (SGB) or red giant branch (RGB), seen in high-quality photometry (e. g., Piotto et al. 2007, 2012; Milone et al. 2012b; Monelli et al. 2013).
- Variations in the Na and O abundances, which are anti-correlated (e. g. Ivans et al. 1999a; Yong et al. 2009; Carretta et al. 2011b, andKacharov et al. 2013). This is seen in all GCs.
- The abundances of C+N+O are found to be constant within the observational uncertainties (e. g. Dickens et al. 1991; Ivans et al. 1999b).
- Variations in Mg and Al abundances. Seen in some, but not all GCs. These are sometimes seen to be anti-correlated (Carretta et al. 2009a, 2013).
- Variations in the He content by up to $\Delta Y = 0.13$ (Piotto et al. 2007)
- In rare cases, variations in the Fe abundance is observed, (e. g. ω Centauri (Norris & Da Costa 1995; Smith et al. 2000; Johnson et al. 2008) or M22 Marino et al. 2009; Da Costa et al. 2009).
- The stars with anomalous light element abundances make up 30-70% of the current population of stars (Carretta et al. 2009a).
- Stars with anomalous abundances are exceedingly rare in the field (Martell & Grebel 2010).
- The abundance anomalies are observed in stars of all evolutionary stages, so an evolutionary explanation for this phenomenon is ruled out.
- There is no significant age spread between the various populations (< 1 Gyr), hence the mechanism responsible for the peculiar abundances acts on a short timescale.

- The stellar populations with anomalous abundances are often found to be more centrally concentrated, e. g. Lardo et al. (2011).

The above list is non-exhaustive in terms of observational facts that need to be explained by models of GC formation and evolution, but outlines the main findings. Normal field stars are found to be O-rich, Na-poor and Mg-rich, Al-poor, whereas a large fraction of GC stars are depleted in O and Mg, and enriched in Na and Al. These stars are usually referred to to as polluted, enriched or second-generation stars. For the remainder of this thesis I shall refer to these stars as *polluted*. It is worth noting that a few giants with these signatures have been discovered also amongst the halo field stars (Martell & Grebel 2010), likely stripped from GCs. The presence of these multiple populations is in fact so common that it has been suggested as a defining feature of GCs. For a recent review we refer the interested reader to Gratton et al. (2012) and references therein.

It has long been known that differences in the strengths of CN and CH molecular features can affect the observed colors of the stars (Bond & Neff 1969). In the context of light element variations in GCs, Grundahl et al. (2002a) showed that the N variations could be traced using Strömgren photometry. Also Yong et al. (2008a) and Marino et al. (2008) found that Na-rich or Na-poor stars could be identified from particular photometric colour combinations in the cluster color-magnitude diagram (CMD). The full connection between abundance variations and photometry was, however, only fully explained through theoretical modeling of the spectra by Sbordone et al. (2011), and was further explored in a study of a number of different photometric indices by Carretta et al. (2011a). Generally speaking, the observed photometric splittings in the CMD become more clear when using blue filters, compared to red, but whether the polluted population appears redder or bluer than its pristine counterpart depends on the exact photometric filter combination used.

In particular, the mechanism responsible for the light element variation is a matter of active research. The variation is commonly agreed to have been caused by self-pollution within the cluster, rather than being linked to the evolutionary state of the stars, since the variations are observed in stars of all stages of evolution, including MS stars. Stars currently on the MS of GCs are of too low mass to reach the temperatures required for nuclear burning that is advanced enough to produce the observed abundance variations (i. e. 25×10^6 K for the Ne-Na burning chain, and 70×10^6 K for Mg-Al, Denisenkov & Denisenkova 1990; Langer et al. 1993; Prantzos et al. 2007). The ejecta from SNe are usually not considered to have contributed to the enrichment because this would be inconsistent with the constant values of the iron-peak ele-

ments observed in most clusters. However, the study by Marcolini et al. (2009) indeed suggests that a combination of Type II and Ia supernovae can also explain the observed abundance variations in some cases.

One of the most widely accepted explanations for the intra-cluster pollution involves an early generation of stars of intermediate mass undergoing the AGB phase (Ventura & D'Antona 2009). Models suggest that these stars are able to activate the required nuclear burning processes, as well as to release the enriched gas in thermal pulses, where the released material has a low enough velocity that it can be retained within the gravitational potential well of the cluster (D'Ercole et al. 2008; Ventura et al. 2011; D'Ercole et al. 2012). This scenario, however, requires the GCs to have been about ten times more massive in the past to reproduce the approximate 1:1 ratio between members of the pristine and polluted populations of stars. If the GCs were significantly less massive, there would be too few AGB stars to provide enough material to form the polluted population. This assumption has recently been challenged by Larsen et al. (2012), who found that GCs in the Fornax dwarf galaxy could have been at most five times more massive in the past. Furthermore, the predicted AGB yields are in some cases at odds with what is derived from observations (Fenner et al. 2004; Bekki et al. 2007). Also, for the AGB scenario to be successful, models predict that only a narrow mass range should contribute to the intra-cluster gas, requiring a non-standard initial mass function (IMF). In addition, substantial disagreement between the yields from different models are also seen in the literature (Denissenkov & Herwig 2003; Karakas 2010; Doherty et al. 2014; Ventura et al. 2014).

The measurement of Mg isotopes may provide additional pieces of information, supplementing what can be inferred from abundance ratios. In most stars, the isotopic distribution is dominated by ^{24}Mg, whereas the amount of the two heavy isotopes, ^{25}Mg and ^{26}Mg, is significantly less , with the Solar values being [79:10:11], given as percentages of the three isotopes, ^{24}Mg, ^{25}Mg, and ^{26}Mg. The production of heavy Mg isotopes is rather complex, as discussed above, and as such, measurements of magnesium isotopes in GC stars can be used to yield detailed information about the polluters, compared to what elemental abundances can deliver.

Obtaining spectra of sufficient quality to measure the magnesium isotopic ratios is observationally challenging, as it requires spectra of very high resolving power ($R = \lambda/\Delta\lambda > 80\,000$), combined with exquisite S/N, preferably ≥ 150. Such measurements only exist for a few GCs, starting with the pioneering work of Shetrone (1996), who used the observed variations in heavy Mg isotopes to rule out deep mixing as the cause of the observed abundance variations. This provided a strong argument for the case of abundance variations being present already in

the gas that formed the polluted generation of stars, the now commonly accepted internal pollution scenario. Measurements of Mg isotopic ratios have been carried out also for NGC 6752 (Yong et al. 2003a), M13 (Yong et al. 2006), M71 (Yong et al. 2006; Meléndez & Cohen 2009) and ω Centauri (Da Costa et al. 2009). In all cases, a correlation has been observed between the amount of heavy Mg isotopes and [Al/Fe], which becomes particularly evident when the [Al/Fe] enhancement reaches values of ≥ 0.5 dex.

The production of heavy Mg isotopes also requires adopting the maximum allowed reaction rates for the $^{25}\mathrm{Mg}(p,\gamma)^{26}\mathrm{Al}$ reaction (Ventura & D'Antona 2008, 2011; Ventura et al. 2011). However, the models also predict that most of the initial ^{24}Mg is converted to ^{25}Mg. An experimental model by Ventura et al. (2011), where the reaction rate for proton capture on ^{25}Mg is increased by a factor of two, is able to explain the most extreme [Al/Fe] enrichmentsrved. This increase in reaction rate also reduces the final amount of ^{25}Mg. On the other hand, the models still predict a $^{25}\mathrm{Mg}/^{24}\mathrm{Mg}$ ratio that is significantly higher than the $^{26}\mathrm{Mg}/^{24}\mathrm{Mg}$ ratio, which is in contrast to the observations. Karakas et al. (2006), on the other hand, achieve $^{26}\mathrm{Mg}/^{24}\mathrm{Mg}$ ratios higher than $^{25}\mathrm{Mg}/^{24}\mathrm{Mg}$ in their models, but their adopted reaction rates also result in a net production of Mg, which is in contrast with the Mg-Al anti-correlation seen in a number of GCs. A similar behaviour is also observed for the most massive models in the computations of Fishlock et al. (2014).

Another popular class of polluter candidates are FRMS (Decressin et al. 2007), which also release light elements into the cluster environment through a slow wind at an early point in the cluster evolution. However, this scenario also requires an anomalous IMF in order to yield sufficient amounts of enriched gas. In addition, when adopting standard nuclear reaction rates, the FRMS only begin to release the heavy isotopes into the ISM once the stellar wind is so fast that the gas will escape the cluster potential. If these stars were to be the sources of the Mg isotope variations in GCs, this can only be achieved by enhancing the reaction rate of the proton capture on ^{24}Mg by three orders of magnitude. This would facilitate the production the heavy Mg isotopes before the onset of the fast stellar wind (Decressin et al. 2007) that appears at the end of their MS life. Such large changes are currently ruled out by nuclear physics (Longland et al. 2010). Such modifications are also required to reproduce the Mg isotopic distribution in the case of the GC NGC 6752, which Decressin et al. (2007) use to compare to their models. Using standard reaction rates, the FRMS provide a net production of Mg, mainly in the form of ^{24}Mg, so this would also result in a modification of the isotopic ratios. This would imply a reduction of the $^{25}\mathrm{Mg}/^{24}\mathrm{Mg}$ and $^{26}\mathrm{Mg}/^{24}\mathrm{Mg}$ ratios between the pristine and polluted populations, rather than the increase that is observed. Furthermore, from the models one

would expect a correlation between Mg and Al, which again contrasts the observations.

A variation of the massive star scenario was proposed by de Mink et al. (2009), who focused on the role of massive, interacting binaries as source of the abundance variations. These models are indeed able to convert some Mg into Al, but they do not provide detailed yields for the individual isotopes. If one assumes that the interacting binaries mainly process ^{24}Mg, then this source could explain some of the observed behaviour. In addition, interacting binaries provide a very efficient mechanism for mass loss, not requiring an anomalous IMF to produce enough enriched material. However, this scenario relies on the assumptions that the IMF of the polluted generation truncates at $\sim 0.8\,M_\odot$, and that all massive stars in the cluster are in interacting binary systems.

It has also been shown by Prantzos et al. (2007) that the conditions required to activate the Mg-Al burning chain can be reached in the core of massive stars ($30\,M_\odot < M < 100\,M_\odot$), but only at the very end of their MS evolution and for a narrow range of temperatures. At this stage in the stellar evolution, there exists no known mechanism that can simultaneously transport the processed material to the surface of the star and release it in a slow fashion. Rather, at this point, the mass loss is dominated by a fast wind, which a typical GC will have difficulties in retaining (Decressin et al. 2007).

Recently, two additional scenarios have been proposed. Bastian et al. (2013) propose that low-mass proto stars accrete enriched material before settling on the main sequence, again providing a mechanism for creating an enriched population of stars. In this scenario, the pollution can be achieved without having a non-standard IMF and without requiring the cluster to have been substantially more massive in the past. It does, however, rely on a number of assumptions about, e. g., the effectiveness of accretion on proto-stars and the survival time of the proto-stellar discs in a dense environment like a GC, which needs further detailed work to be fully applicable to GCs.

Finally, as discussed briefly earlier, Denissenkov & Hartwick (2014) propose supermassive ($M > 10^4\,M_\odot$) stars as a source of light elements. These models are able to activate the Mg-Al burning chain, and should also be considered in the context of GCs. They have the appealing property that they simultaneously explain the Na-O and Mg-Al anti-correlations, as well as the correlations between the heavy Mg isotopes and [Al/Fe]. Furthermore, they are fully convective, so that an efficient transport mechanism is in place.

However, their models need some very specific assumptions to explain the cluster abundance patterns. For instance they need to shut down nucleosynthesis once the helium abundance has increased by $\Delta Y = 0.15$, in accordance with the largest He spread measured in a

GC, by which point a large fraction of the mass of the supermassive star should already be lost to the ISM. Thus only an incomplete H burning has occurred. The shut-down of the nuclear burning can be achieved if it is assumed that these supermassive stars fragment on a relatively short timescale after their formation.

While these models certainly are appealing in terms of nucleosynthesis, they are not without problems. For instance, the depletion of O and simultaneous enhancement of Na, will happen together with an enrichment in He, and as a consequence, GCs with a comparable extent of the Na-O anti-correlation should also show comparable variations in He. This is contrary to what is observed, where very similar clusters in terms of metallicity and Na-O variations show very different He variations (e. g. NGC 228: $[Fe/H] = -1.32$, $\Delta Y = 0.013$ (Carretta et al. 2009b; Piotto et al. 2013); NGC 2808: $[Fe/H] = -1.14$, $\Delta Y = 0.14$ (Roediger et al. 2014; Milone et al. 2012a); NGC 6752: $[Fe/H] = -1.5$, $\Delta Y = 0.035$ Roediger et al. (2014), Milone et al. 2013). For a more in-depth discussion of these issues we refer to Bastian et al. (2015). In addition, Denissenkov & Hartwick (2014) only investigated models at a single metallicity of $[Fe/H] = -1.5$. It would be most interesting to see a larger suite of models covering a broader metallicity range.

In summary, all proposed candidates are able to explain parts of the observed behavior in GCs, but the complete observational picture still lacks a coherent explanation. As discussed by Bastian et al. (2015), even combining the mentioned candidates would not result in a model that can fulfill all of the observed constraints. So even though most of these, or maybe all candidate polluters likely are active at some point during the evolution of GCs, it seems that an additional, currently unknown mechanism is still required.

1.4.1 *The globular cluster 47 Tucanae*

The GC 47 Tucanae (NGC104) is one of the brightest GCs in the sky, with an apparent V magnitude of 4.09 (Dalessandro et al. 2012), rivaled only in brightness by ω Centauri. It is also one of the most massive GCs in the Milky Way, with a total mass of $7 \times 10^5\,M_\odot$ (Marks & Kroupa 2010), and furthermore it is at the metal-rich end of the GC population. Its close distance makes it one of the most well-studied clusters in our Galaxy. Photometric studies during the past decade have revealed that 47 Tuc contains multiple stellar populations. Two SGB populations were discovered by Anderson et al. (2009), who also noted a clear broadening of the MS, but were unable to identify distinct populations. More recently, Milone et al. (2012b) have also been able to identify two populations, identifying them on the MS, as well as on the SGB, RGB, and horizontal branch. They find that $\sim$30% of the stars currently observed

in the cluster belong to the pristine population, so that most stars will have been polluted to some extent. They also identified a third population of stars that make up only ∼8% of the cluster stars and visible only on the SGB.

Additional evidence of multiple populations has been put forward by Richer et al. (2013), who identified different proper motion anisotropies between the blue and the red MS stars, and this is particularly evident for the blue sequence. The stars belonging to the bluer sequence were also found to be more centrally concentrated, in accordance with the findings of Milone et al. (2012b).

A large number of spectroscopic abundance studies of 47 Tucanae are already available in the literature, dating back to the work of Dickens et al. (1979), who noted a variation in the nitrogen abundance, which was later confirmed by Norris & Freeman (1979), Hesser & Bell (1980), and Cottrell & Da Costa (1981), to name a few. Other studies also found evidence of variations in the light element abundances; for example Briley et al. (1994) identified variations in Na and found CN and CH band strengths to be anti-correlated in a number of stars at the MS turn-off, putting stringent limits on mixing scenarios as the cause of the variations. More recent studies have reported variations also in Na and O (Briley et al. 1996; Koch & McWilliam 2008; Alves-Brito et al. 2005; Dobrovolskas et al. 2014; Cordero et al. 2014). The last three studies also report variations in Mg and Al. In addition, indications of a variation of S was found by Sbordone et al. (2009). Numerous other studies have reported abundances for a larger range of elements (e. g., Brown & Wallerstein 1992a; Carretta et al. 2004; Alves-Brito et al. 2005; McWilliam & Bernstein 2008; D'Orazi et al. 2013; and Thygesen et al. 2014). All in all there is ample evidence of multiple stellar populations in 47 Tucanae.

Even though, due to its proximity, 47 Tucanae is exceptionally well-studied, a good understanding of its chemical evolution history is still lacking. Recently, Ventura et al. (2014) have proposed a pollution scenario for 47 Tucanae in the AGB scheme. They are able to explain a large part of the observed variation in Na, O, and Al, when assuming a degree of dilution with pristine gas within the cluster. However, to reproduce the distribution of pristine vs. polluted stars, the study does require the cluster to have been ~ 7.5 times more massive in the past, at odds with the constraints from the Larsen et al. (2012) study, although the Fornax clusters may have had different formation paths, considering the differences in mass (total mass in the 4 Fornax GCs $\sim 1 \times 10^6\,M_\odot$). Ventura et al. (2014) also need to truncate the IMF of the polluted population of stars at $5\,M_\odot$. On the other hand, no single polluter candidate is able to explain the full range of abundance variations observed, without violating one or more of the observational constraints (Bastian et al. 2015).

In Chapter 3 we expand the range of derived abundances in this GC, by analyzing optical spectra of the highest quality (in terms of spectral resolution and signal-to-noise), of 13 bright red giants. With this dataset we conduct a comprehensive study of abundances in 47 Tucanae, covering 27 different elements and adding measurements of Ru, Ce, Pr, and Dy to the previously known abundance pattern.

In Chapter 4, we build on the work of Chapter 3, and derive the magnesium isotopic mixture for the same sample of stars. In addition, we provide the first ever investigation of the influence of the use of 3D model atmospheres on the derived isotopic mixture. We also discuss potential pollution scenarios based on the results from Chapter 3 and 4.

1.5 THE MILKY WAY BULGE

The MW bulge is one of the most poorly understood components of our galaxy, mainly due to the high technical difficulties of observing it, with the stars being far away, and heavily reddened. Its formation and chemical evolution history is still a matter of debate, and much effort is currently put into unraveling this.

A significant amount of the information we possess about the chemical history of the bulge is derived from either photometry, or low-to-medium resolution, low S/N observations, where only a few studies have provided detailed *elemental* abundances from high-resolution spectra of the brightest stars (McWilliam & Rich 1994; Alves-Brito et al. 2005; Fulbright et al. 2006, 2007), or from micro-lensed dwarfs (Bensby et al. 2011a). A number of observational constraints have emerged, which need to be explained by any formation theory for the bulge. The majority of the bulge stars are found to be old ($\sim$ 10 Gyr), even if metal rich (Zoccali et al. 2003; Brown et al. 2010), although the study of Bensby et al. (2011a) identified stars as young as four Gyr. The bulge has a pronounced bar and it is known to have a large stellar population forming a boxy peanut with an X-shaped stellar distribution, composed largely of metal-rich stars ([Fe/H]> -0.5 dex, e. g. McWilliam & Zoccali 2010; Saito et al. 2011; Wegg & Gerhard 2013). In addition there is a more metal-poor population, traced by RR Lyrae stars, that may also be associated with the bar (Pietrukowicz et al. 2012, 2014), although this has been disputed by Dékány et al. (2013), who argued for a spherical distribution. This metal-poor population was also identified as a very minor component of the total stellar population by Wegg & Gerhard (2013), and only becoming pronounced at galactic latitudes $\geq -7.5°$. Several works have also found a vertical gradient in the metallicity above the Galactic plane (e. g. Zoccali et al. 2008; Gonzalez et al. 2011).

Two main scenarios are currently envisioned for the formation of the MW bulge. In the "classical" picture, the bulge is formed from a collapse of gas/merger of smaller systems, at very early times in the MW formation (Eggen et al. 1962; Aguerri et al. 2001). This implies a very short star-formation timescale ($\lesssim$ 0.5 Gyr), and an overall formation of the bulge at a much earlier time than the disk. The chemical signature of the bulge stars should thus be notably different from what is seen in other parts of the MW, like the thin and thick disc, as well as the halo. Early studies of the bulge chemical composition by e. g. Zoccali et al. (2006) and Fulbright et al. (2006, 2007) found significant differences between $\alpha-$elements in the giants of the bulge, and stars of the thin and thick disks in the Solar neighborhood. This led to the conclusion that the bulge was chemically distinct from the other parts of the MW. In particular, the bulge stars were found to be enhanced in the $\alpha-$elements, relative to stars in the disk, even at high metallicity, suggesting a much more rapid and efficient star formation in the bulge. That at least a part of the bulge is formed from several merger events at very early times is also supported by the finding of a bimodal distribution of metal poor RR Lyrae stars (Pietrukowicz et al. 2014).

The classical scenario is, to some extent, supported by simulations of e. g. Saha et al. (2012), who showed that an initially non-rotating classical bulge can be spun up by angular momentum exchange with a galactic bar, resulting in cylindrical rotation in the inner parts. This classical bulge will become part of the boxy/peanut shape and a metallicity gradient would be expected with distance above the plane, in agreement with observations. In addition, Aguerri et al. (2001) found that classical bulges can be puffed up by mergers, creating a steep brightness profile, as seen also in external galaxies with a bulge. These mergers also induce mixing with the inner part of the disk, and in addition, serve to thicken the disk, contributing to establish the thick disk. A prediction of this model is also that the thin disk forms at a much later point, after the bulge is already in place, and hence it should be kinematically and chemically distinct from the bulge.

The second formation scenario is the so-called "pseudo-bulge" scenario, where the MW bulge is formed as a result of one or more dynamical instabilities in the disk, meaning that the main part of the bulge has formed *after* the formation of the MW disk. This will take place on a longer timescale than the classical scenario, with bulge stars showing abundance patterns similar to that of the inner thick disk (Combes & Sanders 1981; Binney 2009). If more than one instability episode occurs, this also allows for the presence of multiple populations, with different chemical and kinematical properties, which is more difficult to produce in the classical collapse scenario.

In the past few years, a number of large, spectroscopic surveys have targeted stars in the bulge, delivering medium to high resolution spectra of tens of thousands of red giants. In particular the Abundances and Radial velocity Galactic Origins Survey (ARGOS) survey ($R = 11\,000$, Freeman et al. 2013) and the APOGEE project ($R = 22\,500$, Allende Prieto et al. 2008) have provided abundances of a number of elements in this part of the MW. The results from these surveys, together with early results from Alves-Brito et al. (2005) and Bensby et al. (2011a), have unveiled a much more complex structure of the bulge than previously thought. In particular, these studies have not found any significant differences between the $\alpha-$element enhancement seen in the thick disk and in the bulge, which has been used as a strong argument for the classical formation scenario. In addition, Gonzalez et al. (2011) also found that the metal-rich stars at high galactic latitude display a chemical composition closely resembling that of the galactic thin disk, suggesting that a part of the bulge population may also have a connection to the thin disk. This is supported by a number of $N-$body studies, showing that a boxy/peanut bulge will arise as a natural consequence of the dynamical evolution of a disk in many cases (see e. g. Kormendy & Kennicutt 2004; Portail et al. 2015a).

It is now well-established that the bulge is composed of a number of stellar populations, separated in [Fe/H], as well as in the abundances of $\alpha-$elements. The exact number of populations is being debated, ranging from two (Hill et al. 2011; Bensby et al. 2011a; Uttenthaler et al. 2012) to up to five (Ness et al. 2013; Bensby et al. 2013), but it is clear that the bulge is a composite stellar structure. The study of Ness et al. (2013) further found that the two principal components show abundances very similar to what is seen in the inner part of the MW disk. These results have spawned renewed interest in the formation history of this MW component.

With the complicated populations that have emerged, no single formation event can be responsible for the stars in the inner Milky Way, in the region of the bulge. Rather, it is likely a combination of the two proposed scenarios. As argued by Ness et al. (2013), the fact that the two main components of the bulge metallicity distribution function (MDF) show a well-defined structure that changes with latitude, strongly suggests that no significant merger event has happened after the formation of these two components. If the opposite was the case, one would expect these two components to have been significantly disturbed and mixed, and should thus be indistinguishable in the MDF of the bulge at all latitudes. Since this is not observed, the "classical" bulge is likely just a minor component of the total stellar population. This is also supported by the simulations of Portail et al. (2015a,b), who used the observed density of red clump giants and kinematics from the BRAVA survey (Rich et al.

2007) to constrain their dynamical models of the bulge. Their results suggest that $20-45\%$ of the stellar mass in the bulge belongs to orbits that take part in the stellar orbits making up the observed X-shape.

While there is a lot of evidence for multiple populations being present in the bulge, a lot of details are still not well-understood, and a coherent picture of the bulge formation is far from established.

The measurement of magnesium isotopes in bulge stars can help addressing potential differences in formation timescales between the populations, as well as add another way of comparing the abundances found in the MW disk, to that seen in the bulge. In the classical formation scenario, the very efficient star formation in the bulge implies that the seed required for production of the heavy Mg isotopes in core-collapse supernovae will be reached at a much earlier point than in the disk. This would suggest that the heavier isotopes should be over-abundant relative to what is observed in the disk, that had less efficient star formation. This is also indicated by simulations of the chemical evolution of the bulge, where Kobayashi et al. (2011) predict the mass fraction of ^{25}Mg and ^{26}Mg in the bulge to be approximately twice the value of that in the thick disk at a metallicity of $[\mathrm{Fe/H}] = -0.5$. On the other hand, if the pseudo-bulge scenario holds, one would expect the Mg isotopic ratios in the MW bulge and the inner disk to be very similar, as the MW bulge essentially formed from the disk, regardless of the metallicity of the stars. As such, the Mg isotopes have the potential to investigate differences between these stellar populations and put additional constraints on their formation timescales.

While, by now, there exists a number of large studies of the elemental abundances in the bulge, it has not been attempted to derive isotopic abundances of any element. The work presented in Chapter 5 represents the first study of isotopes in this MW population.

1.6 STRUCTURE OF DISSERTATION

The thesis is structured as follows:

In Chapter 2 I will discuss the current state-of-the-art of stellar atmospheric models, and provide details about the usage of 3D hydrodynamical atmospheric models to compute spectral synthesis of the MgH features, which has not previously been done. Following this, in Chapter 3, I will present our analysis of a large number of elements in a sample of red giants in the GC 47 Tucanae (NGC104). We provide the most extensive set of measured elements to date for this cluster, and the derivation of the stellar parameters and abundances will be the topic of this chapter. Here, we also provide the first-ever NLTE analysis of Al in any GC. This is found to have significant impact on the abundances of this key element, and may have consequences for studies in other

GCs. With these results, we aim at improving the understanding of the phenomenon of multiple populations in GCs.

In Chapter 4 I expand on the results from Chapter 3 and investigate the distribution of Mg isotopes in the same sample of stars. This has never been attempted for 47 Tucanae, and only one other cluster at similar metallicity has measurements of these isotopes. Thus, we add an important new data point to the sparse sample of isotopic measurements in clusters. In addition, we make use of sophisticated 3D hydrodynamical stellar atmospheres to investigate the effects of 3D on the isotopic distribution measured from the line shapes of the MgH molecular lines. Such an investigation has never been performed before, for any stars, and I demonstrate that the inclusion of full 3D atmospheric models has a non-negligible impact on the derived isotopic distribution. This will have consequences not only for GC research, but also for studies of Mg isotopes in field stars, where similar effects are expected.

In Chapter 5, the focus is changed to the bulge and the inner disk of the MW. Here we aim to add new constraints on the proposed connection between the MW bulge and disk, by investigating the Mg isotopic distribution in red giants in these two stellar components. Due to the large distance to the bulge, this presented an observationally challenging project, pushing the capabilities of existing instruments to their limits. The data obtained here allowed us to derive reliable Mg isotopic ratios for these stars, and provide additional insight into the potential connection between these two stellar populations. This represents, to the best of our knowledge, the first ever study of isotopes *of any kind* of stars in the inner MW disk and the MW bulge.

Finally, in Chapter 6 I present the overall conclusions from the work in this thesis, and propose three additional projects, where Mg isotopic measurements can help to shed light on stellar nucleosynthesis, and the chemical evolution of other components of the MW.

2 STELLAR ATMOSPHERIC MODELS

In order to interpret stellar spectra, as well as, derive stellar parameters, abundances and other diagnostics from spectroscopic observations, models of the stellar atmospheres are crucial. Since all the spectral line-formation as well as the formation of the stellar continuum takes place in the outermost part of the stellar envelope, we require a detailed description of this partly ionized gas, to make reliable interpretations of the observations. This means that a description of, in particular, the temperature and pressure structure of these parts of the star are essential.

A number of detailed codes to compute 1D models of cool stellar atmospheres ($\lesssim 10\,000$ K) have been developed for this purpose[1], with the most commonly used ones being the MARCS models (Gustafsson et al. 2008), the PHOENIX model grid (Husser et al. 2013), MAFAGS-OS (Grupp et al. 2009), and the ATLAS9/12 models (Kurucz 2005), with all work in this thesis using the ATLAS models. Although these models rely on some rather drastic assumptions, they have had remarkable success in explaining a large range of observed phenomena in stars. The vast majority of research in stellar spectroscopy relies heavily on the use of these models, and I will refer to 1D models as 'standard' or 'classical' models throughout this thesis. Although details in the different models differ, they all rely on the same basic assumptions:

- local thermodynamic equilibrium (LTE): The atomic level populations and ionization fractions of the gas are completely determined by the Boltzmann and Saha equations, respectively.
- Hydrostatic equilibrium: The pressure gradient equals the gravitational force on large scales, everywhere in the atmosphere. No macroscopic velocities are present.
- One dimensional: Any quantity of interest can be described by a single parameter, namely the depth in the atmosphere. The atmospheres are thus assumed to be static. The layers in the atmospheric model are generally assumed to be either plane-parallel, or, for very extended atmospheres, the MARCS and PHOENIX models employ spherical symmetry instead of the plane-parallel assumption.

1 For a more extensive list of model codes, also for hotter stars, see Table 1.2 in Stasińska et al. (2012).

- Energy flux conservation: The total radiative and convective energy flux is conserved everywhere in the atmosphere, with the convective energy flux typically being parametrized by some flavor of the MLT.

In addition to the above assumptions, the models are assumed to be chemically homogenous and non-rotating. Furthermore, effects from magnetic fields are ignored, as is chromospheric activity.

When the radiative transfer is computed under the above assumptions, it is clear that some additional broadening of the spectral lines is needed, when confronted with observations of real stars. This is largely a result of the inadequacy of MLT to properly describe convection, which is an intrinsically non-linear, multidimensional and time-dependent phenomenon. This problem is solved by introducing two additional parameters into the classical models, namely the micro- and macro-turbulence, which describe the additional broadening arising from convective gas motions in the outer layers of the star.

Microturbulence describes the gas motions on scales that are smaller than the photon mean free path, and are introduced already during the computation of the radiative transfer through the atmosphere, where the absorption coefficient is convolved with a microturbulent velocity profile:

$$\alpha_v = \alpha * \eta(\Delta v) \tag{2.1}$$

with $\eta(\Delta v)$ being the microturbulence profile and α being the absorption coefficient *without* microturbulence included, but still accounting for the remaining broadening mechanisms, like natural broadening, Stark broadening, pressure broadening and thermal broadening. The velocity profile is typically assumed to be Gaussian.

Macroturbulence, on the other hand, is a parametrization of the large-scale motions of the gas, where the typical size of the motions is larger than the photon mean free path. This additional broadening does not influence the radiative transfer, and is applied to the emergent spectrum, that is convolved with a macroturbulent broadening profile. Several different formulations of this profile exists, from a simple Gaussian profile, to the radial-tangential profile of Gray (2008). Often, a single value of the macroturbulent velocity is assumed, even in the more complicated formulations. For this thesis, we assume a single, Gaussian profile for the macroturbulent velocity.

However, even with the high degree of success of the above models, the simplistic description of convection means that effects arising naturally from convective motions, are not well-described. Inspecting Fig. 2.1, where we show an example of the observed solar surface, it

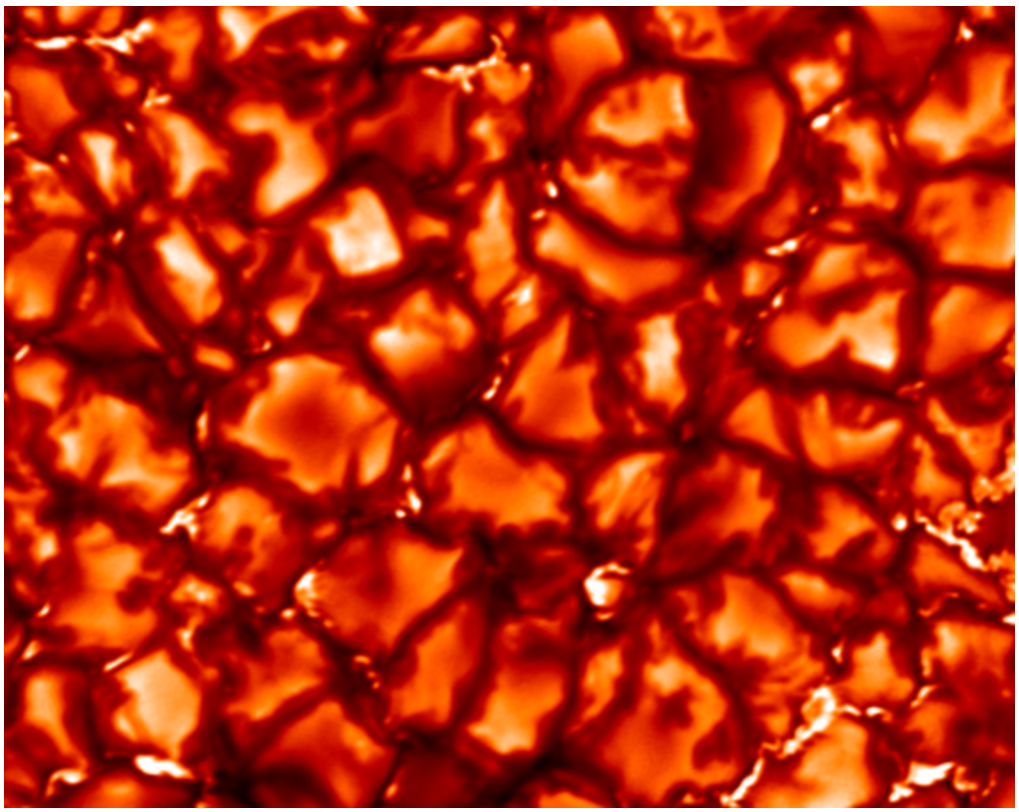

Figure 2.1: An example of an intensity observation of the solar surface, as seen by the Swedish Solar Telescope. The convective pattern is evident. Image credit: the Institute for Solar Physics, Sweden and Vasco Henriques.

is clear that there is a large amount of structure on the surface, that a 1D model is incapable of modeling. The stellar surface is covered in bright patches of hot, upflowing material (granules), interlaced with narrow, downflowing lanes of cooler gas. This is true for all stars with an outer convective envelope, including the giants we are analyzing in the present work.

Although, with very few exceptions, we cannot resolve the surfaces of other stars than the Sun, and thus only observe the integrated effect of the granulation on the stellar surface, the presence of convection still affects the formation of the spectra. The asymmetry in size and brightness between the upflowing granules and the downflowing lanes means that a larger fraction of the surface will move towards the observer, than away, resulting in a net blueshift of the line cores, whereas no such effect is seen in a 1D model, where the stellar surface is static. Furthermore, due to the temperature contrast between the granules and lanes, both the spectral lines, as well as the continuum, will vary in strength, again with the contribution from the granules dominating. This introduces line asymmetries in the observed spectra, which again cannot be

described by standard atmospheric models. In order to take these effects into account, one has to turn to state-of-the-art, three-dimensional, hydrodynamic models of the stellar atmospheres.

2.0.1 *CO^{5}BOLD 3D hydrodynamic models*

In order to make a realistic simulation of stellar convection and investigate the effects on the formation of the molecular MgH features, we computed two red giant models using the COnservative COde for the COmputation of COmpressible COnvection in a BOx of L Dimensions, L=2,3 (CO^{5}BOLD) code for computing 3D hydrodynamical model atmospheres (Freytag et al. 2012) in LTE. The code is capable of two different computation modes, namely star-in-a-box and box-in-a-star. The former is appropriate when dealing with red supergiants and AGB stars, whereas the box-in-a-star mode is suitable for less evolved stars. For our computations we used the box-in-a-star setup, which assumes a cartesian box, covering the outer part of the stellar envelope.

The code solves numerically the hydrodynamic equations for mass conservation:

$$\frac{\partial \rho}{\partial t} + \nabla \cdot (\rho \mathbf{v}) = 0, \tag{2.2}$$

energy conservation:

$$\frac{\partial \rho e_{\mathrm{tot}}}{\partial t} + \nabla \cdot (\rho e_{\mathrm{tot}} \mathbf{v}) + \nabla \cdot P\mathbf{v} + \nabla \cdot \mathbf{F}_{\mathrm{rad}} = 0, \tag{2.3}$$

and momentum conservation:

$$\frac{\partial \rho \mathbf{v}}{\partial t} + \nabla P + \nabla \cdot (\rho \mathbf{v})\mathbf{v} = \rho \mathbf{g} \tag{2.4}$$

in a box extending over the stellar atmosphere and the outer stellar envelope. Here, ρ is the mass density, e_{tot}, the total energy density per volume, F_{rad} the radiative energy flux, P, the pressure and $\mathbf{v}$, the velocity vector. For the box-in-a-star models, the gravity is assumed to be constant over the extent of the box, and the effects of magnetic fields are ignored. The box has periodic boundary conditions in the x and y directions, but open boundaries at both top and bottom, allowing for mass and radiation to flow in/out of the box. Opacities and the equation of state for the gas are not computed on-the-fly, but provided as look-up tables for the appropriate temperature, gravity and chemistry (for the opacity tables), and temperature and pressure for the equation of state.

Table 2.1: Model parameters for our CO^{5}BOLD 3D models.

ID	$T_{\rm eff}$	$\log g$	[Fe/H]	[α/Fe]	model time
HiMet	3970K	1.50	−0.50	+0.2	1472 h
LoMet	4040K	1.50	−1.00	+0.4	1111 h

As a starting point of a new model calculation, CO^{5}BOLD takes a precomputed 3D model with parameters close to those desired for the target model and scales the input structure to the expected values for the new model, with the scaling based on two 1D models matching the 3D model parameters. Each horizontal layer in the 3D model is then scaled by the same factor as the equivalent depth point in the 1D model. Such a simple scaling represents a reasonable starting point, but since several hydrodynamical quantities, like the turbulent pressure, are not scaled, there will be strong gradients present in both pressure, velocity and density. Because of this, the resulting model needs some time to settle into a stable state. Clear signs of the model being in a non-relaxed state is strong temperature trends in the horizontal averages between time steps in the model computation, for the individual layers. Only when the model has reached a stable state with small fluctuations, it can be considered relaxed.

After this initial settling, the model is evolved until the time baseline is long enough to select at least 20 model snapshots[2] that are sufficiently uncorrelated that their emergent spectra can be considered nearly independent (more on this in Sect. 4.2.3.2). For the giants we computed, this corresponds to around 60 days of stellar time for the total length of the simulation, with an approximate 1:1 correspondence to actual computing time on a modern quad-core desktop computer. For the models computed for this work, the atmospheric box is made of a grid containing $[140 \times 140 \times 150]$ cells in [x,y,z], with a total physical size of [4600 Mm $\times$ 4600 Mm $\times$ 2800 Mm]. Two models were computed with parameters appropriate to the stars analyzed in this work (Table 2.1) .

In Fig. 2.2, we plot the emergent bolometric intensity for all selected snapshots in our low metallicity model as an illustration. There is clearly little resemblance between the individual snapshots. The situation for our high-metallicity model is similar, with very little correlation between individual snapshots, as measured using the autocorrelation function.

With this selection of snapshots, the radiative transfer is computed for the spectral regions of interest, to yield the emergent spectrum. This is

2 A snapshot refers to a single instant in time of the full model run.

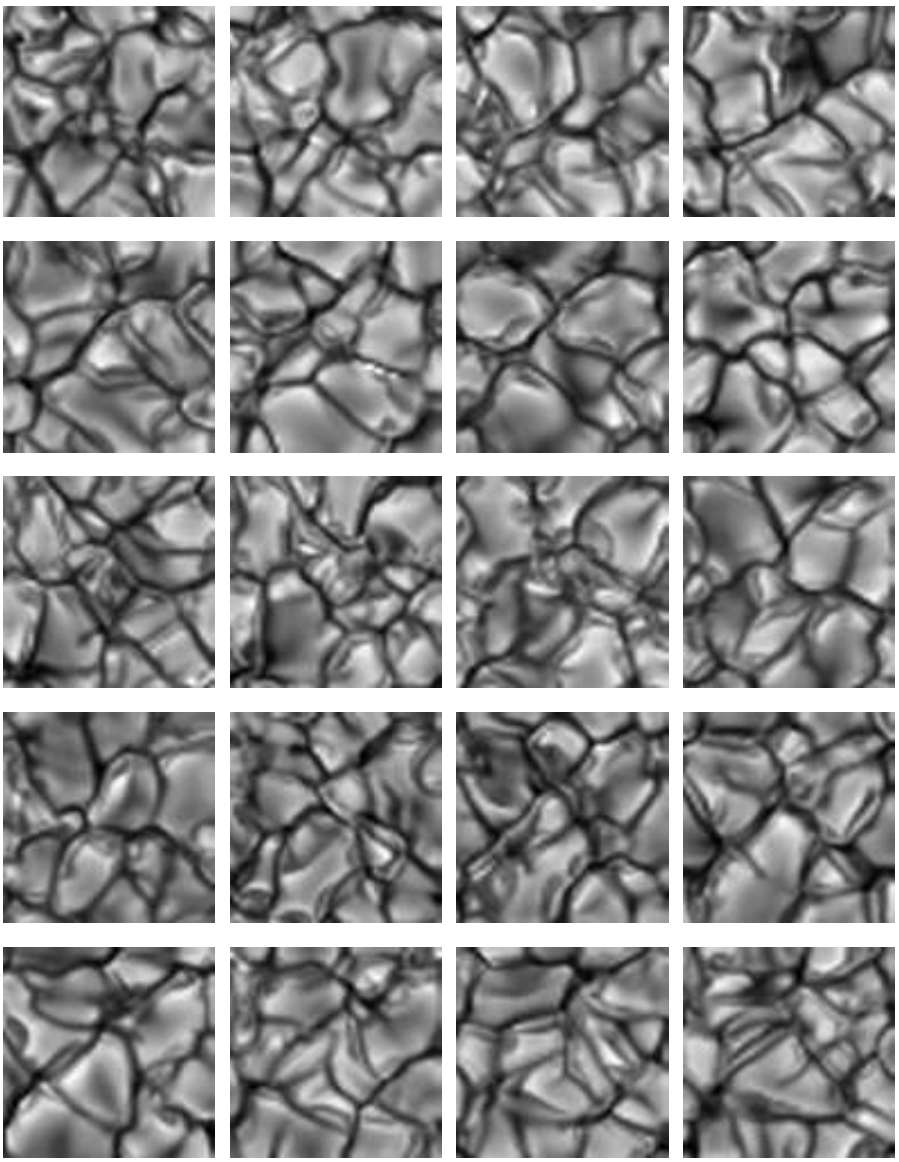

Figure 2.2: The emergent bolometric intensity for the 20 snapshots used in the spectral syntheses from our low metallicity model. Each snapshot has a size of 4600 Mm $\times$ 4600 Mm and $\Delta t = 60$ h of stellar time between each snapshot.

done with the associated code `Linfor3D`[3]. The results of the 3D spectral synthesis will be discussed in more detail in Sect. 2.1.1.

2.1 SPECTRAL SYNTHESIS

To compute the theoretical spectrum of the regions of interest, we apply both traditional 1D computations, as well as 3D computations. In most cases we use the `MOOG` spectral synthesis software (Sneden 1973; Sobeck et al. 2011; Sneden et al. 2012), but in a few cases we use the `SYNTHE` code of Kurucz (1993, 2005) in the Linux-ported version (Sbordone et al. 2004; Sbordone 2005) for our 1D computations.

The basic principles of both codes are very similar. A line list with atomic and molecular data for all transitions in the region of interest is provided by the user, together with a 1D atmospheric model. The radiative transfer is then computed along a number of rays through the stellar atmospheric model and the emergent flux is combined to yield the model spectrum. LTE is assumed everywhere, and since the models are one-dimensional, each layer in the atmosphere (72 in the case of our models) are represented by a single point. The radiative transfer is computed for a given value of the microturbulence, ξ_t, to simulate small-scale gas motion. After the spectrum has been computed, it is convolved with a macroturbulence velocity profile to account for the extra broadening arising from large scale gas motions. As such, any temporal, as well as horizontal variations in the atmospheric structure is neglected in the synthesis computation, which is a rather crude representation of the atmosphere of a star with an outer convective envelope. However, we are only now reaching a stage where the use of 3D atmospheres begins to be practical, although these models are still 2-3 orders of magnitude more time consuming to compute, compared to a standard 1D model. For these reasons, the vast majority of spectroscopic research on stars is still relying on 1D models. Further, 1D syntheses are orders of magnitudes faster to compute than syntheses based on 3D atmospheric models, where only small spectral windows with at most a few hundred transitions can be computed in a reasonable time frame. Considering the approximations done in the standard models, they do a remarkable job at explaining a large range of phenomena.

2.1.1 *Synthesis with `Linfor3D`*

For our 3D spectral synthesis, we use the `Linfor3D` synthesis code, which is made to work with the CO[5]BOLD models. The code computes the radiative transfer for a specified wavelength region, using a user-

3 http://www.aip.de/Members/msteffen/linfor3d

supplied line list with data for the transitions under consideration. In addition, an input file with the chemical composition of the atmosphere is required. The radiative transfer is computed along several rays through the plane-parallel atmospheric models. For each model cell, we compute the radiative transfer for three inclination angles, θ and four azimuthal angles, ϕ, including stricly vertical rays. Both the continuum intensity, I_λ^c, and the line intensity, I_λ^l, are computed for each wavelength step, as well as the absolute line depression, $D_\lambda = I_\lambda^c - I_\lambda^l$. Similarly, the flux and total equivalent width of the lines are computed.

In addition to the full 3D radiative transfer, the code also computes the radiative transfer for a horizontally averaged 3D model structure, <3D>, which is a 1D atmospheric model with the same average thermal and pressure structure as the full 3D model. For a direct comparison, a synthesis from a traditional LHD 1D model (Caffau & Ludwig 2007), with the same input physics as the 3D model is also computed.

For each 3D model, we selected a number of snapshots to cover the temporal evolution, and the influence of the changes in the granulation patterns on the emergent spectrum. The spectra computed for each individual snapshot were subsequently averaged to provide the final spectrum used in our syntheses of the observed MgH bands.

By inspecting the syntheses of the individual snapshots, we can investigate how much influence the changing convective patterns have on the shape of the MgH features. In Fig. 2.3 we present the non-normalized syntheses from the individual snapshots of our low-metallicity model. It is evident that both the line strength, line positions and the continuum level changes as a function of time. This is a direct consequence of the varying asymmetry between the hot granules and the cooler intergranular lanes, which is influencing the formation of molecules, as well as the amount of convective blueshift.

Plotting the same syntheses in Fig. 2.4, but now continuum normalized, it is clear that not only the line strength, but also the line shape change as a function of time.

However, when dealing with real observations, the stars are observed as point sources and the above variations will average out, as the light is integrated over the stellar hemisphere facing us. Thus, the temporal variation of the line asymmetry is only a concern when dealing with observations of a resolved stellar surface, which is only the case for the Sun. The effect of averaging over individual model snapshots in time corresponds, in some sense, to averaging over the stellar disc, as convective patterns on different parts of the stellar surface will not look identical. By averaging over time, this would correspond to observing different parts of the stellar surface, with different looking convective patterns, and then average these.

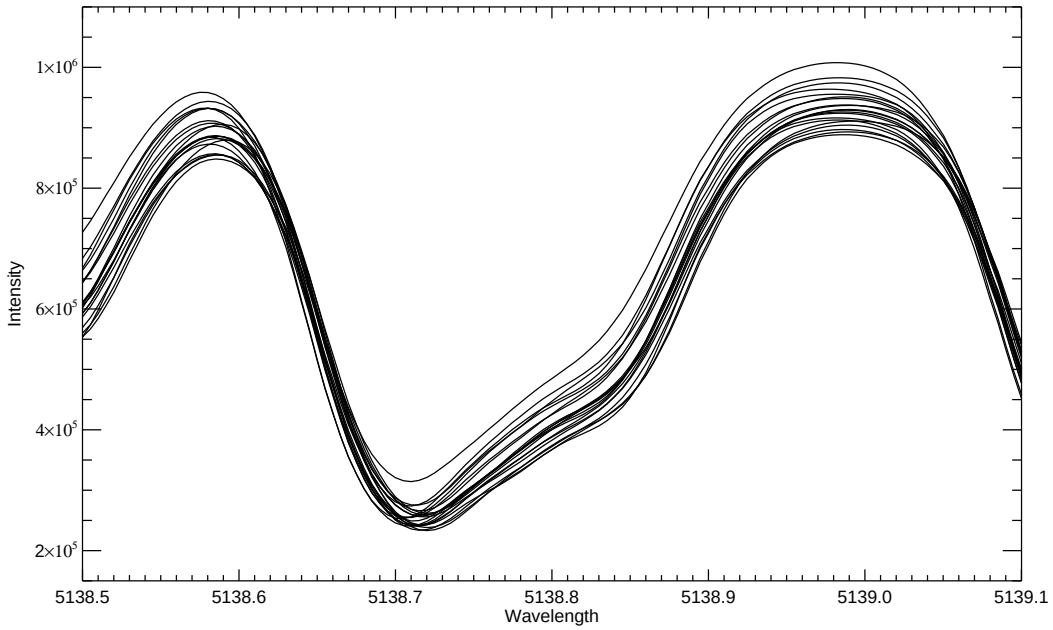

Figure 2.3: Syntheses of the MgH feature at 5138 Å for each individual snapshot of the low metallicity model

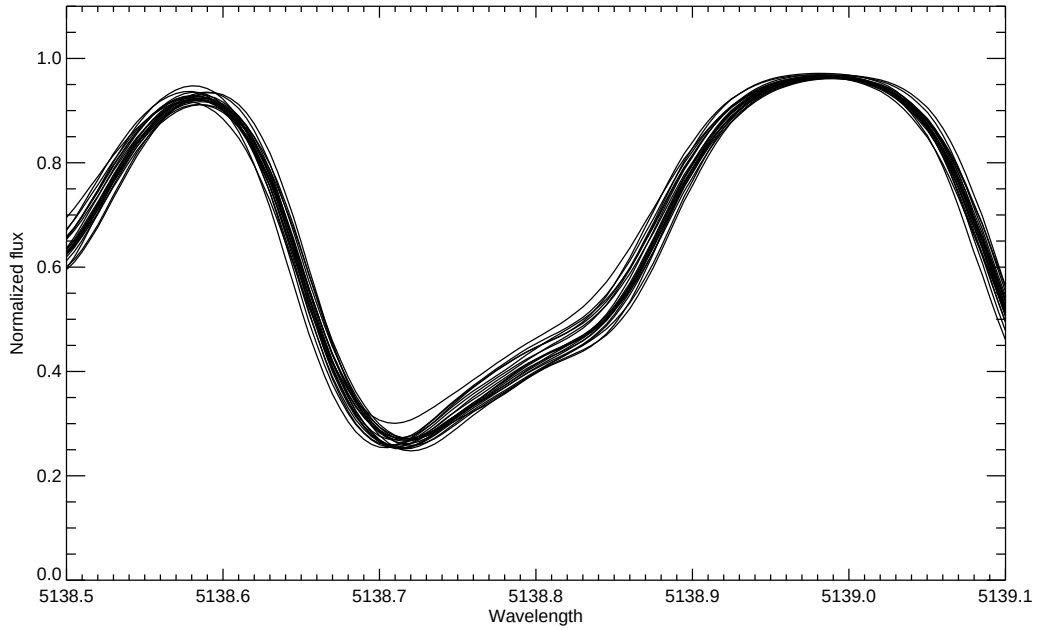

Figure 2.4: Normalized syntheses of the MgH feature at 5138 Å for each individual snapshot of the low metallicity model

Although we found that the average thermal structure of our 1D and 3D atmospheres are almost identical (see Sect. 4.2.3.1), the presence of temperature fluctuations are of importance. Especially for molecules, since the formation of MgH is not a linear function of temperature (Visscher et al. 2010). Thus, even if the average thermal structure is the same between 1D and 3D, we would still expect different molecular line formation in 3D, compared to a 1D model, where no temperature and density fluctuations are present. That there is a significant difference in both the shape and strength of the molecular lines is illustrated in Fig. 2.5, where we plot the continuum intensity map of a single snapshot of our low-metallicity model. Two points are indicated, one situated in a cool, intergranular lane and one in the central part of a hot granule. In the right hand side of the figure, we show the spectra of two MgH features, computed for the hot and cool regions. Both the shape and the strength of the spectral lines are very different in the two cases, with the spectrum originating from the cool part of the atmosphere being significantly broader, but also much weaker than the equivalent syntheses from the hot region. It is also clear that the syntheses from the upflowing granules have a net blueshift in comparison to the downflowing lanes, as one would expect. In addition, the lines are clearly shifted away from the laboratory wavelengths, shown by vertical lines.

Not surprisingly, the bright granules contribute more to the overall emergent intensity, both to the continuum, as well as to the flux in the MgH lines themselves. The very different broadening from the two different regions can be understood as follows. In the center of the granules, the line-of-sight velocity throughout the extent of the atmospheric model shows very little variation. This will result in a very small amount of velocity broadening to the part of the spectrum emerging from such a region. The intergranular lanes, on the other hand, have a much smaller horizontal extent, snaking their way down through the atmosphere, where turbulent eddies will be present at the interface between the downflows and upflowing granules. As such, the line-of-sight synthesis from a intergranular lane is significantly more likely to encounter cells with different velocities, compared to the synthesis from the center of a granule. This will lead to an increased velocity broadening of the synthesis from these regions.

Additional insight into the behaviour of MgH features in a 3D atmosphere can be gained by inspecting the correlation between the total feature EW and the continuum intensity, as in Fig. 2.6. Here, we show the feature EW for every synthesis at all horizontal positions and snapshots for the 5135 Å feature, *normalized to the local continuum*. A lot of variation in line EW is seen at any point in the atmosphere, in particular for the cooler regions, where a large range of line strengths are present. The weak anti-correlation that is present should not be taken as an indi-

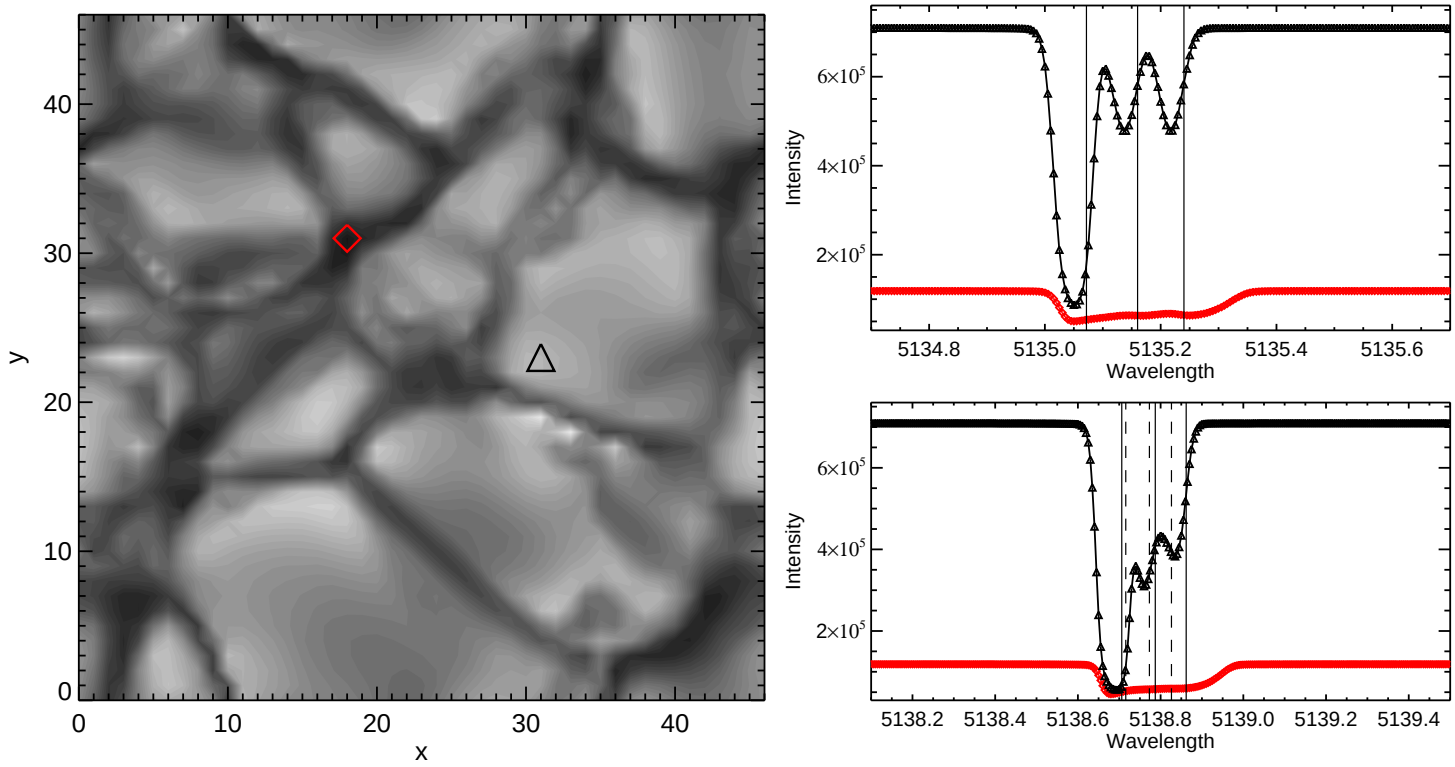

Figure 2.5: Left: The continuum intensity map of a single model snapshot. Bright areas indicate warm, outflowing gas. Indicated are two points for which we compute a spectral syntheses of the two MgH features shown to the right. In each syntheses, the red diamonds are a synthesis from the intergranular lanes, whereas the black syntheses are from the hot granule. Vertical lines show the laboratory wavelengths for the MgH transitions, where the bottom synthesis is a blend of two different MgH transisions (solid and dashed lines).

cation that the cool regions contribute more to the total line EW, as the total line strength is computed as the continuum-weighted horizontal average. As such, the hot regions will contribute more relative to the cool regions, due to the higher continuum flux. Thus, as would also be expected from Fig. 2.5, the cool regions are not contributing much, compared to the hotter regions. This also serves to illustrate that the naïve expectation that hot regions would contribute significantly less to the total line strength (due to more efficient dissociation of MgH), relative to the cooler areas, is not correct. The line behaviour is obviously much more complex than such a simplistic idea would suggest.

Looking now at the full syntheses of the MgH region of interest shown in Fig. 2.7, including all atomic and molecular blends, and averaged over all 20 snapshots, it is clear that the 3D syntheses exhibit both different line asymmetries as well as different line strengths, compared to the standard 1D LHD syntheses also shown. These differences, clearly arising from the different model structures, can be related to either different behaviour of the MgH features themselves, or to the fact that the blending lines respond differently to 3D effects than the MgH lines.

We can investigate this in a number of ways. For spectral lines, as well as the continuum, it is possible to define a contribution function, C, which essentially is the integrand of the formal solution to the radiative transfer equation. These functions can be cast in terms of intensity, flux, or equivalent width, in such a fashion that the integral of the contribution function over the optical depth considered, will yield the total flux/intensity/EW for a given wavelength. As such, the contribution function shows at which optical depth, the main line (or continuum) contributions arise, and can thus be used to determine whether a spectral feature forms predominantly in a deep or shallow layer of the atmosphere. This, in turn, can also be used to probe differences between 1D and 3D models, as the temperature structure, as well as temperature fluctuations in the 3D models, may influence the line formation.

In Fig. 2.8, we plot

$$\frac{dW_F}{d\log(\tau_{\rm Ross})} = \frac{C_F^W(\log(\tau_{\rm Ross}))}{\langle F_\lambda^C \rangle} \tag{2.5}$$

against $\log(\tau_{\rm Ross})$. Here, W_F is the total line equivalent width for the flux spectrum, C_F^W is the line flux contribution function, F_λ^C is the flux in the continuum for the wavelength region of interest, and $\tau_{\rm Ross}$ is the Rosseland optical depth. The division by F_λ^C is necessary to convert from flux to equivalent width.

The contribution function shown in Fig. 2.8, is the average continuum function computed from all selected snapshots in our low metallicity

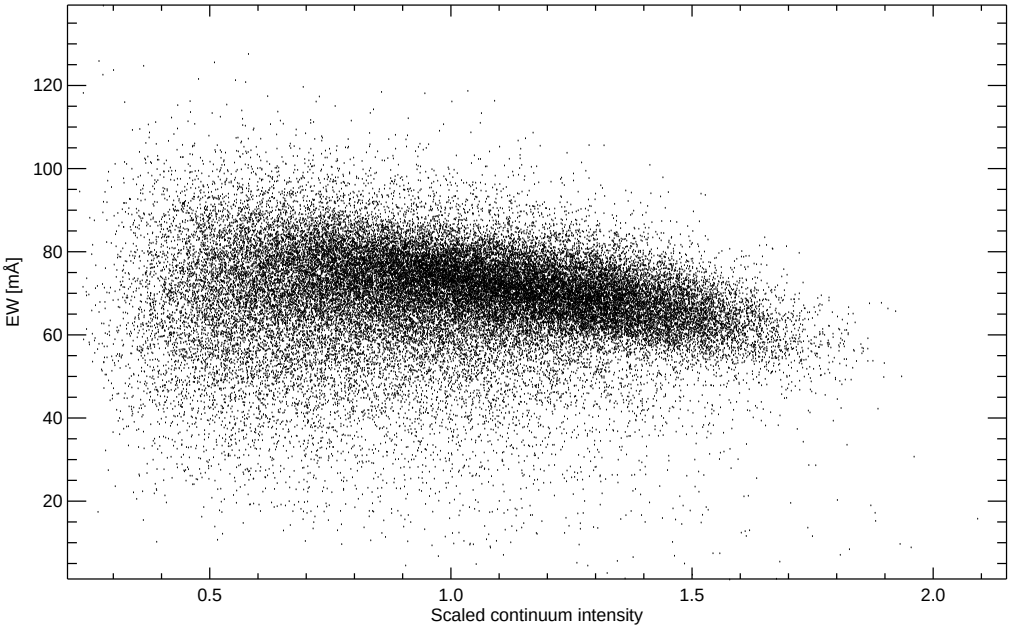

Figure 2.6: The correlation of the continuum intensity (divided by the mean intensity) and the EW of the MgH feature at 5135 Å for all horizontal positions and all snapshots of the low metallicity model

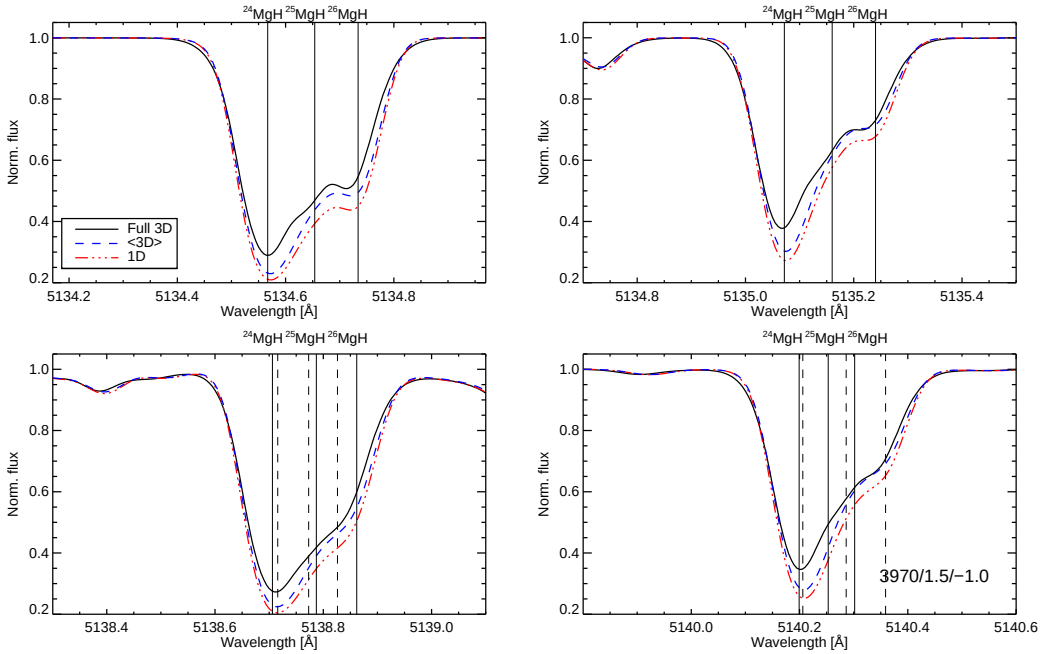

Figure 2.7: Syntheses of the four MgH regions of interest, including all blending lines, for the low metallicity model. Shown are the full 3D (solid), <3D> (red dashed) and 1D LHD (blue dot dashed) syntheses.

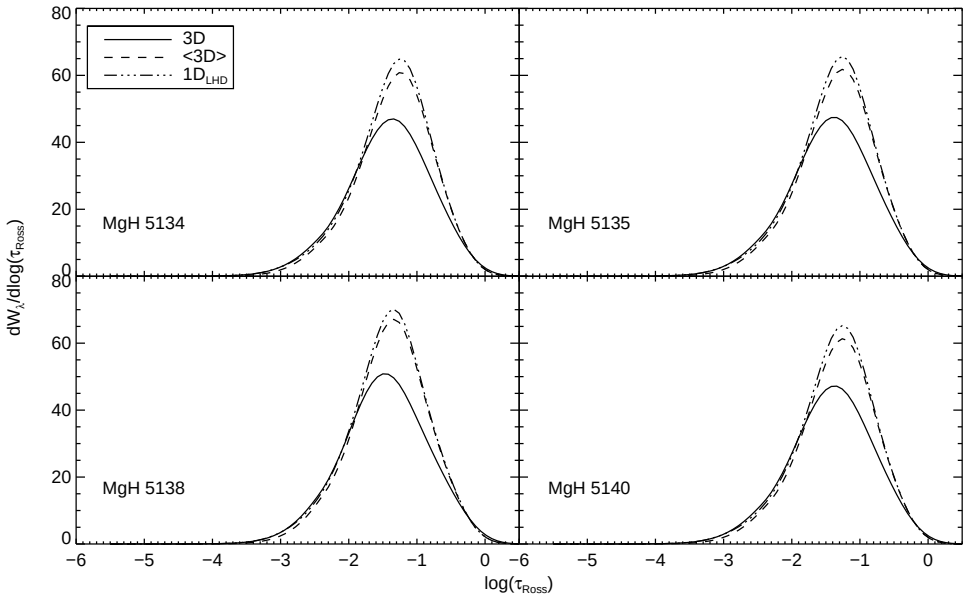

Figure 2.8: Contribution functions of the flux EW for MgH for each of the four features used, as a function of optical depth. Shown for the full 3D (solid), <3D> (dashed) and 1D$_{LHD}$ (triple-dot dashed) models.

model. It is shown for each of the four MgH features, assuming an isotopic mixture of [^{24}Mg:^{25}Mg ^{26}Mg] = [80:10:10]. It is clear that both in 1D and 3D, all four molecular features form relatively deep in the atmosphere, around -2 in log(τ_{Ross}). They show no significant difference in main formation depth, although in the full 3D the main contribution to the lines come from slightly shallower layers. Further, it is seen that the molecular lines form over a fairly large region of the atmosphere.

From the contribution functions it is seen that in 3D, the molecular line-formation appears less efficient than in 1D. This is consistent with what is seen in the actual spectral syntheses, of MgH only, where the features are weaker in 3D than in 1D (Fig. 2.9, top). Thus, the fluctuations in temperature may serve to dissociate molecules more efficiently than in a static 1D atmospheric model, resulting in an overall reduction of the strength of the individual MgH features.

In Fig. 2.9, bottom, we show the same syntheses, but now with the MgH features of the 1D syntheses scaled to have the same core strength as the full 3D syntheses. Clearly, the difference in line asymmetry between 1D and 3D is minor for these lines.

Looking now at Fig. 2.10, where we plot the 3D, <3D> and 1D LHD syntheses of the blending lines, with the MgH features removed, it is clear that the blending features exhibit both a very different shape and significant convective lineshifts in 3D, relative to the 1D models, in particular for the 5135 Å and 5138 Å features. The overall strength of these features, on the other hand, remain roughly the same between 1D and 3D (note the different abscissa scaling compared to Fig. 2.9). The excep-

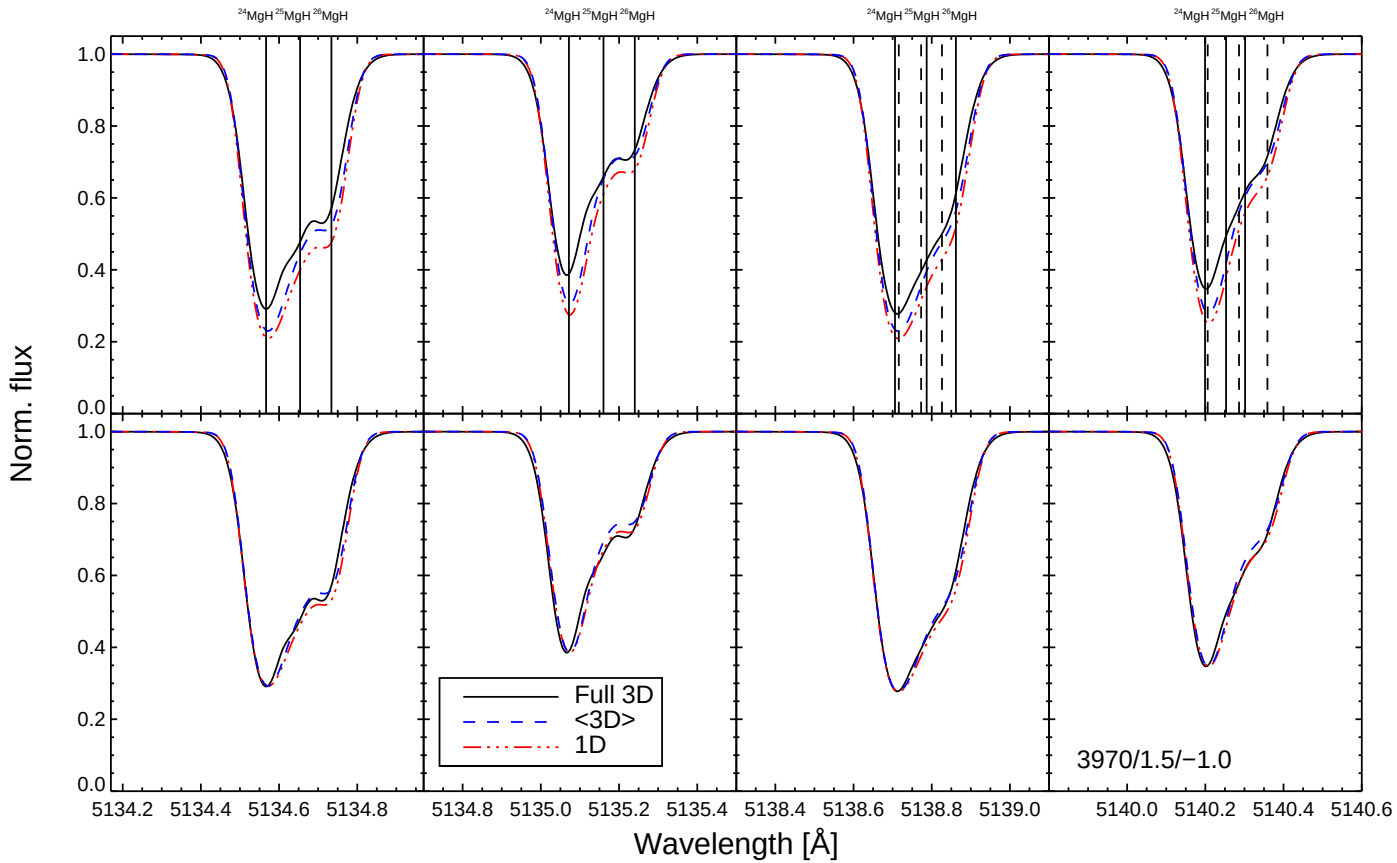

Figure 2.9: Top: Full 3D, <3D> and 1D LHD syntheses of the four MgH features, not including blends from other species. Bottom: As above, but with the 1D syntheses scaled to the same core strength as the full 3D synthesis. In the bottom right corner is shown $T_{\rm eff}/\log g/$[Fe/H] for the model.

tion being the region around 5140 Å, where the blends are very weak in the [Fe/H] $= -1.0$ dex model. Thus, it is seen that the difference in the line strength of the full syntheses of the MgH region is mainly related to the MgH lines themselves, responding differently to 1D and 3D, being weaker in 3D. On the other hand, the difference in the asymmetry of the features arises from the blending lines responding differently to 3D. Most likely, some very temperature-sensitive transitions are included in the line-blends, which could explain the difference between the models. This underlines the importance of ensuring that all blends are properly accounted for, and shows that, whereas 3D effects on the shape of the MgH features themselves does not appear large for the models considered here, one cannot simply ignore 3D effects altogether.

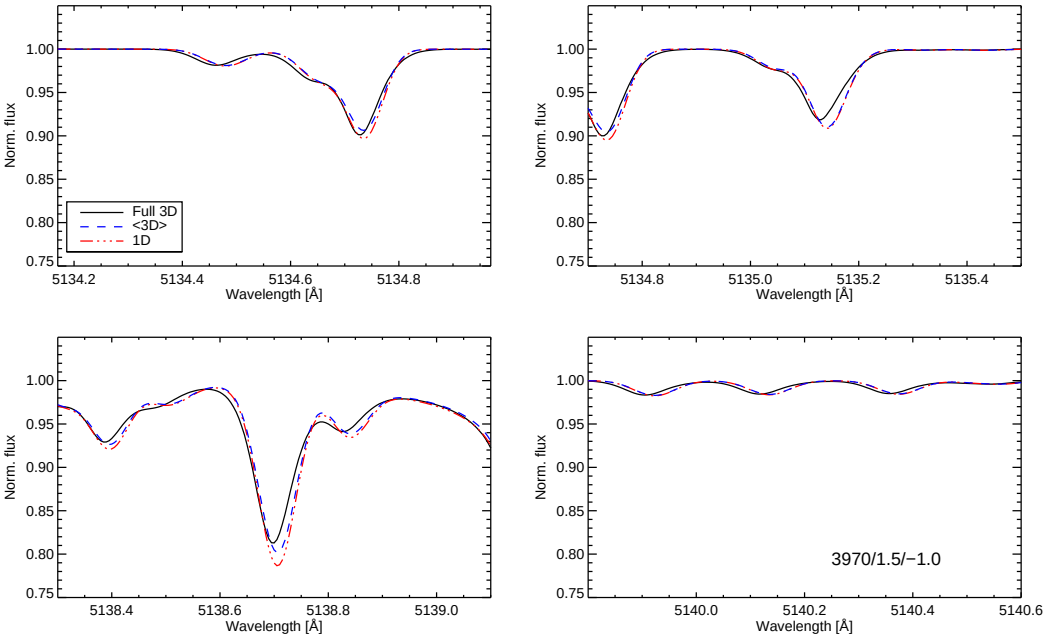

Figure 2.10: Syntheses of each of the four MgH regions, but only including the blending lines. Shown for the low metallicity model.

3

STELLAR PARAMETERS AND ABUNDANCE PATTERN OF RED GIANTS IN THE GALACTIC GLOBULAR CLUSTER 47 TUCANAE

Adapted from Thygesen, A. O., Sbordone, L., Andrievsky, S., Korotin, S., Yong, D., Zaggia, S., Ludwig, H.-G., Collet, R., Asplund, M., Ventura, P., D'Antona, F., Meléndez, J. & D'Ercole, A., 2014, A&A, Vol. 572, P. A108. [1]

3.1 INTRODUCTION

This, and the following chapter is concerned with a detailed abundance analysis of the metal rich globular cluster (GC) 47 Tucanae (NGC 104). In the present chapter, we present the spectroscopic and photometric observations and an overview of the data reduction. In addition we discuss the derivation of the fundamental stellar parameters, as well as derivation of elemental abundances, using standard 1D atmospheric models and a combination of LTE and NLTE spectral synthesis.

In Chapter 4, we expand on the work presented in the current chapter, and add measurements of magnesium isotopic ratios to the elemental abundances. For the first time, the effects of using 3D hydrodynamic model atmospheres to derive the isotopic ratios of Mg are investigated. Using the combined results from Chapter 3 and 4, we discuss different models for self-pollution within the cluster, and finish with a common conclusion for the two chapters.

3.2 OBSERVATIONS AND DATA REDUCTION

For this project we observed a total of 13 red giants. The target selection was performed from UBVI photometry obtained from reduction of archival images taken at the WFI imager at the MPG/ESO 2.2m telescope in La Silla in 2002 under program 69.D-0582(A). The sample of images comprise short and long time exposures carefully chosen in order not to saturate the brighter targets. The data was reduced using the ESO/MVM pipeline (Vandame 2002), properly correcting for the sky illumination and fully astrometrizing the whole dataset. The point-

1 Luca Sbordone fostered the idea for this project, wrote the observing proposal and developed the `Fitprofile` software. The non-LTE synthesis in this chapter was done by Sergei Andrievsky and Sergei Korotin, including part of the written text on non-LTE. Simone Zaggia provided the photometry and contributed text on the photometric analysis. All the remaining work and text was done by me.

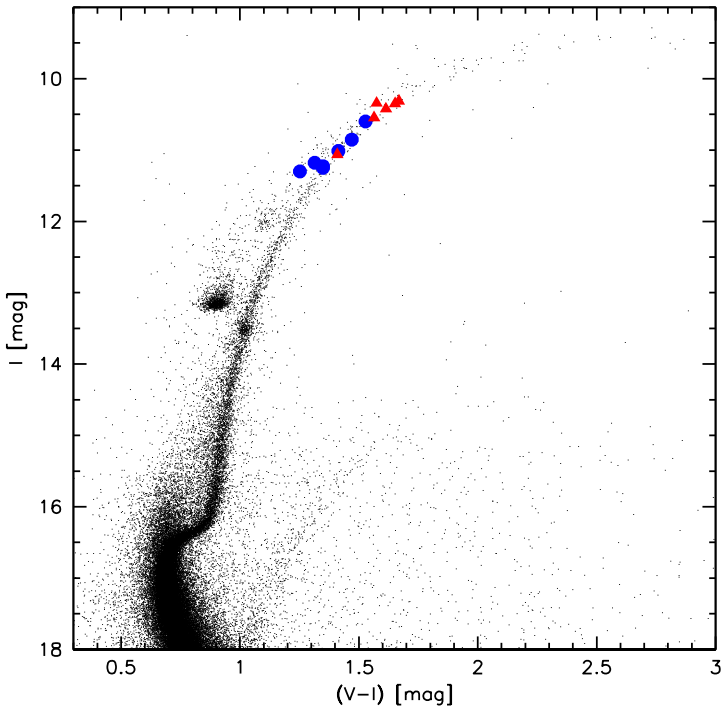

Figure 3.1: Color-magnitude diagram of 47 Tucanae with observed targets indicated. Blue circles and red triangles are used for the pristine and polluted population of stars respectively. See Sect. 3.4.1.1 for population selection criteria.

spread function photometry was extracted using DAOPHOT (Stetson 1987) and combined in a single photometric dataset. Finally, the sample was calibrated using the photometric fields compiled by P. Stetson[2], located inside the WFI field of view of 47 Tuc. The typical rms of the photometry is under 3% for each UBVI band. The target stars were chosen to be bright ($V \lesssim 12.6$), in order to reach the desired S/N (≈ 150@5140Å) in a reasonable amount of time. The GC 47 Tucanae has a very well populated RGB and by restricting the selection to a narrow range of V-magnitudes, we expected to include targets across both populations present in the cluster. However, as is evident from Fig. 3.1, there is no clear separation between the two populations at the magnitudes of our stars, making it difficult to guarantee an even sampling across the populations from photometry alone (see also Milone et al. 2012b). Already published radial velocity measurements were also used in the selection process to confirm cluster membership. We separate the two populations in the CMD, as identified from the spectroscopic analysis (see Sect. 3.4.1.1).

2 http://www3.cadc-ccda.hia-iha.nrc-cnrc.gc.ca/community/STETSON/standards/

All spectroscopic observations for this project were aquired under ESO programs 084.B-0810 and 086.B-0237, using the Ultraviolet and Visible light Echelle Spectrograph (UVES) spectrograph (Dekker et al. 2000) mounted on UT2 of the ESO VLT on Cerro Paranal, Chile. Since the main goal of the observations was to measure the isotopic mixture of Mg from the MgH molecular bands, we required both S/N and high resolution, because the signatures of the heavy Mg isotopes are very subtle. To achieve the required S/N without compromising the resolution, we used image slicer (IS) #3, reaching a resolving power of $R = 110\,000$. We used the 580 nm setting, which covers the wavelength range from 4780 Å to 6810 Å, with a small gap from 5760-5830 Å. This setting was chosen in order to capture the MgH featuress around 5130 Å, which are usually adopted for analyses of Mg-isotopic ratios. An overview of our targets is given in Table 3.1. The targets were selected to have $\log g \leq 1.5$ to be sufficiently bright and $T_{\rm eff} < 5000\,\mathrm{K}$, because the MgH features largely vanish above this temperature.

The spectroscopic data was reduced with the ESO GASGANO pipeline V.2.4.3 (Silva & M. Peron 2004)[3]. The pipeline performs the standard reduction steps of bias subtraction, flat-field correction, order extraction, and wavelength calibration of the observed spectra. Each reduction produces two spectra, one for each chip on the detector. Contrary to the normal procedure for reducing echelle spectra, we did not use the optimal extraction method, but a simpler, average extraction. Optimal extraction cannot be applied to IS spectra, since the cross-order profile of the sliced spectrum is unknown, hence very difficult to model. Also, as the slices fill the individual orders completely, it is not possible to do sky subtraction during the reduction, since there is not enough space to determine the sky background accurately.

After the reduction, the spectra were shifted to laboratory wavelength. First, by correcting for heliocentric motion and subsequently correcting for the radial velocity (RV) of the targets. The velocity shifts were determined using the cross-correlation function (CCF). The spectra for each detector chip were cross-correlated against a synthetic template spectrum with parameters close to what would be expected for our stars ($T_{\rm eff} = 4200\,\mathrm{K}$, $\log g = 1.5\,\mathrm{dex}$, $\xi_t = 2\,\mathrm{km\,s^{-1}}$, $[\mathrm{Fe/H}] = 0.00$ dex) and the resulting CCFs were fitted with a Gaussian to determine the radial velocity of the stars. The quoted uncertainties on the RV in Table 3.1 are the standard deviations of the fitted Gaussians. The spectra from each chip were treated individually. Deriving the RV also served as an independent check of cluster membership, because all stars in the cluster are expected to have roughly the same RV. We find a mean RV of

3 Available from http://www.eso.org/sci/software/gasgano.html

Table 3.1: Properties of the observed targets. Boldface numbers indicate polluted targets. The uncertainties on the magnitudes are at the 3% level.

ID	α(J2000)	δ(J2000)	V	B	I	U	V_{rad}
1062	00:24:04.51	−71:57:11.14	12.0	13.5	10.4	15.4	-22.15 ± 0.24
4794	00:26:28.48	−71:50:12.86	12.4	13.8	11.0	15.3	-28.04 ± 0.19
5265	00:26:57.45	−71:49:13.95	12.1	13.6	10.6	15.4	-18.73 ± 0.25
5968	00:26:27.21	−71:47:44.11	12.1	13.8	10.6	15.2	-21.76 ± 0.21
6798	00:23:12.87	−72:10:19.00	12.3	13.7	10.9	15.2	-18.44 ± 0.23
10237	00:24:45.81	−72:09:10.42	12.5	13.7	11.2	14.9	-25.82 ± 0.20
13396	00:22:06.69	−72:07:15.77	12.6	13.8	11.2	15.0	-9.78 ± 0.25
20885	00:23:05.17	−72:04:27.98	12.6	13.8	11.3	15.0	-15.17 ± 0.27
27678	00:22:30.27	−72:01:41.07	12.0	13.6	10.4	15.4	-24.86 ± 0.21
28956	00:23:22.79	−72:01:03.83	11.9	13.4	10.3	15.3	-17.72 ± 0.26
29861	00:22:07.16	−72:00:32.90	12.6	13.9	11.3	15.2	-11.65 ± 0.35
38916	00:24:15.81	−72:00:41.50	12.5	13.8	11.1	15.3	-20.72 ± 0.24
40394	00:24:05.09	−72:00:03.35	12.0	13.5	10.3	15.3	-18.67 ± 0.25

$-19.50 \pm 5.29\,\mathrm{km\,s^{-1}}$, consistent with the results from Alves-Brito et al. (2005) and Koch & McWilliam (2008).

3.3 ABUNDANCE ANALYSIS

3.3.1 *Fundamental stellar parameters*

To determine the fundamental stellar parameters of our targets, we adopted the traditional spectroscopic approach of combining 1D LTE atmospheric models with equivalent width (EW) measurements of a number of Fe I and Fe II lines. We enforce abundance equilibrium, using the Fe I lines, to derive $T_{\rm eff}$ and microturbulence, ξ_t; and ionization equilibrium between Fe I and Fe II to derive $\log g$.

EWs of all iron lines were measured by hand, using the `splot` task in `IRAF` (Tody 1986, 1993). Each line was identified by comparing with lines present in the synthetic spectrum that was also used for the CCF calculations. Preferably, only isolated, unblended lines were used for this purpose, and great care was taken to place the continuum at the right level. In the few cases where blends were present, the lines were appropriately deblended, using either Gaussian or Voigt profiles, depending on the strength and shape of the lines under consideration. For the first pass at parameter determination, we selected lines by comparing synthetic lines to a high-resolution spectrum of Arcturus, choos-

ing only lines that were reproduced well in the synthesis to minimize the impact of low-quality atomic line data. This selection of lines resulted in between 60 and 80 iron lines for each star, but since stellar parameters determined from iron lines are highly sensitive to the specific choice of lines, we chose to include only lines that were in common for at least eight stars from the initial pass at EW measurements. In cases where lines were missing from this master linelist, great effort was put into recovering the missing lines, although this was not always possible, usually due to atmospheric emission lines or noise spikes being present in the feature. Typically 45 Fe I and 12 Fe II lines were used in each star. The full line list is presented in Table A.1. The list is also available online.

Having measured the EWs, the results were passed to the spectral analysis code MOOG (2013 version, Sneden 1973; Sobeck et al. 2011; Sneden et al. 2012), where interpolated, α-enhanced ATLAS9 1D LTE models (Castelli & Kurucz 2004, $[\alpha/\mathrm{Fe}] = +0.4$ dex) were used in an initial pass at determining the stellar parameters. For each star, we determined T_{eff} by requiring no correlation between the abundance of Fe I and lower excitation potential, E_{low}. As a starting point, we used the mean value of the photometric T_{eff}, using the calibrations of Ramírez & Meléndez (2005) and González Hernández & Bonifacio (2009). The photometric T_{eff} was derived using an interstellar reddening of $\mathrm{E(B-V)} = 0.04$ (see Grundahl et al. 2002b and references therein), where we used the calibration of Taylor (1986) to convert from E(B−V) to E(V−I). The photometric T_{eff} is quoted in Table 3.2 for reference. ξ_t was determined by requiring no correlation between the abundance of Fe I and reduced EW, $\log(\mathrm{EW}/\lambda)$. Finally, the surface gravity was determined by enforcing ionization equilibrium between Fe I and Fe II. We used atomic data from Version 4 of the linelist for the Gaia-ESO Survey (GES), (Heiter et al. in prep.), with the exception of oscillator strengths for Fe II, which were adopted from the work of Meléndez & Barbuy (2009), in cases where the GES linelist used other sources. Using $\log(gf)$ values from a single study were found to yield more homogeneous Fe II abundances. After the initial best-fitting model had been determined, we proceeded to measure the abundances of O, Na, Mg, Al, Si, Cr, Ti, and Ni for each star (see Sect. 3.3.2).

Since this work is concerned with cool giants with a variation in light elements, it is desirable to take this into account in the atmospheric modeling, as these elements are important electron donors. Since the strength of many lines is sensitive to the electron pressure in the atmosphere, it is important that the number of free electrons are properly accounted for. Failing to do so can have a significant impact on the derived abundances, which may in turn lead to erroneous conclusions, as illustrated for instance, by Mucciarelli et al. (2012) in the case of NGC

Table 3.2: Photometric $T_{\rm eff}$'s for each sample star. Subscripts "R" and "G" refer to the calibrations of Ramírez & Meléndez (2005) and González Hernández & Bonifacio (2009), respectively.

ID	$T_{eff,B-V,R}$	$T_{eff,V-I,R}$	$T_{eff,B-V,G}$
1062	4036	4098	4131
4794	4193	4228	4245
5265	4033	4096	4129
5968	3746	3899	3952
6798	4151	4192	4214
10237	4347	4371	4366
13396	4305	4331	4332
20885	4342	4366	4362
27678	3950	4033	4074
28956	3983	4057	4096
29861	4278	4305	4310
38916	4236	4266	4277
40394	3987	4060	4098

2419. In particular, the correct abundance of Mg is important, since this is the most important electron donor in the atmospheres of cool stars.

Therefore, with an initial set of abundances determined from using ATLAS9 models, we computed new, tailored atmospheric models for each star with the abundance pattern and fundamental parameters derived as described above. We utilized the GNU Linux-ported version of the ATLAS12 code (Kurucz 2005; Sbordone et al. 2004; Sbordone 2005) for this purpose, where the main difference between this code and ATLAS9 is that the latter uses a precomputed set of opacity distribution functions, calculated for a fixed abundance mixture, whereas ATLAS12 uses opacity sampling, which allows for the opacities to be calculated on-the-fly for any given element mixture. The models were subsequently ported to a `MOOG`-friendly format and the stellar parameters were rederived. Since the atmospheric structure changes compared to the initial models, a few iterations were typically required to re-establish ionization and abundance equilibrium with the ATLAS12 models. In each iteration, the entire set of measured abundances was updated to ensure as close a match to the free electron density as possible.

The impact of wrong abundances of the main electron donors is lower in a high-metallicity case like 47 Tucanae, since the variation in Mg is smaller than for NGC 2419, where the variation in [Mg/Fe] spans al-

most 2 dex, but the variation is still visible. Inspecting Fig. 3.2, where we plot the fractional contributions to the total number of free electrons for the five most significant electron donors as a function of optical depth, even the effect of small variations in Mg to the electron budget can be seen. The two panels show star 10237 (top), which is the most Mg-depleted star, [Mg/Fe] = 0.32 dex and star 38916 (bottom), the most Mg-enhanced star, [Mg/Fe] = 0.52 dex. Slight variations in the electron pressure can also be seen, compared to using a standard scaled Solar ATLAS9 model as can be seen in Fig. 3.3. On the other hand, the ATLAS12 model can hardly be distinguished from the equivalent ATLAS9 α-enhanced model.

For the less evolved giants in our work i. e., $T_{\rm eff} > 4000$ K, $\log g > 1.0$ dex, we found that the differences between using interpolated ATLAS9 α-enhanced models and dedicated ATLAS12 models were negligible. However, slight differences in the electron pressure were found for the low gravity models. These differences had a small effect on the derived $\log g$ values, where we found differences of up to 0.13 dex. This may, in turn, affect the derived abundances slightly, especially for pressure-sensitive species. However, the variation in $\log g$ is smaller than our typical uncertainty. The effects on $T_{\rm eff}$ and ξ_t were found to be negligible in all cases.

3.3.1.1 *Parameter uncertainties*

To estimate the uncertainties on the fundamental parameters of our stars, we adopted the uncertainty of the fitted slope of $\log\epsilon$(Fe) vs. EW and excitation potential (EP) and performed the following exercise. For a representative star (6798) we perturbed the best-fitting model by $\pm$200 K in steps of 50 K for $T_{\rm eff}$, and $\pm$0.3 km s^{-1} in steps of 0.1 km s^{-1} for ξ_t, around the adopted best values. Only one of the parameters was perturbed at a time. Each of the perturbations will change the slope of the best-fitting line. This exercise allowed us to produce the $\Delta T_{\rm eff}$ vs. EP-slope and the $\Delta\xi_t$ vs. EW-slope relations by making a linear fit to the observed changes. From this, we can easily calculate $\Delta T_{\rm eff}$ and $\Delta\xi_t$ corresponding to the uncertainty of the zero-slope model. This corresponds to uncertainties of 80 K in $T_{\rm eff}$ and 0.1 km s^{-1} in ξ_t, which we adopted for all stars, after checking that these values did not depend on the absolute values of the stellar parameters. To check whether an offset of the metallicity scale affected $T_{\rm eff}$ and ξ_t, we also perturbed the overall metallicity, [M/H], of the star by changing it by $\pm$0.15 dex, which is the typical line-to-line scatter of our iron abundances, which were used as a proxy for overall metallicity for this purpose. As can be seen in Table 3.3, this had only a negligible effect on the remaining parameters.

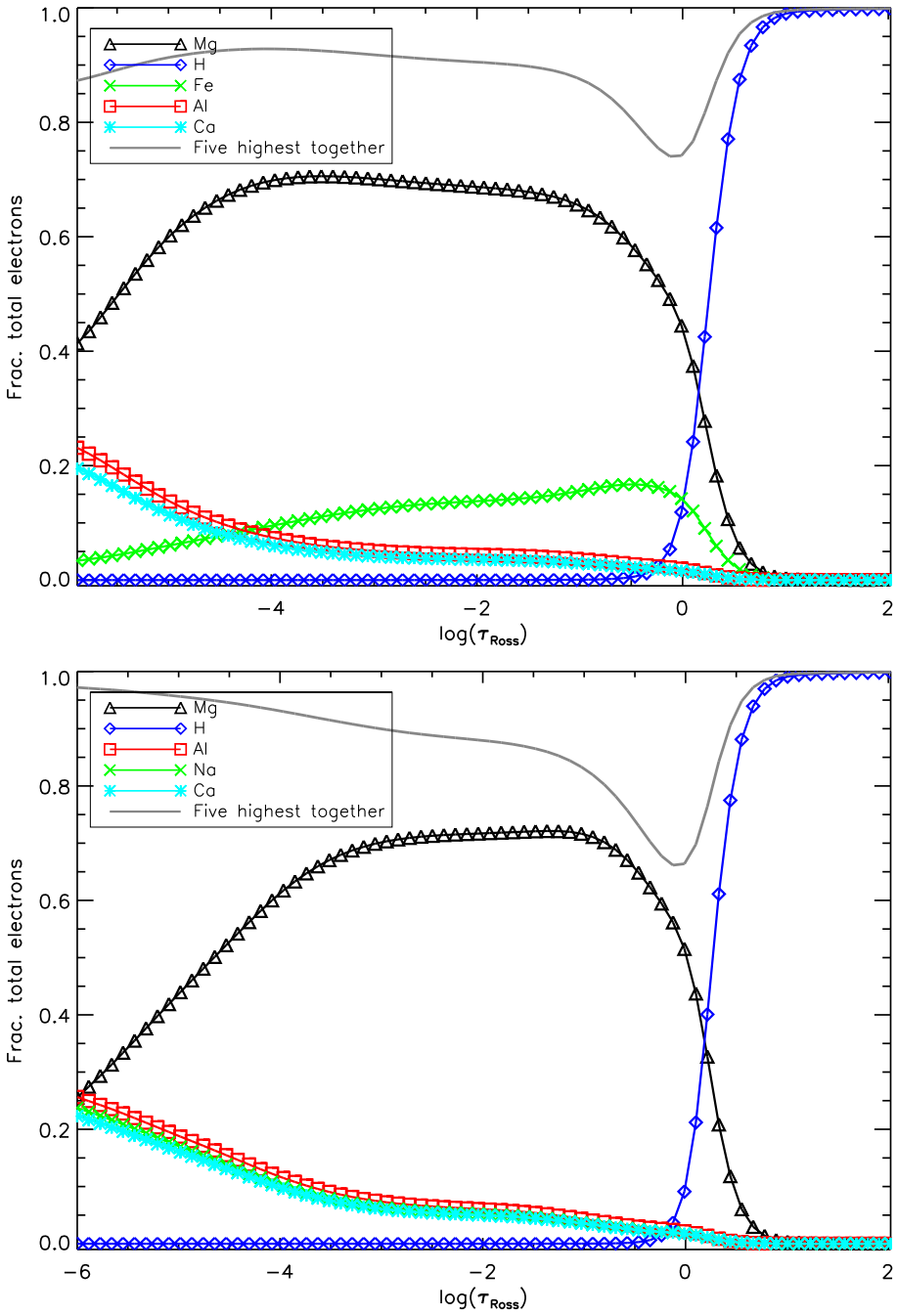

Figure 3.2: Fractional contribution of free electrons for the top five electron donors as a function of optical depth. The solid, gray line shows the total contribution from the 5 species. Top: 10237, which is the most Mg-depleted star. Bottom: 38916, the most Mg-enhanced star.

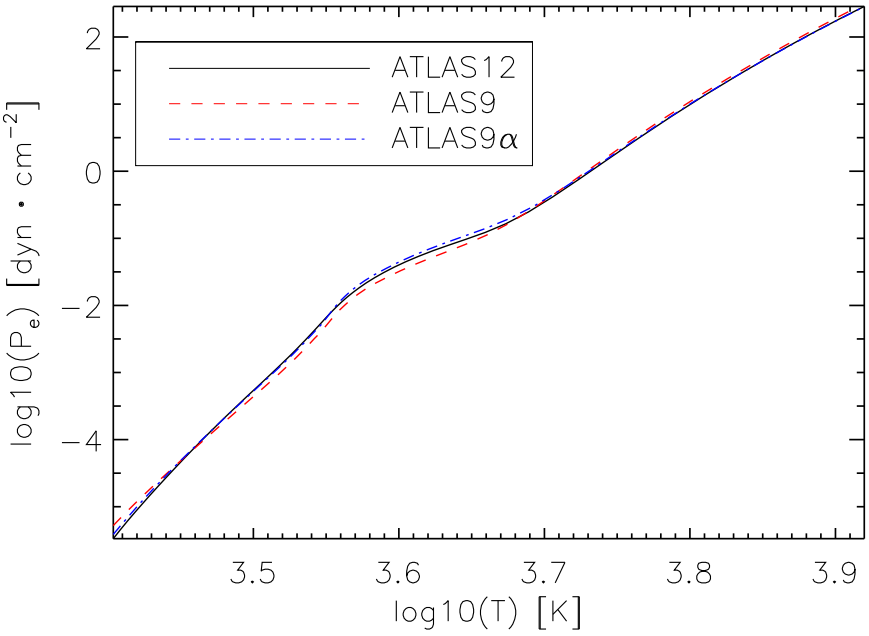

Figure 3.3: Electron pressure as a function of temperature for three different models of the star 10237. The solid black line shows the ATLAS12 model with tailored abundance pattern, and the red dashed line shows the interpolated, scaled solar ATLAS9 model. Finally, the α-enhanced ATLAS9 model is shown as the blue dot-dashed line.

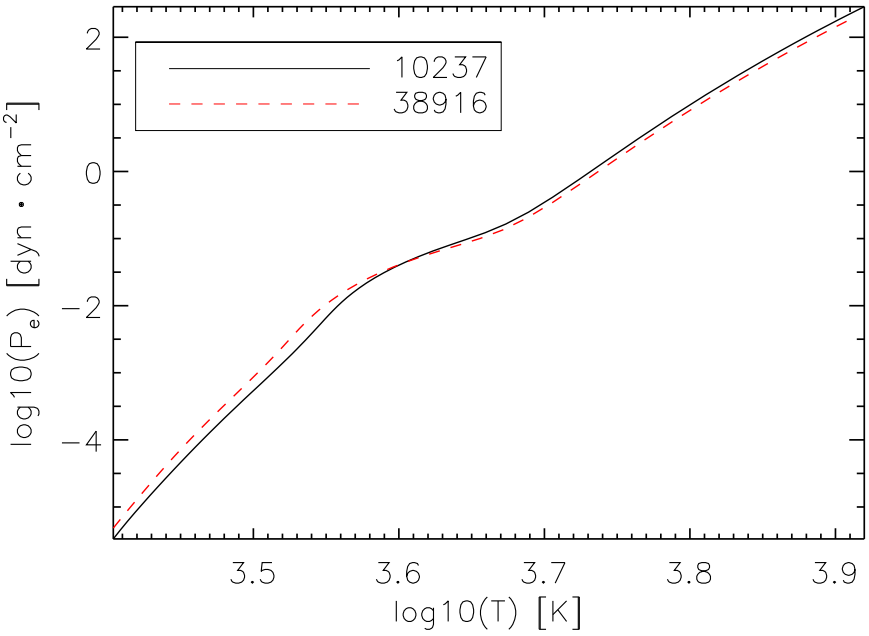

Figure 3.4: Difference in electron pressure as a function of temperature between star 10237 and star 38916.

To determine the uncertainty on $\log g$ we adopted a similar approach, but this time inspecting the changes in the abundance of Fe II, because it is strongly influenced by the surface gravity. Again, we perturbed the models by ± 0.3 dex in steps of 0.1 and used the change in iron abundance vs. change in $\log g$ to estimate the uncertainty. The change in $\log g$ that corresponded to a difference between Fe I and Fe II equal to the standard deviation of the best-fitting Fe II abundance was taken as the uncertainty of $\log g$, resulting in a value of 0.20 dex.

Whenever one of the model parameters is perturbed, it will influence the remaining parameters to some extent. For instance, changing $T_{\rm eff}$ will also introduce small changes to the abundance vs. EW slope, as well as to the derived mean iron abundance. To give an indication of the sensitivity of each parameters to changes in any of the others, we give in Table 3.3 the changes to each of the fundamental parameters when one is changed within the uncertainties, while the others are kept fixed. The changes are given as best fit minus perturbed. The quoted $\Delta\log g$ reflects the change needed in $\log g$ to bring the Fe II abundance back into agreement with Fe I, within the accepted difference between the two species (0.04 dex). As can be seen, the small parameter changes affect each other; most noticeably, changes in $T_{\rm eff}$ have a significant influence on $\log g$, as $T_{\rm eff}$ changes have a strong impact on the Fe II abundance. Thus, the $\log g$ needs to be changed by an appreciable amount to re-establish ionization equilibrium. On the other hand, Fe I, ξ_t, and $T_{\rm eff}$ itself are hardly changed from perturbations of the other parameters. We adopt the following values as the final uncertainties of our fundamental parameters, $\sigma_{T_{eff}} = \pm 80$ K, $\sigma_{\log g} = \pm 0.20$ dex and $\sigma_{\xi_t} = \pm 0.10$ km s^{-1}.

We note that the Fe II lines appear to be affected slightly more by temperature changes, compared to changes in $\log g$. We investigated this further, using the `MyGisFOS` analysis software (Sbordone et al. 2014), which produced similar results. In addition, the changes in the Fe II abundances with changing parameters are not associated with an increased line-to-line scatter, but merely reflects a change in the mean abundance.

NLTE effects on iron may potentially influence the derived stellar parameters, as illustrated by Bergemann et al. (2012) and Lind et al. (2012) among others. In order to check whether this was important for our stars, we used the `INSPECT` online database[4], which requires input stellar parameters as well as the EW of the line under investigation. The database then interpolates in a large grid of models to provide a NLTE correction. The corrections for iron were computed based on the work of Bergemann et al. (2012) and Lind et al. (2012).

4 http://inspect.coolstars19.com/

We chose the star 10237 as a representative example for this exercise. Of the 42(12) Fe I (Fe II) lines used for the parameter determination, only 6 Fe I and 12 Fe II lines were present in the database. However, as the NLTE corrections will be very similar for different lines with the same EP and $\log(gf)$, we adopted corrections for lines that matched a line with computed NLTE corrections, within 0.2 eV in EP and 0.2 in $\log(gf)$, to assess the magnitude of NLTE on the parameters. Nevertheless, 16 of the lines used in the LTE analysis had to be discarded, because no satisfactory matches could be found. The NLTE corrections were on the order of 0.02 dex. Applying these corrections to the matching lines resulted in parameter changes of $\Delta T_{\rm eff} = 45\,{\rm K}$, $\Delta\log g = 0.05\,{\rm dex}$, $\Delta\xi_t = 0.02\,{\rm km\,s^{-1}}$, and $\Delta[{\rm Fe/H}] = 0.05\,{\rm dex}$, which should be compared to typical uncertainties of 80 K, 0.2 dex, $0.1\,{\rm km\,s^{-1}}$, and 0.15 dex, respectively. We thus do not consider NLTE effects on either Fe I or Fe II to have a significant effect on our derived stellar parameters.

3.3.2 *Element abundances*

In the initial pass on abundance measurements, using the ATLAS9 models, we derived abundances of the α-elements (O, Mg, Si, Ca, Ti) as well as Na, Al, Cr, Fe, Ni and Zn. With the exception of O and Na, all initial abundances were derived using EW measurements, as for the iron lines. After these abundances had been determined from the ATLAS9 models, tailored ATLAS12 models were calculated, matching the measured abundance pattern as described above. All abundances were subsequently derived again in the fashion described in the following.

3.3.2.1 *Equivalent width measurements*

The abundances of Si, Ca, Ti, Cr, Fe, Ni, and Ce were derived with `MOOG` using EW measurements. With a few exceptions, all atomic line data were adopted from Version 4 of the GES linelist (Heiter et al., in prep.). For Ti we used the recent results of Lawler et al. (2013) (Ti I) and Wood et al. (2013) (Ti II). As with the iron lines, deblending was taken into account when needed, but only clean lines were used as far as possible. Whenever individual lines showed large deviations from the mean abundance, they were inspected in detail by comparison with a synthetic spectrum as well as with an observed spectrum of a star with similar fundamental parameters, in which the line was not discrepant. In most cases, this resulted in a remeasure of the discrepant line, which would remedy the deviation. These deviations were in most cases due to improper continuum placement. The star-to-star comparison was particularly useful here, because it allowed us to determine the continuum more easily in cases where one spectrum suffered from atmospheric

Table 3.3: Changes to the fundamental parameters when perturbing a typical star (6798) by the estimated uncertainties. Changes given as best fit minus perturbed.

Result/Change	$\Delta T_{\rm eff} = \pm 80$K	$\Delta\xi_t = \pm 0.1$km s^{-1}	$\Delta\log g = \pm 0.2$	Δ[M/H] $= \pm 0.15$
$\Delta T_{\rm eff}$	$-$	$+34/-30$	$-33/+38$	± 8
$\Delta\xi_t$	$+0.02/-0.03$	$-$	$-0.02/+0.02$	± 0.01
$\Delta\log g$	$-0.20/+0.20$	$-0.05/+0.05$	$-$	0.00
ΔFe I	$+0.00/-0.02$	$+0.02/-0.04$	$-0.04/+0.03$	$-0.03/+0.03$
ΔFe II	$+0.16/-0.18$	$+0.03/-0.03$	$-0.12/+0.12$	$-0.06/+0.07$

emission in the continuum area near the line under investigation. In some cases, this approach also enabled us to identify overlooked blends with atmospheric lines or noise spikes in the lines themselves. In these cases, the lines were discarded.

For Ce, only one line at 5274.23 Å was used to derive the abundance. If it is not deblended properly or continuum placement is not being done carefully, the derived abundance may be systematically off. However, checking against a spectral synthesis, it was found that the abundances from EW measurements agreed with the abundances derived from syntheses to within 0.1 dex. Thus, we trust that the deblending was done in a reliable way. Based on the synthesis deviation, we adopt 0.1 dex as the measurement uncertainty of the abundance for this element.

3.3.2.2 *Spectral synthesis*

Not all element abundances can be derived reliably from EW measurements due to line-blending problems if, for instance, these are strong or if the lines under investigation are in regions with a large number of weak molecular features. To derive reliable abundances one has to employ spectral synthesis. This technique was used to derive abundances of O, Na, Mg, Zn, Mo, Ru, and Dy.

The derivation of the oxygen abundance is difficult owing to the very few lines of appreciable strength in the optical range. In our case we utilized the two forbidden [OI] lines at 6300.3 Å and 6363.8 Å. The former suffers from a close blend with a Ni line, whereas the latter is in the extended wings of the Ca autoionization line at 6360 Å. Both things make it difficult to use EW measurements and deblending methods to reliably derive the abundances. `MOOG` was used to synthesize both lines. For the Ni I line at 6300.34 Å, blending with the [OI] 6300 Å line, we used the data from Johansson et al. (2003). For each star we adopted the Ni abundance derived from the EW measurements, updating after each iteration. Initially, we synthesized a 20 Å window around the line of interest. This was done to ensure an accurate continuum placement. With the continuum set, the O abundance was adjusted until a minimum of the χ^2 value between the observed and synthetic spectrum was found. When synthesizing the lines we also allowed for small variations in the macroturbulent broadening to ensure the best possible fit to the observed line profile, but in most cases it was found that a single value could be applied to both lines. For slow rotators such as evolved red giants, we cannot reliably disentangle rotational broadening and macroturbulence, so we treat them as a single broadening, which we refer to as macroturbulent broadening throughout the paper. The presence of a telluric absorption line at 6300.598 Å could in principle be contaminat-

ing the oxygen line, but the radial velocity of the stars were sufficient to shift the oxygen away from the contaminated region.

To assess the uncertainty of the measurement, the abundance was subsequently changed until a significant deviation from the best fit was observed, as judged by eye. This typically required changes in the oxygen abundance on a level of 0.07 dex, which can easily be distinguished from the best-fitting model, as illustrated in Fig. 3.5, where we also show a synthesis without any oxygen in the atmosphere. That some lines are seen to increase in strength when lowering the O abundance is due to less carbon being locked in CO molecules, thus increasing the strength of C_2, CH and CN molecular lines also present in this region. Also, sky emission lines are visible redward of each of the two oxygen lines. These did not, however, affect our derived abundances.

A discrepancy in the abundance between the 6300 Å and 6363 Å lines has been observed in the Sun, as well as in other dwarf stars, but in the case of giants, both lines give consistent abundances (see Caffau et al. 2013b). In studies of the Sun, Caffau et al. (2008) found that NLTE effects were negligible for these lines at solar metallicities and low $T_{\rm eff}$ (see also Kiselman 1993). This result is expected to also hold for the parameter range of this sample of stars (Fabbian et al. 2009). In the case of the star 13396, only the 6300 Å line was used, owing to atmospheric emission being present in the 6363 Å line. In two other cases (stars 5265 and 6798), some emission was present in the wings of both oxygen lines, so the derived abundance should be considered as a lower limit. For stars 20885 and 38916, strong emission was present in both lines, which made it impossible to derive a reliable oxygen abundance.

The synthesis of the sodium lines followed a similar approach. That the stars in this work are fairly evolved giants, combined with the Na lines typically being strong (>70m Å), makes them susceptible to NLTE effects. To assess this, we again used the `INSPECT` database. For the EW, we used the measured width of the best-fitting, *synthetic* line, calculated as a single line, without including any lines in the vicinity to by-pass blending issues. This provides a NLTE correction for each line under investigation, using the computations from Lind et al. (2011). Following the recommendation in this study, we only used the 6154 Å and 6160 Å lines. However, the lowest $T_{\rm eff}$ and $\log g$ values available in the grid (4000 K, 1.00 dex) are somewhat higher than the parameters of the most evolved giants treated in our work. For these stars, we used the 4000 K, 1.00 dex NLTE correction, which in the most extreme cases are off by 150 K and 0.55 dex respectively. In Fig. 3.6 we plot the NLTE corrections vs. different stellar parameters as well as the EW for the two lines used. We began at the extremes of the parameters available in the precomputed NLTE grid and used the EWs from star 6798, because this object is representative of our sample and has the lowest $T_{\rm eff}$ that still falls

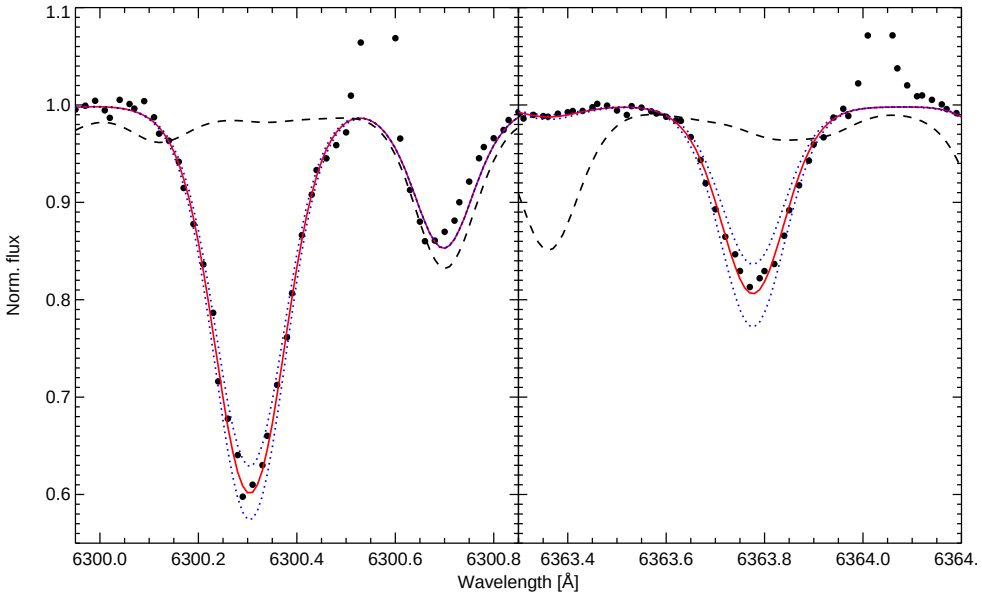

Figure 3.5: Example of the oxygen synthesis for the two lines used to derive the O abundance in this work, shown here for star 10237. Solid red line shows the optimal fit and the dotted blue lines changing the O abundance by ± 0.07 dex. The black, dashed line show a synthesis without oxygen.

within the grid calculated by Lind et al. The value of $\log g$ of 0.9 dex is marginally outside the available parameters, but as can be seen in Fig. 3.6, the size of the correction is mostly sensitive to the line EW and not to the actual stellar parameters within the range in our sample. In each of the panels only one parameter is changed, whereas the rest are kept fixed at the values shown in red in the remaining panels. The variation in the NLTE corrections due to changes in ξ_t are also non-negligible, but at least a factor of two smaller than the corrections from varying the EW. We note that in no case does our derived value of ξ_t extend beyond the available grid. Thus, we are confident that using the corrections from the lowest possible grid values will not deviate significantly from the true corrections, since they are insensitive to $T_{\rm eff}$ and $\log g$ changes. The size of the corrections was never more than -0.15 dex.

For the final abundance determination of Mg we performed a spectral synthesis of the lines at 6318.72 Å, 6319.24 Å, and 6319.50 Å using the line data of Meléndez et al. (2012). These lines are in the vicinity of the atmospheric lines at 6318.85 Å and 6319.59 Å. As for the oxygen lines, we checked whether the radial velocity of each star was high enough to shift the Mg lines away from the telluric lines. In all stars except star 29861, at least two of the three Mg lines were free of telluric contamination so reliable Mg abundances could be derived. For star

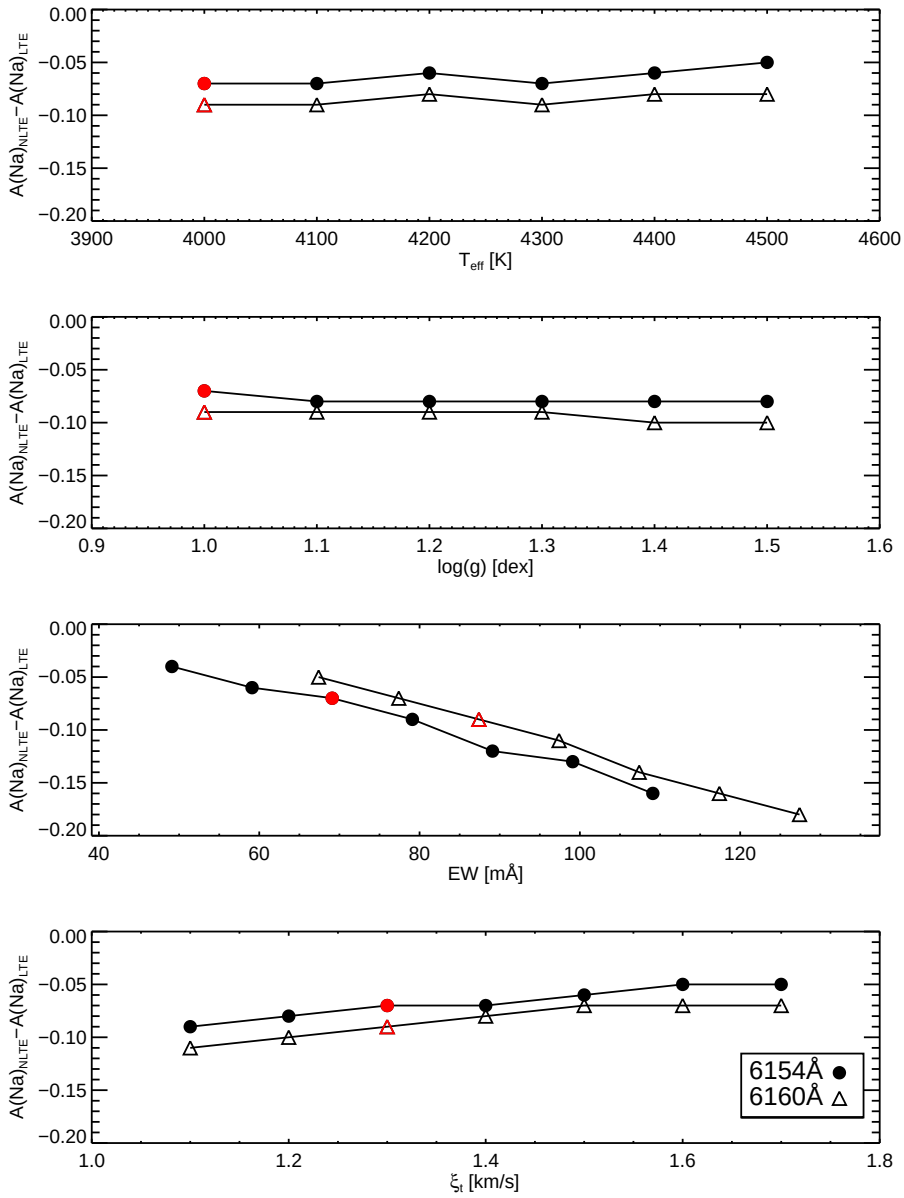

Figure 3.6: NLTE corrections ($A(Na)_{NLTE}$-$A(Na)_{LTE}$) as a function of T_{eff}, $\log g$, EW, and ξ_t. The red points shows the actual values for the star 6798.

29861 only the 6319.24 Å line was free of contamination. For this line we adopt the mean uncertainty derived from the remaining lines. Using the MULTI code (Carlsson 1986; Korotin et al. 1999), we checked for the impact of NLTE on the used lines by performing an NLTE synthesis for the two stars with the most extreme parameters. We found that the corrections were ≤ 0.05 dex, which we considered negligible compared to our typical uncertainties and thus only a standard LTE synthesis was applied.

The abundances of Zn, Mo, Ru, and Dy were also derived from a standard spectral synthesis. The Zn line at 4810.53 Å is strongly blended with a Cr I feature and the Dy line at 4890.10 Å is suffering from a blend with a Ti I line, as well as several weak C_2 and CN molecular lines that make a standard EW analysis overestimate the abundances. Similar blending issues are affecting the Mo and Ru lines. The uncertainties on the abundances includes the uncertainty in the continuum placement (less than 0.1 dex variation), as well as the change in abundance needed to produce a noticeable deviation from the best-fitting abundance, as judged by eye.

3.3.2.3 *Ba and Al NLTE synthesis*

Barium is an important probe of s-process enhancement in stars, and this element is thus very useful for investigating the contribution from different polluter candidates, relative to more r-process-dominated species like Eu. However, deriving Ba-abundances requires great care, as the lines suffer hyperfine splitting (HFS) and are very strong at the metallicity of 47 Tucanae, making them prone to NLTE effects that can be quite significant (see, e. g., Short & Hauschildt 2006; Andrievsky et al. 2009). To take all of the above into account, we performed a full NLTE synthesis for all Ba lines, using the code MULTI (Carlsson 1986; Korotin et al. 1999), with the line data from Andrievsky et al. (2009).Three Ba II lines are available in our program spectra for the abundance analysis: 5853.68 Å, 6141.71 Å, and 6496.91 Å.

Individual line-profile fits were made for each of the three lines, allowing for a variation in the macroturbulence to ensure the best possible match between the synthesis and the observations. The macroturbulence was treated as a Gaussian broadening of the spectral lines. All barium lines used here, are to some extent blended with lines of iron in particular. The effect is fairly significant for the 6141.71 Å and 6496.91 Å lines. To solve this problem, we folded the NLTE (MULTI) calculations into the LTE synthetic spectrum code SYNTHV (Tsymbal 1996), which enable us to calculate synthetic spectra for each Ba II line region taking all the lines in each region listed in the Vienna Atomic Line Database (VALD)

database[5] into account. For the barium lines, the corresponding departure coefficients (so-called b-factors: $b = n_i/n_i^*$ - the ratio of NLTE-to-LTE level populations) are fed into SYNTHV, where they are used in calculating the line source function and barium line profiles.

In all cases we were able to produce excellent matches between the calculated and observed spectra (see the example shown in Fig. 3.7). In one case (star 6798), we could not use the 6141 Å line because of strong atmospheric emission, therefore only two lines were used for this star. The size of the NLTE correction varied from star to star and line to line, but reached levels as high as 0.5 dex in some cases, which is clearly non-negligible. The individual macroturbulence values used for the lines in each star were found to be in excellent agreement with each other, typically differing by less than $0.3\,\mathrm{km\,s^{-1}}$, with the largest difference found to be $0.5\,\mathrm{km\,s^{-1}}$.

That the NLTE corrections are indeed important is further illustrated in Fig. 3.8, where we plot [Ba/Fe] vs. T_{eff}, showing both the LTE and NLTE results. If NLTE is not taken into account, a clear correlation between abundance and T_{eff} is observed, which would suggest a problem with the atmospheric models, whereas this behavior vanishes when NLTE is considered in the abundance derivation.

It is known that aluminum lines are affected by strong NLTE effects (see, for instance, Gehren et al. 2004), especially in metal-deficient stars with reduced electron concentration in their atmospheres. To derive NLTE aluminum abundances we used the Al I lines at 5557.06 Å, 6696.02 Å, and 6698.67 Å. Our Al atomic model is described in detail in Andrievsky et al. (2008). The atomic data for aluminum was taken from Buurman et al. (1986). The same method of the blending line treatment, as used for barium lines, was applied to the aluminum lines listed above. It should be noted that the NLTE corrections strongly depend on the stellar parameters as shown in Fig. 3.9. As in the case of the Ba abundances, our [Al/Fe] ratios also show a significant trend in LTE, which is fully explained by NLTE effects, as illustrated in Fig 3.10.

3.3.2.4 *HFS lines*

Lines of a number of elements of interest (Sc I, V I, Mn I, Co I, Cu I, Y II, Zr I, La II, Pr I, Nd II, Eu II) suffer from HFS, making a standard EW analysis overestimate the actual abundance. These lines were analyzed by calculating a grid of syntheses around each line of interest using the SYNTHE code. For each line, syntheses were computed, varying the abundance of the element by ± 0.5 dex in steps of 0.05 dex around the starting abundance, which was taken to be the solar-scaled value for the metallicity of the star. Each synthesis was subsequently convolved with

5 http://ams.astro.univie.ac.at/vald/

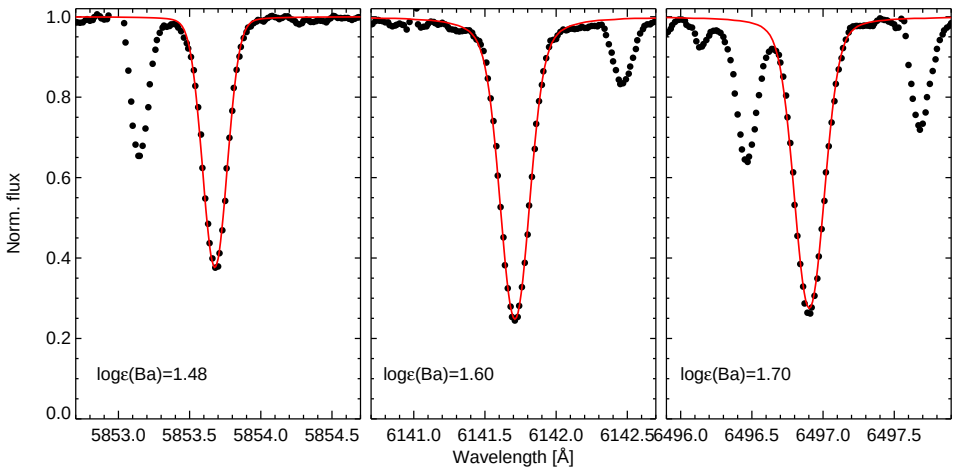

Figure 3.7: Example of the NLTE line profile fitting of the three Ba lines used here. Shown is the star 10237. In each panel, we give the abundance used in the fit.

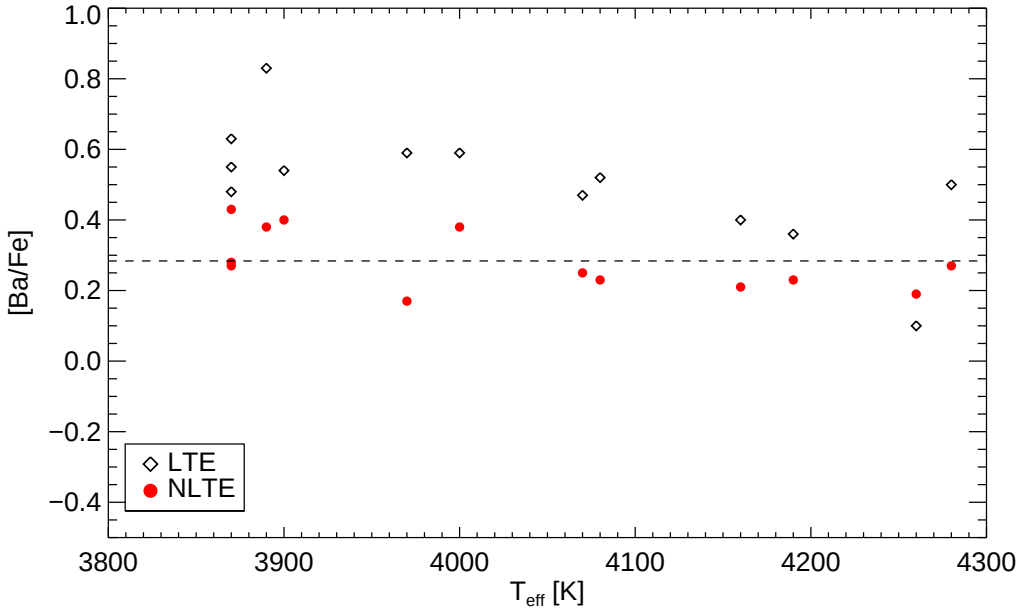

Figure 3.8: [Ba/Fe] vs. $T_{\rm eff}$ for both LTE (black) and NLTE (red). Taking NLTE into account removes the correlation between abundance and $T_{\rm eff}$.

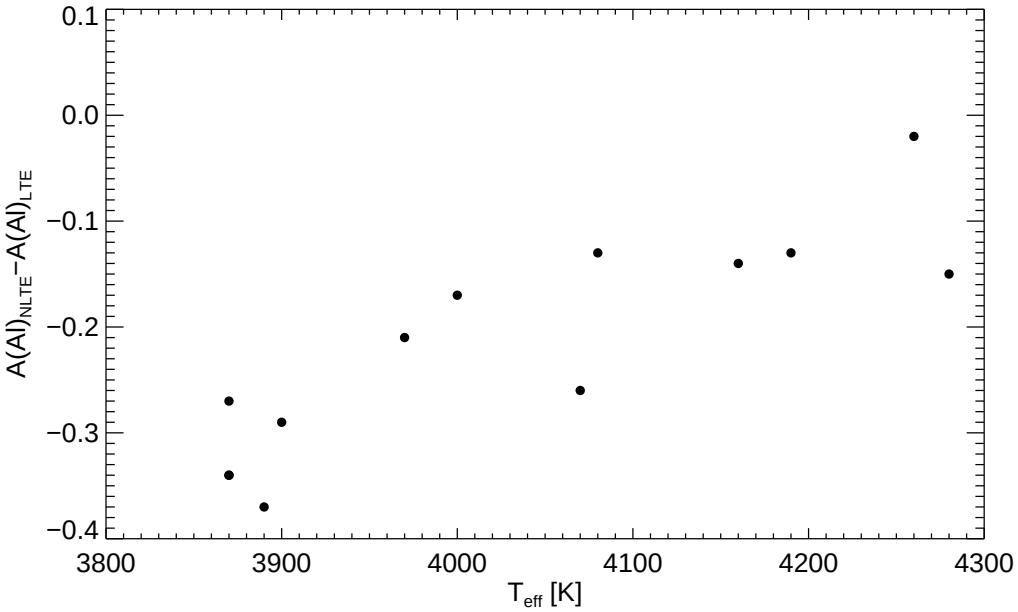

Figure 3.9: Size of the NLTE corrections for Al vs. $T_{\rm eff}$.

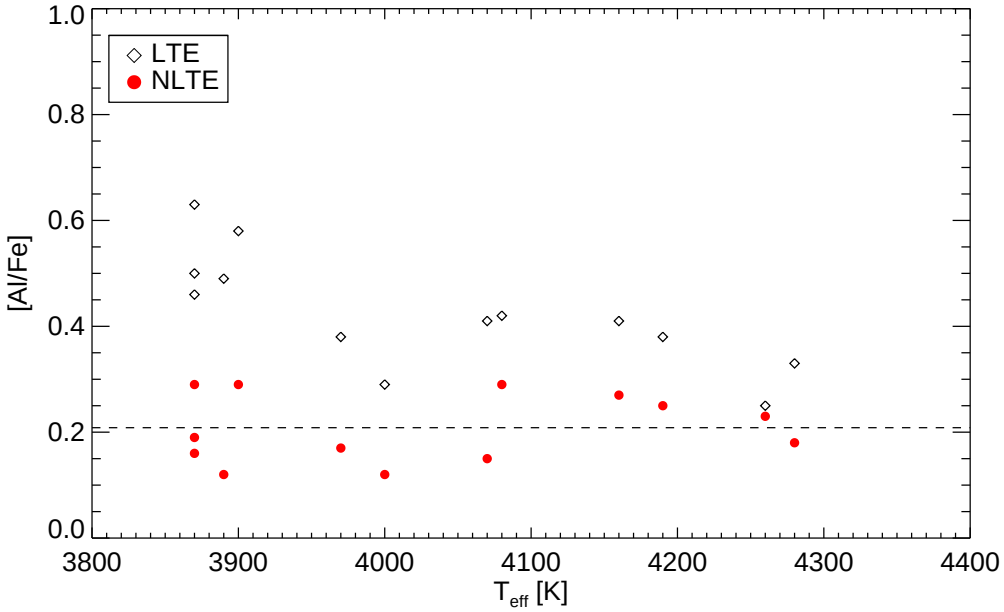

Figure 3.10: As Fig 3.8 but for the measured [Al/Fe] ratios.

a Gaussian (details to follow) to match the observed spectra. HFS data were taken from Version 4 of the GES line list with the exception of Y and Zr, which were taken from McWilliam et al. (2013). The full line list, split into HFS-components, is given in Table A.2.

For each star, fitting regions were determined for each line, along with carefully selected continuum intervals bracketing each feature of interest. Using the continuum regions, the observed spectra were pseudo-normalized, before determining the best fitting abundance by minimization using the `MINUIT` package (James & Roos 1975; Lazzaro & Moneta 2010). The fitting routine (`Fitprofile`) allowed for small velocity shifts of the lines (± 3.0 km s^{-1}), as well as small adjustments of the continuum level to ensure an optimal fit when performing the minimization. `Fitprofile` will be described in more detail in Chapter 4, since it was developed for fitting the MgH molecular features.

When performing the fitting, our software provides for multi parameter fits, allowing the velocity broadening of the lines to be included as a fitting parameter. This assumes a single Gaussian convolution, taking instrumental broadening into account, as well as rotational velocity and macroturbulence as a whole. Initially, the macroturbulent broadening had been determined by synthesizing five clean Fe I lines across the wavelength coverage of the spectrograph. This exercise already yielded broadenings with a significant line-to-line scatter. Also, by inspecting the individual fits for the various HFS lines, it was noticed that the average value of the macroturbulent broadening determined from the Fe I lines was underestimating the broadening needed to produce satisfactory fits to the line profiles. Thus, we decided to also include the macroturbulent broadening as a fitting parameter, allowing for a maximum variation of ± 1.5 km s^{-1} around the mean value initially determined.

Adjusting the broadening for individual lines has the potential of affecting the abundances in a non-negligible fashion. We therefore tested the behavior of the abundances, keeping the broadening fixed at the mean value, as well as when leaving it free. The mean value of the abundances changed by at most 0.05 dex, well below the typical line-to-line scatter, but when the broadening was left free, the scatter became significantly lower. Further, the mean values of the fitted macroturbulence did not show a large scatter, neither across the entire set of lines nor when inspected on a element-by-element basis, the typical standard deviation being on the order of 0.6 km s^{-1}. Also, as suspected from the initial determination of the macroturbulent broadening, the fitted values were found to be higher.

In addition, studies of 3D hydrodynamical model atmospheres confirm that the velocity fields differ at different depths in the atmosphere (Asplund et al. 2006b; Collet et al. 2007), which is not captured in 1D atmospheres when adopting a single value for the macroturbulence. We

thus consider it justified to allow for a (modest) variation in the macroturbulent broadening when fitting spectra with 1D models. The final mean values of the macroturbulent broadening are given in Table 3.6.

3.3.2.5 *Abundance uncertainties*

To derive reliable conclusions from the abundance pattern of the cluster stars, a realistic treatment of the uncertainties is required. We took the following approach. For each element, we derived the mean value of the abundance and assumed the random uncertainty of this value as the standard error of the mean, $\sigma_{\rm rand} = \sigma/\sqrt{N}$, where σ is the standard deviation of our measurements, and N the number of lines used.

The random uncertainties on the fundamental parameters will also affect the derived abundances, so these also need to be taken properly into account. Thus, we derived the abundances again, using atmospheric models perturbed by the aforementioned parameter uncertainties. We then calculated the change in abundance on the [X/Fe] scale, relative to our best-fitting model, using the Asplund et al. (2009) solar abundances. We use the abundance of Fe I for neutral species and Fe II for ionized species. For each parameter perturbation, we then adopted the difference from the best-fitting mean value as the uncertainty of the abundance caused by that particular parameter. The uncertainties of the abundance ratios were then calculated as

$$\sigma_{\rm param,[X/Fe]} = \sqrt{\sigma^2_{\Delta T_{\rm eff}} + \sigma^2_{\Delta \xi_t} + \sigma^2_{\Delta \log g} + \sigma^2_{\Delta [\rm M/H]}}. \tag{3.1}$$

This was done for all elements. Since our stars are very close to each other in fundamental parameters, we only performed this exercise for star 6798 because it falls in the middle of the range considered. The exception is Ce, where we do not have measurements from this star. Instead, we adopted the result from star 10237 for this particular element. The deviations are quoted in Table 3.4. We note that this exercise was also performed with full NLTE analysis for Al and Ba. The influence of the parameter uncertainties on the abundance ratios for 6798 were then assumed to be representative of our complete sample and adopted for all stars.

To yield the total uncertainty for each abundance ratio, we added the random error on [X/H] and [Fe/H] to the uncertainty from the stellar parameters, resulting in an uncertainty of

$$\sigma_{\rm tot} = \sqrt{\sigma^2_{\rm param,[X/Fe]} + \sigma^2_{\rm rand,[X/H]} + \sigma^2_{\rm rand,[Fe/H]}}. \tag{3.2}$$

We also tested the effect of using ATLAS12 models vs. ATLAS9 models on the abundances of a few selected species. For this exercise we

Table 3.4: Changes to derived abundances relative to best-fitting model, when perturbed by the uncertainties on the fundamental stellar parameters. Shown for the star 6798.

	$\Delta T_{\rm eff}$ [K]		$\Delta \log g$ [dex]		$\Delta \xi_t$ [km s^{-1}]		Δ[M/H]		$\sigma_{\rm param}$
Elem.	+80	−80	+0.2	−0.2	+0.10	−0.10	+0.15	−0.15	
Δ[O/Fe]	−0.02	0.05	−0.04	0.05	−0.02	0.04	−0.03	0.01	0.07
Δ[Na/Fe]	−0.09	0.12	0.05	−0.02	−0.01	0.04	0.03	−0.06	0.12
Δ[Mg/Fe]	0.03	0.01	0.02	0.02	−0.01	0.06	0.04	−0.04	0.06
Δ[Al/Fe]	−0.04	0.06	0.01	−0.01	0.00	−0.03	0.02	−0.01	0.06
Δ[Si/Fe]	0.08	−0.07	−0.02	0.03	−0.01	0.03	0.00	0.00	0.08
Δ[Ca/Fe]	−0.09	0.10	0.06	−0.05	0.03	−0.02	0.02	−0.03	0.12
Δ[Sc I/Fe]	−0.10	0.18	0.00	−0.02	0.00	0.02	0.04	0.00	0.14
Δ[Sc II/Fe]	−0.17	0.14	−0.03	−0.04	0.01	−0.04	0.01	−0.07	0.17
Δ[Ti I/Fe]	−0.12	0.15	0.04	−0.02	0.03	0.00	0.02	−0.02	0.14
Δ[Ti II/Fe]	−0.11	0.13	0.04	−0.04	0.04	−0.04	0.02	−0.03	0.14
Δ[V/Fe]	−0.14	0.13	0.00	0.02	0.01	−0.02	0.02	−0.02	0.14
Δ[Cr/Fe]	−0.08	0.10	0.04	−0.03	0.00	0.02	0.02	−0.03	0.10
Δ[Fe I/H]	0.00	−0.02	−0.04	0.03	0.02	−0.04	−0.03	0.03	0.06
Δ[Fe II/H]	0.16	−0.18	−0.12	0.12	0.03	−0.03	−0.06	0.07	0.22
Δ[Mn/Fe]	−0.08	0.12	0.02	0.02	0.01	0.04	0.02	−0.04	0.11
Δ[Co/Fe]	−0.02	0.03	−0.03	0.05	−0.01	0.02	0.00	0.01	0.05
Δ[Ni/Fe]	0.04	−0.02	0.00	0.02	0.01	0.01	0.00	0.01	0.03
Δ[Cu/Fe]	−0.28	0.30	0.09	−0.08	0.06	−0.04	0.08	−0.08	0.32
Δ[Zn/Fe]	0.10	−0.03	0.02	0.04	0.06	−0.01	0.01	−0.02	0.08
Δ[Y/Fe]	−0.15	0.19	0.03	−0.04	−0.03	0.02	0.01	−0.03	0.18
Δ[Zr/Fe]	−0.15	0.18	0.02	0.02	0.06	−0.01	−0.01	0.00	0.17
Δ[Mo/Fe]	−0.12	0.12	0.01	−0.01	0.00	0.01	0.03	−0.02	0.12
Δ[Ru/Fe]	−0.09	0.09	0.00	0.01	−0.02	0.04	0.00	−0.01	0.10
Δ[Ba/Fe]	−0.22	0.21	0.10	−0.06	0.04	−0.09	0.03	0.00	0.24
Δ[La/Fe]	−0.18	0.19	0.03	−0.04	−0.03	0.02	0.00	−0.01	0.19
Δ[Ce/Fe]	0.00	0.34	0.20	0.12	0.15	0.17	0.01	−0.02	0.28
Δ[Pr/Fe]	−0.19	0.22	0.05	−0.05	−0.01	0.01	0.01	−0.02	0.21
Δ[Nd/Fe]	−0.20	0.23	0.05	−0.06	−0.01	0.01	0.03	−0.04	0.22
Δ[Eu/Fe]	−0.13	0.16	0.04	−0.03	−0.02	0.03	0.01	−0.03	0.15
Δ[Dy/Fe]	−0.23	0.24	0.05	−0.07	−0.03	0.01	0.04	−0.06	0.25

Table 3.5: Changes to derived abundances, relative to a tailored ATLAS12 model when using ATLAS9 scaled Solar model and an ATLAS9 model with +0.4 dex α-enhancement. Both models have the same fundamental parameters. Shown here for star 1062.

Elem.	ATLAS9	ATLAS9α
Δ[O/Fe]	0.05	−0.02
Δ[Na/Fe]	−0.07	0.01
Δ[Mg/Fe]	−0.03	0.00
Δ[Si/Fe]	−0.02	−0.02
Δ[Ca/Fe]	−0.06	−0.05
Δ[Ti I/Fe]	−0.02	−0.04
Δ[Ti II/Fe]	0.01	−0.02
Δ[Cr/Fe]	−0.05	−0.02
Δ[Fe I/H]	0.06	−0.02
Δ[Fe II/H]	0.11	−0.06
Δ[Ni/Fe]	0.00	−0.01
Δ[Zn/Fe]	−0.05	−0.04
Δ[Ce/Fe]	0.02	−0.02

used star 1062 as a test case. We report the results of this exercise in Table 3.5, and as might be expected, the differences between the tailored model and the α-enhanced model are small, whereas more pronounced effects are seen if one simply uses a model atmosphere with a Solar abundance mixture scaled to the metallicity of the star.

3.4 RESULTS

The fundamental parameters for our targets are presented in Table 3.6. Our targets span a rather narrow range in all parameters, with the widest spread seen in $\log g$. We find a mean metallicity of [Fe/H] $= -0.78 \pm 0.07$ dex, in excellent agreement with the study of Koch & McWilliam (2008), who found [Fe/H] $= -0.76 \pm 0.01 \pm 0.04$ dex, confirming that the metallicity is marginally lower than previous studies (-0.66 ± 0.12, Alves-Brito et al. 2005, -0.70 ± 0.03, Carretta & Gratton 1997).

The stars 20885 and 29861 are also part of the sample of Koch & McWilliam (2008) (Stars 3 and 1 in their work, respectively). We find good agreement between the fundamental parameters found in their study and our results. We find differences in $T_{\rm eff}$ of [−55 K, −36 K], in $\log g$ [0.09, −0.11], in ξ_t [0.2, −0.04], and in [Fe/H] of [−0.08, −0.09],

which should be compared to our uncertainties of 80 K, 0.2 dex, 0.1 km s^{-1} and 0.06 dex, respectively. Thus both $\log g$ and $T_{\rm eff}$ agree within the uncertainties. The higher ξ_t found for 20885 is likely related to differences in the line selection. We note that in this work, as well as the work of Koch & McWilliam (2008), this star represents an outlier in terms of ξ_t. For comparison, Koch & McWilliam (2008) quote uncertainties of 40 K/0.2 dex/0.1 km s^{-1}/0.04 dex, and they did not enforce ionization equilibrium, which may serve to explain some of the differences.

We also have three stars in common with the work of Alves-Brito et al. (2005) (4794, 5265, and 5968; M8, M11, and M12 in their work). Good agreement is found for $T_{\rm eff}$ (mean difference 53K) but substantial differences are found for $\log g$. Compared to their work we find $\log g$ lower by 0.33, 0.9 and 0.6 dex respectively, which will have a significant impact on the derived abundances of elements derived from pressure-sensitive lines. Since the authors used essentially the same method for deriving the parameters, and also published their EW measurements, we did a line-by-line cross-comparison to investigate this issue. This was done for both Fe I and Fe II. For all three stars, we found that our measured EWs of Fe I was slightly higher than the comparison work, with median offsets of 0.75, 0.5, and 0.8 mÅ for stars 4794, 5265, and 5968, respectively. For Fe II we found corresponding differences of -0.4, 1.9, and 0.9 mÅ. However, individual differences were found to be as large as 13 mÅ in a few cases. We are able to reproduce the results of Alves-Brito et al. (2005) for the Fe II lines, but this requires placing the continuum level significantly lower than can be justified from our spectra.

If the continuum level tends to be underestimated, it will result in a lower EW, which is reflected in a higher value of $\log g$. We use the same $\log(gf)$ values for Fe II as in the comparison study, but for Fe I we adopt the values from the GES line list that, on average, are higher than those used by Alves-Brito et al. (2005). We attribute the main source of the discrepancy to the different continuum placements and the different $\log(gf)$ values applied for Fe I. Minor differences will also arise from the use of different model atmospheres (ATLAS9 Solar-scaled vs. ATLAS12 $\alpha-$enhanced) as mentioned previously.

3.4.1 *The abundance pattern*

In Fig. 3.13 we present the full abundance pattern for our sample stars. The boxes give the interquartile range (IQR), incorporating 50% of our measurements, with the horizontal line indicating the median value. The whiskers indicate the total range of our measurements or extend to 1.5 times the second and third quartile ranges for elements where the full range is greater than this. Any measurements deviating by more

Table 3.6: Fundamental atmospheric parameters for our stars.

ID	$T_{\rm eff}$	log(g)	ξ_t	[Fe/H]
1062	3870	0.30	1.30	-0.83
4794	4070	0.80	1.30	-0.74
5265	3870	0.50	1.20	-0.67
5968	3970	1.00	1.30	-0.75
6798	4000	1.00	1.30	-0.73
10237	4280	1.45	1.60	-0.82
13396	4190	1.35	1.60	-0.87
20885	4260	1.35	1.90	-0.86
27678	3850	0.60	1.20	-0.72
28956	3900	0.75	1.60	-0.84
29861	4160	1.25	1.50	-0.86
38916	4040	1.00	1.40	-0.83
40394	3890	0.45	1.10	-0.70

than this amount is shown. The full lists of all measured abundances ratios are also given in Tables A.3–A.8 in the appendix.

3.4.1.1 *Light elements*

The proton-capture elements Na and Al can be created in the hydrostatic burning in the cores of massive stars during the main sequence phase, as well as at the base of the convective envelope in AGB stars, via the so-called hot bottom burning mechanism (Renzini & Voli 1981). Thus, these elements act as important tracers of the burning conditions required by the polluters, in order to create the abundance patterns observed today.

In essentially all GCs where these elements have been studied, wide spreads of Na have been observed (e. g., Carretta & Gratton 1997; Gratton et al. 2012 and Carretta et al. 2013). Spreads of Al have also been reported for a number of clusters, although this is not as common as the Na variation. With respect to sodium, 47 Tucanae is no different, and we find a spread in [Na/Fe] of ~ 0.5 dex, in the range $[0.01; 0.50]$ dex, which falls within the range reported by other studies (Cordero et al. 2014; Alves-Brito et al. 2005). That the spread is significant compared to the uncertainties on the abundance ratios themselves can be seen by inspecting Table 3.7, where we give the IQR for all elements, as well as the median uncertainty on the measurements. We choose the IQR as a measurement of the spread, since this is more robust towards outliers

and potentially skewed data than the standard deviation. We also give the mean value of the abundance ratios.

The abundance of Na is usually observed to be anti-correlated with that of oxygen. Inspecting Fig. 3.11, we confirm this behavior for our stars in 47 Tucanae. The stars 5265 and 6798 have telluric emission present in one wing of the oxygen lines, so the derived [O/Fe] should be considered only as a lower limit. In our case, the anti-correlation is much more pronounced than seen in the study of Koch & McWilliam (2008), who only observed a small scatter with no clear correlation. However, a clear anti-correlation was recently reported by Cordero et al. (2014), who analyzed a sample of more than 160 giants in 47 Tucanae. Our range in both elements is fully consistent with this study.

Computing the Kendall τ correlation coefficient for the set of measurements yields $\tau = -0.88$, indicating a strong anti-correlation with a statistical significance of 0.001, allowing us to reject the null hypothesis of no correlation with more than 99% confidence. To quantify the strength of the correlation, we performed a bootstrapping exercise, changing the value of both abundance ratios by adding perturbations to the measured values. The perturbations were drawn from a Gaussian distribution with mean zero and standard deviation corresponding to the total uncertainties of our measurements. The two stars with only lower limits of the oxygen abundance were excluded from this exercise. Ten thousand realizations were made for each abundance ratio, and the Kendall τ was computed for each set of ([Na/Fe], [O/Fe]). The distribution of the abundances is shown in Fig 3.12, using a bin size of 0.01. For convenience, we overplot the actual measurements, including the stars with only lower limits. Inspecting the distribution of the τ values, we found that they follow a Gaussian distribution. From this, we computed the mean value of the Kendall τ, finding $\tau = -0.60 \pm 0.15$, so a weaker correlation is found from this exercise.

The pristine population of stars in 47 Tucanae should be indistinguishable from field stars at the same metallicity, and it is thus possible to separate the polluted stars from the pristine using their [Na/Fe] ratio. We adopt a comparison sample from the recent study of abundances in 714 stars in the solar neighborhood by Bensby et al. (2014), although we note that their their sample consists primarily of dwarf stars, whereas our program stars are all giants. The Na abundances from the Bensby et al. (2014) study has been corrected for NLTE effects using the same source as we applied for our stars. We take the mean of their [Na/Fe] measurements for stars with $-0.9 < [\mathrm{Fe/H}] < -0.6$ as a measure of the typical value of [Na/Fe] for stars in the field with a metallicity comparable to 47 Tucanae. We find $[\mathrm{Na/Fe}]_{\mathrm{field}} = 0.09 \pm 0.05$ dex. Taking the mean value plus twice the standard deviation as an upper limit of the [Na/Fe] ratio in typical field stars, we consider stars with

Table 3.7: IQR, median value, and median uncertainty ($\bar{\sigma}$) for all measured elements.

Elem.	IQR	Median	$\bar{\sigma}$
[Fe I/H]	0.12	-0.79	0.06
[Fe II/H]	0.14	-0.80	0.22
[O/Fe]	0.26	0.30	0.10
[Na/Fe]	0.23	0.21	0.14
[Mg/Fe]	0.06	0.44	0.08
[Al/Fe]	0.11	0.21	0.08
[Si/Fe]	0.05	0.32	0.09
[Ca/Fe]	0.12	0.24	0.13
[Sc I/Fe]	0.19	0.01	0.15
[Sc II/Fe]	0.06	0.21	0.17
[Ti I/Fe]	0.08	0.33	0.15
[Ti II/Fe]	0.16	0.41	0.15
[V/Fe]	0.12	0.17	0.14
[Cr/Fe]	0.08	-0.03	0.11
[Mn/Fe]	0.08	-0.20	0.13
[Co/Fe]	0.10	-0.00	0.07
[Ni/Fe]	0.03	-0.12	0.04
[Cu/Fe]	0.18	-0.14	0.35
[Zn/Fe]	0.05	0.26	0.13
[Y/Fe]	0.20	0.07	0.19
[Zr/Fe]	0.16	0.41	0.17
[Mo/Fe]	0.07	0.55	0.13
[Ru/Fe]	0.09	0.51	0.13
[Ba/Fe]	0.09	0.25	0.24
[La/Fe]	0.21	0.07	0.21
[Ce/Fe]	0.13	-0.04	0.32
[Pr/Fe]	0.09	-0.04	0.24
[Nd/Fe]	0.09	0.04	0.24
[Eu/Fe]	0.22	0.32	0.19
[Dy/Fe]	0.15	0.70	0.27

[Na/Fe] $\geq$ 0.19 dex to belong to the polluted population of stars. This approach allow us to separate the stellar populations in 47 Tucanae, even if we are not sampling the full range of the Na variations. The stars identified as belonging to the polluted population are indicated with red triangles in Fig. 3.11 and in all other relevant figures. We also identify them by boldface numbers in all relevant tables.

Turning our attention to the measured aluminum abundances in Fig. 3.11, it is evident that they show very little spread, with a mean and standard deviation of $[\mathrm{Al/Fe}]_{mean} = 0.21 \pm 0.06$ dex. This should be compared to the uncertainty of the individual [Al/Fe] determinations, which are on the order of ± 0.08 dex, so our results are consistent with a single value for the total sample of stars. This contrasts with the the results presented by both Carretta et al. (2009a) and Cordero et al. (2014), who reports a significant variation in their measured Al abundances. On the other hand, if we inspect the IQR of the *polluted* population alone, we find a spread of 0.13 dex, which is marginally larger than our uncertainties and larger than what is seen for the pristine population of stars. This may indicate that a small amount of Mg has indeed been processed to Al in the polluted population, even if we do not detect any Mg-Al anti-correlation. On the other hand, no offset in Al is observed between the pristine and polluted population, so the larger IQR likely just reflects our small sample size.

That we do not observe any significant spread in Al in our sample of stars is a consequence of treating the Al synthesis in NLTE, rather than relying on a standard LTE analysis. If the Al lines are treated in LTE, we observe a broader range of abundances, as discussed in more detail in Sect. 3.5.1. The disappearance of the Al variation in this case is more related to the small sample of stars in our study, combined with the spread in our stellar parameters. It does not imply that no Al variation exists within the cluster. The presence of a variation is evident from previous studies by Carretta et al. (2009a) and Cordero et al. (2014), who report significant variations in Al for stars with identical parameters, as do others. Because NLTE corrections are governed by the stellar parameters, such variation would not disappear as a consequence of a full NLTE analysis of their stars. In our case, the sample simply does not cover the full range of Al variations for a given set of stellar parameters.

The two bottom panels in Fig. 3.11 show [Al/Fe] vs. [O/Fe] and [Na/Fe] vs. [Al/Fe]. No correlations are visible in either of the two plots, for the sample as a whole, in accordance with our finding that [Al/Fe] for our stars are consistent with a single value. This also indicates that, at least for the stars in our sample, the polluted generation has been enriched by material from stars where the Mg-Al burning cycle was not activated to any significant extent.

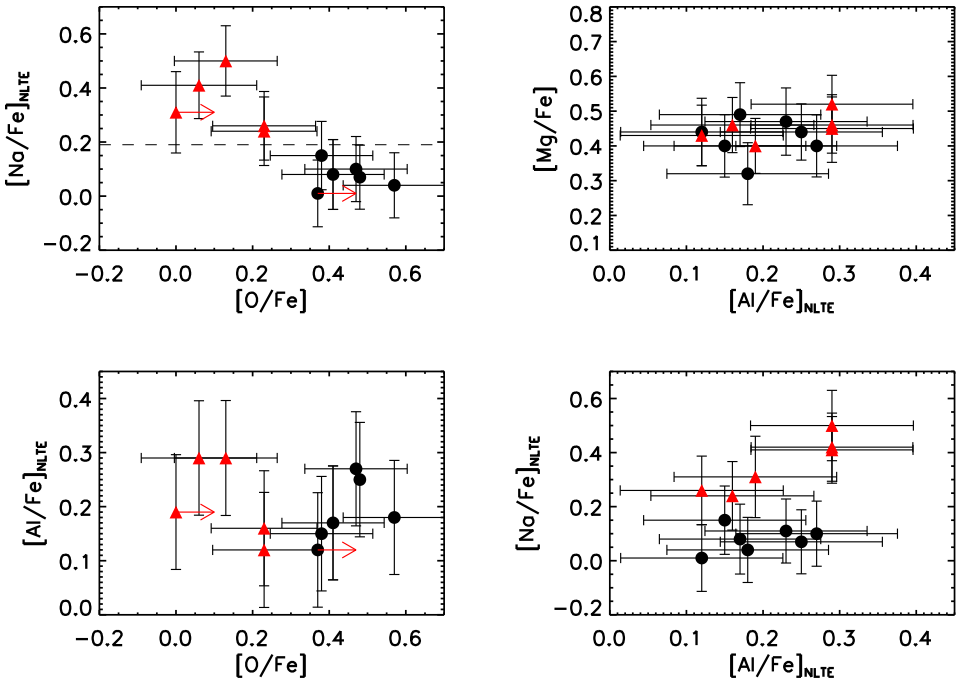

Figure 3.11: Correlations between the light elements. Top left: [Na/Fe] vs. [O/Fe], top right: [Mg/Fe] vs. [Al/Fe], bottom left: [Al/Fe] vs. [O/Fe], bottom right: [Na/Fe] vs. [Al/Fe]. The dashed line indicates the adopted cut between the pristine (black circles) and polluted (red triangles) population of stars. The red arrows indicate lower limits on the [O/Fe] abundance.

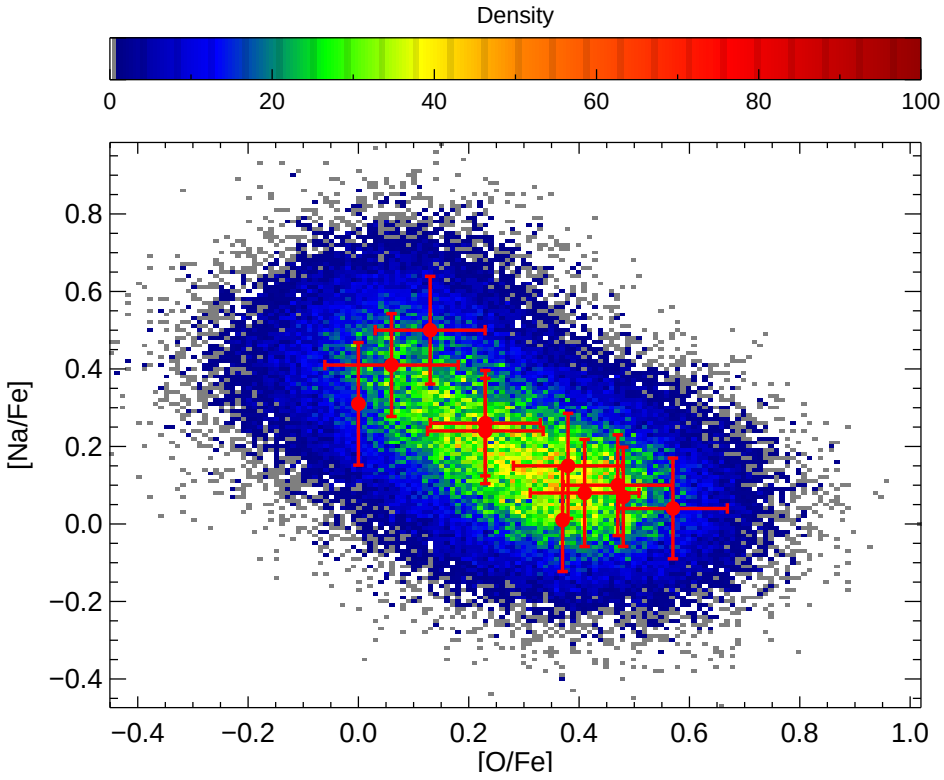

Figure 3.12: Distribution of [Na/Fe] vs. [O/Fe] from our bootstrapping exercise, shown as a density plot. Bin-size is 0.01. The measurements are shown in red. The two targets with no oxygen errorbars only got lower limits, so were excluded from the bootstrapping calculations.

3.4.1.2 *α-elements*

The α-elements (O, Mg, Si, Ca, and Ti are enhanced in ATLAS12 models) show roughly constant behavior, with a mean enhancement of 0.34 ± 0.04 dex relative to iron, in good agreement with what is found by other studies of 47 Tucanae (e. g., $[\alpha/\mathrm{Fe}] = 0.41$ dex; Koch & McWilliam (2008); 0.29 dex, Cordero et al. (2014); 0.3 dex, Alves-Brito et al. 2005). In Table 3.7, oxygen is the only exception, because it shows a variation and the well-known anti-correlation with Na, as discussed earlier. Excluding oxygen from the calculation of the α-enhancement, we find a mean value of $[\alpha/\mathrm{Fe}] = 0.35 \pm 0.03$ dex, hence an insignificant change compared to using the entire set of abundances.

We note that Ti exhibits a large scatter, as well as discrepancies between the neutral and ionized species, which is a well-known issue that still has not been entirely resolved, although improvements were clearly made with the recent update of the $\log(gf)$ values by Lawler et al. (2013). The remaining part of the discrepancy can likely be attributed to NLTE effects on Ti I as investigated by Bergemann (2011), who shows that the abundance from lines of the neutral species are systematically underestimated in LTE. Following the recommendations in her work, we adopt the Ti II abundances as the best measure of Ti in the stars, since the ionized species have negligible NLTE corrections. Furthermore, in a high-metallicity environment like 47 Tucanae, the usable Ti lines are very strong and enter the saturated part of the curve of growth, making them very weakly sensitive to changes in abundances.

Scandium is intermediate between pure α elements and iron-peak elements, and the formation processes is not entirely clear at present. In Fig. 3.13, a clear offset is seen between the Sc I and Sc II abundances, with the median values differing by about 0.2 dex. This is most likely related to NLTE effects influencing the lines of the neutral species. Whereas this effect has not been studied in giants, Zhang et al. (2008) find for the Sun that NLTE corrections are positive and on the 0.2 dex level for the neutral species, bringing Sc I and Sc II back into agreement. While not directly applicable to our sample of stars, their study at least suggests that NLTE effects could be responsible for the observed disagreement.

3.4.1.3 *Iron-group elements*

Each of the iron group elements (V, Cr, Mn, Fe, Co, Ni) are found to be constant, and we see no evidence for an intrinsic spread of any of them (see Table 3.7). Mn and Ni appears to be slightly underabundant compared to Fe, whereas Co is found to be overabundant. This is seen also in studies of other GCs such as M75 (Kacharov et al. 2013), M71 (Boesgaard et al. 2005), NGC 1851 (Carretta et al. 2011b), M4 and M5

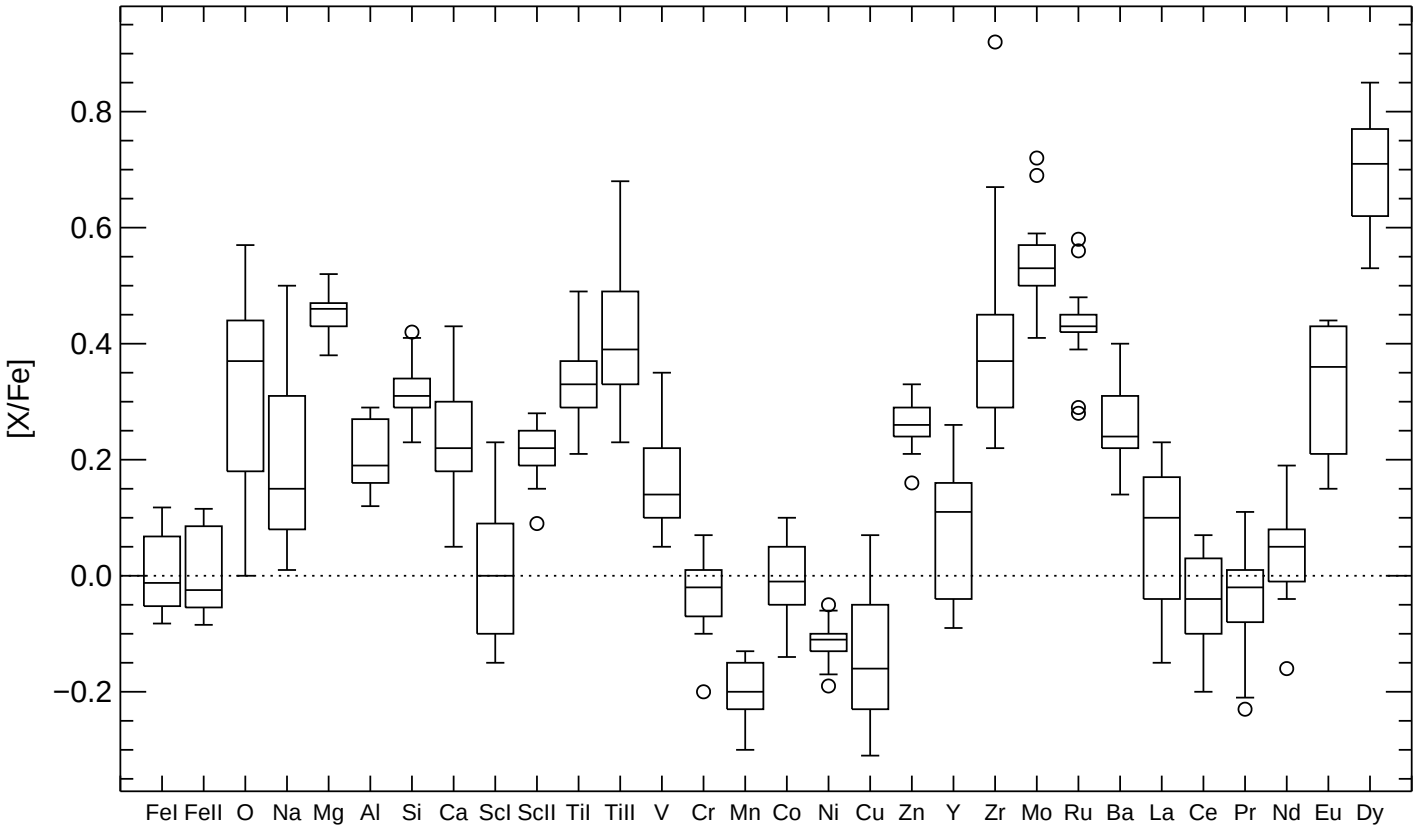

Figure 3.13: Abundance pattern for our sample stars. Shown are the interquartile ranges. The most extreme outliers are indicated with open circles.

(Yong et al. 2008b), as well as in globular clusters in the Large Magellanic Clouds (Colucci et al. 2012).

3.4.1.4 *Neutron-capture elements*

All elements beyond Ni are produced by neutron captures, either in the rapid(r) process associated with a very high neutron flux during neutron star mergers or SN II explosions, or, alternatively, in the slow(s) process, taking place on longer timescales in AGB stars, for example. Many elements can be created through both processes, but a few can be associated in large part with one of the two mechanisms. The s-process elements Y and Zr both show a scatter that does not appear to be correlated with either stellar parameters or the light element abundance variations (See Fig A.2 in the appendix). However, the IQRs for [Zr/Fe] and [Y/Fe] are 0.16 dex and 0.20 dex, which should be compared to typical uncertainties for individual stars of 0.19 and 0.18 dex respectively. The abundance dispersion is thus consistent with a delta function convolved with the measurement uncertainty; i.e., there is no evidence for an abundance variation given the measurement uncertainty (also see Table 3.7). Lines of both elements have been treated in LTE. We note that while NLTE effects on Zr-I lines may influence our derived abundances, given the narrow range in stellar parameters of the program stars, it is unlikely that neglect of NLTE effects masks the presence of a genuine abundance spread for Zr in 47 Tucanae. A recent study by Velichko et al. (2010) indicates that both ionization stages of Zr are influenced by NLTE, in particular Zr I. They find corrections as large as 0.3 dex, increasing with decreasing $T_{\rm eff}$, $\log g$, and metallicity. Their study only treated the 4241 Å and 4687 Å Zr I lines, and since NLTE corrections can be strongly line-dependent, the potential NLTE corrections of the lines used in this work may differ from theirs by a non-negligible amount.

The heavy s-process elements La and Ba show no correlation with any of the light elements that exhibit the abundance variations, being fully consistent with just a single value (See Fig A.3 and Table 3.7). This result suggests that low-mass AGB stars have not contributed strongly to the enrichment of the gas incorporated in the polluted population of stars, because these elements are predominantly produced in lower mass AGB stars (Straniero et al. 2014).

The elements Mo, Ru, Pr, and Nd have almost equal contributions from both slow and rapid neutron capture processes (Bisterzo et al. 2014), so it is difficult to interpret their abundances in terms of polluter candidates. None of these elements exhibit any intrinsic scatter or correlations with the light elements. We note that Mo and Ru appear enhanced, compared to Pr and Nd, which is seen in some GCs where these elements have been studied (M75, Kacharov et al. 2013), whereas

Roederer et al. (2011) find the opposite behavior in their study of M22. This cluster also shows a spread in iron, so the reason for this behaviour may also be linked to the fact that the different populations have seen additional SNe contributions to their abundance patterns, which is not expected to be the case for 47 Tucanae. Using Mo and Ru to distinguish between different polluters is further complicated by the complex formation channels for this element (see Hansen et al. 2014).

The r-process element Eu is found to be constant within the measurement uncertainties (see Table 3.7), and whatever small variation is observed is also not correlated with the light element variation (Fig A.3). Since Eu is almost exclusively produced in the r process (94%, Bisterzo et al. 2014), this element is often used as a measure of the overall r-process enrichment. When comparing Eu to the s-process-dominated species Ba (85% s process, Bisterzo et al. 2014), we find a value of $\log\epsilon(\mathrm{Ba/Eu}) = 1.59 \pm 0.17$, which is close to the Solar value of 1.66 based on the Arlandini et al. (1999) values, suggesting that the neutron capture elements in 47 Tucanae have seen a prevalent s-process contribution, since the pure r-process value is 0.97 for the same abundance ratios. This is at odds with what was found by the study of Cordero et al. (2014), who compared Eu to La (76% s-process, Bisterzo et al. 2014), suggesting that the neutron capture elements in 47 Tucanae were r-process-dominated. Indeed, if we use the same element ratios as in their study, we find $\log\epsilon(\mathrm{La/Eu}) = 0.33 \pm 0.04$, which would suggest a larger r-process contribution compared to the s process, because the pure r-process ratio is 0.27, compared to the Solar ratio of 0.69 (Arlandini et al. 1999). However, both La and Ba indicate that 47 Tucanae has seen some s-process contribution, although the amount differs. This also in agrees with what was seen by Alves-Brito et al. (2005) for example, who found $[\mathrm{Ba/Fe}] = 0.31 \pm 0.07$ dex to be significantly higher than their [La/Fe] ratio of 0.05 ± 10.

We decided not to use Dy as an s-process probe (84% s process, Bisterzo et al. 2014), because this element appears more enhanced than any other element, and in particular it is enhanced with respect to Eu. Dy has only been measured in clusters in a few cases. A mild enhancement relative to Eu was found in both M75 (Kacharov et al. 2013) and M22 (Roederer et al. 2011), whereas Carretta et al. (2011b) find [Dy/Fe] to be equal to [Eu/Fe] in the GC NGC 1851. Cohen & Meléndez (2005), on the other hand, find that Dy was depleted relative to Eu in both M3 and M13, so the behavior of this element is unclear at present, but may be cluster dependent. Finally, we note that Roederer et al. (2010) argues, albeit in a different metallicity regime, that measuring abundance ratios of Pb is the only definitive way to examine whether an s-process contribution has occurred within a stellar population.

3.5 DISCUSSION

The majority of our results show good agreement with previous studies of 47 Tucanae, but a few points warrant a deeper discussion. Several studies (Brown & Wallerstein 1992a, BW92, James et al. 2004, J04, Alves-Brito et al. 2005, AB05, Wylie et al. 2006, W06, McWilliam & Bernstein 2008, McW08) have reported abundances of the s-process peak elements, Y, Zr, and Ba, but the disagreement between the individual studies is significant. This is clearly seen in Table 3.8, where we quote the mean values from the relevant studies, as well as the values found in this work, given as the mean $\pm$ the standard deviation. The reason for the disagreement of the [Y/Fe] ratios can be understood easily, since the Y II lines used to derive the yttrium abundances suffer from HFS. If this is not properly taken into account, the abundance will be overestimated. The studies of Brown & Wallerstein (1992a) and Wylie et al. (2006) do not apply an HFS analysis, and thus they find a higher abundance than any of the other quoted studies. Our mean abundance is slightly higher than the two remaining studies that reported Y abundances. A direct comparison to the James et al. (2004) study is difficult, since they use a different set of lines that fall outside our spectral range. They also find an offset in the abundance between main sequence turn-off and subgiant stars, with the former having an [Y/Fe] of $+0.06 \pm 0.01$, so in better agreement with our measurements. No explanation for this offset is given, but we chose to compare our results to the measurements of subgiants, because they are more similar to our sample than the dwarf stars yielding the higher abundance ratio. McWilliam & Bernstein (2008), on the other hand, use integrated light spectroscopy and derive their abundance based on only a single line, making a comparison to our results difficult, although one would expect the mean derived from multiple stars to be comparable to what would be measured from integrated light, assuming that the integrated light lines can be synthesized correctly.

Turning our attention to the [Zr/Fe] ratio, there is again no clear picture of the actual abundance ratio. The study of Alves-Brito et al. (2005) relies on the synthesis of the 6143 Å line, and they do not report taking HFS into account in their analysis. Thus it is surprising that we find a higher abundance, even when performing an HFS analysis. We do note, however, that the 6143 Å line yields a systematically lower abundance, compared to the two additional lines we used, but never more than 0.1 dex, which is insufficient for reconciling our measurements with those of Alves-Brito et al. (2005). Inspecting our abundances on a star-by-star basis, we never see line-to-line scatter larger than 0.1 dex, suggesting that our abundance measurements are internally robust. However, as can be seen from Table 3.4, the Zr abundance is very sensitive to changes

Table 3.8: [Y/Fe], [Zr/Fe], and [Ba/Fe] as reported by several other studies, as well as what is found in this work.

Source	[Y/Fe]	[Zr/Fe]	[Ba/Fe]
BW92	$+0.48 \pm 0.11$	-0.22 ± 0.05	-0.22 ± 0.12
Jo4	-0.11 ± 0.10	–	$+0.35 \pm 0.12$
ABo5	–	-0.17 ± 0.12	$+0.31 \pm 0.07$
Wo6	$+0.65 \pm 0.18$	$+0.69 \pm 0.15$	–
McWo8	-0.13	$+0.05$	$+0.02$
This work	$+0.09 \pm 0.11$	$+0.39 \pm 0.20$	$+0.28 \pm 0.07$

in the $T_{\rm eff}$ scale, which can explain part of the difference found. Comparing the three stars in common between our sample and the study of Alves-Brito directly, the most deviant star in terms of parameters (5265) would have its Zr abundance lowered by ∼0.2 dex if the parameters were changed to force agreement with the Alves-Brito study. This can explain part of the disagreement. The remaining disagreement can probably be explained by a combination of differences in continuum placements, as discussed earlier for the iron lines, and the use of different model atmospheres (see Table 3.5). Our results are in somewhat better agreement with the MWo8 study and we note that we use the same atomic line data as in their study, although we still find a significantly larger Zr abundance.

Our results for Barium compare well with what has been found by most other studies, although we find a higher abundance than the McWilliam study, which again might be related to their use of integrated light spectroscopy. Also, we are using slightly different atomic parameters, which will also lead to differences in the derived abundances.

3.5.1 *NLTE effects for Al*

As mentioned previously, we found that NLTE was relevant for Al and sensitive to the stellar parameters, which may introduce problems with abundances derived from a LTE analysis. Since Al is a key element for constraining possible polluter candidates in GCs, this is important to consider. Significant NLTE effects on Al lines, even at high metallicity have been reported by Gehren et al. (2004, 2006), who studied the effect in a large sample of dwarf stars, showing that the effects were non-negligible even at solar metallicity. We confirm this behavior in our giants, although the corrections are in the opposite direction of that in the dwarf stars.

A variation in the Mg and Al abundances has been reported in more than 20 GCs, with a large part (18) of the data coming from the study of bright giants by Carretta et al. (2009a). However, the Al abundances in the literature are all derived under the assumption of LTE and often based on a small number of bright stars. When inspecting Fig. 3.14 where we plot both the LTE and NLTE values of [Al/Fe] it is immediately apparent that the total range of the [Al/Fe] ratio for our sample decreases by more than a factor of two when treated in NLTE, making our results consistent with only a single abundance across our sample of stars. As discussed previously, this is related to our sampling of stars in the CMD, underlining the importance of dense sampling of the parameter space in order to unambiguously claim a variation in Al. Unless one samples stars with near-identical parameters one may overestimate the actual spread in [Al/Fe] in LTE, in particular if the extremes in [Al/Fe] coincide with extremes in stellar parameters. In the case of 47 Tucanae, however, significant variations in Al has been observed in stars with identical parameters (Carretta et al. 2013; Cordero et al. 2014) so this cluster exhibits a genuine spread. The latter study uses the 6696 Å and 6698 Å lines, so it is directly comparable to ours, whereas Carretta et al. (2013) uses the near infrared (NIR) lines in the region around 8773 Å, which may have different NLTE corrections. But even allowing for corrections of a different magnitude for the NIR lines would not result in a disappearance of the observed variation in their study. Another effect of treating the aluminum lines in NLTE is an overall shift to lower values as can also be seen by comparing the LTE and NLTE results in Fig. 3.14. This result will be valid in general and implies that the overall enhancement of Al relative to iron may be overestimated in earlier works. However, this needs to be investigated in a larger sample of stars and ideally in multiple GCs to determine its true extent.

Interestingly, the stars in our sample do not separate clearly in Fig. 3.14. One would expect that stars that are enhanced in Al and depleted in Mg would also be enhanced in Na and depleted in O, since the Mg-Al anti-correlation is created by a more advanced burning stage. However, a variation in Na-O does not imply a variation also in Mg-Al. We see no evidence of the Al abundance being correlated with either O or Na in our sample of stars (See Figs. 3.14 and A.1). Depending on the polluter candidate, it is certainly possible to create an Na-O anti-correlation, without activating the Mg-Al burning cycle responsible for the anti-correlation of the latter (See, e. g., Decressin et al. 2007; Bastian et al. 2013). This is also a well-known observational fact, where only a subset of the globular clusters show significant variations in Al (see, e. g., Carretta et al. 2009a). Indeed, Cordero et al. (2014) also do not find a correlation between Na and Al in their much larger sample of stars in

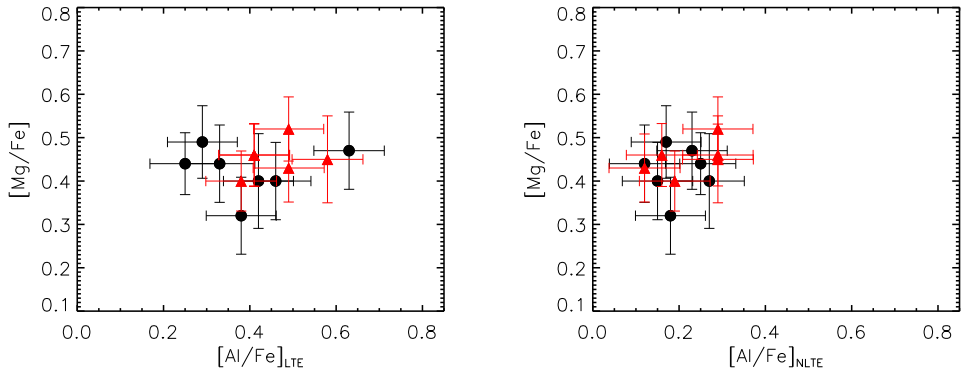

Figure 3.14: [Mg/Fe] vs. [Al/Fe] in LTE (left) and NLTE (right). The observed range in [Al/Fe] decreases when NLTE is taken into account.

47 Tucanae (See their Fig. 8), but merely find a variation in Al for any given Na abundance, consistent with our findings here.

3.5.2 *Comparison with M71*

The GC M71 has a [Fe/H] $= -0.71$ (Ramírez et al. 2001), and is thus a close match to 47 Tucanae in terms of metallicity but is not nearly as massive ($1.7 \times 10^4\,M_\odot$ Marks & Kroupa 2010). Also for this cluster, only a small dispersion is seen in the [Mg/Fe] ratio (Δ[Mg/Fe] $=$ 0.11), which is very similar to what we observe for our sample of stars (Ramírez & Cohen 2002 and Meléndez & Cohen 2009), suggesting that the smaller variation observed may be related to the high metallicity of the cluster. Our values of [Mg/Fe] are offset by around 0.2 dex, compared to Meléndez & Cohen (2009), whereas better agreement is seen with the range reported by Ramírez & Cohen (2002). Both studies also found only a narrow range in aluminum abundances (Δ[Al/Fe] $= 0.16$), which is comparable to what we observe, but we note that 47 Tucanae certainly exhibits larger variations than what we found, as discussed above.

Inspecting the behavior of the elements heavier than iron, we again see a good agreement with the observed abundance pattern of M71 (Ramírez & Cohen 2002), with the exception of Y and Zr, where we find an overabundance relative to iron, opposite to what is reported by Ramírez & Cohen (2002). However, the more recent study of Meléndez & Cohen (2009), reports an overabundance of Zr, albeit lower than what we find for 47 Tucanae. This may indicate that 47 Tucanae has seen a stronger contribution from the weak s-process than M71. Regarding La and Ba, M71 appears to be slightly more enhanced in these elements

than 47 Tucanae, in particular La, indicating that even though the two clusters have essentially the same metallicity, they have not undergone identical evolutions, which is not surprising considering the mass difference between the two clusters. We note that the same trend of Ba being enhanced to the level of Eu, as well as being more enhanced than La, is seen in both cases.

4

MAGNESIUM ISOTOPES IN RED GIANTS AND POLLUTION HISTORY OF THE GALACTIC GLOBULAR CLUSTER 47 TUCANAE

Adapted from Thygesen, A. O., Sbordone, L., Ludwig, H.-G., Ventura, P., Yong, D., Collet, R., Christlieb, N., Melendez, J. Zaggia, S. A&A, submitted.[1]

4.1 INTRODUCTION

In this chapter we build on the results from Chapter 3 and determine the isotopic mixture of magnesium in the same sample of stars. In addition, we present the first, initial study of the effects of using 3D atmospheric models and spectral synthesis when deriving the isotopic mixture. Finally, we discuss the results from the two chapters in relation to the chemical evolution history of 47 Tucanae, and how Mg isotopes can help constrain this, finishing with a common conclusion.

4.2 ANALYSIS

The isotopic shifts of the atomic lines of Mg are much smaller than the natural broadening of the spectral lines, so in order to measure the isotopic mixture, one has to utilize molecular lines of magnesium hydride (MgH). We use the features from the electronic A-X transitions around 5135 Å, where the isotopic shifts are observed as an asymmetry in the red wing of the dominating ^{24}MgH feature.

4.2.1 *Line selection*

Traditionally, three molecular MgH features are used for the derivation of magnesium isotopes (McWilliam & Lambert 1988) at:

- 5134.6 Å, which is a blend of the $0-0Q_1(23)$ and $0-0R_2(11)$ electronic transitions.
- 5138.7 Å, which is a blend of the $0-0Q_1(22)$ and $1-1Q_2(14)$ electronic transitions.

1 L. Sbordone developed the `Fitprofile` software and provided text on the section describing the software. P. Ventura computed and provided the AGB pollution models. All remaining work and text was done by me.

- 5140.2 Å, which is a blend of the $0-0R_1(10)$ and $1-1R_2(14)$ electronic transitions.

All of the MgH features mentioned above, suffer from blends with both atomic lines as well as molecular lines of C_2, CN and CH. However, it is believed that these three features are suffering the least from blends, compared to other MgH transitions in the vicinity.

Compared to previous investigations of Mg isotopic ratios, we used new, updated line positions and level energies taken from Shayesteh & Bernath (2011) for ^{24}MgH and from Hinkle et al. (2013) for ^{25}MgH and ^{26}MgH, where all previous studies have been using the pioneering work of Bernath et al. (1985). The changes in line position between our data and the work of Bernath et al. (1985) were typically small, so this did not have a large impact on the derived results, compared to employing the linelist used in earlier works. For CH we used line information from Masseron et al. (2014), whereas for C_2 we use Brooke et al. (2013), and Sneden et al. (2014); Brooke et al. (2014) for CN. For the atomic blends, we used the line information from Version 4 of the GES linelist (Heiter et al. in preparation), with a few lines added from the VALD database (Kupka et al. 2000). We include atomic blends from Ti, V, Cr, Fe, Co, Y, Nb, Mo, Ce and Pr. We used the elemental abundances measured in Thygesen et al. (2014) where available. In cases where the elemental abundances could not be measured, we used scaled Solar values.

We checked our line list against Arcturus, which is admittedly more metal-rich, and it was found that some C_2 lines (two at the 5134.6 Å feature and two at the 5140.2 Å feature) appeared much too strong, when Arcturus was fitted with the stellar parameters and abundances from Ramírez & Meléndez (2005). In fact, carbon had to be depleted by more than an order of magnitude to being able to fit the two mentioned MgH features. This points towards either a wrong $\log(gf)$ or the presence of 3D effects on the C_2 lines, the latter which we did not investigate. The C_2 lines in Arcturus are so overestimated, that a much better fit is obtained by simply removing them from the syntheses, which suggests that the culprit C_2 lines potentially have erroneous line data. From this exercise, we also identified a previously unused MgH molecular feature at 5135.1 Å ($0-0R_1(11)$ transition)that was found to be insensitive to the C abundances.

While the C_2 lines blending with the MgH features appear to be too strong, at least for stars as metal-rich as Arcturus, they are also temperature-sensitive and increases in strength with increasing temperature. We found that simply removing the few problematic C_2 lines was not advisable in the case of our stars. A complete removal resulted in spurious trends of the isotopic ratios with temperature for the results from the 5134.6 Å and 5140.2 Å features in our sample of stars, sug-

gesting that the removal of the problematic C_2 lines amounts to over-compensation. More likely, these lines are real, but their $\log(gf)$ values are in error.

Meléndez & Cohen (2009) and Yong et al. (2003a) used two different regions to estimate the C abundance in their sample of giants, namely a C_2 feature at 5136 Å, and the C_2 features around 5635 Å. In our sample of stars, we cannot derive an useful C abundance from the 5136 Å feature, but the 5635 Å region was found to be useful for the hotter stars, although the bands are very weak for stars with the parameters in our sample. Due to the faintness of these bands and blending with other molecules, we only consider our measurements as upper limits of the C. As can be seen in Fig. 4.1, the 5134.6 Å and 5140.2 Å MgH features are rather sensitive to the C abundance, but nonetheless, we are able to fit these two bands with the C abundance estimated from the 5635 Å features. However, keeping in mind the result from the test on Arcturus, even with a correct C abundance, the isotopic ratios derived from these two features should not be considered as reliable as what can be derived from the 5134.1 Å and 5138.7 Å features, which do not show such sensitivity.

For the low $\log g$ stars in our sample, on the other hand, the observed spectra are so cluttered with other molecular features, that we cannot derive any reliable C measure from either of the two regions. Thus, for these stars we took a different approach; When comparing our estimates of the C abundance, from the hot sample of stars, to the carbon measurements from Carretta & Gratton (1997), for stars with similar [Na/Fe] and [O/Fe] values, we find good agreement. Then, for our low gravity stars, where we do not have an estimates of C from our spectra, we adopt the carbon measurements from Carretta & Gratton (1997), using values for stars with the same [Na/Fe], [O/Fe] and [Fe/H]. While their measurements are from sub-giants, we assume that their measurements reflects the variation in carbon between the polluted and pristine populations, also for giants. However, we note that additional C depletion is to be expected as the stars ascend the giant branch, but as can also be seen from Fig. 4.1, the impact of C depletion beyond $[C/Fe] = -0.3$ dex, on the band shape is marginal, especially for the 5134 Å feature. All the low $\log g$ stars have an [C/Fe] of at least -0.3, so even if the C abundance is significantly depleted beyond this, it will only have a small impact on the final isotopic ratios

When calculating the average Mg isotopic fractions, we only give half weight to the results from the 5134.6 Å and 5140.2 Å features, although we were able to fit the features with similar isotopic fractions to the 5135.1 Å and 5138.7 Å features in most cases. Full weight was given to the 5135.1 Å and 5138.7 Å features. This was done for all stars in the

sample, including the ones where we do have our own estimates of C, due to the potential $\log(gf)$ problems discussed above.

We also note that the trends with $T_{\rm eff}$ discussed above, are not observed when we fit the MgH bands with the C_2 features kept in the line list. One could speculate that NLTE effects on MgH, which are unaccounted for, could also manifest themselves through correlations with the stellar parameters, but as shown by Yong et al. (2004), MgH does not appear to show any NLTE effects that could explain such trends.

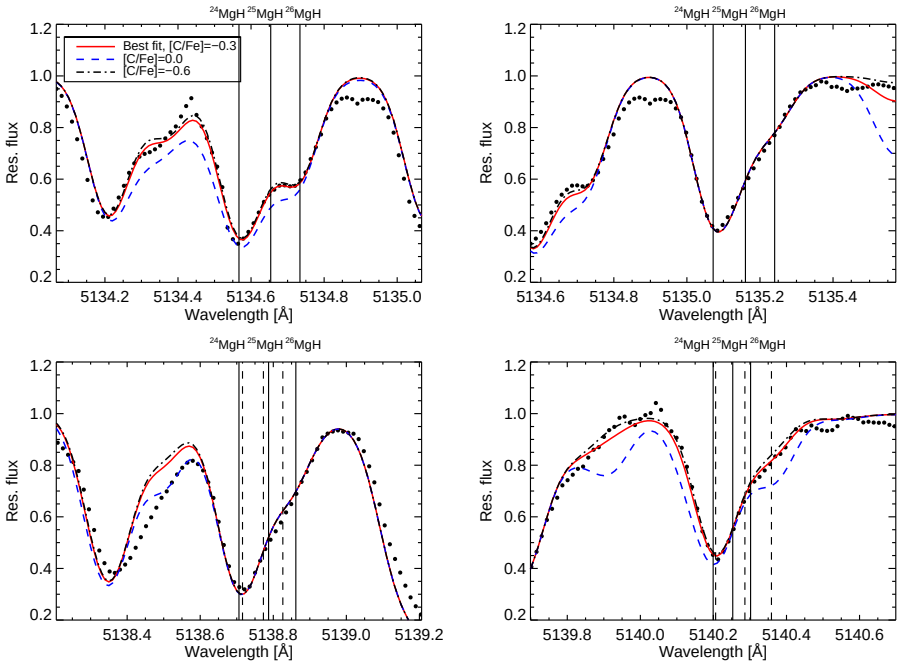

Figure 4.1: Synthesis of the four MgH features used to derive the isotopic fractions of Mg in star 5265. The red line shows the synthesis using the best-fitting [C/Fe], whereas the dashed lines show the change of the line shape when the [C/Fe] is changed by ± 0.3 dex around this value.

Since N is also varying strongly within GCs, we tested the influence on the MgH features by varying [N/Fe] (Fig 4.2). Clearly the CN blends we include are not strong enough to have a significant impact on the synthesis, even when varied by one dex. In principle, also blends of TiO could influence our results. We tested this by calculating a synthesis for all four features, using all known transitions of TiO from Plez (1998). We included lines of all stable Ti isotopes and used the Solar isotopic mixture. This was done for our coolest star (star 5265), where the formation of TiO molecules should be most pronounced. Including the TiO features had negligible impact on the line shapes, and we discarded them in the synthesis for all remaining stars.

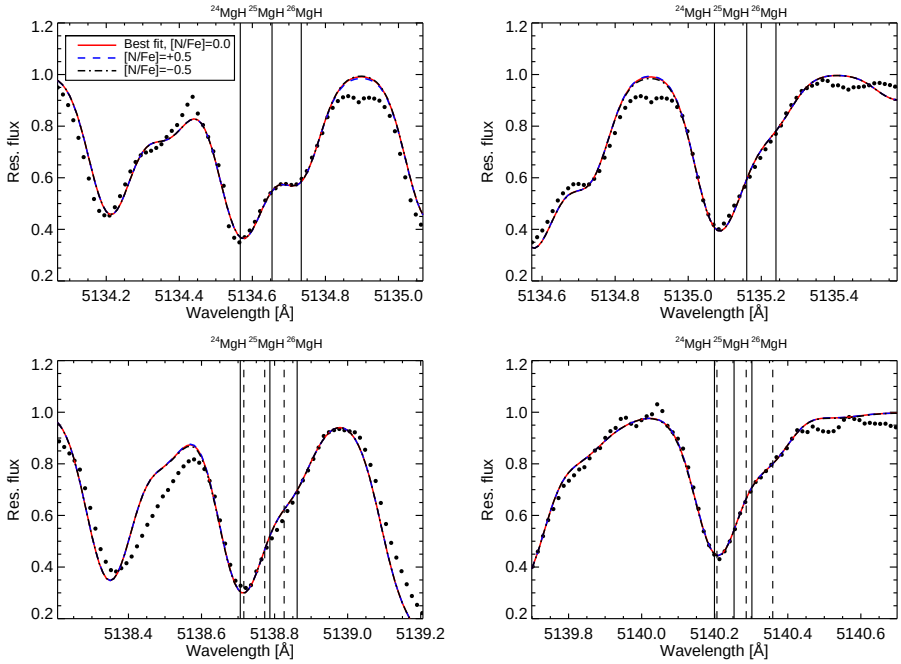

Figure 4.2: Synthesis of the four MgH features used to derive the isotopic fractions of Mg in star 5265. The red line shows the synthesis using a scaled Solar value for [N/Fe] whereas the dashed lines show the change of the line shape when the [N/Fe] is changed by ± 0.5 dex.

4.2.2 *Mg isotopes with* `MOOG`

We synthesized the MgH features using the 2013 version of the `MOOG` spectral synthesis code (Sneden 1973; Sobeck et al. 2011; Sneden et al. 2012), for our 1D analysis. We used the same ATLAS12 models as for the abundance analysis in Chapter 3 as the basis for our syntheses. Initially a 10 Å piece of the spectrum was synthesized in order to set the continuum level. Using this normalization, we determined the initial best fitting isotopic mixture by eye, where we varied the isotopic mixture as well as the abundance of Mg, until a satisfactory fit was achieved. This was done individually for each of the considered regions. The isotopic mixture variations were accomplished by adjusting the $\log(gf)$-value of the molecular transition so that the fractional strength of each isotopic component corresponded to the fractional abundance of that isotope. With the quality of the observations available here, variations as small as 3% for ^{25}Mg and ^{26}Mg can easily be distinguished by eye. The abundance of Mg is a free parameter in the fits, and is solely used to adjust the overall strength of the MgH features. Following the procedure in Meléndez & Cohen (2009), we revisited our broadening, by synthesizing Fe I lines at 6056.0, 6078.5, 6096.7, 6120.2 and 6151.6 Å. The broad-

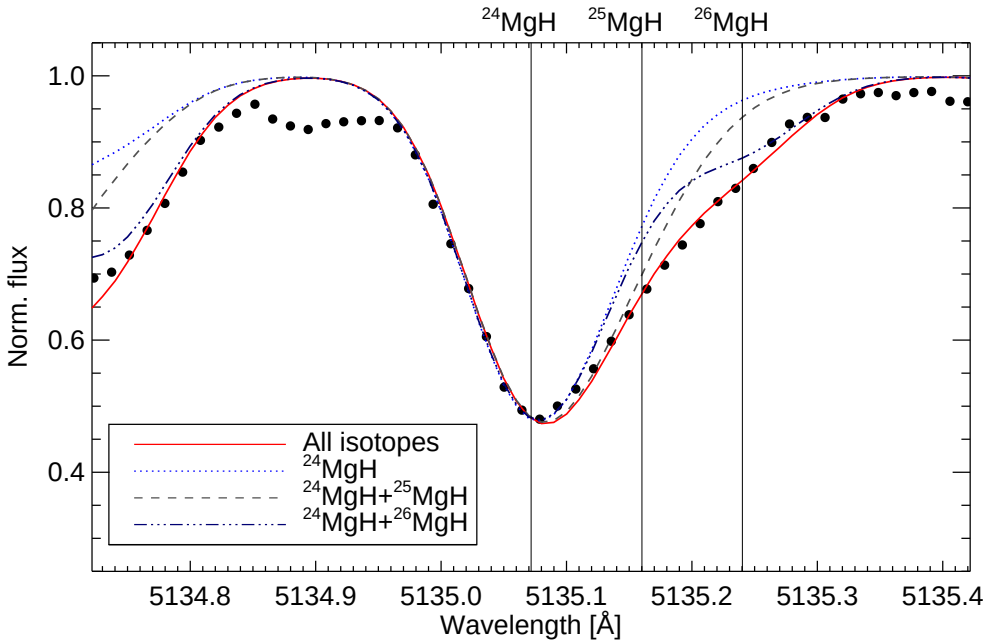

Figure 4.3: 1D syntheses of the 5135.07 Å MgH feature for different isotopic components.

ening derived from these lines were subsequently adopted, assuming a Gaussian broadening profile for each star, representing the instrumental resolution, macroturbulence and rotational broadening as a whole.

Even though the isotopic splittings of the MgH features are small, it is immediately evident that all three isotopic components are required to produce a satisfactory match between the observed spectra and the syntheses. This is illustrated in Fig. 4.3 where we show the best-fitting syntheses for the 5135.07 Å feature in star 5265, including various isotopic components of the MgH feature. In all cases are ^{24}Mg +^{25}Mg +^{26}Mg kept constant. Only the synthesis with all three components provide a satisfactory fit to the observed spectrum.

Using our by-eye fits as a first estimate of the isotopic ratios, we refined the synthesis, determining the best fit by doing a χ^2-minimization between the observed spectrum and a grid of synthetic spectra following the method of Yong et al. (2003a). This was done iteratively, in each step varying the isotopic ratios ^{25,26}Mg/^{24}Mg as well as the total magnesium abundance. Initially, we explored a large parameter space, but for the final result we adopted a finer sampling to refine our results. Each of the four MgH features used was fitted independently. In total, more than 1300 different syntheses were calculated in each iteration for each feature. The differences between the isotopic fractions found by eye, compared to the χ^2-fitting were small, typically 1% but never larger than 3%. An example of individual fits, as well as the χ^2 distributions for the fitted isotopic ratios are shown in Fig. 4.4 for the star 4794. For the 1σ fitting precision we use the value for $\Delta\chi^2 = 1$ follow-

ing (Wall & Jenkins 2012). The final isotopic mixture from this method is given as a weighted mean of the individual results, with full weight given to the 5135 Å and 5138 Å features. We only gave half weight to the results from the features at 5134 Å and 5140 Å, which suffered from C_2 molecular blends.

4.2.3 *Mg isotopes with* CO^{5}BOLD*/Linfor3D*

When deriving the Mg isotopic ratios from the line asymmetries in the MgH features it is important to take into account all potential effects that could create such asymmetries. Blending with other atomic and molecular lines is one effect that could cause discrepancies in the observed isotopic ratios, as discussed above. Also the convective motions of gas in the stellar atmospheres are known to cause line asymmetries (see e.g. Dravins 1982). Convection is an intrinsically multi-dimensional phenomenon and cannot be modeled in 1D. In the ATLAS12 models, convection is approximated by the MLT formulation, and the usual macro- and micro-turbulence quantities are used to parametrize large- and small-scale gas motions respectively.

4.2.3.1 *Model setup*

Three-dimensional, hydrodynamical atmospheres do not rely on MLT approximation or similar approximate descriptions for treating convective energy transport, nor on micro-/macro-turbulence parameters for the modeling of convective broadening of spectral lines. We used the CO^{5}BOLD atmospheric code (Freytag et al. 2012) to calculate two box-in-a-star 3D LTE models. We calculated models with parameters representative for the less evolved stars in our sample. The model parameters are listed in Table 4.1. In 3D atmosphere models, $T_{\rm eff}$ is not a control parameter as in the 1D case. Rather, it is an outcome of the simulation, indirectly controlled by the inflowing entropy. Hence why the 3D model $T_{\rm eff}$ is not the same in the two cases. We did not calculate 3D models for our more evolved giants, since the horizontal temperature fluctuations become so large in these models that the radiative transfer code breaks down and provides unphysical results. In addition, the box-in-a-star approximation is challenged for low gravity models. Rectifying these problems would be a major theoretical undertaking, well beyond the scope of this paper.

One of the main results of 3D hydrodynamical modelling of stellar atmospheres, is the prediction of average atmospheric temperature stratifications that are in general significantly different from the ones predicted by traditional 1D models. This is particularly evident for the lowest metallicities (e.g. Collet et al. 2007), where a net cooling effect

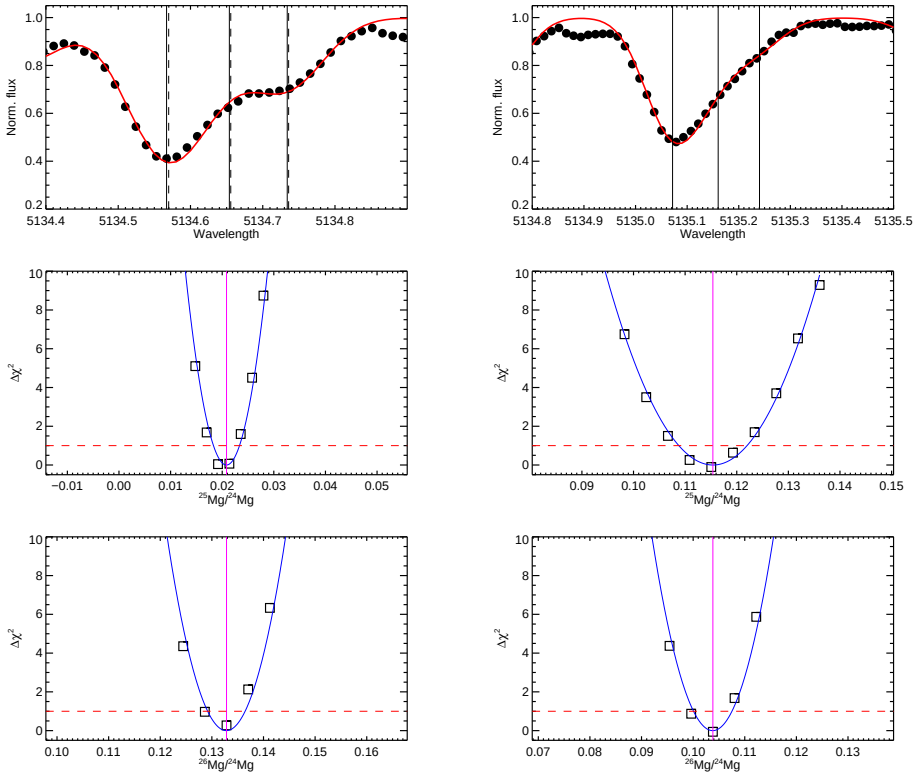

(a) MgH 5134 Å (b) MgH 5135 Å

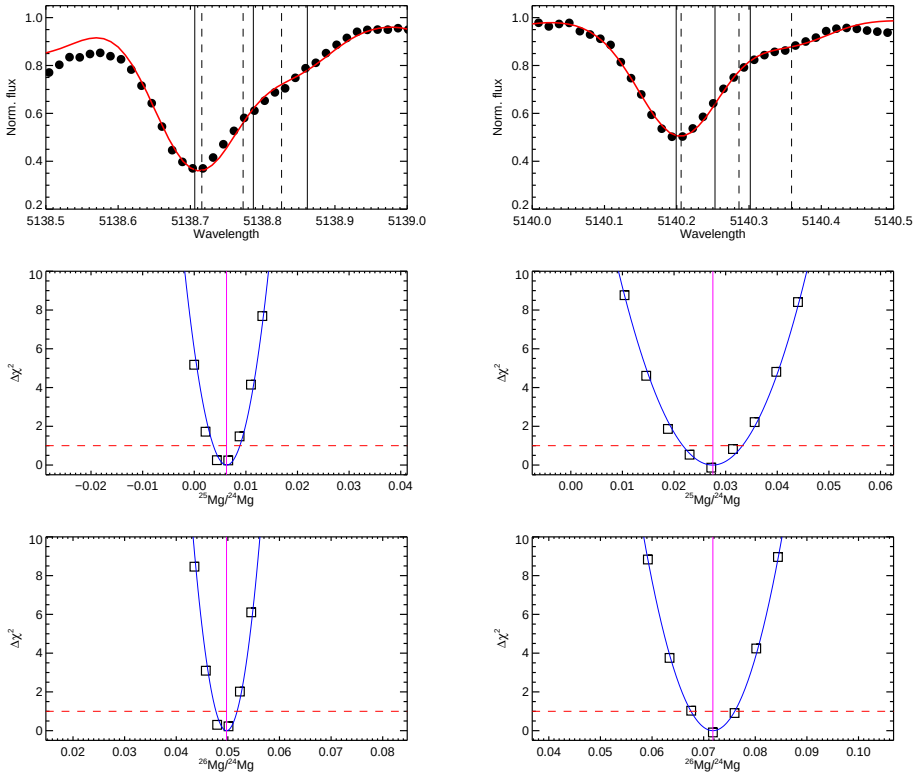

(c) MgH 5138 Å (d) MgH 5140 Å

Figure 4.4: Line fits and χ^2 distributions for the fitted isotopic ratios for all MgH features in star 4794. Vertical, magenta lines show best-fitting values. The red dashed lines indicate 1σ fitting precision.

Table 4.1: Model parameters for our CO^{5}BOLD 3D models.

ID	$T_{\rm eff}$	$\log g$	[Fe/H]	[α/Fe]	model time
HiMet	3970K	1.50	−0.50	+0.2	1472 h
LoMet	4040K	1.50	−1.00	+0.4	1111 h

is manifested in 3D. In Fig. 4.5 we plot the average thermal structure of the two 3D models, as well as the structure of the ATLAS12 models ($\alpha_{\rm MLT} = 1.25$), as well as two reference LHD (Caffau & Ludwig 2007) 1D models ($\alpha_{\rm MLT} = 0.5$), that are calculated with the same input physics as the CO^{5}BOLD models. Also indicated are the mean temperature fluctuations in our 3D models. As is evident, at the metallicities treated here, the average thermal structure of the photospheres in the 3D models are nearly identical to the equivalent 1D models. On the other hand, the convection still causes significant variation in the thermal structure of our 3D model. The similarity of the average structures implies that differences between the 1D and 3D synthesis are mostly related to the temperature fluctuations, rather than changes in the overall atmospheric structure.

4.2.3.2 *3D synthesis*

With the models computed, we selected 20 model snapshots, with near-equidistant time steps as a basis for the spectral synthesis. These were selected such that they covered nearly the full model time, to give good temporal coverage. Since the convective motions are responsible for a large part of the line asymmetries, the snapshots should ideally be sampled so that they represent uncorrelated convective patterns in the simulation. By computing the auto-correlation between the horizontal, gray intensities for all our model instances, we can gain insight into the typical lifetime of a convective cell. Having computed the auto-correlation, we performed a spline interpolation for a range of model times, so that our snapshot time step was included. From this, the value of the auto-correlation between two consecutive time steps could readily be determined. This showed that there is typically a 13% correlation between our individual snapshots (Fig 4.6), which is sufficiently uncorrelated for our purpose. We note that the time axis is truncated, so that the decrease in the auto-correlation is visible. The total length of the simulation is significantly longer than indicated in the figure ($\sim$ 1400h).

Furthermore, we ensured that the mean $T_{\rm eff}$, and RMS scatter of the $T_{\rm eff}$ in our snapshot selection was nearly identical to the $T_{\rm eff}$ and RMS found from the complete model grid. This represents a compromise between computational time and model coverage, so that the temperature

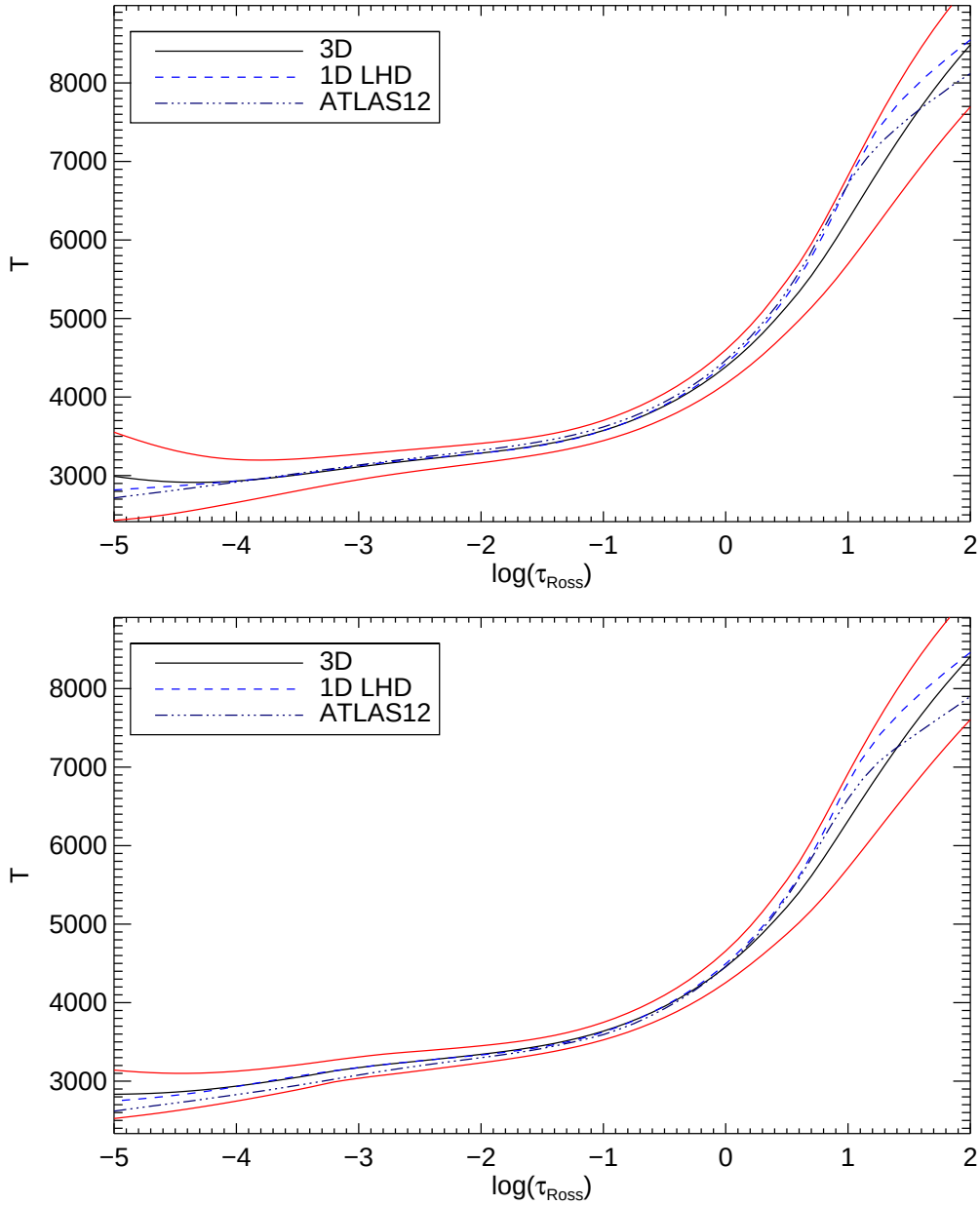

Figure 4.5: Average thermal structure of the 3D models (solid line) as well as an equivalent 1D ATLAS12 (triple dot-dash) and LHD (dash) model. The red lines indicate the RMS variation of the temperature in the 3D models. Top panel: HiMet, bottom: LoMet.

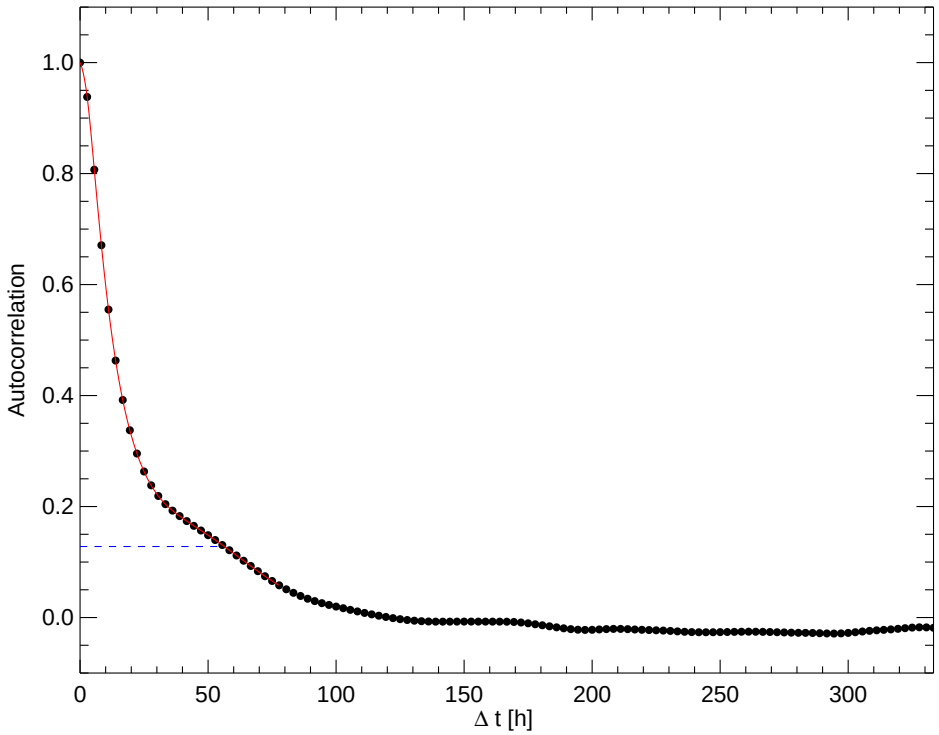

Figure 4.6: The auto-correlation of the horizontal grey intensity for the HiMet model. The blue, dashed line, shows the value for the time step between two consecutive snapshots.

variations from the 3D model are kept intact in the spectral synthesis. For each snapshot we calculated the full 3D radiative transfer using the Linfor3D code[2], to yield the emergent spectrum. The snapshot syntheses were subsequently averaged and normalized, to yield the final, synthetic spectra.

For each 3D model, we calculated a grid of syntheses with $-0.50 < \Delta[\mathrm{Mg/H}] < 0.50$, in steps of 0.2, relative to the input mixture. The isotopic fractions of the heavy Mg isotopes were varied between $0 < \mathrm{frac}(^{25}\mathrm{Mg}) < 0.21$ and $0 < \mathrm{frac}(^{26}\mathrm{Mg}) < 0.21$ in steps of 0.03. The isotopic fraction of ^{24}Mg was calculated as $^{24}\mathrm{Mg} = 1.0 - ^{25}\mathrm{Mg} - ^{26}\mathrm{Mg}$. The relative strength of the isotopic components of the MgH lines were set by adjusting their $\log(gf)$ value. Similar to the 1D syntheses, the Mg abundance was used to adjust the MgH feature strengths. We used an abundance mixture identical to the mixture used in the model computation as a starting point of our syntheses, as stated in Table 4.1. The line list is identical to what was used in MOOG.

Due to the velocity fields in the atmospheres of the 3D models, lines synthesized in 3D will exhibit a small velocity shift, relative to an equivalent 1D synthesis. To account for this, we synthesized a single ^{24}MgH line in both 1D and 3D and cross-correlated the two spectra to determine the velocity shift. This gave shifts of $0.26\,\mathrm{km\,s^{-1}}$ and $0.38\,\mathrm{km\,s^{-1}}$ for the $[\mathrm{Fe/H}] = -0.50$ and -1.00 models, respectively. By synthesizing only a single line, we bypass potentially different behaviour of line-blends between 1D and 3D, which could mimic an overall velocity shift. Before performing any analysis, we shifted the 3D spectra by this amount, to be as consistent with the 1D analysis as possible. It was, however, found that some additional velocity shifts were needed for some features, which was also the case for our 1D fits. The synthesis of the single ^{24}MgH transition also revealed that 3D effects introduced a weak line asymmetry (Fig. 4.7), which is expected also to be present for the two heavy MgH components of the feature. This can explain part of the different line shapes between 1D and 3D.

After shifting the spectra, the final 3D spectrum was convolved with the instrumental profile of UVES to yield the broadened spectrum. We assumed a Gaussian profile. In the absence of strong rotation, this should account for all the line-broadening present in the observed spectra, because the effects of micro- and macroturbulence arises as a natural consequence of the gas motions in the 3D models. Because this work deals with cool, evolved giants, we consider them non-rotating for all practical purposes, and did not impose any additional broadening to the spectra. This is further justified by the similarity of the V_{macro} measurements reported in Chapter 3. With the syntheses calculated for both

2 http://www.aip.de/Members/msteffen/linfor3d

models, we performed a simple, linear interpolation in metallicity between the spectra, to match the observed metallicities of our stars. The grid of syntheses were subsequently given as input to the `Fitprofile` code, described below, to fit the observed spectra.

Due to the issues with the C_2 blends discussed earlier, we chose only to calculate 3D synthesis for the 5135 Å and 5138 Å features, which do not suffer from strong carbon blends. If we were to synthesize also the 5134 Å features and 5140 Å features, it would require adding an extra dimension to our parameter space for the syntheses, namely C abundance variations. Since we are already varying the Mg abundance, as well as the fractions of ^{24,25,26}Mg, it would become very computationally expensive to also include variations in the carbon abundance.

In Figs. 4.8, 4.9 the effects of the 3D atmospheres are illustrated. Three different syntheses are shown. A full 3D synthesis, a synthesis using the horizontally averaged 3D temperature structure (<3D>), and finally a synthesis using a 1D atmosphere calculated with the same input physics as the 3D model. The HiMet and LoMet syntheses both have the same Mg-depletion (-0.10 dex) relative to the input mixture. As is evident, both the strength of the features, as well as the line shapes, change between 1D and 3D. Whereas some differences can be observed between 1D and <3D>, it is clear that in this case, one needs the full information from the 3D synthesis to capture the differences between 1D and 3D. This underlines that the main reason for the different behaviour of the MgH features is related to the temperature fluctuations and not changes in the average thermal structure, as already discussed in Chapter 2. Interestingly, Ramírez et al. (2008) found that the overall strength of the MgH features were increasing when 3D atmospheres were applied to a K-dwarf model, where we, on the other hand find that the features are decreasing slightly in strength, relative to a standard 1D analysis.

As discussed in Sect. 2.1.1, both the MgH lines as well as the lines of the blending species feel the effect of the 3D model atmospheres, with different effects on the MgH lines and the line blends, with the majority of the differences in line asymmetry arising from the blending lines, and not from MgH itself, especially true for the 5135 Å and 5138 Å features. From the inspection performed in Sect. 2.1.1, this likely also holds for the remaining two features, but no firm assessment of the 3D effects can be made before the issue with the C_2 blending lines has been resolved, as discussed earlier.

4.2.3.3 *Fitting the 3D syntheses with* `Fitprofile`

The software used for the 1D fitting of the MgH features using `MOOG` calculates spectral synthesis on the fly, which is not feasible to do in 3D, where the computational overheads are significantly higher. Thus,

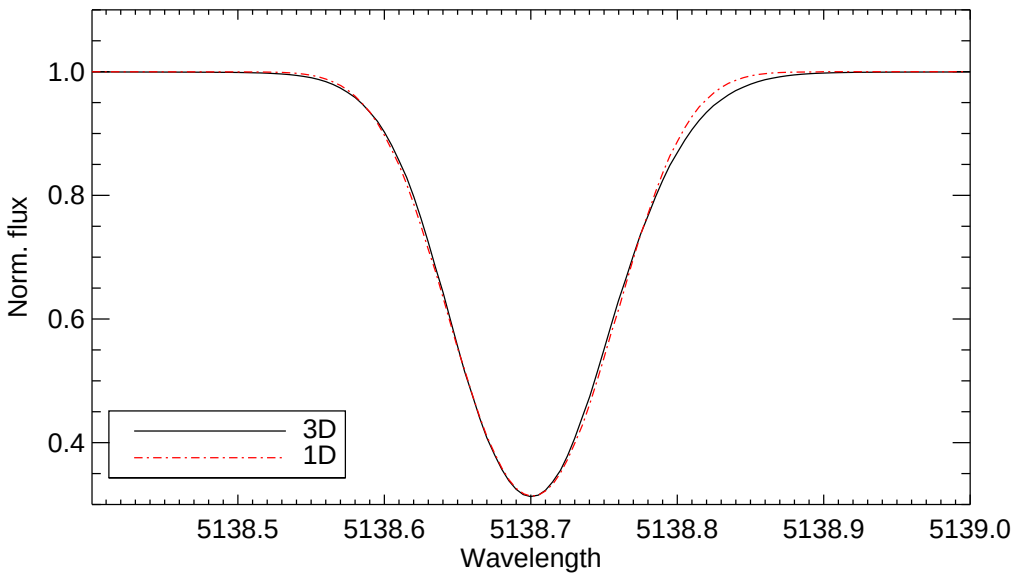

Figure 4.7: Comparison of the syntheses of the 5138 Å feature for ^{24}MgH. Note the line asymmetry in the red wing. The syntheses have been scaled to have the same overall strength.

for the purpose of determining the best-fitting 3D synthetic profile we developed the multi-parametric fitting code `Fitprofile`, which uses a pre-computed grid of syntheses. Before applying to our 3D synthesis, we tested that the 1D synthesis provided near-identical results to our 1D fitting routines using `MOOG`.

`Fitprofile` shares much of the general inner workings and a relevant amount of code with the automated parameter determination and abundance analysis code MyGIsFOS (Sbordone et al. 2014). As MyGIsFOS it is written in Fortran 90 (with Intel extensions) and uses the CERN function minimization library `MINUIT` (James & Roos 1975; Lazzaro & Moneta 2010) as χ^2 minimization engine. The `Fitprofile` code was developed to provide a flexible line-fitting tool that could both perform simple, general purpose line fitting for single lines, and more sophisticated multi-parameter, multi-region fitting such as the one needed for the present study. `Fitprofile` was used already in Chapter 3, to derive abundances from elements with lines that showed hyperfine splittings.

`Fitprofile` reads in a grid of synthetic spectra varying in up to four parameters, an observed spectrum against which the fit is to be performed, and a list of spectral regions to be used in the fit. Two types of regions are accepted: pseudo-continuum regions are used to pseudo-normalize the observed spectrum as well as the synthetic grid, and to determine the S/N ratio, while fitting regions define the spectral ranges over which the actual fitting is performed. We used the same fitting regions for each feature as in the 1D case.

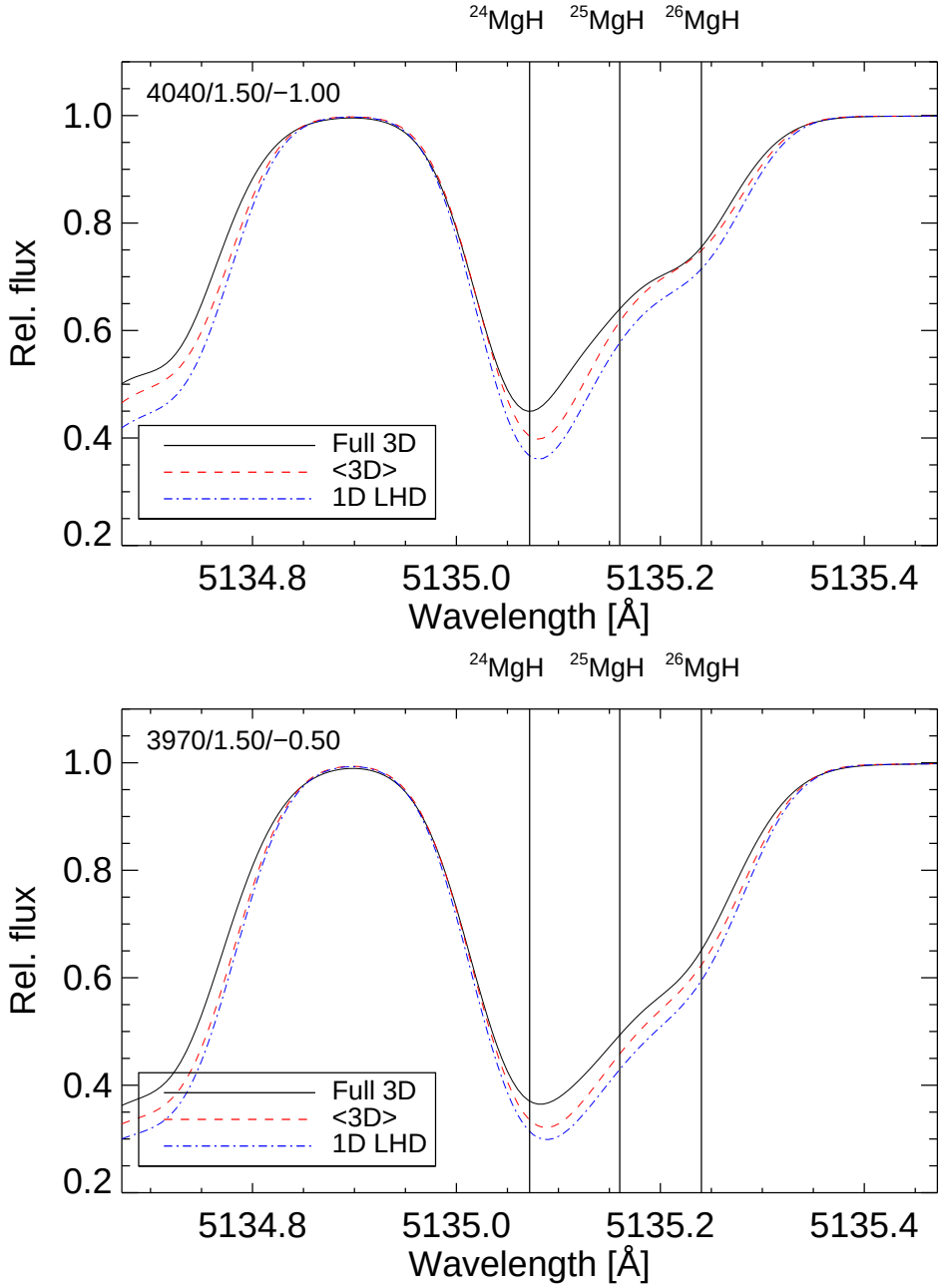

Figure 4.8: Syntheses of the MgH feature at 5135.07 Å. Shown is the full 3D synthesis (solid), the <3D> synthesis (dashed) and the 1D LHD synthesis (dot-dashed). Indicated is also the central position of each of the MgH components. Top: LoMet, bottom: HiMet.

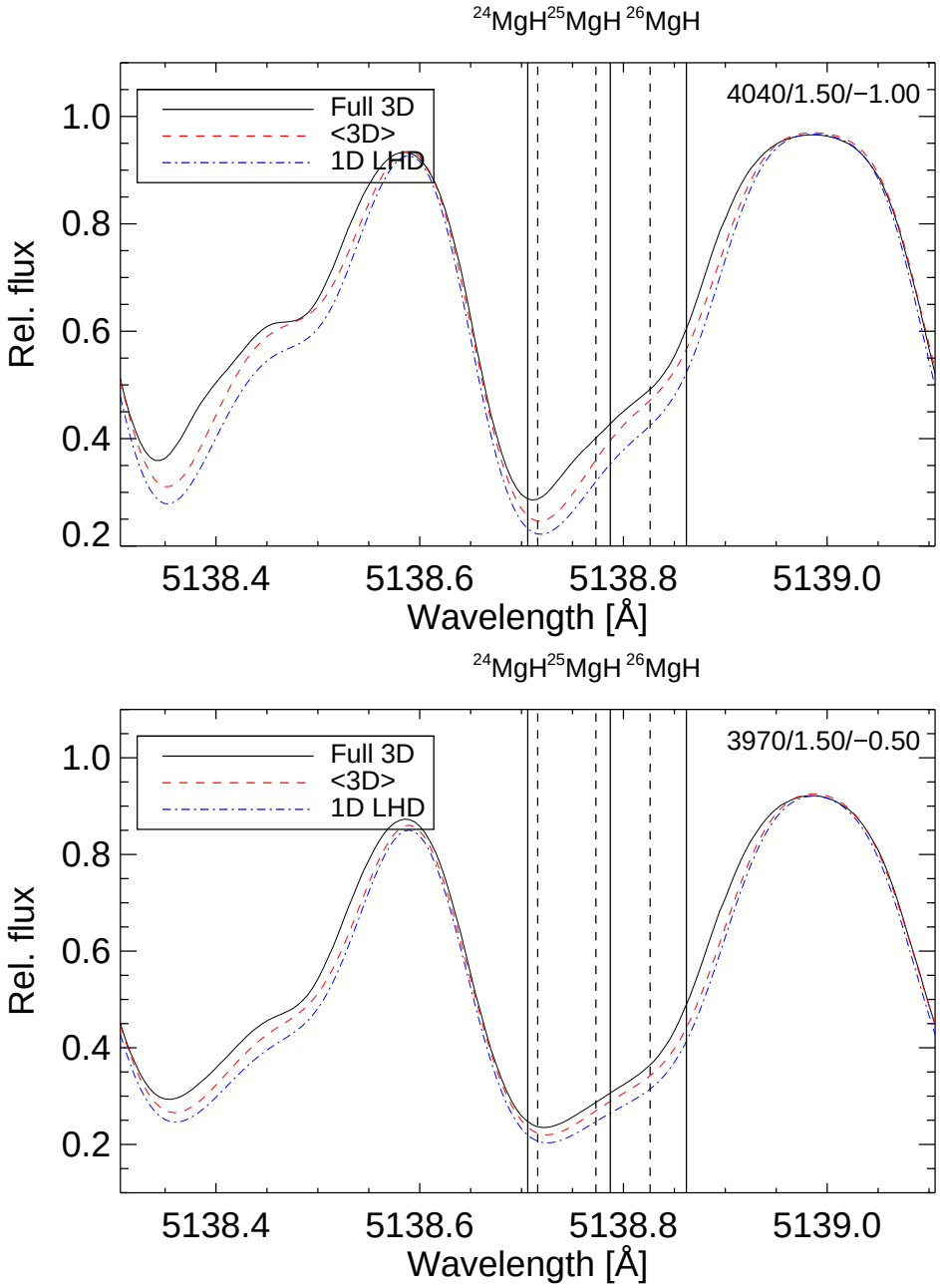

Figure 4.9: As Fig. 4.8, but for the MgH feature at 5138.71 Å. This feature is a blend of two MgH transitions, indicated with solid and dashed vertical lines.

The up-to-four parameters varying in the grid can represent any quantity varying from one spectrum to another in the synthetic grid. Any number of them can be fitted, or kept fixed to an user-chosen value. In the case of the present work, for instance, the provided grid parameters were set to total Mg abundance, ^{25}Mg fraction and ^{26}Mg fraction (and all were fitted), while the fourth parameter was not used. From this, the ^{24}Mg fraction could easily be calculated. The grid must be equispaced and rectangular in any parameter it contains.

If the user provides pseudo-normalization regions, they are used to locally estimate the S/N and to construct a pseudo-continuum spline that is used to pseudo-normalize the synthetic grid and observed spectrum. Both quantities are estimated as constant if one single pseudo-continuum interval was provided, as a linear interpolation if two pseudo-continua are given, and as a spline for three or more pseudo-continua. Both quantities can be kept fixed, providing a pre-normalized spectrum and an estimation of S/N. Due to the lack of suitable continuum regions in the immediate vicinity of the MgH features, we used pre-normalized spectra with a S/N estimate for our fitting. The normalization was identical to what was used in `MOOG`.

Fitting regions can be contiguous or not. A contiguous region is, for instance, a typical spectral region covering a spectral line one wants to fit. A non-contiguous region is called in `Fitprofile` a "region group", as it is, indeed, a group of contiguous regions that are fitted as one, i.e. a single χ^2 is computed for all the pixels contained in the contiguous regions composing the group. `Fitprofile` produces fit values for each provided region group. To apply this to the present work, one could have fitted all the MgH features together, deriving a single best fitting set of Mg isotopic ratios, by including them all in a single group. Or, as we did, fit each feature independently, producing multiple sets of best fitting values that can then be averaged. In fact, within `Fitprofile` every contiguous feature fitted on its own is described as a one-feature group.

During the fitting, two additional parameters can be allowed to vary, namely some adjustment of the continuum value (up to a fraction of the local S/N), and some amount of Doppler shift (within user-defined limits). These adjustments are applied to the pre-computed syntheses grid and applied per feature group. Both parameters can be be disabled if the user so desire. In this case, we allowed for small continuum adjustments as well as a small velocity shift, both of which are included in the fitting. Upon a successful fit, `Fitprofile` provides the best fitting values of the grid parameters for each group as well as an average among the groups and fitted profiles for each group for inspection of the results. For each individual group, `Fitprofile` also provides the best-fitting doppler shift.

Another useful capability of `Fitprofile` is to allow parameter space mapping, i.e., aside from the `MINUIT` χ^2 minimum search, the χ^2 value is computed at each grid point, allowing to estimate the uncertainty of the fit, and the parameter correlation.

4.2.4 *Estimating uncertainties*

When one has spectra of such exquisite quality available as is the case here, the precision with which the individual features can be fit is remarkable. For our 1D analysis, we determined the minimum χ^2-value for the three fitting parameters, ^{25}Mg/^{24}Mg, ^{26}Mg/^{24}Mg and $\log\epsilon$(Mg). This was done for each of the four features individually. Typical fitting precision of the ratios are ± 0.005.

Whereas the individual fits are extremely precise, the feature-to-feature agreement is not as satisfactory. For most stars, the 5134 Å feature yields systematically higher ^{26}Mg fractions, up to a factor two above the mean value. On the other hand, the 5135 Å feature yields ^{25}Mg fractions that are higher by a similar amount, relative to the typical mean. The former may be linked to the unknown carbon abundance, but we note that other studies of Mg isotopes find a similar behaviour for this line, even in cases where the carbon abundance is known. If carbon is enhanced slightly, this would result in a lower fraction of the heavy Mg isotopes. However, any enhancement of carbon would make it close to impossible to fit the 5140 Å feature, so this is unlikely to be the only explanation for the disagreement. We consider unknown blends to be the most likely cause of the disagreements between the features. These inconsistencies mean that the uncertainty of our final isotopic ratios become dominated by the feature-to-feature scatter. For the final values, we report the weighted mean of the isotopic fractions determined from each of the four features, and calculate the uncertainty from line-to-line scatter, as the weighted standard error on the mean, with half weight given to the 5134 Å and 5140 Å features as discussed earlier.

Uncertainties in the atmospheric parameters of the stars will also contribute to the uncertainties of the Mg isotopic fractions. To investigate this, we repeated the fits of each of the four features, using atmospheric models perturbed by the uncertainties of the stellar parameters, following the method in Chapter 3. We use star 6798 as a representative example again, as it has parameters in the middle of our range. We then assume that the influence of the parameter changes found for this star, is representative for our full sample. In Table 4.2 we report the changes to the mean value of the isotopic fractions, when the atmospheric parameters are changed. For the total influence of atmospheric parameters on the uncertainty, we take the mean of the absolute change of the fractions, from each parameter perturbation, and add them in quadrature.

Table 4.2: The change in mean value of the isotopic percentages of Mg due to atmospheric uncertainties, relative to the best fit. Shown here for star 6798.

ΔParam.	Δ^{24}Mg	Δ^{25}Mg	Δ^{26}Mg
$\Delta T_{\rm eff} = +80$K	0.2	0.0	−0.2
$\Delta T_{\rm eff} = -80$K	−1.0	0.2	0.8
$\Delta \log g = +0.2$	0.0	−0.1	0.1
$\Delta \log g = -0.2$	−0.6	0.4	0.2
$\Delta \xi_t = +0.1\,\mathrm{km\,s^{-1}}$	0.2	0.0	−0.2
$\Delta \xi_t = -0.1\,\mathrm{km\,s^{-1}}$	−0.5	0.3	0.3
Δ[M/H] = +0.15	−1.1	0.7	0.4
Δ[M/H] = −0.15	0.3	0.0	−0.3
$\sigma_{\rm parameters}$	±1.0	±0.5	±0.7

We note here, that we keep the continuum, and the velocity shift fixed in all cases, and thus the real uncertainty will likely include terms also reflecting this, as well as influence of unidentified blends, and uncertainties in the abundances of the blending atomic species. We assume that such effects are small, and do not include them in our uncertainty budget.

As our final uncertainty of the isotopic fractions we add in quadrature the effects from atmospheric uncertainties to the standard error of the mean. As can be seen in Table 4.2, the isotopic fractions are not very sensitive to changes in the atmospheric parameters, highlighting one of the advantages of using Mg isotopic abundances as opposed to elemental abundances, which often show a higher parameter sensitivity.

4.3 RESULTS

In the 1D analysis, we were able to use all four MgH features to estimate the isotopic fractions for most stars in our sample. In a few cases we had to discard one or two of the features, due to atmospheric emission being present, making them useless for the isotope derivation. This was the case for stars 20885 (two features), 28965 (one feature) and 29861 (one feature).

In Fig. 4.10 we present the results from our 1D analysis, plotting the percentage of the three isotopes of the total Mg abundance vs. [Na/Fe]. In the absence of a clear Mg-Al anti-correlation, we initially plot the isotopic fractions against [Na/Fe] rather than [Al/Fe], as this allows a clear separation between the stellar populations in 47 Tucanae. We use

Table 4.3: Median value, interquartile ranges and σ_{IQR} for all three isotopes. Shown for the total sample and split in populations.

	median	IQR	σ_{IQR}
^{24}Mg prist.	88.6	2.1	2.4
^{24}Mg poll.	89.5	4.1	2.0
^{24}Mg all	88.7	2.4	2.2
^{25}Mg prist.	4.1	1.6	1.4
^{25}Mg poll.	2.9	1.1	0.9
^{25}Mg all	3.9	2.0	1.3
^{26}Mg prist.	7.3	0.6	1.1
^{26}Mg poll.	8.8	2.7	1.4
^{26}Mg all	7.3	2.0	1.3

the same separation criterion as in Chapter 3 to distinguish between pristine (black triangles) and polluted (red triangles) stars, namely 2σ above the mean value of [Na/Fe] for field stars at the same [Fe/H]. As this criterion is somewhat arbitrarily chosen, we checked our results also using a 1σ or a 3σ selection criteria, but this did not change any conclusions presented in Sect. 4.4. The results from each of the fitted features, as well as the weighted means, are presented in Table 4.4. In Table 4.5 we include the [Fe/H] and the light element abundance ratios from Chapter 3, as well as the mean isotopic fractions, for convenience. Bold face names indicate stars belonging to the polluted population. All abundances are quoted relative to the Asplund et al. (2009) Solar abundances.

We note that one star (10237) appears to show an anomalously high fraction of ^{25}Mg, compared to the rest of the sample. This will be discussed in more detail in Sect. 4.4.1

4.3.1 *Results from 3D*

Due to the lack of suitable 3D atmospheric models we were unable to investigate 3D effects for our full sample of stars. It is, however, still possible to investigate the importance of the improved spectral synthesis for the stars 4794, 13396 and 29861. These stars have parameters that are relatively close to the parameters of our 3D models. We refer to Table 4.5 for the stellar parameters. Because of an emission spike in the 5135 Å feature for star 29861, we were only able to derive isotopic ratios from the 5138 Å feature.

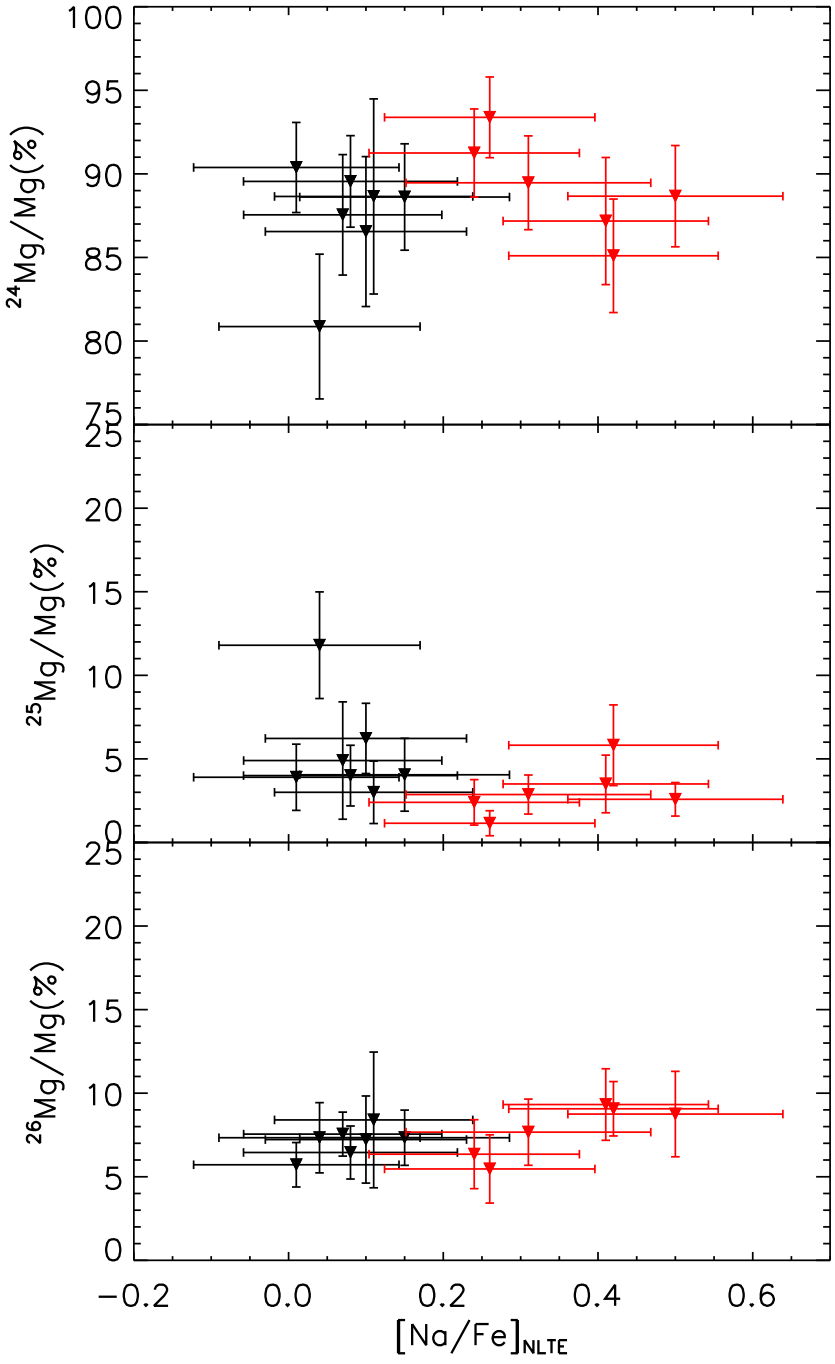

Figure 4.10: Percentage of ^{24}Mg vs. [Na/Fe] (top), ^{25}Mg vs. [Na/Fe] (middle) and ^{26}Mg vs. [Na/Fe] (bottom). Black triangles indicate the pristine populations and red triangles the polluted population.

Table 4.4: Mg isotopic fractions for individual features, given as percentage [^{24}Mg:^{25}Mg:^{26}Mg]. Also shown are the weighted means and associated uncertainties. Boldface IDs indicate polluted stars.

ID	5134.57 Å	5135.07 Å	5138.71 Å	5140.20 Å	Mean	$\sigma_{tot.}$
4794	86.7 : 1.6 : 11.7	82.4 : 9.0 : 8.6	94.6 : 0.7 : 4.7	91.0 : 3.3 : 5.7	88.6 : 4.1 : 7.3	3.2 : 2.2 : 1.7
5968	86.9 : 2.4 : 10.7	85.0 : 8.1 : 6.9	95.2 : 1.2 : 3.6	90.0 : 3.0 : 7.0	89.6 : 4.0 : 6.5	2.7 : 1.8 : 1.6
6798	88.3 : 2.4 : 9.3	85.5 : 8.4 : 6.1	95.6 : 0.8 : 3.6	91.8 : 2.6 : 5.6	90.4 : 3.9 : 5.7	2.7 : 2.0 : 1.3
10237	76.6 : 11.3 : 12.1	72.5 : 18.4 : 9.1	88.5 : 5.3 : 6.2	86.6 : 12.1 : 1.3	80.9 : 11.8 : 7.3	4.3 : 3.2 : 2.1
13396	86.7 : 3.2 : 10.1	80.1 : 13.1 : 6.8	94.3 : 0.0 : 5.7	89.8 : 0.0 : 10.2	87.6 : 4.9 : 7.6	3.6 : 3.5 : 1.3
20885	82.9 : 4.8 : 12.4	Discarded	Discarded	94.4 : 1.2 : 4.4	88.7 : 3.0 : 8.4	5.8 : 1.9 : 4.1
29861	76.3 : 11.0 : 12.7	Discarded	90.7 : 5.0 : 4.3	88.5 : 3.9 : 7.6	86.5 : 6.2 : 7.2	4.5 : 2.1 : 2.6
1062	85.0 : 2.2 : 12.8	88.7 : 5.3 : 6.0	96.2 : 0.8 : 3.0	92.7 : 0.0 : 7.3	91.2 : 2.4 : 6.3	2.6 : 1.4 : 2.1
5265	84.3 : 2.8 : 12.9	86.8 : 4.2 : 9.0	95.6 : 0.5 : 3.9	87.7 : 5.0 : 7.3	89.5 : 2.9 : 7.7	2.8 : 1.2 : 2.0
27678	82.2 : 1.6 : 16.2	86.6 : 4.2 : 9.2	95.2 : 0.9 : 3.9	86.2 : 3.7 : 10.1	88.7 : 2.6 : 8.8	3.0 : 1.0 : 2.6
28956	Discarded	82.8 : 5.4 : 11.8	93.4 : 0.7 : 5.9	83.5 : 5.3 : 11.2	87.2 : 3.5 : 9.3	3.8 : 1.7 : 2.1
38916	81.8 : 5.0 : 13.1	79.4 : 11.2 : 9.4	92.4 : 1.6 : 6.0	85.2 : 4.3 : 10.5	85.1 : 5.8 : 9.1	3.4 : 2.4 : 1.6
40394	87.6 : 0.9 : 11.5	91.7 : 2.4 : 5.9	98.1 : 0.1 : 1.8	93.1 : 1.0 : 5.9	93.4 : 1.2 : 5.5	2.4 : 0.7 : 2.0

Table 4.5: Summary of the mean Mg isotopic fractions, as well as stellar parameters and light element abundances. Boldface IDs indicate polluted stars.

ID	$T_{\rm eff}$	log(g)	ξ_t	[Fe/H]	[O/Fe]	[Na/Fe]	[Mg/Fe]	[Al/Fe]	[^{24}Mg:^{25}Mg:^{26}Mg]
4794	4070	1.15	1.30	−0.66	0.38	0.15	0.40	0.15	88.6 : 4.1 : 7.3
5968	3970	0.85	1.40	−0.79	0.41	0.08	0.49	0.17	89.6 : 4.0 : 6.5
6798	4000	0.90	1.30	−0.69	0.37	0.01	0.44	0.12	90.4 : 3.9 : 5.7
10237	4280	1.20	1.60	−0.83	0.57	0.04	0.32	0.18	80.9 : 11.8 : 7.3
13396	4190	1.45	1.60	−0.83	0.48	0.07	0.44	0.25	87.6 : 4.9 : 7.6
20885	4260	1.35	1.90	−0.84	–	0.11	0.47	0.23	88.7 : 3.0 : 8.4
29861	4160	1.20	1.50	−0.84	0.47	0.10	0.40	0.27	86.5 : 6.2 : 7.2
1062	3870	0.45	1.30	−0.78	0.23	0.24	0.46	0.16	91.2 : 2.4 : 6.3
5265	3870	0.30	1.25	−0.69	0.00	0.31	0.40	0.19	89.5 : 2.9 : 7.7
27678	3870	0.35	1.20	−0.76	0.13	0.50	0.45	0.29	88.7 : 2.6 : 8.8
28956	3900	0.30	1.60	−0.86	0.06	0.41	0.46	0.29	87.2 : 3.5 : 9.3
38916	4080	0.85	1.40	−0.83	–	0.42	0.52	0.29	85.1 : 5.8 : 9.1
40394	3890	0.45	1.10	−0.71	0.23	0.26	0.43	0.12	93.4 : 1.2 : 5.5

Table 4.6: Mg isotopic ratios [^{24}Mg:^{25}Mg ^{26}Mg] derived from 1D and 3D syntheses respectively.

ID	4794 [^{24}Mg:^{25}Mg:^{26}Mg]	13396 [^{24}Mg:^{25}Mg:^{26}Mg]	29861 [^{24}Mg:^{25}Mg:^{26}Mg]
$1D_{5135}$	82.4 : 9.0 : 8.6	80.1 : 13.1 : 6.8	Discarded
$3D_{5135}$	76.7 : 14.7 : 8.7	73.5 : 19.0 : 7.5	Discarded
$1D_{5138}$	94.6 : 0.7 : 4.7	94.3 : 0.0 : 5.7	90.7 : 5.0 : 4.3
$3D_{5138}$	90.3 : 4.6 : 5.1	84.6 : 11.1 : 4.3	86.6 : 9.2 : 4.2
$Mean_{1D}$	88.5 : 4.9 : 6.6	87.2 : 6.6 : 6.3	90.7 : 5.0 : 4.3
$Mean_{3D}$	83.5 : 9.6 : 6.9	79.0 : 15.1 : 5.9	86.6 : 9.2 : 4.2
σ_{1D}	6.2 : 4.2 : 2.0	7.1 : 6.6 : 0.5	–
σ_{3D}	6.9 : 5.0 : 1.8	5.5 : 4.0 : 1.6	–

Due to the issues with carbon blends mentioned earlier, we cannot directly compare the overall values of the Mg isotopic fractions from 1D and 3D, since we only synthesize the 5135 Å and 5138 Å features in 3D. But even just comparing the 1D and 3D results for these two features is informative to assess the potential impact of 3D.

In Fig. 4.11 we plot the best-fitting syntheses for the two features, for star 4794. It is evident that the 3D syntheses are reproducing the observations better than the 1D syntheses. In particular, the fitting of the asymmetric wings used to derive the isotopic ratios is improved. Typical precision of the fitted percentage of each isotope are 0.7%, 0.4% and 0.3% for ^{24}Mg, ^{25}Mg and ^{26}Mg respectively. However, inspecting the distribution of isotopes that gives the best fit, in 1D and 3D respectively, it is clear that they provide rather different results, as seen in Table 4.6. In particular disagreement is seen for the 5135 Å feature. Here, the 3D results give a higher fraction of ^{25}Mg. This is also the case for the 5138 Å feature, although the increase, relative to the 1D results, is smaller. The ^{26}Mg fraction, on the other hand, remains essentially unchanged. Comparing the mean value of the results from these two features in 1D and 3D, respectively, the 3D results suggest a higher abundance of ^{25}Mg, than what was previously reported. The feature-to-feature agreement, on the other hand, stays about the same both in the 3D and 1D synthesis. As can also be seen from Table 4.6, the same tendency of a significant increase in ^{25}Mg is observed also in the two other stars.

4.4 DISCUSSION

The presence or absence of correlations between the Mg isotopes and the abundance ratios of the light elements can provide insight into the underlying mechanism responsible for the abundance variations.

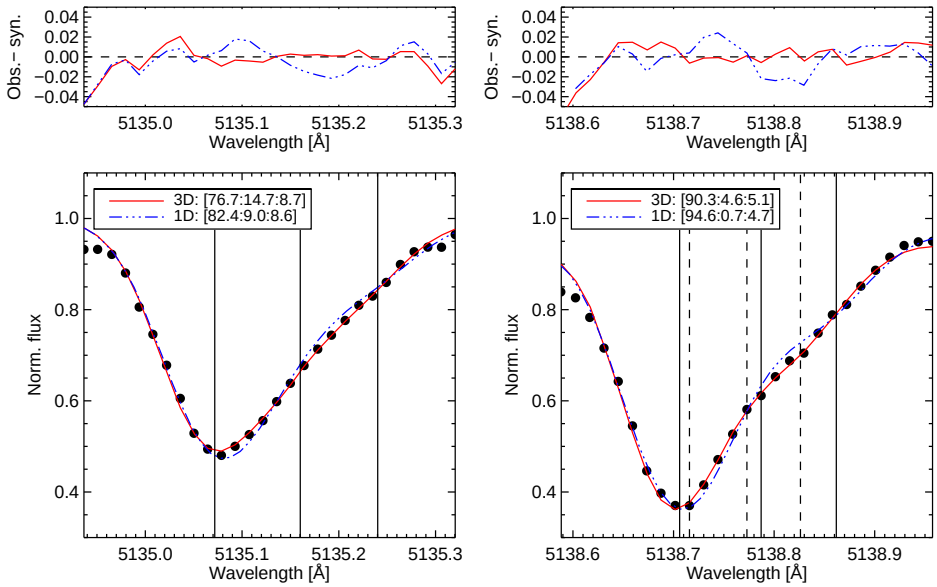

Figure 4.11: Best-fitting synthesis from 3D (red, solid line) and 1D (blue, triple-dot dash line) for the star 4794. Also shown are the residuals of the two fits, as well as the central positions of the MgH features.

As illustrated in Fig. 4.12, our ^{24}Mg and ^{25}Mg isotopic fractions appear to show a correlation with $T_{\rm eff}$. However, the trend is fairly weak for both affected isotopes, in particular if the outlier that appears strongly depleted in ^{24}Mg and enhanced in ^{25}Mg is discarded. There may be some justification for this, as will be discussed later. Our ^{26}Mg measurements, on the other hand, show no trend with $T_{\rm eff}$. Since the formation properties are identical for all three isotopic components of MgH, we attribute this weak parameter correlation to blends from other lines, which will influence the isotopic components differently. It is difficult to determine whether the apparent correlation is real, since the bulk of our polluted stars also happen to be the coolest giants in our sample. This is unfortunate, and makes it very difficult to assess whether the variations we see are due to problem with our analysis procedure, as noted in Chapter 3. There, we discussed the correlation of abundances with parameters, where our initial abundance ratios, [Ba/Fe] and [Al/Fe], showed a trend with temperature, but this was found to be fully explained by NLTE effects. Thus, we have confidence in our stellar parameters, but cannot fully rule out a potential systematic effect. We also note that for a given $T_{\rm eff}$, we observe a range of isotopic ratios.

In Fig. 4.13 we present the measured isotopic fractions vs. [Al/Fe]. This is a natural choice, since it is expected that the heavy isotopes are created together with Al, if the Mg-Al chain is responsible for the production of the heavy Mg isotopes. It is clear from the figure, that we do not observe a large spread in the Mg isotopes in either of the two

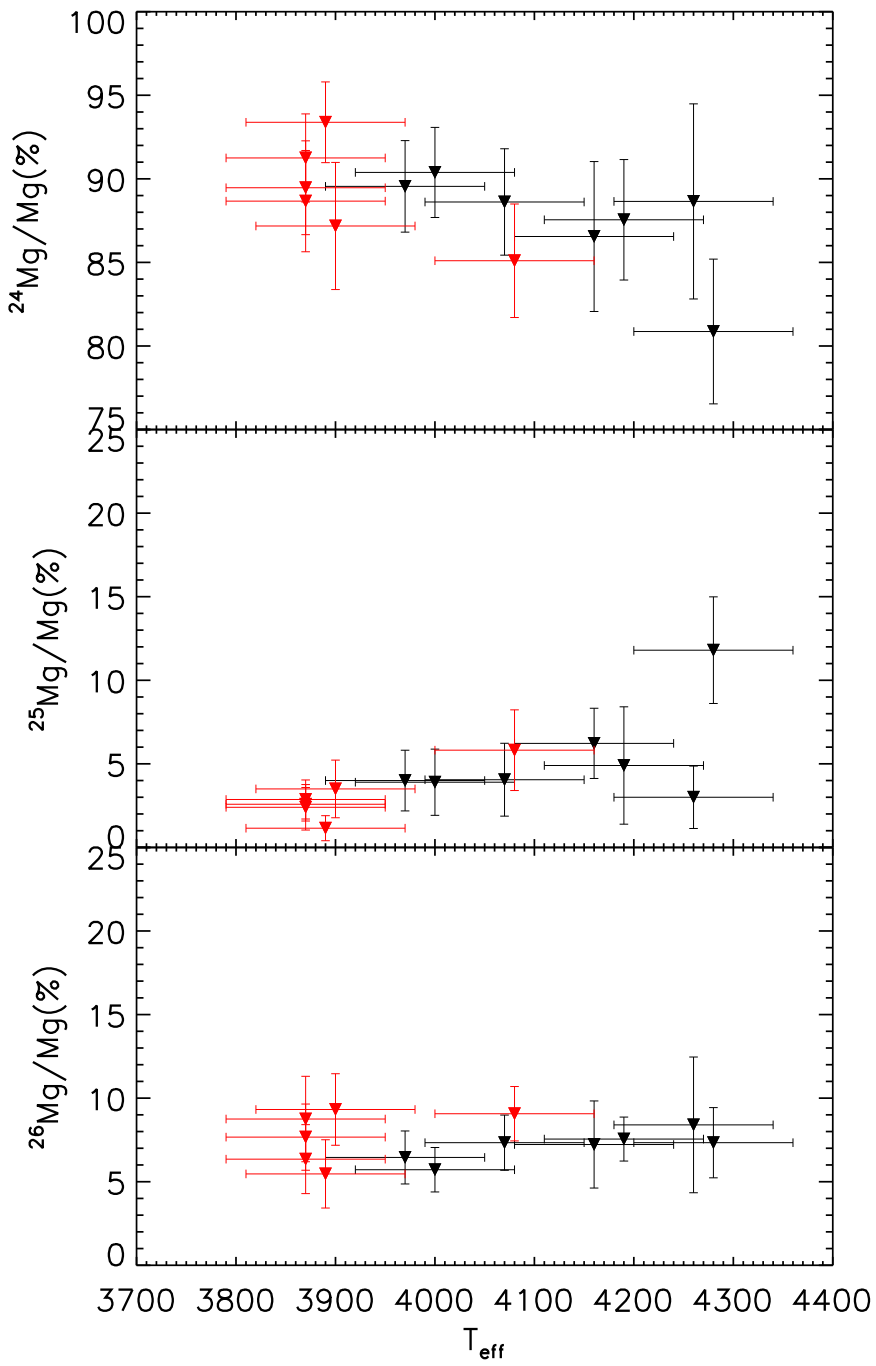

Figure 4.12: Percentage abundances of the Mg isotopes vs. $T_{\rm eff}$.

populations of stars. To inspect the spread in our data we compute IQRs and median values, both for our sample as a whole, as well as separately for the two populations (Table 4.3). In the case of a normal distribution of measurements, the IQR extends to $\pm 0.7\sigma$ from the mean. Since we assume Gaussian uncertanties, we scale the reported 1σ uncertainties by this value, and call it σ_{IQR}. If we measure an IQR significantly larger than this, we can claim an intrinsic spread in our data. These values are reported in Table 4.3.

Whereas the sample as a whole only shows spreads that are comparable to the typical uncertainties of our measurements, there does appear to be a difference when inspecting the populations separately. Most notably, the polluted population of stars show a spread in ^{24}Mg that is about twice as large as the spread of the pristine population, and it does also show a spread in ^{26}Mg that is more than four times as large as that of the pristine population. Furthermore, the IQRs of these isotopes in the polluted stars are about twice the value of the σ_{IQR}. However, the measured spreads in Mg isotopes are in almost all cases only marginally larger than the typical uncertainties of our measurements, and there does not appear to be any clear offset between the two populations in ^{24}Mg and ^{26}Mg. The pristine population seems to be offset to slightly higher values of ^{25}Mg, which is surprising, since ^{25}Mg is supposed to be produced, not destroyed, when the Mg-Al chain is active. The nuclear reaction rate for proton capture on ^{24}Mg is significantly higher than the reaction rates for the production of ^{26}Mg, so as soon as the temperatures are high enough for the Mg-Al chain to be active, ^{25}Mg will be produced, typically in larger amounts than ^{26}Mg. Thus, an enhancement would be expected in the polluted population. However, we do note that the difference in ^{25}Mg between the two populations is marginal, and well within the typical uncertainties. There may also be an intrinsic variation in [Al/Fe] where the polluted population has an IQR of 0.13 dex, which should be compared to typical uncertainties of [Al/Fe] of 0.08 dex. This is again different for the pristine population, where the IQR of [Al/Fe] is only 0.08 dex.

Inspecting the plot of our Mg isotopic fractions against [Al/Fe] in Fig. 4.13, there seems to be a trend of ^{24}Mg and ^{26}Mg with the Al abundance, particularly evident for the polluted population. To investigate the strength of any potential trend, we performed linear fits to the observed values, taking into account uncertainties on both [Al/Fe], as well as on the individual Mg isotopic fractions. We used the `MPfitexy` routine, described in Sect. 4 of Williams et al. (2010), which builds on the `MPfit` package of Markwardt (2009). Linear fitting was done both using the sample as a whole, as well as when split into the pristine and polluted populations sub-samples. We consider the fitted trend significant if the resulting slope is different from zero by more than two σ_{slope}, with

σ_{slope} being the uncertainty on the best-fitting value of the line slope. For none of the fitted populations were we able to detect a significant trend of the Mg isotopes with [Al/Fe].

4.4.1 *Star 10237*

An outlier in our sample is the star 10237. It appears depleted in ^{24}Mg, 2σ below the sample mean. It is also found to be enhanced in ^{25}Mg, being $\sim 3\sigma$ above the mean value for the full sample. It is also the star with the highest derived T_{eff} in our sample. This behaviour is rather striking and there can be a number of explanations. In particular the ^{25}Mg abundance is surprising, as this has not been seen for any other star in our sample, and even compared to the remaining GCs with Mg isotope measurements, it is amongst the highest values observed.

One possible explanation could be that this star is in a binary system, where mass-transfer has occurred in the past, and thus it got enhanced in ^{25}Mg from material accreted from a companion AGB star. However, in this case, an enhancement in ^{26}Mg would also be expected, which we do not observe. With only one epoch of observations, we cannot tell whether this star is member of a binary system. A potential companion white dwarf would not make itself known by double lined spectra, and in any case we do not see any evidence for this. In this case, we would also expect to see other signatures of AGB nucleosynthesis, which we do not. The expected signature, does naturally depend on the yield of the adopted AGB model, and the assumptions about dilution. For instance the models of Ventura et al. (2014) do not predict a very strong oxygen depletion, although Na can get enhanced by almost an order of magnitude.

Since only massive AGB stars reach temperatures high enough to activate the Mg-Al burning chain, we rule out self-pollution as a potential explanation. At the age of 47 Tucanae, stars with $M \gtrsim 4\text{M}_{\odot}$ will already have evolved well beyond the AGB stage.

This star shows the lowest magnesium abundance in our sample ([Mg/Fe] = 0.32 dex), which makes the MgH features weaker, compared to any other star in our sample. The high abundance of ^{25}Mg seems robust, though, as all MgH features indicate this, albeit with some scatter between the different features, as is also seen for the remaining stars. One could speculate that there might be undetected blends that only become important at these higher temperatures, but considering the excellent agreement of the isotopic fractions between the MgH features, this does not seem to be a reasonable explanation. Blends that are not accounted for would result in an over-estimation of the Mg abundance. Thus, if this was the case, the measured abundance of Mg would become even lower.

Another option could be that this star is in fact not a member of the cluster. Whereas both the position in the CMD and the radial velocity reported in Chapter 3 is consistent with membership, we may see indications in the abundances that this is an interloper. Considering that this star has the highest [O/Fe] of all stars in our sample, and that at SN II may have contributed with some heavy Mg isotopes in the field at this metallicity, this could indicate that this star has been polluted by more supernova material than the remaining sample. This star also has one of the highest [Eu/Fe] values of the stars in our sample. Indeed comparing our results to the investigation of Mg isotopes in field stars by Yong et al. (2003b), the average isotopic fractions at this metallicity is 80:10:10, which compares well to what we observe for this star (80.9:11.8:7.3). The isotopic fraction of heavy Mg in the field stars is also significantly higher than what is seen for the rest of our cluster stars, at this metallicity. Thus, we cannot rule out that this star may be a non-member.

4.4.2 *Comparison with earlier works*

Several other studies have also investigated Mg isotopes in globular clusters, and used these results to constrain the nature of the intra-cluster polluters (NGC 6752, Yong et al. 2003a; M13, Shetrone 1996; Yong et al. 2006; M71, Meléndez & Cohen 2009, hereafter MC09 and ωCen, Da Costa et al. 2009).

The most obvious candidate for a direct comparison is M71, as it has a nearly identical metallicity to 47 Tucanae ([Fe/H] $= -0.72$ dex, MC09). These authors separated their sample into CN-strong and CN-weak stars and inspected the Mg isotopes for these populations. They found that the CN-strong stars were depleted in ^{24}Mg and enhanced in ^{26}Mg, relative to the CN-weak stars, but still found that the overall variation was rather small, albeit slightly larger than what we see in our sample.

To allow for a better comparison between the studies, we adopt the same population separation criterion, based on the [Na/Fe] value for M71. Before making the separation, we shift the results of MC09 to the abundance scale of Asplund et al. (2009). We use the same [Na/Fe] value to split the M71 population as we used in Chapter 3. In Fig. 4.13 we plot our measurements, as well as the ones of M71, when using the same population discriminant, as a function of [Al/Fe]. Clearly, the behaviour of the isotopes is very similar to what we see in 47 Tucanae. A small variation is seen in ^{24}Mg and ^{26}Mg, and an approximately constant value of ^{25}Mg. The MC09 stars appear to be slightly more enhanced in ^{25}Mg, compared to ours. The small differences found can likely be attributed to differences in the choice of MgH features, where

MC09 used the 5134.3 Å and not the 5134.6 Å feature that we are considering. They did also not use the 5135.3 Å feature, which we chose to include. Differences in the selection of blending atomic lines will also play a role. In addition, we do not expect the chemical evolution of the two clusters to have been exactly the same, since 47 Tucanae is significantly more massive than M71. It is worth noting that when splitting the MC09 sample based on their [Na/Fe] values, only two stars are found to belong to the polluted population of stars. These two, however, do show the largest ^{24}Mg depletion and ^{26}Mg enhancement in the MC09 sample, suggesting that these stars are made up of a larger fraction of processed material, compared to the remaining stars in the sample. A third star in the MC09 sample falls very close to our cut between the two populations, and could in principle belong also to the polluted population. This star shows the highest fraction of ^{25}Mg and ^{26}Mg of the pristine stars selected this way, so it would not change the conclusion about the polluted population in the MC09 sample.

Comparing now to the remaining studies of Mg isotopes in GCs, which are shown in Figs. 4.14, 4.15 and 4.16, our results fall nicely on the trend shown by these works. It is evident that the amount of ^{24}Mg only starts to change appreciably once the cluster has seen a significant activation of the Mg-Al burning chain. Until [Al/Fe] reaches approximately 0.5 dex, there is no significant variation in the isotopes. Only for more aluminum-enhanced stars do we begin to see a strong depletion of ^{24}Mg and a simultaneous increase in the ^{26}Mg abundance. The only exception here, being the results from ω Centauri, where all stars appear depleted in ^{24}Mg. However, this cluster also shows a spread in metallicity, and the stars analyzed do indeed have different [Fe/H] values, so it has likely had a more complicated formation history, compared to the rest of the GCs. It is also worth noting that even for the clusters with the largest ranges in [Al/Fe] (NGC 6752 and M13), the abundance of ^{25}Mg stays approximately constant. We note that since we employ one new feature, compared to the remaining studies, there may be a small offset between our results and the comparison studies. However, considering the overall good agreement with other clusters, for the same [Al/Fe] values, we do not expect this to have a large impact.

Assuming that AGB stars are the main source of heavy Mg isotopes, the lack of variation in the isotopes in 47 Tucanae, may be linked to its higher metallicity, which lowers the temperature at the bottom of the convective envelope, where HBB occurs in AGB stars. This, in turn, results in less efficient nucleosynthesis compared to the low metallicity cases. This may also be linked to the smaller Al-variations, often seen for high-metallicity clusters, but it is clearly not the full story, as also some high metallicity clusters show a substantial range in Al-abundances, like for instance NGC6388 (Δ[Al/Fe] $\sim$ 0.8 dex (Carretta

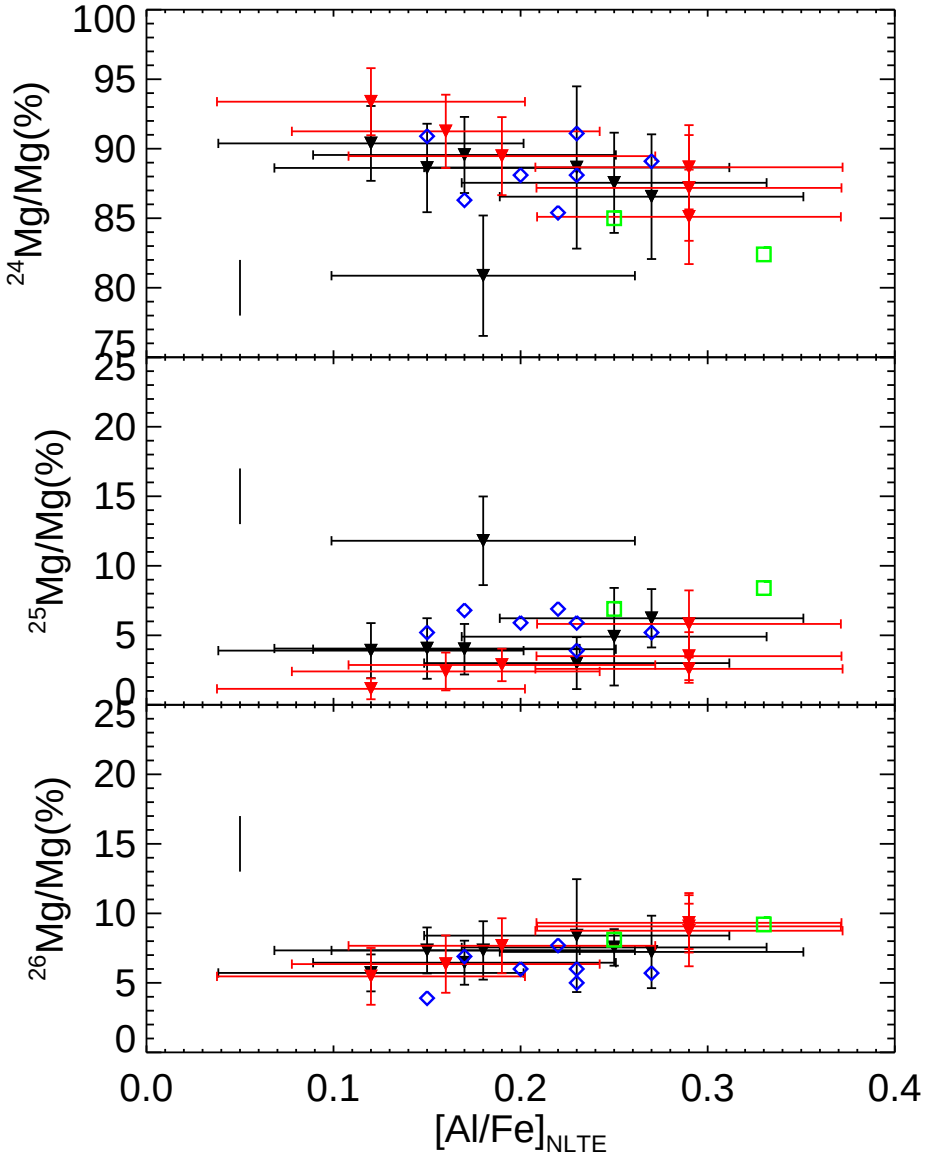

Figure 4.13: Percentage of ^{24}Mg vs. [Al/Fe] (top), ^{25}Mg vs. [Al/Fe] (middle) and ^{26}Mg vs. [Al/Fe] (bottom). Black triangles indicate the pristine populations and red triangles the polluted population. Also shown are the results from Meléndez & Cohen (2009) for M71. In the M71 sample, the polluted population is indicated with green, open squares. Blue open diamonds show the pristine population. Typical uncertainties of the isotope measurements for M71 is also shown.

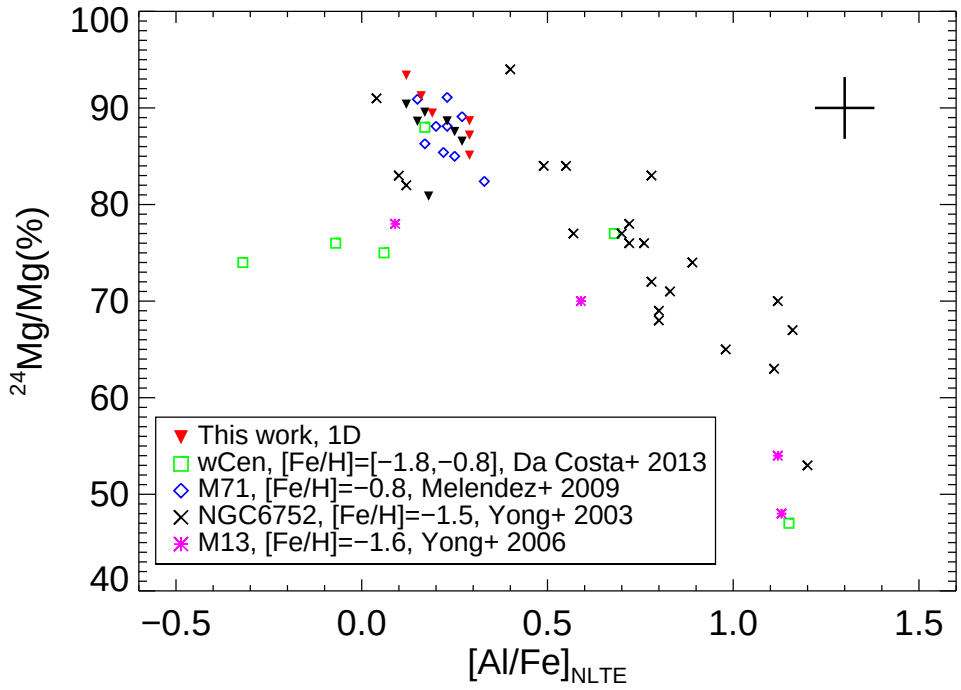

Figure 4.14: Linear fraction of ^{24}Mg vs. [Al/Fe]. Our results are shown as black and red triangles. For comparison the results from Da Costa et al. 2009 (green squares), Meléndez & Cohen 2009 (blue diamonds), Yong et al. 2003a (black crosses) and Yong et al. 2006 (pink asterisks) are shown.

et al. 2009a))and M71 (Δ[Al/Fe] $\sim$ 0.5 dex (Carretta et al. 2009a) and Cordero et al. 2015). We note here that both studies of M71 present stars with identical parameters, but significantly different [Al/Fe] values, a fact that would not change, even if the NLTE effects discussed in Chapter 3 are taken into account, since the NLTE corrections are driven by the stellar parameters.

4.4.3 *Pollution scenarios*

The results presented here, together with the results of Chapter 3, allow us to investigate potential pollution scenarios in more detail. Whereas our sample of stars does not cover the entire range of [Al/Fe] in the cluster, we can still gain insight into its chemical evolution.

As discussed in the Introduction, heavy isotopes of magnesium can form in a number of different nucleosynthesis processes. It is indeed possible for supernovae with massive progenitors to form ^{25}Mg and ^{26}Mg through α-captures on Ne, in the ^{22}Ne$(\alpha, n)^{25}$Mg and ^{22}Ne$(\alpha, \gamma)^{26}$Mg processes (see e.g. Kobayashi et al. 2011). This formation channel requires an initial seed of Ne, and is thus found to increase with increasing metallicity of the supernova progenitors. Up to a metallicity

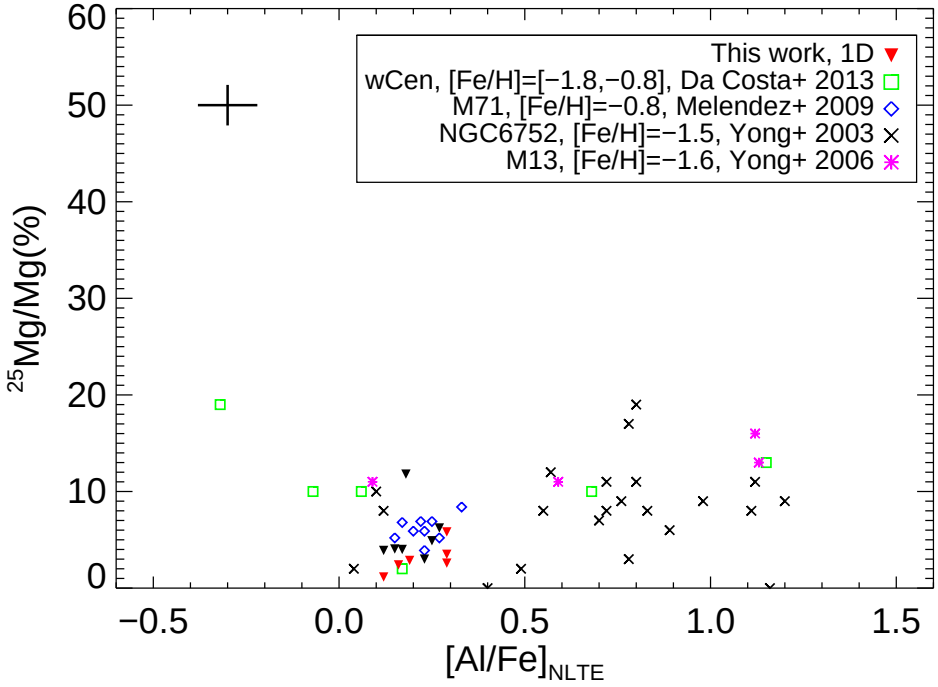

Figure 4.15: Same as in Fig. 4.14, but for ^{25}Mg.

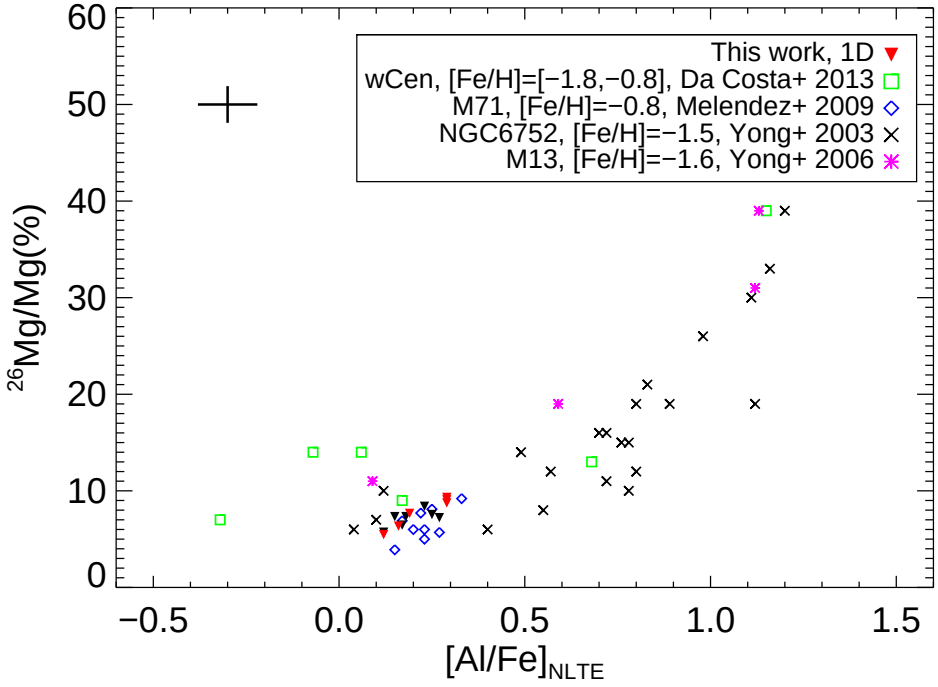

Figure 4.16: Same as in Fig 4.14, but for ^{26}Mg.

of about [Fe/H] $= -1.0$ dex, no significant production is expected from this channel (Alibés et al. 2001; Prantzos et al. 2007; Kobayashi et al. 2011). In AGB stars it is also possible to produce some heavy Mg isotopes from the above process, since some primary production of Ne is possible. However, the AGB production of heavy Mg isotopes is dominated by the Mg-Al chain during HBB, and .

In Fig 4.17 we present our measured isotopic ratios. In addition, we plot the isotopic ratios predicted from the supernova yields of Nomoto et al. (2006) and Tominaga et al. (2007), and it is clear that some non-SNe contribution must have occurred also for the pristine population of stars. From the work of Nomoto et al. (2006), we present yields from a range of progenitor masses at both z $= 0$ and z $= 0.004$, the latter corresponding roughly to the metallicity of 47 Tucanae. We also indicate their average yields, weighted by the IMF. In addition, we show results from Tominaga et al. (2007), but here only given as the IMF-weighted values. Finally, we show the isotopic ratios predicted for the MW halo from the chemical evolution study of Kobayashi et al. (2011).

For metal-poor clusters, it is typically assumed that the proto-cluster cloud consisted of fully mixed gas, enriched by the yields of metal-free supernovae, which is clearly a bad assumption in the case of 47 Tucanae. Whilst the measured ratios in the cluster are still below the Solar values of $^{25}Mg/^{24}Mg = 0.127$ and $^{26}Mg/^{24}Mg = 0.139$, both the pristine and polluted populations show ratios that are higher than what is predicted from supernova yields alone. In particular, the zero-metallicity supernovae only produce trace amounts of the heavy isotopes, clearly inconsistent with our observations. This was noted already in the study of NGC 6752 by Yong et al. (2003a), and the same pattern is observed for other GCs with measured isotopic ratios of Mg. Even considering yields from supernovae at the metallicity of 47 Tucanae, there is still a marked under-production of the heavy isotopes from the supernova channel alone, in particular true for ^{26}Mg.

It is also worth noting that even when one looks at the general MW evolution, as done in the Kobayashi et al. (2011) study, there are still not enough heavy isotopes being produced in the models. This was noted by the authors already in the original study, when comparing to measurements from field stars, where the field stars have even higher isotopic ratios than what is observed in the clusters. That field stars at this metallicity tend to have higher isotopic ratios is not surprising, since these stars are younger and should thus have incorporated more material from massive rotating stars and AGB stars. GCs, on the other hand, are old and expected to show little pollution from these mechanisms in the pristine population, in particular at lower metallicities.

However, it is clear also from the abundance pattern of 47 Tucanae, that the proto-cluster cloud has seen some s-process contribution (e.g.

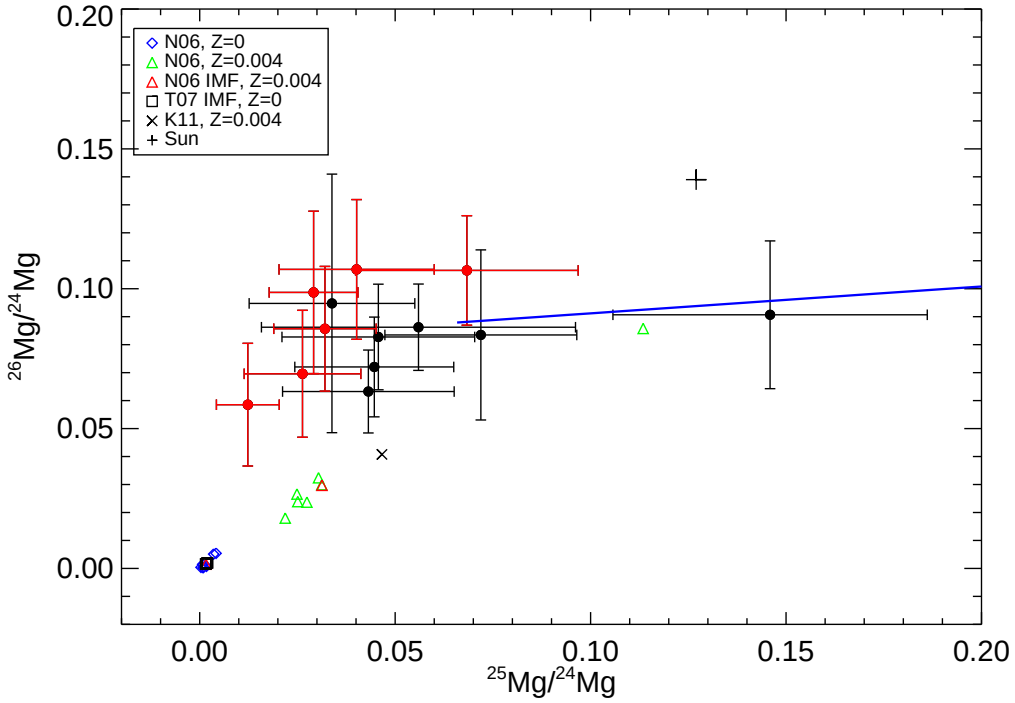

Figure 4.17: $^{26}Mg/^{24}Mg$ vs. $^{25}Mg/^{24}Mg$ measured in our sample. Shown are also isotopic ratios from the supernova yields of Nomoto et al. (2006) ($Z = 0$, blue diamonds; $Z = 0.004$, green triangles; $Z = 0.004$ IMF weighted value, red triangle), Tominaga et al. (2007) ($Z = 0$, black squares) and from the chemical evolution model of Kobayashi et al. (2011) (black X). Shown is also the dilution curve for the isotopes using the model form Ventura et al. (2014). The Solar position is shown with a black cross.

Cordero et al. 2014 and Thygesen et al. 2014). Since the s-process elements are also produced by AGB stars, one would expect that also the Mg isotopes should be elevated to levels above that of pure supernova yields. Our 1D results in Fig. 4.17 reinforce the interpretation that the proto-cluster cloud has seen contributions from processes other than type II supernovae, even in the pristine generation of stars in GCs.

4.4.3.1 *The AGB scenario*

Ventura et al. (2014) recently proposed a pollution scenario for 47 Tucanae, under the AGB scheme. They were able to reproduce the light element abundance variations in a large fraction of the observed stars from the Carretta et al. (2013) sample, assuming a varying degree of dilution of the AGB ejecta with pristine material. Our results for [O/Fe] and [Na/Fe] for the polluted stars place them within the range covered by their proposed dilution curve for the abundance ratios, when the

abundances are offset by −0.2 dex and −0.3 dex, respectively, as done in their work. The pristine stars, on the other hand, fall just outside the range covered by their models. We note that the AGB models of their work can only create a 0.2 dex variation in [O/Fe] without violating the constraints on the maximum He variations within the cluster, obtained from analyses of the horizontal branch (HB) (di Criscienzo et al. 2010), and the width of the MS (Milone et al. 2012b). Since the [O/Fe] variations span more than 0.8 dex in 47 Tucanae (Cordero et al. 2014), some additional source of light element variation may be needed. A possible solution to this could also be extra mixing processes in giants, which can result in an additional depletion of oxygen in the polluted population of stars, as investigated by D'Antona & Ventura (2007). This is expected only to happen in stars of the most extreme chemistry, and these stars are expected to also be strongly enhanced in He. While the overall He spread in 47 Tucanae is small, a small population of extreme chemistry stars may exist, which is also supported by the fact that only a handful of stars with such strong oxygen depletion has been found by e. g. Cordero et al. (2014).

The AGB polluters in Ventura et al. (2014) are in a mass range where the stars experience a mild HBB, which is where the Mg-Al burning chain is activated. Their models predict an enhancement of the AGB surface abundances of Al of up to +0.5 dex, whereas the overall Mg abundances are only barely touched, with a depletion of at most 0.04 dex. Considering that the pure AGB ejecta need to be diluted with gas of pristine composition, no detectable variation in the Mg abundance is expected, consistent with our results. On the other hand, one would expect a small variation in [Al/Fe] in the polluted stars, which has indeed been reported by both Carretta et al. (2013) and Cordero et al. (2014). We also see indications of a variation in [Al/Fe] in our polluted population of stars, although our range in Al is significantly smaller than either of the two cited works. But as discussed in Chapter 3, this is likely a consequence of our small sample size.

During the burning chain that creates the Al enhancement in AGB stars, production of primarily ^{25}Mg, but also ^{26}Mg is occurring, and one would thus expect a change in the isotopic distribution between the pristine and polluted populations. Indeed, the AGB models of Ventura et al. (2014) predict a strong decrease of ^{24}Mg whereas ^{25}Mg should increase by almost an order of magnitude. Thus, one would expect the ^{25}Mg abundances to correlate with [Al/Fe] for the polluted population. As discussed earlier, our analysis does not give any indication of such a correlation being present. This is further illustrated in Fig. 4.18, where we plot the dilution curve (solid line) for the Mg isotopic fractions vs. [Al/Fe], using the models of Ventura et al. (2014). The maximum allowed fraction of AGB material is 0.3, as imposed by the constraints from

the He abundance variation . Whereas our [Al/Fe] values are within the model prediction, we see no evidence for a strong increase in ^{25}Mg. Thus, our observations are somewhat in disagreement with the predictions of the AGB models of Ventura et al. (2014), where an increase in ^{25}Mg would be expected, even if the Mg-Al chain is only weakly activated.

The dashed blue line in Fig. 4.18 shows the position of the dilution curve, if we assume that the lowest observed value of [Al/Fe] in our pristine stars reflects the actual abundance in the pristine population, and shift the dilution curve by this amount (+0.12 dex). The agreement is now significantly better, but the models still over-produce ^{25}Mg, compared to what we observe, in particular in the [Al/Fe] enhanced region. The ^{26}Mg vs. [Al/Fe] on the other hand, shows good agreement with the models.

The lack of observed variation of ^{25}Mg is a well-known problem, also in other GCs, where the observed values of ^{25}Mg are found to be approximately constant across 1 dex in metallicity, and about 1.5 dex in [Al/Fe], so it is not a phenomenon reserved for high-metallicity clusters like 47 Tucanae. Furthermore a significant variation in ^{26}Mg is observed for the lower metallicity clusters, which is not predicted by the AGB polluters.

In Fig. 4.17, we show the dilution curve for ^{26}Mg/^{24}Mg vs. ^{25}Mg/^{24}Mg, using the same AGB models as in Ventura et al. (2014). We note here, that the pristine composition assumed by Ventura et al. (2014) starts out with a higher initial fraction of the heavy Mg isotopes than our results would suggest for the pristine population. The amount of AGB material increases from left to right in the plot, with the leftmost point giving the pristine composition assumed in their models. Clearly, the bulk of our measured isotopic ratios fall well below the predicted value, even when considering a composition of purely pristine material. However, if one started from a composition with a lower abundance of heavy Mg isotopes, the curve would shift to the left, and show much better agreement with the observations.

4.4.3.2 *Other pollution mechanisms*

Whereas AGB star models have seen the most research in the GC context, they are not the only sources capable of producing heavy Mg isotopes. Indeed, the recently proposed scenario of Denissenkov & Hartwick (2014) is able to simultaneously reproduce the Na-O and Mg-Al anti-correlations, as well as the observed variation in heavy Mg isotopes and their correlation with [Al/Fe] for the clusters with reported Mg isotope measurements. They invoke supermassive stars ($> 10^4\,M_\odot$) to explain the abundance patterns, and these are indeed able to undergo

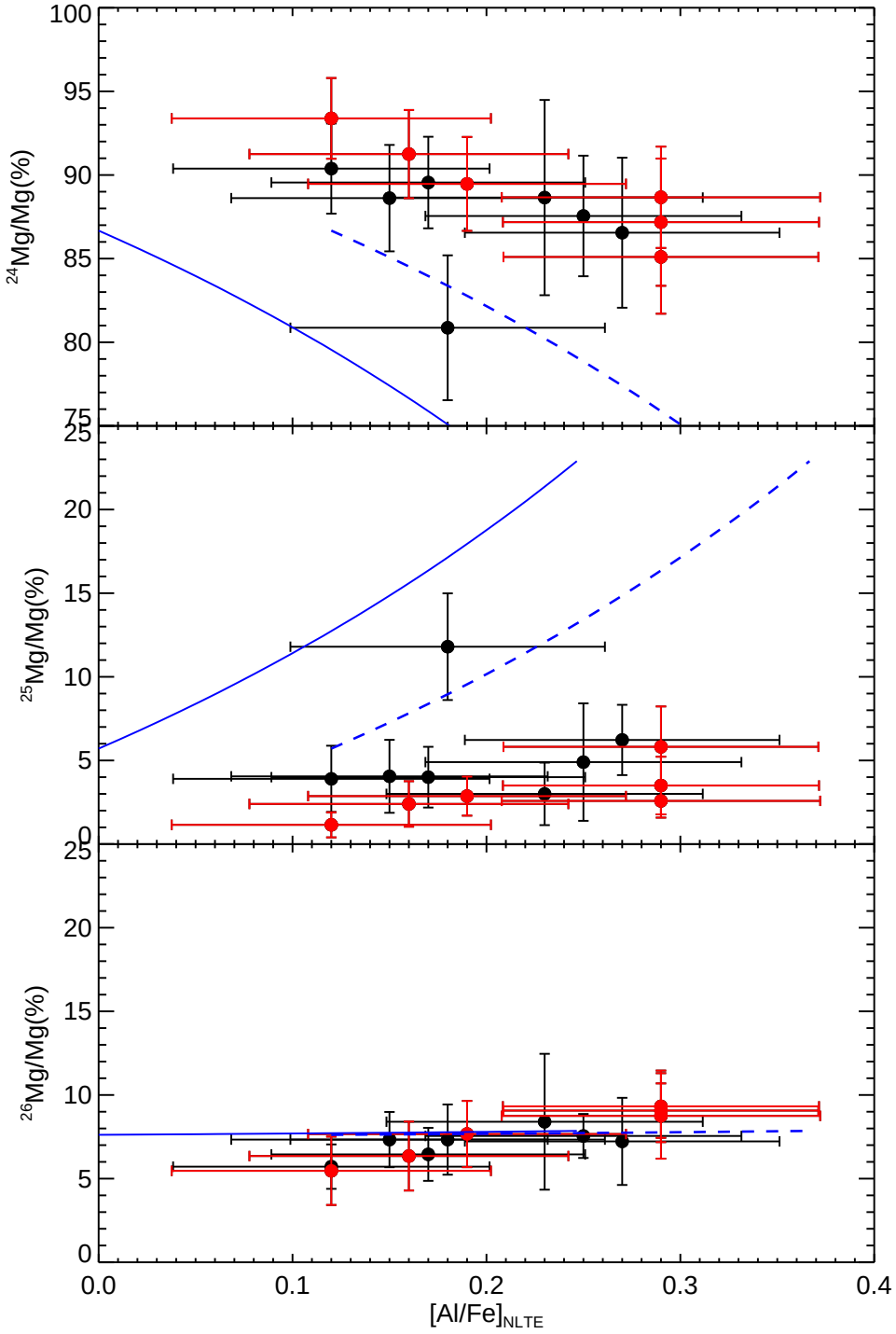

Figure 4.18: Isotopic fractions vs. [Al/Fe]. The solid blue lines is the predicted composition of the stars from Ventura et al. (2014). The dashed lines shows the dilution curve, when shifted by +0.12 dex in [Al/Fe].

the required nuclear burning. Their models are fully convective and processed material can easily be transported to the surface, and lost to the cluster where it is mixed with pristine material to a smaller or larger degree. In their models, they need to shut off nuclear burning once the central He abundance has increased by $\Delta Y = 0.15$ in order to not violate the maximum observed He variations in Galactic GCs. This is proposed to happen due to fragmentation of the supermassive stars. Although their model is appealing from many aspects, it is not without problems. For instance, a given extent of the Na-O anti-correlation requires a certain amount of processed material, that will also be enhanced in He. This poses a problem, since clusters with comparable Na-O variations show significantly different He variations (Bastian et al. 2015). Indeed, Denissenkov et al. (2015) explore the GC M13 in some detail and from their model it is suggested that this cluster should exhibit a variation in He of $\Delta Y = 0.13$, in contrast with the maximum observed variation of $\Delta Y = 0.04$ found by Dalessandro et al. (2013).

Unfortunately, Denissenkov & Hartwick (2014) only presents models for a single metallicity ([Fe/H] $= -1.5$ dex), so their predictions are not directly comparable to the case of 47 Tucanae. Nevertheless, if it is assumed that the yields of the supermassive stars scale so that the yields are proportionally the same at the metallicity of 47 Tucanae, we can still make a qualitative assessment of the feasibility of this candidate. Inspecting their predictions for the variation of the Mg isotopes, corresponding to our total measured range of [Al/Fe]$\sim$ 0.2 dex, the models of Denissenkov & Hartwick (2014) indeed suggest an insignificant variation in the ^{24}Mg and ^{26}Mg fractions ($< 5\%$), as less than 10% of the supermassive star ejecta will need to be incorporated in the material making up the polluted population. On the other hand, taking into account the additional constraints from the Na-O anti-correlation, this changes the picture. If the yields are shifted by $+0.1$ dex in [O/Fe] to match our most oxygen-rich star (excluding star 10237), 30-70% material from the supermassive stars is required to explain the variation in our observed sample. This would imply a variation of [Al/Fe] of about 1.2 dex, and a depletion of ^{24}Mg by up to 35%, with an increase of ^{26}Mg by an equivalent amount, relative to the pristine mixture. This is in stark contrast to what we observe, and thus supermassive stars are not able to explain the full set of abundance variations in the case of 47 Tucanae. The large amount of polluted material required to explain the Na-O anti-correlation would also imply a large He variation ($\Delta Y \sim 0.1$). This is in contrast to the observed spread in He of $\Delta Y =\sim 0.03$ (di Criscienzo et al. 2010).

However, if one considers only the variations in [Al/Fe] and in the heavy Mg isotopes, a significant variation in He may not be required. This is indeed consistent with the observations here, but would then

require a separate mechanism for explaining the Na-O variations, in particular a mechanism that does not simultaneously produce large amounts of He. In this respect it would be of interest to see models at higher metallicities, as the nuclear burning is not a metallicity-independent process.

Whereas the AGB stars and supermassive stars scenarios are the only ones able to *produce* the heavy Mg isotopes, other mechanisms could explain the observed Na-O anti-correlation. The lack of a correlation between [Na/Fe] and the Mg isotopes suggest that the mechanism responsible for the small spread in Mg isotopes is not necessarily connected with the mechanism behind the Na-O anti-correlation. In addition, some alternative models may be able to modify ^{24}Mg, which would also change the isotopic ratios. Unfortunately, the lack of models at metallicities appropriate for 47 Tucanae means that it is not possible to make as detailed a comparison as for the AGB stars.

Decressin et al. (2007) proposes fast rotating, massive stars ($20\,M_\odot < M < 120\,M_\odot$, FRMS) as polluter candidates. The central idea is that the abundance variations are created during hydrostatic burning and subsequently transported to the surface through rotationally-induced mixing. Here, the gas is ejected from the star through a slow wind, so that it is possible to retain the enriched gas within the cluster. The models considered in their work ([Fe/H]≈ -1.5), exhibit a strong enhancement in Na at the stellar surface, together with depletion in O, when their models reach the end of the MS. The stellar wind is slow at this evolutionary stage, and thus has a composition appropriate for the polluted population of stars in GCs. At the metallicity considered in their study, the increase in Na is between 0.8 and 1.6 dex, depending on the adopted reaction rates, while O is depleted by about 1.0 dex, compared to their initial values. This is expected to hold also at higher metallicities, where the core temperatures tend to increase, due to the increased opacity. This should result in an even more efficient burning. Even just assuming that the yields stay the same at the metallicity of 47 Tucanae, these models can easily accommodate the 0.48 dex depletion we find in [O/Fe], as well as the associated 0.49 dex increase in [Na/Fe]. However, dedicated models at higher metallicities are much called for, as the yields are complex functions of nuclear burning, stellar evolution and mass-loss, all of which are influenced by metallicity to some extent. As mentioned earlier, these models result in a net production of Mg, largely in the form of ^{24}Mg, so one would expect ^{24}Mg to increase with increasing Al enhancement, clearly contradicting observations.

The scenario proposed by de Mink et al. (2009), hereafter dM09, is exploring the viability of massive interacting binaries as the source of the enrichment. This polluter candidate has some appealing properties, compared to the AGB and FRMS scenarios. In particular, it provides a

very efficient way of releasing large amounts of enriched material into the cluster environment through mass transfer, whereas the two other scenarios require the cluster to either have been significantly more massive in the past, or have a very peculiar IMF. Unfortunately, this candidate has seen very little additional research, and dM09 only consider the single case of a $12\,M_\odot$ and $20\,M_\odot$ system at a metallicity of [Fe/H] ≈ -1.5 dex. Their yields are similar to what is found by Decressin et al. (2007), with their average yields showing a 0.12 dex depletion of oxygen, a 1.0 dex increase in sodium and a 0.13 dex increase in Al, the latter from processing of Mg, which is slightly depleted. Whereas dM09 do not provide yields for the individual isotopes of Mg, this could result in an increase in the $^{25}Mg/^{24}Mg$ and $^{26}Mg/^{24}Mg$ ratios, if it is assumed that the Al production comes mainly from burning of ^{24}Mg.

Their most extreme values for abundance variations are somewhat higher, and can easily accommodate the range we observe, under the assumption of identical yields at higher [Fe/H]. Furthermore, since the mass transfer between the massive binaries will spin up the companion star (de Mink et al. 2013), rotationally induced mixing may alter the abundances of the distributed material further. But as with the FRMS scenario, a larger suite of models would be most welcome to investigate this proposed mechanism in more detail. We note here that the pollution scenario using early disk accretion (Bastian et al. 2013) uses the same interacting binaries as the main polluter source, so the chemical abundance pattern in from the accretion mechanism will be similar to what is provided by the interacting binaries.

Furthermore, all models discussed above predict an overproduction of He, if the full range of Na and O abundances is to be explained (Bastian et al. 2015). As such, a currently unknown mechanism may be active in GCs

4.4.4 *Isotopes in 3D. A potential solution to the ^{25}Mg problem*

The discrepancy between the observed values for ^{25}Mg, and what is predicted to be produced by AGB stars, has been a long-standing issue, and the essentially constant, low fraction of ^{25}Mg is seen in all GCs where this has been studied, as mentioned earlier. Despite the improvements in AGB nucleosynthesis over the last decade, the predicted isotopic ratios are still at odds with the observations. Da Costa et al. (2009) propose two different scenarios that could potentially explain the observed behaviour. Both scenarios require modification of nuclear reaction rates at levels that are essentially ruled out by nuclear physics.

Our 3D results may resolve part of this discrepancy, as can be seen by inspecting Fig 4.19. Here we show the mean values for the isotopic ratios for the three stars for which we have performed a full 3D synthesis.

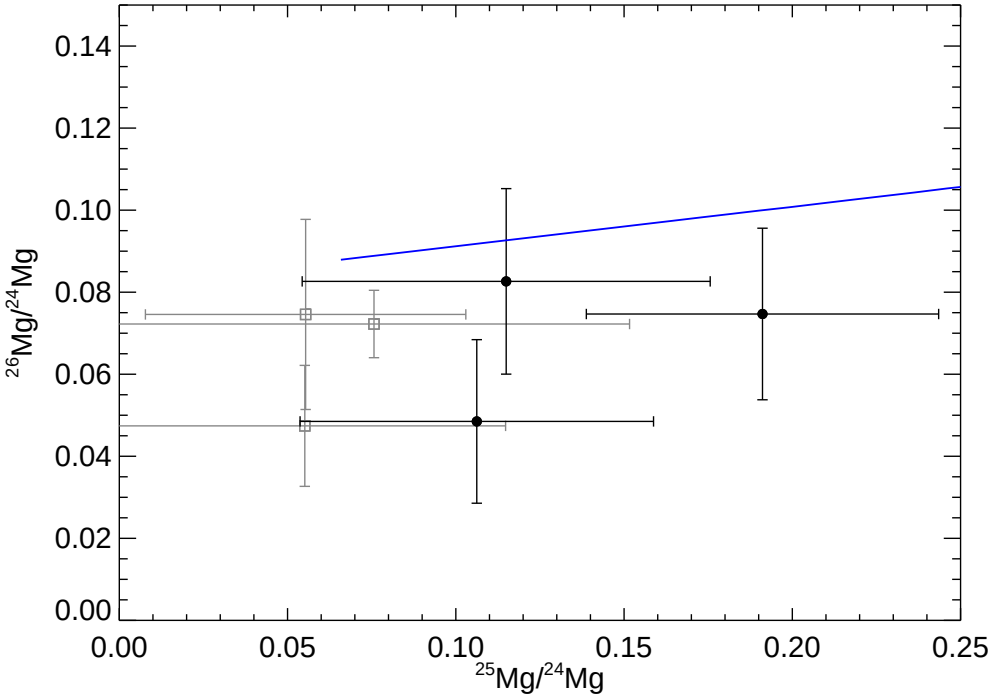

Figure 4.19: Isotopic ratios of magnesium from 1D (gray, open squares) and 3D (black, filled circles), together with the dilution curve for AGB star ejecta. Results are shown for stars 4794, 13396 and 29861.

For comparison, we also show the 1D results. We note that these mean values differ somewhat from what was shown in Fig 4.17, since we only use the 5135 Å and 5138 Å features. This is also the explanation for the increased uncertainties which we give as the RMS error of the mean value. For star 29861, where we only have results from one feature, we use the mean of the uncertainties of the two others stars as an estimate of the typical scatter.

The effect of the 3D synthesis is evident. We observe a factor of $2 - 2.5$ increase in the ^{25}Mg/^{24}Mg ratios, with respect to 1D, whereas the ^{26}Mg/^{24}Mg values stay essentially unchanged, compared to 1D. The measurements now show a significantly better agreement with the predictions from the AGB models. The ^{25}Mg/^{24}Mg ratios are now well within the ratios predicted for almost-pristine composition stars in 47 Tucanae, whereas there still seems to be a small offset in ^{26}Mg/^{24}Mg, compared to the models. This may potentially be rectified if results from the 5134 Å and 5140 Å features are included, as they tend to yield higher ^{26}Mg fractions, compared to the two bands investigated here. It is also worth noting that in all cases, the amount of ^{25}Mg is now *above* that of ^{26}Mg, which is in much better agreement with the predictions from AGB stars.

That the effects of 3D atmospheres are indeed improving the agreement with the AGB models can also be seen in Fig. 4.20, where we again plot the isotopic fractions vs. [Al/Fe], as in Fig. 4.18. The two dilution curves have the same meaning as before. The ^{24}Mg and ^{25}Mg fractions now fall very close to the dilution curve, if we apply the +0.12 dex shift to the [Al/Fe] predictions from the models. This shows that if the AGB models start out with a slightly different initial composition, it may indeed be possible to get a good agreement between models and observations of 47 Tucanae.

Whereas these results are encouraging, and may hopefully resolve a large part of the discrepancy between the observations and the predictions for AGB polluters in GCs, it may introduce another problem. If this result holds in general, an increase of ^{25}Mg would be expected also for giants in the field. Here, the predictions from chemical evolution models suggest that the models under-produce the amount of heavy isotopes (Kobayashi et al. 2011), and our results indicate that this discrepancy will increase in magnitude, if the field stars are investigated with 3D atmospheres.

However, we caution that a larger grid of 3D stellar atmosphere models is needed before the full impact of 3D synthesis can be determined. Whereas our syntheses are interpolated to the observed metallicities, we only cover a single value of $T_{\rm eff}$ and $\log g$. It would be desirable to cover also these dimensions in the parameter space, to allow us to interpolate to the exact stellar parameters, rather than our current approach. This may change the observed ratios somewhat, but we consider our model parameters to be close enough to the actual stellar parameters, to give at least a qualitative indication of the expected 3D effects for giants at these parameters. Efforts are currently ongoing to expand the available parameter space of our 3D models, so that these issues can be addressed in more detail. This also holds for analysis of stars in the field, where a larger range in model metallicities will also be required.

These results do not provide an answer either to the discrepancy between the observed and predicted behaviour of the *polluted* population of stars. Here, the AGB models predict a significant increase in the ^{25}Mg/^{24}Mg ratio and a ratio that should be larger than the ^{26}Mg/^{24}Mg ratio for the same stars. Since the stars for which we investigate the 3D effects, all belong to the pristine population, the results shown here cannot be used to determine any differences between the two populations. So while 3D effects are likely to explain a large part of the apparent lack of ^{25}Mg previously reported, they are unlikely to resolve the problem of the lack of variation between the populations. However, since our polluted population of stars all have significantly lower log(g) values, we cannot rule out a possible differential 3D effect, since the convective broadening of spectral lines tend to increase with decreasing surface

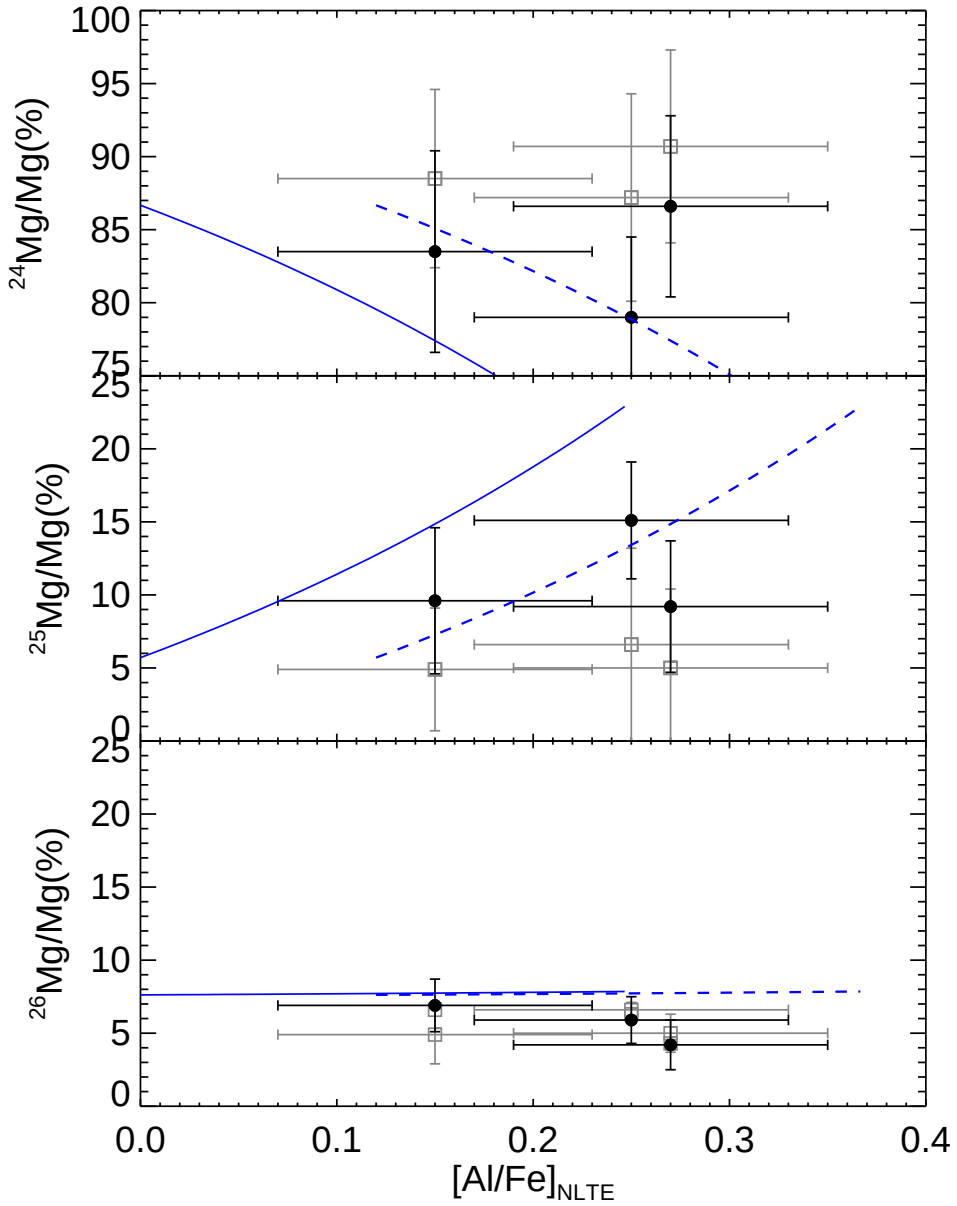

Figure 4.20: Isotopic fractions vs. [Al/Fe] for the stars with 3D results. The solid blue lines is the predicted composition of the stars from Ventura et al. (2014). The dashed lines shows the dilution curve, when shifted by +0.12 dex in [Al/Fe]. Symbols have the same meaning as in Fig. 4.19.

gravity. However, we have no a priori reason to believe that the changes in the isotopic composition due to 3D effects should be significantly different for the polluted population of stars, compared to the pristine population, for similar stellar parameters.

4.5 CONCLUSIONS

In Chapter 3, we derived abundances for a total of 27 elements in the globular cluster 47 Tucanae, spanning the range from O to Dy, using observations of unprecedented quality. We confirmed the known anti-correlation of Na and O, whereas we find no indication of an anti-correlation between Mg and Al, which has previously reported by Carretta et al. (2009a), among others, but we expect this to be a consequence of not sampling the full extent of the [Al/Fe] enhancement in our sample of stars. The variation in Na and O confirms that at least two populations of stars are present in 47 Tucanae, in line with what is seen in studies of both photometry and spectroscopy. We found a mean α-enhancement of $[\alpha/\mathrm{Fe}] = 0.34 \pm 0.03$. For the overall metallicity we find a value of $[\mathrm{Fe/H}] = -0.78 \pm 0.07$, which is in good agreement with other recent studies of 47 Tucanae. Inspecting the iron-peak elements, we saw no indication of a variation within the measurement uncertainties, as is consistent with a mono-metallicity. The same holds for the s-process- and r-process-dominated species. Inspecting abundance ratios of the s-process-dominated species (Ba, La) to that of Eu, we saw indications that 47 Tucanae has seen some s-process contribution to the abundances. Finally, abundance of the trans-iron elements Mo, Ru, Pr and Nd were found to be constant across all stars in our sample to a very high degree. We also did not observe any statistically significant correlations between [Na/Fe] and any other element, besides [O/Fe], consistent with the interpretation that no intrinsic variation is present in our sample of stars.

The use of a full NLTE synthesis of the Ba and Al lines eliminated spurious trends with T_{eff} found for both species, and it reduces the overall scatter significantly. We found that the observed range in [Al/Fe] decreased by a factor of $\sim$two, with a value consistent with a single abundance across our sample of stars. Even though the sample as a whole is consistent with a single value of [Al/Fe], we do observe a larger spread in the polluted population, compared to the pristine. We found an IQR of 0.13 dex for the polluted population, whereas the IQR of [Al/Fe] is only 0.08 dex in the pristine stars. This should be compared to the typical uncertainty of 0.08 dex, and could suggest a weak activation of the Mg-Al chain, but not to a level where a clear anti-correlation can be observed. We note that the lack of any strong variation is due to our small sample of stars, which is not covering the full range of Al abundances

in the cluster and should not be taken as an indication that no Al spread exits in 47 Tucanae. We further found that the overall enhancement of Al decreased compared to the abundances derived from an LTE analysis. If this is confirmed in other clusters, this may affect the constraints put on the polluter candidates. Since we only observe a small sample of giants here, this issue will need to be studied in a larger number of stars and in additional clusters before any firm claims can be made.

In Chapter 4 we presented the first ever measurements of the Mg isotopic distribution in 47 Tucanae. The sample shows very little variation in the isotopic fractions, but given the known, small variation in Al, this is not unexpected. In lower-metallicity clusters like NGC 6752 (Yong et al. 2003a), where a stronger Al enhancement is observed, the isotope variations are always found to be more substantial. However, we do detect a larger spread in ^{24}Mg and ^{26}Mg for the polluted stars, compared to the pristine population. In both cases, the spread is larger than the typical uncertainties of the individual measurements. We were not able to detect any significant correlation between the isotopes and [Na/Fe] or [Al/Fe], which has been observed in clusters with larger Al variations.

The detection of the larger spread in the magnesium isotopes for the polluted population may, however, be a sign of a marginal activation of the Mg-Al burning chain in the AGB stars polluting the intra-cluster environment, even if no clear correlation could be established. That some activation of the Mg-Al chain has occurred is also supported by the variations in [Al/Fe] seen by other authors (Carretta et al. 2013; Cordero et al. 2014). We note that this holds true, also for their LTE analysis, as both studies report a range of [Al/Fe] for stars with identical parameters. A NLTE analysis would thus not affect this.

In addition, we provide the first, detailed investigation of Mg isotopes with the use of 3D hydrodynamical atmospheres and full 3D spectral synthesis. The 3D synthesis provides an improved fit to the observed features, with significant changes in the ^{25}Mg/^{24}Mg ratio, by up to a factor of 2.5. This isotopic ratio is found to increase in both MgH features investigated. The ^{26}Mg/^{24}Mg ratio, on the other hand, is essentially unchanged. A particularly interesting aspect is that the fraction of ^{25}Mg is now found to be higher than that of ^{26}Mg, which has not been observed before. This helps to resolve a large part of the discrepancy between the AGB model yields and observations for this cluster, where the observed amounts of ^{25}Mg, based on 1D model atmospheres, are significantly below what is predicted. In particular if it is assumed that the most [Al/Fe] poor star in our sample represents the pristine composition. However, a larger sample of stars is needed to establish this firmly. Whereas the 3D results are encouraging, we caution that the use of 3D syntheses are unlikely to resolve the discrepancy between the

observed and predicted variations of Mg isotopes between the pristine and polluted population under the AGB scheme. The increase in the $^{25}Mg/^{24}Mg$ ratio would be expected to be similar in field stars, and this may result in increased tension between the predictions from chemical evolution models of the Milky Way, and the observed abundance ratios.

The main reason for the different results between 1D and 3D was found to be related to the temperature fluctuations in the 3D models, since the average thermal structures are almost identical at these metallicities. Since we did not investigate 3D effects for all four MgH features used, it would be premature to draw conclusions on the overall effect of 3D on the isotopic abundances. This will require a larger model grid as well as a much more detailed investigation, which is beyond the scope of this paper. The results are encouraging and certainly warrant more detailed research into the effects of 3D atmospheres on Mg isotopes, for a broader range of parameters and metallicities. In particular it would be interesting to also investigate this for field stars in the Galactic halo, where the Mg isotopic ratios are predominantly derived from sub-dwarfs (52/61 stars Yong et al. 2003b), where the effects of 3D atmospheres will likely be different. On the other hand, the nine giants also investigated, have isotopic ratios similar to the dwarfs at the same metallicity.

Our small sample size likely prevents us from detecting the full extent of the isotopic variations of Mg in 47 Tucanae, since this is expected to coincide with the most Al-enriched stars, which we do not necessarily cover. Even though we likely cover the full extent of [Na/Fe] values, this does not imply a complete sampling of the [Al/Fe] variations. This is clearly shown by both Carretta et al. (2013) and Cordero et al. (2014), who both found stars with near-identical parameters and identical [Na/Fe] values, but very different [Al/Fe] enhancements.

The results will help constrain the mechanisms responsible for creating the light element abundance variations seen in this cluster, but it would be desirable to obtain observations at the extremes of the [Al/Fe] variations. This way, the true extent of the isotope variations can be investigated. If the variation is found to be larger than what reported in the current work, this could provide additional support for massive AGB stars having contributed significantly to the intra-cluster pollution of 47 Tucanae at early times.

5

MAGNESIUM ISOTOPES IN RED GIANTS IN THE INNER MILKY WAY DISK AND THE MILKY WAY BULGE

Adapted from Thygesen, A. O., Sbordone, L., Andrievsky, S., Korotin, S., Collet, R., Yong, D., Asplund, M. and A. I., Karakas, in prep. [1]

5.1 INTRODUCTION

In this Chapter we perform an investigation of the isotopic distribution of magnesium in three giant stars in the Milky Way (MW) bulge, and five stars in the inner disk. Two of the bulge stars are members of the globular cluster (GC) NGC 6522. The goal is to demonstrate that accurate isotopic ratios can be determined, and use these to address the proposed connection between the MW disk and the bulge (see Sect.1.5). Furthermore, NGC 6522 has been proposed as the oldest GC system in the MW (Barbuy et al. 2009), and it would thus be of interest to determine Mg isotopic ratios in this cluster, to investigate whether it has experienced a different chemical evolution than other, younger GCs in the MW.

This study represents the first ever investigation of Mg isotopes in this region of the Galaxy.

5.2 OBSERVATIONS AND DATA REDUCTION

Acquiring observations of stars with the purpose of deriving Mg isotopes from the MgH features is challenging, since only a narrow range in $T_{\rm eff}$ is suitable for this type of analysis. We wanted to restrict ourselves to stars warmer than 3700K, to avoid too much molecular contamination of the MgH features from other molecules. Furthermore, stars hotter than $\sim$ 5100K are also not good targets, since the MgH molecule starts to dissociate strongly above these temperatures.

For this project, we selected three bulge giants in the desired parameter range from the sample of Fulbright et al. (2006), located in Baade's

1 The non-LTE synthesis in this chapter was done by Sergei Andrievsky and Sergei Korotin. Amanda Karakas provided data from the chemical evolution model, David Yong kindly provided spectra and results for the comparison stars. The development of this idea, writing of the observing proposal, preparation of the observations and remaining work was done by me. I would like to thank Prof. Michael Rich for providing accurate finding charts for the observations of the bulge targets.

Table 5.1: Observing log of all targets in the sample. Boldface indicate bulge star and italic the GC stars. Exp. time is the individual exposure time. The number of sub-exposures are provided in the last column.

ID	RA(J2000)	DEC(J2000)	V	Exp. time	$\#_{exp}$
I-264	18 : 03 : 38.10	−30 : 00 : 52.9	14.41	2700 s, 1800 s	6, 1
IV-203	18 : 03 : 23.80	−30 : 01 : 56.9	14.02	2700 s, 1800 s	5, 2
I-322	18 : 03 : 50.20	−30 : 01 : 46.20	14.50	2700 s, 1800 s	6, 1
J05115688	05 : 11 : 56.88	−08 : 55 : 47.00	11.40	2160 s	1
J142728406	14 : 27 : 28.41	−23 : 40 : 30.28	11.06	1800 s	1
J14574719	14 : 57 : 47.19	−38 : 24 : 30.30	11.80	3000 s	1
J15040305	15 : 04 : 03.05	−39 : 11 : 35.80	11.80	3000 s	1
J192058957	19 : 20 : 58.96	−16 : 21 : 20.65	11.15	1800 s	1

Window. Since the bulge is located far from the Sun ($\sim$ 8 kpc), we were limited in the choice of feasible targets, and made a simple selection, based on magnitude. The chosen stars are already so faint that they require more than 6h of observing time per star on an 8m class telescope to reach the desired S/N. Two of the selected stars (I-264 and IV-203) belong to the globular cluster NGC 6522, which is amongst the oldest clusters in the MW (Barbuy et al. 2009), whereas the third bulge star is a metal-rich field giant.

In addition, we observed five red giants from the MW disk, selected from Bensby et al. (2011b). Four of these are located in the inner part of the disk, at least 6 kpc from the Sun, whereas one star (J05115688) is located in the anti-center direction, around 12 kpc from the Sun. The targets were chosen to cover the same metallicity as the metal-rich bulge giant, to allow for a direct comparison between the two populations. Unfortunately, no low-metallicity stars with the right stellar parameters were found in the sample of Bensby et al. (2011b). An overview of all targets are provided in Table 5.1, with boldface indicating bulge stars and italics the GC stars.

All observations for this project were done with the UVES spectrograph (Dekker et al. 2000) mounted on the VLT UT-2 telescope at Paranal, Chile, in service mode under program 091.D-0383. The simultaneous requirement of high S/N ($\gtrsim$ 100) and the highest spectral resolution makes the observations challenging. To be less constrained by bad seeing, and to receive as much flux from the targets as possible, we used the IS #3 in the red 580nm setup, covering the wavelength range [4800Å- 6800Å] in one exposure. Due to the faintness of our bulge targets, we did several sub-exposures of these stars to facilitate the removal of cosmic rays in the observed spectra.

5.2.1 *Data reduction*

We reduced all observations with the ESO `GASGANO`[2]–based pipeline v. 2.4.8, performing the standard tasks of bias subtraction, flat-fielding, wavelength calibration and spectral order extraction. We used a simple, average extraction to extract the individual orders, as it is not possible to use optimal extraction for IS spectra, due to the complex cross-order profile of the spectrum. After the reduction of the individual exposures, each spectrum was corrected for barycentric motion using the `IRAF` (Tody 1986, 1993) `dopcor` task. After shifting the spectra, the individual sub-exposures of the bulge stars were combined, using the `IRAF scombine` task. We used a median combine, with an average sigma clipping for rejecting cosmic ray hits.

After combining the spectra, we performed a cross-correlation with a synthetic template spectrum to determine any additional velocity shifts. We performed a Gaussian fit to the computed CCF and took the mean value and standard deviation of the fitted Gaussian as the radial velocity and uncertainty of the radial velocity, respectively. The spectra were subsequently corrected for these shifts by one additional application of the `dopcor` task.

Whereas the usage of the IS allows for more relaxed seeing constraints on the observations, it turned out that this choice posed a problem when wanting to merge data from the sub-exposures of the bulge stars. Because the individual slices of the observed spectra fill out the spectral orders entirely, it is not possible to perform a reliable sky subtraction, so all sky emission will be imprinted on top of the stellar spectra. Whereas this is not much of an issue when the S/N of the individual exposures is high, as is the case for our disk stars, it turned out to be problematic when combining the exposures from the much fainter bulge stars. Since the sky signal stays approximately constant, when adding the sub-exposures we did not only increase the S/N of the stellar spectra, but also that of the sky emission lines. As most of these sub-exposures were done in sequence, the sky emission did not average out, as would have been the case if the observations had been obtained on different nights. This made correct continuum placement more challenging in the analysis, and meant that some lines had to be discarded due to strong sky emission. The disk stars, on the other hand, all reached a S/N > 100 in a single exposure. Conversely, the final S/N of the bulge spectra was only around 80 in the region of interest, somewhat lower than anticipated.

2 http://www.eso.org/sci/software/gasgano.html

5.3 ANALYSIS

To derive the fundamental stellar parameters of the stars, we took a purely spectroscopic approach. This approach is not sensitive to interstellar reddening, which can make photometric temperature estimates problematic, in particular for stars in the bulge, which are typically highly reddened. We measured equivalent widths (EWs) of approximately 90 Fe I and 10 Fe II lines in each star, using the same line list as in Fulbright et al. (2006). These lines have been inspected in detail to ensure they were free of any strong blends that could influence the derived parameters. This is especially important for the high-metallicity giants in our sample, where problems with blending from both molecular and atomic species becomes increasingly severe. In addition, we added a number of lines from the studies of Bergemann et al. (2012) and Lind et al. (2012). We did not use lines stronger than 150 mÅ, since such strong lines are saturated, and even a small change in the measured EW results in a large abundance difference, so they are unreliable compared to weaker lines. This, in turn, makes parameter diagnostics more uncertain. Furthermore, strong lines are more prone to suffer from NLTE effects.

We used interpolated ATLAS9 models (Castelli & Kurucz 2004), rather than computing tailored ATLAS12 models, since it was shown in Chapter 3 that this had negligible impact, unless one has strong anomalies in the main electron donors, compared to the standard mixtures (solar-scaled and $[\alpha/\mathrm{Fe}] = +0.4$) used in the ATLAS9 models. We observed no such anomalies in any of our stars, and we thus consider the use of interpolated models adequate. For the two GC stars, we used α-enhanced models, whereas a scaled Solar mixture was assumed for the disk giants and the metal-rich bulge giant. We use the Solar abundances from Asplund et al. (2009) as the reference abundances in this work.

Using our EW measurements, we performed a standard spectroscopic analysis, enforcing abundance equilibrium for the Fe I lines to determine T_{eff} and ξ_t, and ionization equilibrium between Fe I and Fe II, to determine $\log g$. Lines where the abundances deviated by more than three standard deviations from the sample mean, in more than six stars, were discarded from the analysis, and we attribute these discrepancies to likely erroneous $\log(gf)$ values.

Fulbright et al. 2006 (hereafter Fo6) published EW measurements for all stars in their sample, so we can make a direct comparison between their automated EW measurements, and the ones done by hand in this work. In Fig. 5.1 we plot the difference in EW between their work and ours, for both Fe I and Fe II. We also give the mean difference and the standard deviation. It is clear that the differences between our measurements and theirs are small, and no trends are seen with EW, except for

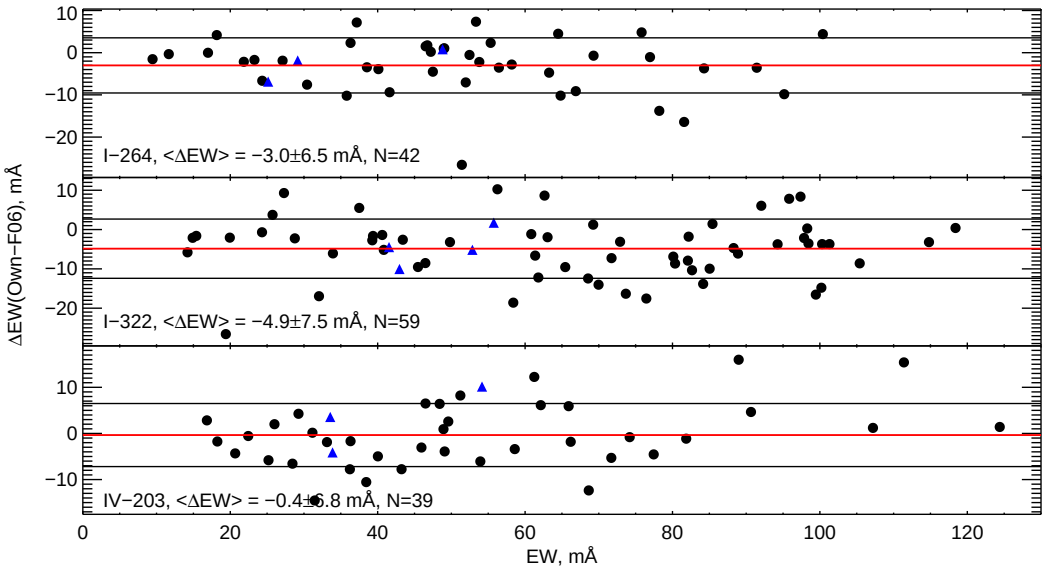

Figure 5.1: Comparison between our EW measurements and the measurements of Fulbright et al. (2006). Black circles is Fe I lines and blue triangles Fe II. The red lines show the mean difference and black lines ± the standard deviation.

IV-203, where we find systematically higher EW for the very strongest lines. However, the abundances from strong lines are only weakly sensitive to the line equivalent width, so we do not expect this to have a significant impact on our derived abundances. We note that the total number of lines used in our analysis is not reflected in Fig. 5.1, since not all the lines that Fo6 used in their original study could be measured in each of our stars. On the other hand, we also include some lines that they had discarded from their analysis. In particular the inclusion of a few Fe II lines from Bergemann et al. (2012) may influence the derived parameters, since the number of useful Fe II lines is already sparse. We further note that the Fo6 observations were obtained with $R = 45\,000$ and S/N = 85, 130 and 70 for stars I-264, I-322 and IV-203 respectively, so our observations have comparable S/N, but more than twice the resolution.

Following the recommendations from Meléndez & Cohen (2009), we determined the macroturbulent velocity, V_{macro}, by synthesizing five isolated Fe I lines at 6056.0 Å, 6078.5 Å, 6096.7 Å, 6120.2 Å, and 6151.6 Å. When synthesizing these lines we allowed for the Fe abundance to vary within the measured line-to-line scatter. We took the mean and standard deviation of the derived values as our best estimate of V_{macro} and associated uncertainty, respectively.

When concerned with spectral analysis of giants, NLTE effects on Fe I may have a non-negligible impact on both the Fe I abundance, as well as

the stellar parameters, as not all Fe I lines are affected to the same extent. In particular strong (> 60 mÅ), low excitation potential lines (< 3 eV), exhibit weaker NLTE corrections, compared to weaker lines (Bergemann et al. 2012). The direction of the corrections would lead to an underestimation of $T_{\rm eff}$ in LTE. However, as shown by Ruchti et al. (2013), the effect on $T_{\rm eff}$ for giants at the metallicities shown here, are minor and comparable to our typical uncertainties. Lind et al. (2012) also inspected the effects of NLTE for stars for a wide range of parameters, but as shown in their Figs. 2 and 4, the average corrections to Fe I and $\log g$ are less than 0.02 dex for their model with parameters closest to ours (4000 K, $\log g = 1.0$), with the corrections decreasing for decreasing $T_{\rm eff}$ and increasing [Fe/H]. Thus, we consider NLTE effects on iron negligible for the stars treated here.

5.3.1 *Elemental abundance measurements*

With the fundamental stellar parameters set, we proceeded to derive abundances of O, Na, Mg, Al, Ti, and Ni. The abundances of Ni were derived by standard EW measurements, using atomic data from Version 4 of the Gaia-ESO survey line list (Heiter et al. in prep.).

Abundances of the remaining elements were derived using the July 2014 version of the spectral synthesis code MOOG (Sneden 1973; Sobeck et al. 2011; Sneden et al. 2012). Typically we did an initial synthesis of a 15 Å chunk of the spectrum, centered on the feature of interest, in order to ensure correct continuum placement. With the continuum set, we refined the syntheses, inspecting only a narrow wavelength range around the feature of interest. For all stars in our sample, we included molecular blends of CH (Masseron et al. 2014), CN (Brooke et al. 2014; Sneden et al. 2014) and C_2 (Brooke et al. 2013). In addition, we included TiO (Plez 1998) for the metal-rich field stars. Whereas TiO lines are often neglected, we found that they had a significant impact on the overall appearance of the spectra for our metal-rich giants, and neglecting them would result in a wrong continuum placement, rendering the derived abundances unreliable in many cases. We assumed a Solar isotopic composition for all molecular species.

Initially, we derived Ti abundances from EW measurements of both neutral and singly ionized lines, but the resulting abundances differed by up to 0.35 dex, and the abundances from each species also showed a significant scatter. Suspecting that this was due to a combination of NLTE effects and unaccounted blends in the EW measurements, we changed our initial approach to deriving the abundance of this element. Following the recommendation of Bergemann (2011), we discarded the measurements of neutral Ti and derived titanium abundances using five Ti II lines. This is a better approach than the EW measurements, since the

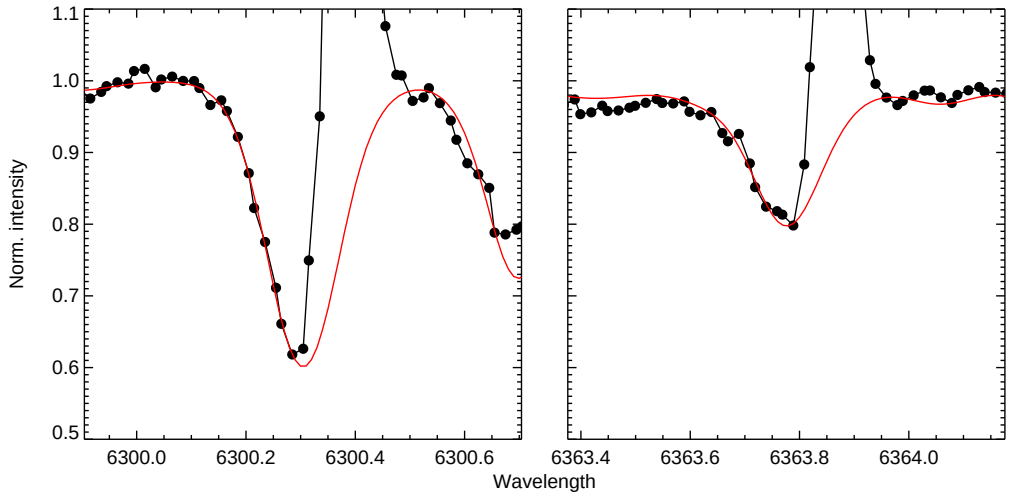

Figure 5.2: Syntheses of the two forbidden [OI] lines in the star J192058957. Only a lower limit on the O abundance can be derived.

lines from neutral Ti are strongly influenced by NLTE effects, whereas the Ti II lines do not show departures from LTE behaviour (Bergemann 2011). By synthesizing the lines, we can also account for blends from other species. Synthesizing the Ti lines provided a significant improvement in the results, compared to the EW measurements, with the line-to-line scatter decreasing by at least a factor of two. The atomic line data was taken from Wood et al. (2013) for Ti II.

Oxygen abundances were derived using the two forbidden [OI] lines at 6300 Å and 6363 Å. The best-fitting abundance for each line was derived by χ^2-minimization. The precision on the abundance for the individual fits was set to be when a significant deviation from the best-fitting abundance was observed, as judged by eye. The typical fitting precision was ± 0.10 dex. The derivation of reliable oxygen abundances were unfortunately hampered by the presence of atmospheric emission lines in a few cases, and we could only derive a lower limit on the O abundance for the star J192058957 (Fig. 5.2). For the stars I-264 and J15040305 there was too much emission present in the lines to derive meaningful limits on the abundance. For the remaining stars, their radial velocities were sufficient to shift the atmospheric absorption lines away from the stellar lines, and we do not consider this an issue for our derived abundances.

Na and Mg abundances were derived in a similar fashion, where we again included TiO blends in the syntheses. As seen in Fig. 5.3, the inclusion of the TiO lines has a significant impact on the shape of the

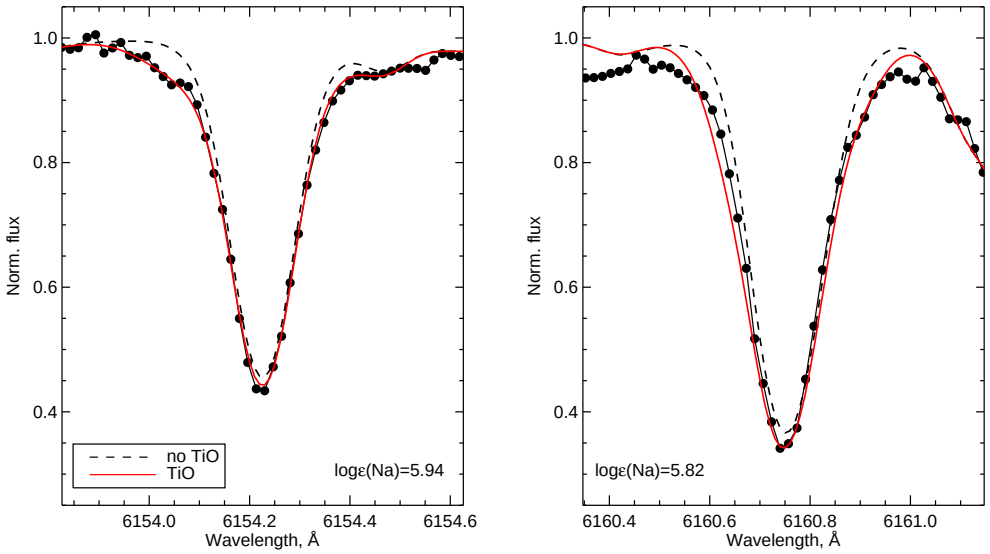

Figure 5.3: Syntheses of the Na lines at 6154 Å and 6160 Å, with and without inclusion of the TiO blends in the syntheses, for the star J15040305.

spectrum. Neglecting them results in an over-estimation of the actual abundance. We used the Na lines at 6154 Å and 6160 Å to derive the sodium abundance. These lines grow very strong at the parameters of these stars, entering the saturated regime of the curve-of-growth, making them weakly sensitive to abundance variations. This resulted in a typical fitting precision of 0.2 dex. The line-to-line difference was typically around 0.15 dex. For Mg, we used the three neutral lines around 6139 Å. Individual fitting precisions of 0.15 dex were reached in most cases. Again, the inclusion of TiO blends improved the line-to-line agreement, compared to leaving them out.

As discussed in Chapter 4, the presence of blends from carbon-bearing molecules, in particular C_2, has a strong influence on the shape of the 5134.6 Å and 5140.2 Å MgH features. To inform us about the C abundance in our stars, we used the C_2 molecular features at 5635 Å. This provided us with a reliable upper limit on the C abundance, although the high metallicities of most of our targets made the measurements complicated, due to blending with other molecular species. Overall we found carbon to be depleted, which is known to happen during the ascent of the giant branch, where C is processed in the burning envelope

5.3.1.1 *Al and Ba NLTE analysis*

As shown in Chapter 3, NLTE effects on the aluminum lines are important, even at high metallicity, when concerned with very evolved giants. Thus, we also performed an NLTE synthesis for Al in the sample of stars presented here. The NLTE computations were done with the `MULTI` code

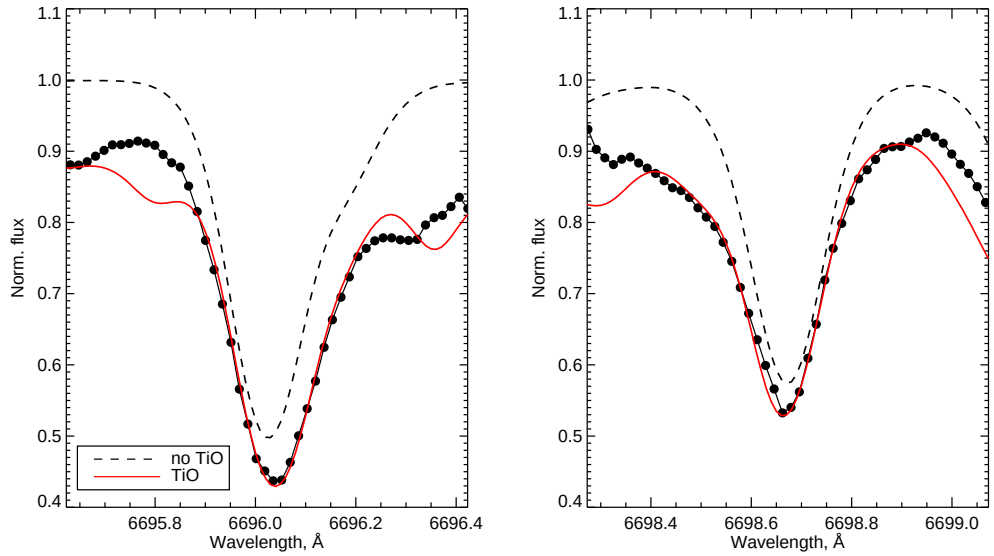

Figure 5.4: Syntheses with (red, solid) and without (black, dashed) TiO bands in the star J142728406 of the Al features at 6696.02 Å, and 6698.67 Å, together with the observed spectrum. The syntheses are computed with identical Al abundances. Note that no artificial shift has been applied to any of the syntheses.

(Carlsson 1986; Korotin et al. 1999), using the atomic data presented in Tables A.1 and A.2. We synthesized the Al I lines at 5557.06 Å, 6696.02 Å, and 6698.67 Å.

Contrary to the analysis presented in Sect. 3.3.2.3, we did not fold the Al NLTE synthesis with an LTE spectrum computed for the blending species in the present case. Rather, we first computed the LTE abundance of Al, using MOOG (including TiO). Using this derived abundance, an LTE analysis was computed with `MULTI` for the same abundance. Subsequently we computed an NLTE synthesis that matched the line EW for the Al lines. We took this approach since the `MULTI`-LTE synthesis does not account for the TiO lines, which has a significant impact on the derived abundances (Fig. 5.4). By matching the EWs of the LTE and NLTE syntheses in this fashion, we circumvent this problem. Similar to the results from Sect. 3.3.2.3 we found that NLTE effects were important for Al, and that the NLTE abundances were lower than the equivalent LTE abundances. Further, the NLTE abundances from the individual lines were in much better agreement than the abundances derived from LTE. The mean NLTE abundances were found to be $0.15 - 0.30$ dex lower than the ones derived from the LTE analysis.

In addition, we also performed a full NLTE synthesis of the three barium lines at 5148 Å, 6142 Å, and 6496 Å in the two GC stars, I-264 and IV-203. Due to the low metallicity of these stars, blending with TiO could be safely neglected. Unfortunately, these lines are heavily satu-

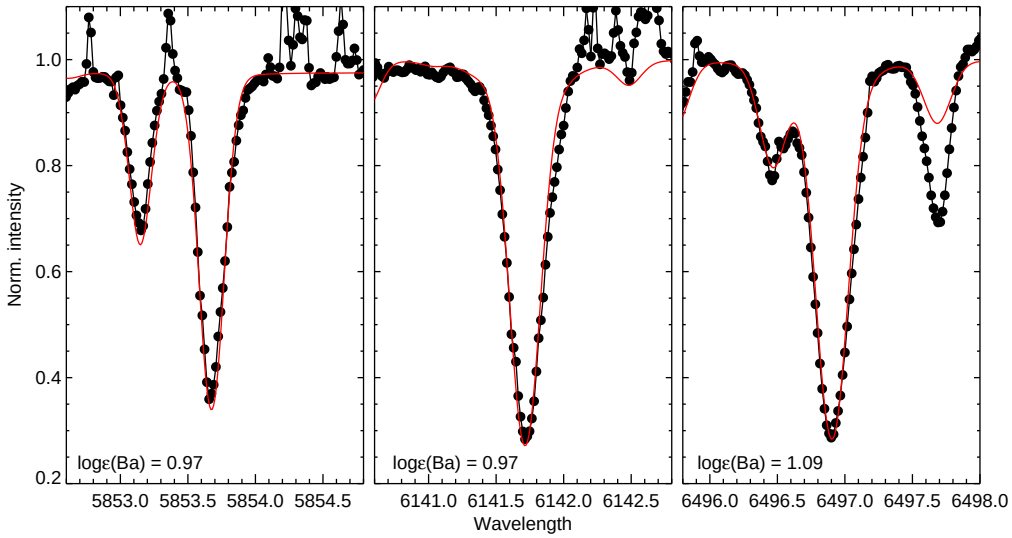

Figure 5.5: NLTE synthesis of the three Ba II lines in the bulge star IV-203. Some residual sky emission is also visible in the spectra.

rated in the metal-rich stars in our sample, and we were not able to derive meaningful abundances for the field stars. The two metal-poor GC stars, on the other hand, could be fit well, although we were unable to fit the 6142 Å feature in star I-264. Inspecting Fig 5.5, the NLTE synthesis produces very consistent abundances for all three features.

5.3.2 *Magnesium isotope measurement*

The isotopes of magnesium were derived from syntheses of the MgH features at 5134.6 Å, 5135.1 Å 5138.7 Å, and 5140.2 Å. We used MgH line data from Shayesteh & Bernath (2011) for ^{24}MgH, and from Hinkle et al. (2013) for ^{25}MgH and ^{26}MgH.

Considering the impact of blending TiO features on the synthesis of atomic lines, one would expect that TiO bands influence the regions we used for the MgH feature fitting. Thus, we computed a number of syntheses, both with and without TiO features included. As can be seen in Fig. 5.6, the inclusion of TiO has some impact on the shape of the MgH features, in particular the 5134 Å and 5140 Å features. However, a careful analysis shows that the isotopic fractions are not strongly affected, changing by at most 3%, and this only for the two most strongly affected giants (J142728406 and J14574719). An effect on the overall strength of the feature is also observed, albeit a minor one, with the best-fitting synthesis that includes TiO requiring an Mg abundance lowered by up to 0.05 dex, relative to the no-TiO syntheses. In the case of the two

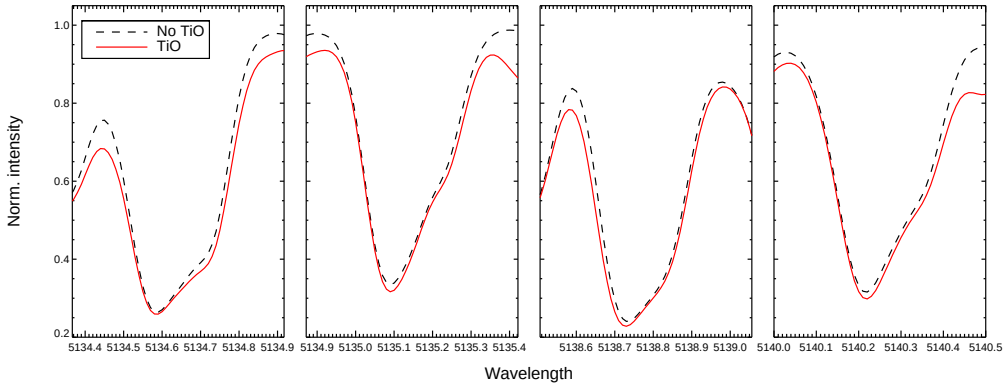

Figure 5.6: Syntheses of the four MgH bands, with and without the inclusion of TiO blends.

metal-poor GC stars, the inclusion of TiO transitions had no impact on the line-shapes and they could be safely neglected. We did, however, include them in all syntheses of the MgH bands for the disk giants, as well as for the metal-rich bulge star.

We use the method of Yong et al. (2003a) to fit the MgH features. The method performs a simple χ^2-minimization between the observed spectrum and a grid of synthetic spectra computed with MOOG. The abundance of Mg and the isotopic ratios ^{25}Mg/^{24}Mg and ^{26}Mg/^{24}Mg, were varied in each synthesis. As a first step, we determined the best-fitting isotopic ratio by eye, and we took these values as starting values. From this we initially computed a grid of syntheses covering a large range of Mg abundances and isotopic ratios, which was passed to the χ^2-minimization routine. After the best-fitting values had been determined from the coarse grid, we reduced the grid-spacing to get a better estimate of the parameter values corresponding to the minimum of the χ^2 distribution. Two examples of the best-fitting syntheses and the χ^2 distributions are shown in Figs. 5.7 and 5.8, where we also indicate the 1σ fitting uncertainty, computed as $\Delta\chi^2 = 1$, the best-fitting value and the positions of the central positions of the MgH isotopic features. The typical precision of the fitted values are 0.011 and 0.009 for ^{25}Mg/^{24}Mg and ^{26}Mg/^{24}Mg respectively. In Fig. 5.7 we further show syntheses for changes of $\pm$5% to the fractions of ^{25}Mg and ^{26}Mg, which is the typical by-eye precision for the metal poor stars. In Fig 5.8, the same is shown, but here $\pm$3%. The Mg abundance in the fit is used as a free parameter and is merely used as a scale factor controlling the strength of the features. Thus, it should not be taken as a measure of the actual Mg

abundance. For this, we use the values derived from the syntheses of the atomic lines of Mg.

For the final isotopic ratios, we compute the weighted mean of the individual features, using the fitting precision determined from the χ^2 analysis as weights. From these ratios we compute the individual Mg isotope fractions as

$$^{24}\mathrm{Mg} = \frac{1}{1 + {}^{25}\mathrm{Mg}/{}^{24}\mathrm{Mg} + {}^{26}\mathrm{Mg}/{}^{24}\mathrm{Mg}} \tag{5.1}$$

and

$$^{25,26}\mathrm{Mg} = \frac{^{25,26}\mathrm{Mg}}{^{24}\mathrm{Mg}} \times {}^{24}\mathrm{Mg}. \tag{5.2}$$

For the star J192058957 we had to discard the feature at 5135 Å due to atmospheric emission being present in the line, prohibiting a reliable determination of the Mg isotopic ratios.

5.3.3 *Determining uncertainties*

When deriving the fundamental stellar parameters from excitation and ionization equilibrium, one has to decide when the slopes of Fe I vs. excitation potential (EP) and reduced equivalent width (EW), are sufficiently close to zero. For the EP fitting, we accepted a slope of maximum 0.007 dex/eV, corresponding to $\sim$ 50 K, whereas we accepted a slope of 0.04 dex/EW, which corresponds to a change of approximately 0.05 km s^{-1} for ξ_t, relative to the zero-slope value. When determining $\log g$, we accepted a difference of at most 0.05 dex in Fe I $-$Fe II when establishing ionization equilibrium. However, in most cases, the final slopes, and abundance differences were smaller than these values. I will refer to these values as the intrinsic parameter uncertainties, $\sigma_{\mathrm{int.,N}}$, with N={T_{eff},$\log g$,ξ_t }. In addition, each of the slopes have an uncertainty, due to the scatter in the measured values of Fe I and Fe II.

In order to determine the uncertainties of the stellar parameters, we took the same approach as described in Sect. 3.3.1.1. In that case, the stars of our sample were sufficiently similar, that we considered a single star to be representative for all stars in the sample. In the present case, on the other hand, our observed targets span a wider range of parameters. To account for this, we perturbed the best-fitting model for every star by $\pm$200K in T_{eff}, $\pm$0.4 dex in $\log g$, and $\pm$0.3 km s^{-1} in ξ_t, with step-sizes 50 K, 0.1 dex and 0.1 km s^{-1}, respectively. For each perturbation we noted how the slopes of Fe I vs. EP and EW, as well as the abundances of Fe I and Fe II, changed as a function of the perturbations.

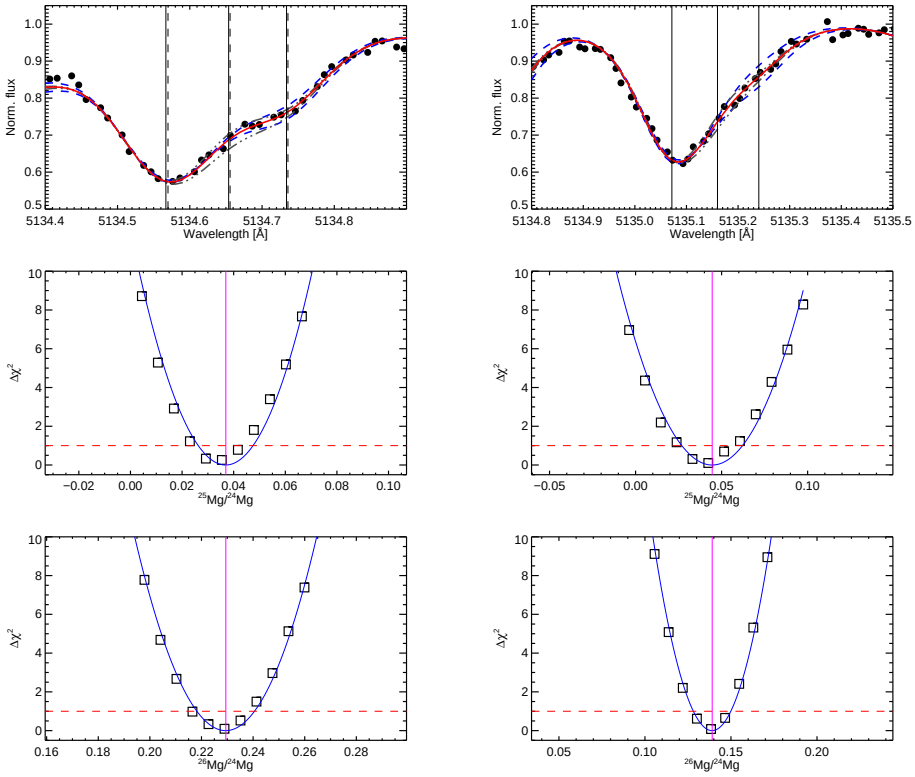

(a) MgH 5134 Å (b) MgH 5135 Å

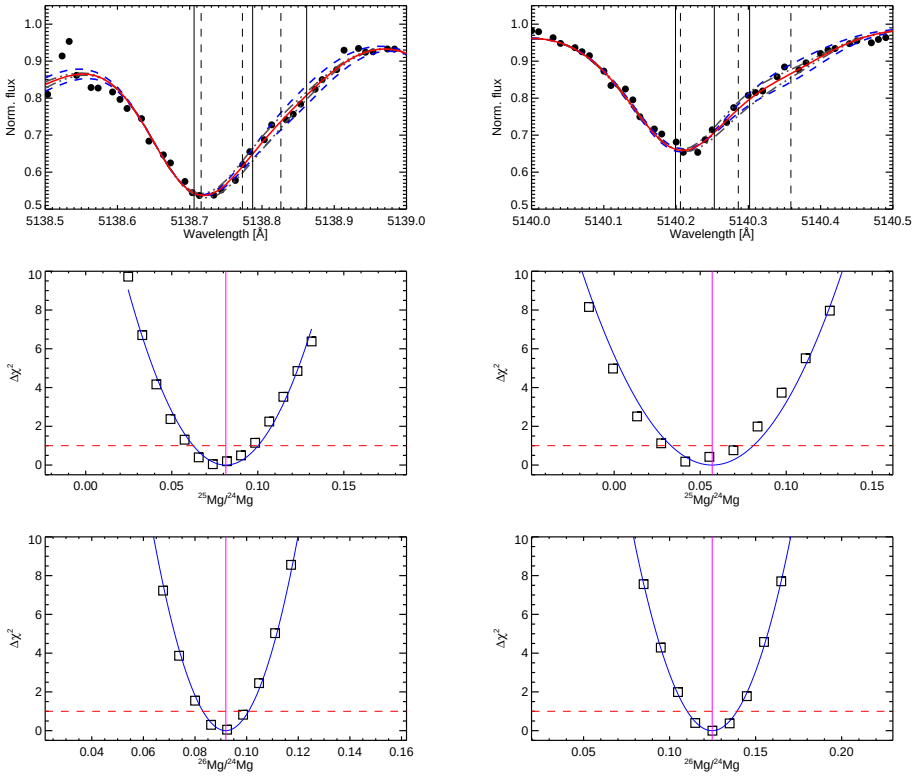

(c) MgH 5138 Å (d) MgH 5140 Å

Figure 5.7: Best-fitting MgH syntheses and χ^2-distributions for $^{25}Mg/^{24}Mg$ and $^{26}Mg/^{24}Mg$ for each feature in IV-203. The MgH transitions are indicated. Grey dot-dashed and blue dashed line shows syntheses with $\pm 5\%$ ^{25}Mg and ^{26}Mg respectively. Red dashed lines show the 1σ uncertainty. Vertical magenta lines: Best-fitting values.

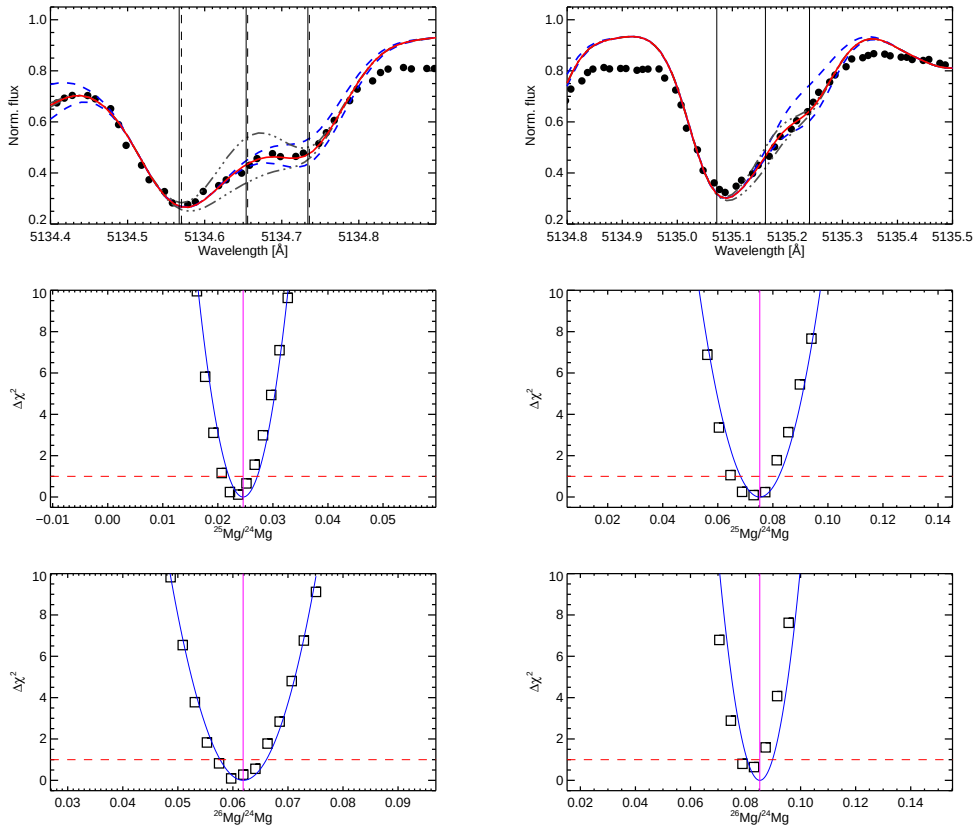

(a) MgH 5134 Å (b) MgH 5135 Å

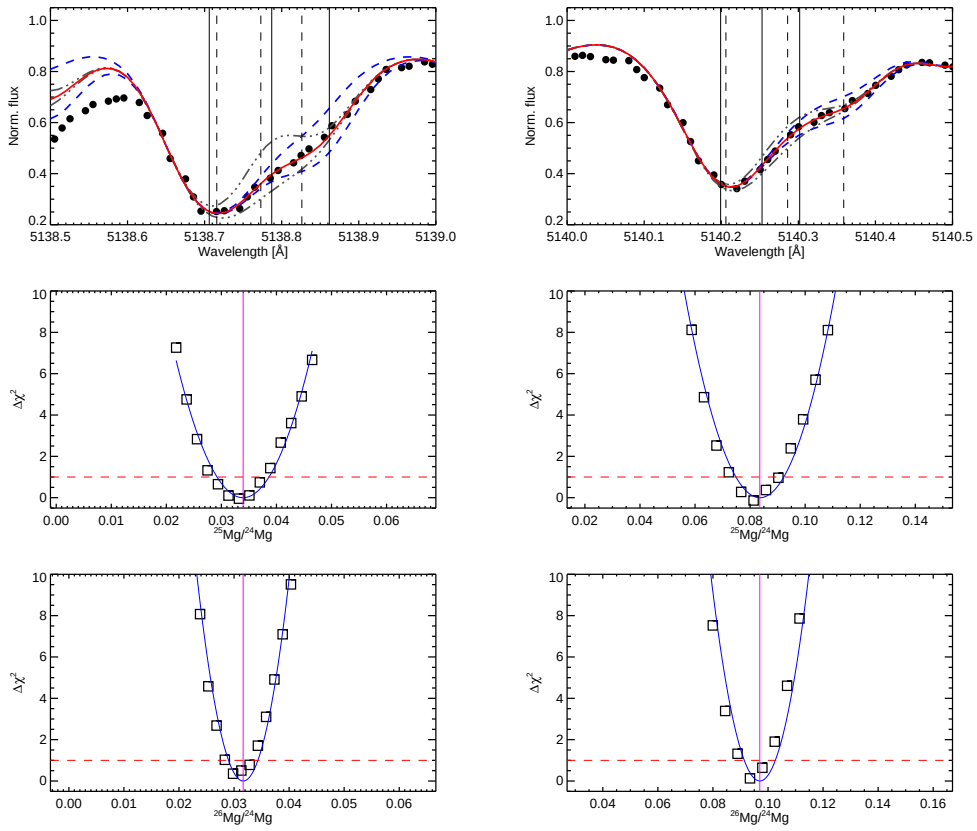

(c) MgH 5138 Å (d) MgH 5140 Å

Figure 5.8: As Fig. 5.7 but for the metal-rich field giant J14574719. Grey dot-dashed and blue dashed line shows syntheses with ±3% ^{25}Mg and ^{26}Mg respectively.

Similar to what was seen for the 47 Tucanae giants in Chapter 3, we found that the Fe II lines were highly sensitive to changes in $T_{\rm eff}$, which is what drives their large uncertainties (Table 5.4).

For the perturbations in $T_{\rm eff}$ and ξ_t, this allows us to construct $\Delta T_{\rm eff}$ vs. $slope_{\rm EP}$, and $\Delta\xi_t$ vs. $slope_{\rm EW}$ relations. Further, we inspected how Fe I − Fe I changed with changes in $\log g$, for each star. From these relations, it is trivial to compute the uncertainty of each parameter. We compute this as the quadratic sum of the parameter change needed to force the slopes on the original Fe I vs. EP and EW fits to zero, and the parameter change needed to change the slope by ± the uncertainty on the fitted slope:

$$\sigma_{\rm tot.,N} = \sqrt{\sigma^2_{\rm int.,N} + \sigma^2_{\rm N}} \tag{5.3}$$

with N={$T_{\rm eff}$,$\log g$,ξ_t }. The parameter uncertainties are given in Table 5.3.

The uncertainties of the stellar parameters will also influence the derived abundances. To take this into account, we re-derived abundances for all elements, using stellar atmosphere models perturbed by $\pm\sigma_{\rm tot.,N}$ for all parameters. We then took the mean differences between our best-fitting abundance ratios, and the abundance ratios from each model perturbed by $\pm\sigma_{\rm tot.,N}$, as the uncertainty associated with the particular stellar parameter. For the coolest, metal-rich giants, the perturbations of $T_{\rm eff}$, had a significant influence on the strength of the blending TiO features. In these cases, we re-normalized the observed spectra, to match the synthetic spectra, before the perturbed abundances were derived. This is justified, since we would have made a different choice on the continuum placement, also in the best-fitting analysis, had the temperature been different by the derived $\sigma_{T_{eff}}$.

As the total abundance ratio uncertainty, we added in quadrature the uncertainties from the stellar parameters, and the standard error on the mean of the abundance from the best fitting model, in the cases where we had measurements from multiple lines. In cases where only a single line was measured, we used the internal fitting precision in place of the standard error on the mean. We here note that the large uncertainties reported for the ionized species, is a consequence of the strong temperature-sensitivity of Fe II. Although the abundances of the other ionized species also respond to temperature changes, they are not as sensitive, and thus fairly large changes to the abundance ratios are observed when computing these relative to Fe II.

For the Mg isotopic ratios we performed a similar exercise. However, since the isotopic ratios are rather insensitive to stellar parameter changes, we only computed perturbed values for three stars, I-264, J142728406 and J192058957, which we took to be representative for the

low-metallicity stars, low gravity stars, and high-gravity stars, respectively. We show the effect of the parameter perturbations in Table 5.2. As the full uncertainty from parameter changes, we took the mean change introduced by $\pm N$, and add these in quadrature.

These uncertainties were subsequently added in quadrature to the standard error on the mean from the individual features, with the mean value computed from the weighted mean of the isotopic ratios. The reason for the larger influence of the parameters for the two disk stars is a consequence of, primarily, the strong temperature sensitivity of the TiO bands. Even a modest change in $T_{\rm eff}$ can change their strength substantially, and the already subtle signatures of the heavier isotopes are more strongly affected by this than the dominating ^{24}MgH feature.

We note, that the uncertainties presented here are not accounting for correlations between the stellar parameters, which will often serve to lower the effects of changing parameters, and hence the uncertainty estimates are probably somewhat conservative.

5.4 RESULTS

In Table 5.3 we present the fundamental stellar parameters of the stars in our sample. Boldface IDs indicate stars located in the bulge, with the two stars in italics being the NGC 6522 members. As is evident, they are all very evolved red giants, but we note that we do not see any indication of mass-loss in the spectra of either of the stars, suggesting that they have not yet evolved to the AGB phase.

For the bulge stars, our temperatures are in good agreement with the results of Fo6, with at most 100 K difference. Regarding $\log g$, our two GC stars have about 0.4 dex lower gravity than what found by Fo6, whereas our values for the field star is slightly higher. This is a consequence of us relying on a purely spectroscopic analysis, whereas they used photometric gravities. Fo6 also do not establish ionization equilibrium between neutral and ionized iron. Inspecting their results, their gravities would need to be changed in direction of our results to establish equilibrium. We also find systematically lower values for the microturbulence, ξ_t, which is likely due to differences in the lines used. Whereas we do use the same line list, we chose to include some lines that Fo6 had discarded for these particular stars. In addition, as discussed above, we also included lines from Bergemann et al. (2012) and Lind et al. (2012), meaning that only roughly half of the lines we use were also used in the comparison work. We attribute the main difference in ξ_t to this.

Regarding the disk stars which we selected from Bensby et al. (2010), our results are offset to slightly lower temperatures by 100 K on average, so our results are in agreement within the combined uncertainties of our

Table 5.2: Changes of the Mg isotopic ratios, relative to the best fitting value, when perturbed with the atmospheric parameter uncertainties. Shown for three representative stars.

	I-264		J142728406		J192058957	
ΔParam.	$\Delta(^{25}\mathrm{Mg}/^{24}\mathrm{Mg})$	$\Delta(^{26}\mathrm{Mg}/^{24}\mathrm{Mg})$	$\Delta(^{25}\mathrm{Mg}/^{24}\mathrm{Mg})$	$\Delta(^{26}\mathrm{Mg}/^{24}\mathrm{Mg})$	$\Delta(^{25}\mathrm{Mg}/^{24}\mathrm{Mg})$	$\Delta(^{26}\mathrm{Mg}/^{24}\mathrm{Mg})$
$+\Delta T_{\mathrm{eff}}$	$+0.001$	0.000	$+0.013$	-0.025	$+0.003$	-0.017
$-\Delta T_{\mathrm{eff}}$	0.000	-0.003	-0.025	$+0.032$	-0.010	$+0.029$
$+\Delta \log g$	-0.005	$+0.002$	$+0.001$	$+0.003$	-0.001	0.000
$-\Delta \log g$	$+0.008$	0.000	$+0.004$	-0.005	-0.003	-0.002
$+\Delta \xi_t$	-0.001	-0.004	-0.003	-0.003	0.000	-0.004
$-\Delta \xi_t$	0.000	0.006	$+0.008$	-0.002	0.000	-0.001
σ_N	± 0.007	± 0.005	± 0.020	± 0.029	± 0.007	± 0.023

results and theirs (75 K). We also find systematically lower gravities, by a similar amount as for the bulge stars, but we note that they quote a 0.30 dex uncertainty of their $\log g$ measurements. The difference we see is likely related to different line list and different continuum placement when the measurements were made, as well as the difference in the amount of deblending done for these very metal-rich stars. If we systematically place the continuum of the Fe II lines higher than Bensby et al. (2010), this would tend to promote lower gravities in our stars. Such an effect would be more severe for Fe II than Fe I, due to the small number of lines. This was also illustrated above in the direct comparison with the Fo6 measurements, where we, on average, find good agreement, but the differences between individual lines is still large in some cases. However, without a direct comparison of the individual line EWs, we cannot tell whether this is the case. We note that our observations are obtained at twice the resolving power of that used by Bensby et al. ($R = 55\,000$ vs. 110 000), which should allow for more reliable deblending, which is crucial for metal-rich giants, where line-blending typically is severe. Finally, although Bensby et al. derive the microturbulence in the same way as we do, they did not publish their measured values, so we have no means of comparing our values to theirs.

Table 5.3: Fundamental parameters for the bulge and disk stars and their uncertainties.

ID	$T_{\rm eff}$	$\log g$	ξ_t	[Fe/H]	$V_{\rm macro}$	$V_{\rm rad}$
I-264	4000 ± 64 K	0.40 ± 0.19	1.20 ± 0.09 km s^{-1}	-1.18 ± 0.04	5.78 ± 0.10 km s^{-1}	-15.5 ± 0.2 km s^{-1}
IV-203	3930 ± 79 K	0.00 ± 0.15	1.80 ± 0.15 km s^{-1}	-1.35 ± 0.05	7.86 ± 0.12 km s^{-1}	-15.6 ± 0.3 km s^{-1}
I-322	4050 ± 98 K	1.00 ± 0.12	1.10 ± 0.12 km s^{-1}	-0.31 ± 0.04	4.85 ± 0.17 km s^{-1}	-70.4 ± 0.2 km s^{-1}
J05115688	4080 ± 83 K	1.10 ± 0.10	1.00 ± 0.10 km s^{-1}	-0.32 ± 0.05	4.48 ± 0.08 km s^{-1}	-9.7 ± 0.12 km s^{-1}
J142728406	3750 ± 111 K	0.45 ± 0.30	1.20 ± 0.13 km s^{-1}	-0.41 ± 0.11	5.73 ± 0.13 km s^{-1}	-94.7 ± 0.16 km s^{-1}
J14574719	3910 ± 118 K	0.85 ± 0.25	0.60 ± 0.30 km s^{-1}	-0.22 ± 0.12	4.62 ± 0.12 km s^{-1}	$+54.8 \pm 0.17$ km s^{-1}
J15040305	3950 ± 82 K	0.80 ± 0.18	1.10 ± 0.15 km s^{-1}	-0.55 ± 0.07	4.50 ± 0.12 km s^{-1}	-19.1 ± 0.15 km s^{-1}
J192058957	4150 ± 101 K	1.15 ± 0.11	1.50 ± 0.10 km s^{-1}	-0.72 ± 0.04	4.65 ± 0.17 km s^{-1}	-25.4 ± 0.13 km s^{-1}

Table 5.4: The measured values of [Fe I/H], [Fe II/H] and [C/Fe], uncertainties, and number of lines used, for all stars in the sample. [C/Fe] is an upper limit.

ID	[FeI/H]	σ	N	[FeII/H]	σ	N	[C/Fe]
I-264	−1.18	0.04	90	−1.20	0.15	8	−0.26
IV-203	−1.35	0.05	72	−1.34	0.21	6	−0.24
I-322	−0.31	0.04	91	−0.35	0.20	10	−0.46
J05115688	−0.32	0.05	92	−0.31	0.19	11	−0.56
J142728406	−0.41	0.11	82	−0.34	0.35	8	−0.23
J14574719	−0.22	0.12	78	−0.18	0.31	7	−0.28
J15040305	−0.55	0.07	88	−0.58	0.19	8	−0.22
J192058957	−0.72	0.04	92	−0.76	0.20	12	−0.15

5.4.1 *Elemental abundances*

In Tables 5.4, 5.5 and 5.6, we present our measured abundance ratios. We also list the number of lines used for each individual element, as well as the uncertainties. The uncertainties represent the full uncertainty, taking into account the line-to-line scatter, as well as the effect of the stellar parameters. The only exception being [C/Fe], which we only consider an upper limit. All abundances are measured relative to the Asplund et al. (2009) Solar abundances, with the exception of Al, where we use a value of $\log_{\epsilon,\odot} = 6.43$ dex, from the NLTE analysis of Andrievsky et al. (2008), to be consistent. However, this is only marginally different from the abundance in the Asplund composition ($\log_{\epsilon,\odot,\mathrm{Asp}} = 6.45$ dex). For the ionized species, we measure the [X/Fe] value with respect to Fe II, whereas the remaining abundance ratios are computed with respect to Fe I. For the two GC stars, we also have NLTE measurements of Ba, which was not possible for the disk stars, due to their high metallicity, as discussed earlier. These results are presented in Table. 5.7.

It is clear from the tables, that the uncertainties on the single, ionized element, Ti II, is large. This is, in part, a consequence of our Fe II abundances having large uncertainties, as is evident from Table. 5.4. This is due to Fe II being very sensitive to changes in the stellar parameters, a behaviour that was also seen for the giants in 47 Tucanae in Chapter 3. Furthermore, the renormalization of the metal-rich stars, due to the changing appearance of the TiO bands also contributes to the total uncertainty budget.

Table 5.5: As Table. 5.4 but for [O/Fe], [Na/Fe] and [Mg/Fe]. [Al/Fe] has been derived using NLTE.

ID	[O/Fe]	σ	N	[Na/Fe]	σ	N	[Mg/Fe]	σ	N
I-264	–	–	–	0.60	0.11	2	0.22	0.06	3
IV-203	0.13	0.06	2	0.47	0.10	2	0.36	0.09	3
I-322	−0.20	0.07	2	0.21	0.18	2	0.17	0.06	3
J05115688	−0.11	0.07	2	0.21	0.13	2	0.09	0.05	3
J142728406	−0.04	0.15	1	−0.13	0.33	2	0.30	0.09	2
J14574719	−0.10	0.17	1	−0.24	0.36	2	0.11	0.10	3
J15040305	–	–	–	0.19	0.15	2	0.34	0.05	2
J192058957	0.33	–	1	0.14	0.13	2	0.36	0.06	3

Table 5.6: As Table. 5.4 but for [Al/Fe], [Ti/Fe] and [Ni/Fe].

ID	[Al/Fe]	σ	N	[Ti II/Fe]	σ	N	[Ni/Fe]	σ	N
I-264	0.61	0.07	3	0.52	0.12	3	−0.22	0.05	17
IV-203	0.49	0.10	2	0.41	0.17	3	−0.14	0.05	18
I-322	−0.09	0.15	3	0.15	0.13	3	−0.12	0.06	10
J05115688	−0.33	0.10	3	0.03	0.26	4	−0.10	0.05	22
J142728406	−0.43	0.22	3	0.14	0.25	3	−0.01	0.04	20
J14574719	−0.34	0.30	3	0.40	0.21	3	−0.03	0.05	20
J15040305	0.09	0.17	3	0.34	0.22	4	−0.02	0.04	19
J192058957	−0.06	0.13	2	0.34	0.20	4	−0.08	0.04	18

ID	[Ba/Fe]	σ	N
I-264	0.71	0.18	2
IV-203	0.38	0.15	3

Table 5.7: $[Ba/Fe]_{NLTE}$ measurements for the two GC stars. Measured relative to Fe II.

5.4.2 *Magnesium isotopes*

In Table 5.8 we present the individual best-fitting Mg isotopic fractions, given as percentage [^{24}Mg:^{25}Mg:^{26}Mg]. Further we give the mean value, computed from the weighted mean of the isotopic ratios, as well as the total uncertainty computed by standard error propagation through Eqns. 5.1 and 5.2. We note here, that because of this, the uncertainties on the individual fractions will be correlated. This is a consequence of the constraint that the fractions must add to one.

As is evident from the table, there is a substantial feature-to-feature scatter, as was also found for the results from the 47 Tucanae giants presented in Chapter 4. We attribute this large scatter to the presence of unknown blends in the regions of the MgH features used here. The 5135 Å feature was discarded for star J192058957 due to strong atmospheric emission being present.

5.5 DISCUSSION

In Figs. 5.9 and 5.10 we present the abundance ratios of the full sample of stars. Red symbols are used for stars in the bulge, with the two circled points at low metallicity being the two stars belonging to the globular cluster NGC 6522. The disk stars are shown with black triangles. For comparison, we have overplotted abundance measurements of several large-scale compilations of stellar abundances in the Milky Way disk (Venn et al. 2004; Bensby et al. 2014; Hinkel et al. 2014).

The abundance trends for NGC 6522 and the disk/bulge will be discussed separately below.

5.5.1 *NGC 6522*

The GC NGC 6522 is a relativel massive cluster with a mass of $\sim 3 \times 10^5\,M_\odot$ (Boyles et al. 2011), and has only been the subject of a few, dedicated spectroscopic abundance studies (Barbuy et al. 2009; Ness et al. 2014; Barbuy et al. 2014). Here, certain chemical peculiarities was initially claimed by Barbuy et al. (2009), most notably a strong overabundance of the neutron capture elements from the s-process. This was interpreted by Chiappini et al. (2011) as a signature of Population III spin-stars having contributed to the enrichment of cluster, suggesting that clusters belonging to the bulge have had a different chemical evolution than GCs in the MW halo.

This finding was later disputed by Ness et al. (2014), who did not see any signatures of strong s-process variation. The re-analysis of this cluster by Barbuy et al. (2014), did not confirm the s-process over-abundances

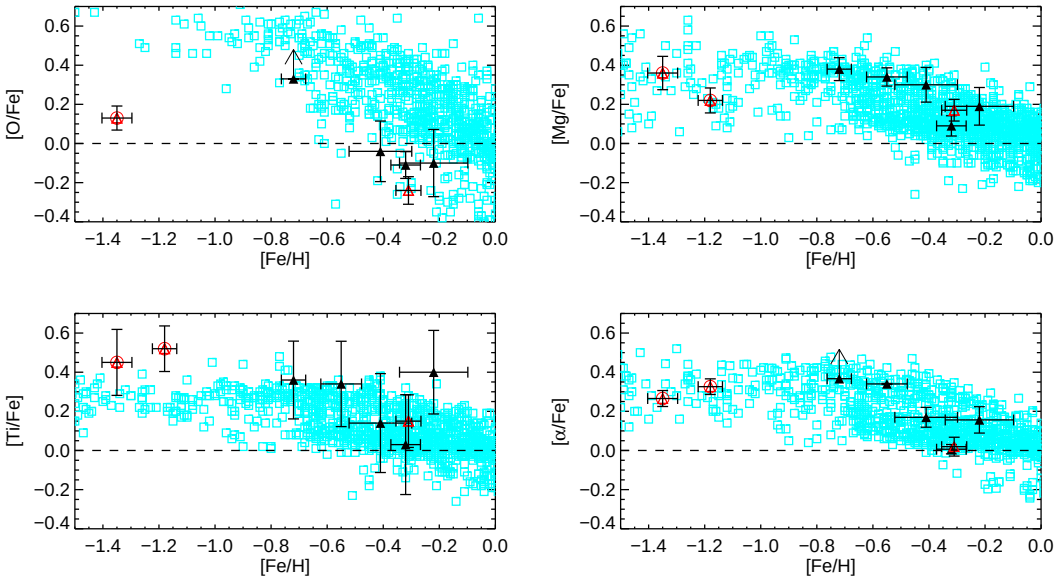

Figure 5.9: Abundance ratios [O/Fe], [Mg/Fe], [Ti/Fe] and [α/Fe] vs. [Fe/H]. Filled black symbols: disk targets, open, red triangles: bulge field star, red circles: NGC 6522 stars. The disk star with an arrow only has a lower limit on the oxygen abundance. The dashed line shows the solar value. Shown is also abundance measurements from Venn et al. (2004); Bensby et al. (2014) and Hinkel et al. (2014) for comparison purposes.

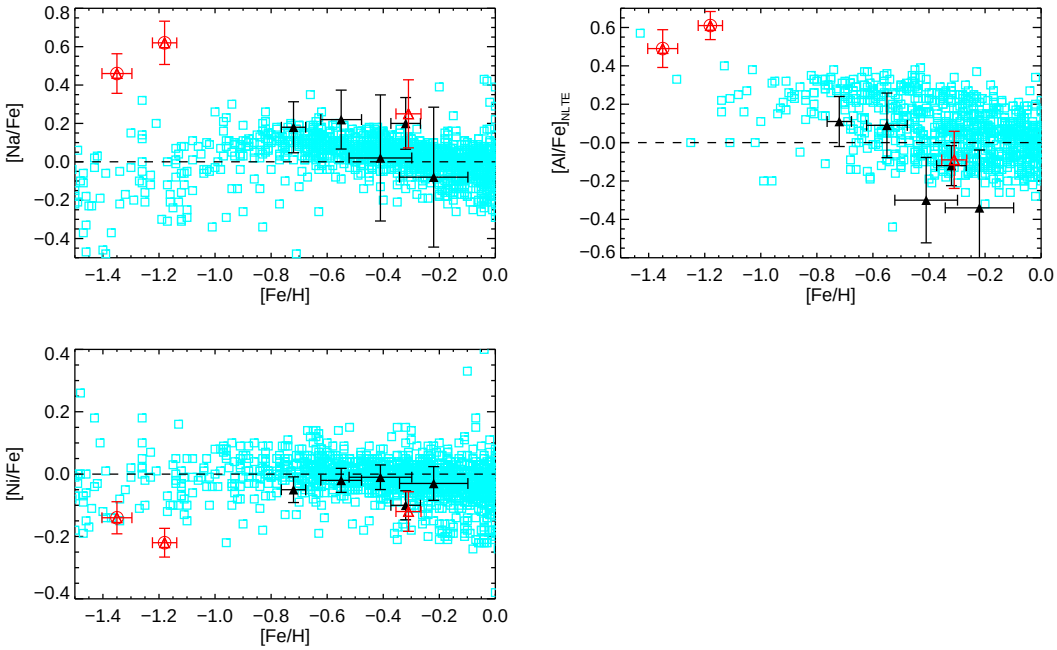

Figure 5.10: [Na/Fe], [Al/Fe], and [Ni/Fe] vs. [Fe/H]. Symbols have the same meaning as in Fig. 5.9. Note the different scaling of the abscissas.

Table 5.8: Individual Mg isotopic fractions, weighted mean and total uncertainty given as percentage ^{24}Mg:^{25}Mg:^{26}Mg.

ID	5134.2 Å	5135.5 Å	5138.0 Å	5140.2 Å	Mean	σ
I-264	63.0 : 5.7 : 31.3	67.5 : 16.2 : 16.3	79.1 : 2.2 : 18.7	65.8 : 6.2 : 28.0	70.5 : 6.4 : 23.1	3.5 : 3.0 : 3.6
IV-203	79.0 : 2.9 : 18.1	84.5 : 3.8 : 11.7	85.3 : 6.9 : 7.8	84.6 : 4.8 : 10.6	83.6 : 4.3 : 12.1	1.5 : 1.0 : 2.2
I-322	77.9 : 9.5 : 12.6	63.8 : 23.0 : 13.24	84.0 : 2.9 : 13.1	84.3 : 2.7 : 13.0	80.7 : 6.2 : 13.1	6.2 : 4.8 : 2.8
J05115688	81.8 : 7.6 : 10.6	72.4 : 16.3 : 11.3	89.5 : 7.1 : 3.4	84.0 : 16.0 : 0.0	83.0 : 10.6 : 6.4	3.8 : 2.7 : 3.3
J142728406	93.9 : 6.1 : 0.0	85.3 : 7.2 : 7.5	90.7 : 6.8 : 2.5	91.4 : 3.4 : 5.2	90.6 : 5.5 : 3.9	2.3 : 2.1 : 3.4
J14574719	92.1 : 2.2 : 5.7	86.2 : 6.5 : 7.3	93.6 : 3.4 : 3.0	84.8 : 7.0 : 8.2	90.5 : 3.8 : 5.8	2.5 : 1.4 : 2.2
J15040305	86.5 : 6.8 : 6.7	79.6 : 11.9 : 8.5	91.0 : 4.7 : 4.3	75.4 : 19.2 : 5.4	84.9 : 8.9 : 6.2	3.4 : 3.6 : 3.0
J192058957	80.3 : 11.3 : 8.4	–	86.4 : 9.3 : 4.3	82.8 : 7.0 : 10.2	83.2 : 9.5 : 7.3	2.2 : 1.4 : 2.6

originally reported. Thus, the cluster does not appear significantly different from the halo GC population, in terms of chemistry. In addition, it is unclear if NGC 6522 is a bulge GC proper. Terndrup et al. (1998) presented proper motion measurements, arguing that this cluster is confined to the bulge, consistent with the recent analysis of Rossi et al. (2015). However, Dinescu et al. (2003) also derived the proper motion and space velocitiy of NGC 6522, clearly putting it on a halo orbit. Thus it is at the present not clear whether NGC 6522 is *of* the bulge, or merely *in* the bulge. If it is indeed just passing through the bulge but is on a halo orbit, then any chemical peculiarities are not due to its current position in the bulge.

From the spectra, we found a mean radial velocity of $-15.6 \pm 0.1\,\mathrm{km\,s^{-1}}$, which is in good agreement with Ness et al. (2014), who found $-13.4 \pm 4.9\,\mathrm{km\,s^{-1}}$, and Harris (1996), with $-15.0 \pm 3.3\,\mathrm{km\,s^{-1}}$, as well as the re-analysis by Barbuy et al. (2014), who reported $-14.3 \pm 0.5\,\mathrm{km\,s^{-1}}$.

We find a mean $[\mathrm{Fe/H}] = -1.27 \pm 0.12$ dex for NGC 6522, which is consistent with the results of Ness et al. (2014), who found $[\mathrm{Fe/H}] = -1.15 \pm 0.16$ dex, whereas Barbuy et al. (2009) and Barbuy et al. (2014) found somewhat higher values of $[\mathrm{Fe/H}] = -1.00 \pm 0.20$ and $[\mathrm{Fe/H}] = -0.95 \pm 0.15$ dex, respectively.

Judging from the Fe I measurements, the two GC stars appear to have a different metallicity, which is surprising, considering that they belong to the same cluster, so one would not expect an iron spread. Variations in [Fe/H] within a GC have only been reported in a few cases, like ω Centauri (Norris & Da Costa 1995; Smith et al. 2000; Johnson et al. 2008), M54 (Carretta et al. 2010) and M22 (Marino et al. 2009; Da Costa et al. 2009), although the latter finding was recently disputed by Mucciarelli et al. (2015). Common for all these clusters is that they belong to the most massive GCs in the MW. On the other hand, Ness et al. (2014) reported values of [Fe/H] ranging from -0.95 to -1.37 dex, although the measurements from their larger sample is consistent with a single metallicity with some scatter. Based on measurements of only two stars, we cannot determine if the measured difference is real, or if we are simply sampling the tails of the metallicity distribution. Furthermore, the iron abundances in the two stars do agree within the uncertainties, if we consider our Fe II measurements. We note that Fo6 also found these two stars to have different [Fe/H], namely -1.10 and -1.25 dex for I-264 and IV-203, respectively, whereas Alves-Brito et al. (2010) found essentially identical [Fe/H] values for these two stars. These differences may also be related to different stellar parameters, as discussed earlier, as well as different adopted $\log(gf)$ values.

Inspecting the light element abundances of the two GC stars in Figs. 5.9 and 5.10, it is evident that both stars show the chemical peculiarities

seen in the polluted stellar populations of other GCs. They are strongly enhanced in Na and Al, well above the typical values for field stars at the same metallicity. IV-203 is also significantly depleted in oxygen, consistent with the interpretation that these stars were born from pre-enriched material within the cluster. Unfortunately we were unable to measure oxygen in I-264, but considering the peculiarities in the other light elements, it would be expected to be depleted in oxygen. This was indeed found by Fulbright et al. (2007) and Alves-Brito et al. (2010). The same holds for the other light elements. We find that these two stars are less enhanced in [Na,Mg,Al/Fe] relative to the comparison works. We expect this to be due to a combination of different stellar parameters, as well as our inclusion of TiO bands in the synthesis of these lines. By performing a full spectral synthesis, we account more accurately for line blends than when relying on EW measurements. We note in passing that it is not surprising that the differences are in the same direction for both comparison works, since Alves-Brito et al. (2010) adopted the EW measurements of Fulbright et al. (2006) for their analysis.

Both stars appear enhanced in [Ba/Fe] (Table 5.7), I-264 more strongly so, than IV-203. The previous studies of NGC 6522 also found variations in [Ba/Fe], ranging from $0.22 < [\mathrm{Ba/Fe}] < 0.55$ (Barbuy et al. 2014) to $0.10 < [\mathrm{Ba/Fe}] < 0.80$ (Ness et al. 2014), consistent with the range we found here. So there may indeed be a intrinsic variation in barium in this cluster, although we note that our measurement uncertainties are quite large for this abundance ratio. Although not a common feature, spreads in Ba have been seen in several MW GCs, e. g. M4 and M5, (Ivans et al. 2001), M15, (Sobeck et al. 2011), M2, (Lardo et al. 2013) and M22, (Brown & Wallerstein 1992b; Marino et al. 2009), although we note that some of these clusters also exhibit a spread in iron, pointing to a more complicated formation history.

Turning our attention to the Mg isotopic measurements of these two stars presented in Fig. 5.11, there is a notable difference between the two stars, with I-264 being strongly enhanced in the heavy Mg isotopes, whereas IV-203 is more moderately enhanced. This is also consistent with I-264 being more enhanced in aluminum, and somewhat depleted in Mg, as would be expected if the Mg-Al burning chain is responsible for the isotopic variation observed in GCs, as discussed in Chapter 4. This finding is also consistent with what is seen in other GCs with Mg isotope measurements, where a significant enhancement of the heavy Mg isotopes is only observed when high values of aluminum enrichment are reached around $[\mathrm{Al/Fe}] > 0.5$ dex (Yong et al. 2003a, 2006; Da Costa et al. 2013). It would be interesting to obtain observations also of stars belonging to the pristine population in this cluster, to see whether they also show values above what is predicted from supernova yields at these metallicities. This has been seen in NGC 6752 (Yong et al. 2003a),

M13 (Yong et al. 2006) and ω Centauri (Da Costa et al. 2009), suggesting that even the first generation of GC stars have seen chemical enrichment that is different from what is observed in field stars at the same metallicity. Considering that NGC 6522 has been proposed to be one of the oldest GCs in the MW, such an investigation would be particularly important, as a positive detection would imply a non-supernovae source of enrichment being present even at very early times.

5.5.2 *Field stars*

Turning our attention to the field stars, it is clear that the $\alpha-$elements show very similar behaviour to what is observed in the Solar neighborhood and the MW disk (Fig. 5.9). In particular, they all follow the decline in $[\alpha/\mathrm{Fe}]$, from a value of ~ 0.4 dex at a metallicity of approximately $[\mathrm{Fe/H}] = -0.8$ dex, approaching the Solar value when the metallicity increases, fully consistent with what is seen in the large spectroscopic surveys. This is in agreement with the findings of Bensby et al. (2010), although we find lower values for both [Mg/Fe] and [Ti/Fe] than their work. We expect this to be due to differences between spectral synthesis and EW measurements, as was the case for the bulge stars. We also note that Bensby et al. (2010) relied on Ti I lines for their [Ti/Fe] values, which are susceptible to strong NLTE effects, which is not the case for the Ti II lines we use for our titanium measurements (Bergemann 2011).

The bulge star, I-322, appears to have a very low oxygen abundance, also significantly lower than what is reported by Bensby et al. (2010), which we attribute to the culmulative effect of different stellar parameters and our use of spectral synthesis, compared to using EW measurements in the comparison study. The lower gravity we find will also tend to lower the abundance compared to the work of Bensby et al. (2010). It is certainly in the low part of the measured oxygen abundances, but not unreasonably so. The remaining α-elements in I-322 are indistinguishable from our sample of disk stars at the same metallicity. We specifically point out that I-322 does not show the rather strong enhancement in Mg, which has previously been used as an argument for a different chemical history of the bulge and the MW disk (Fulbright et al. 2007). However, it is worth noting that all our disk stars appear to be on the high end of the [Mg/Fe] distribution in the disk, which could suggest a slightly more efficient star formation in the inner disk.

Also the proton capture elements, Na and Al, look very similar in the bulge star and in the stars from the inner disk, with sodium having approximately Solar values for all field stars. The Al abundances, on the other hand, are rather low, in particular for the two disk stars, J142728406 and J14574719. As discussed in Sect. 5.3.1.1, the NLTE corrections are negative, and will thus decrease the [Al/Fe] ratios with respect

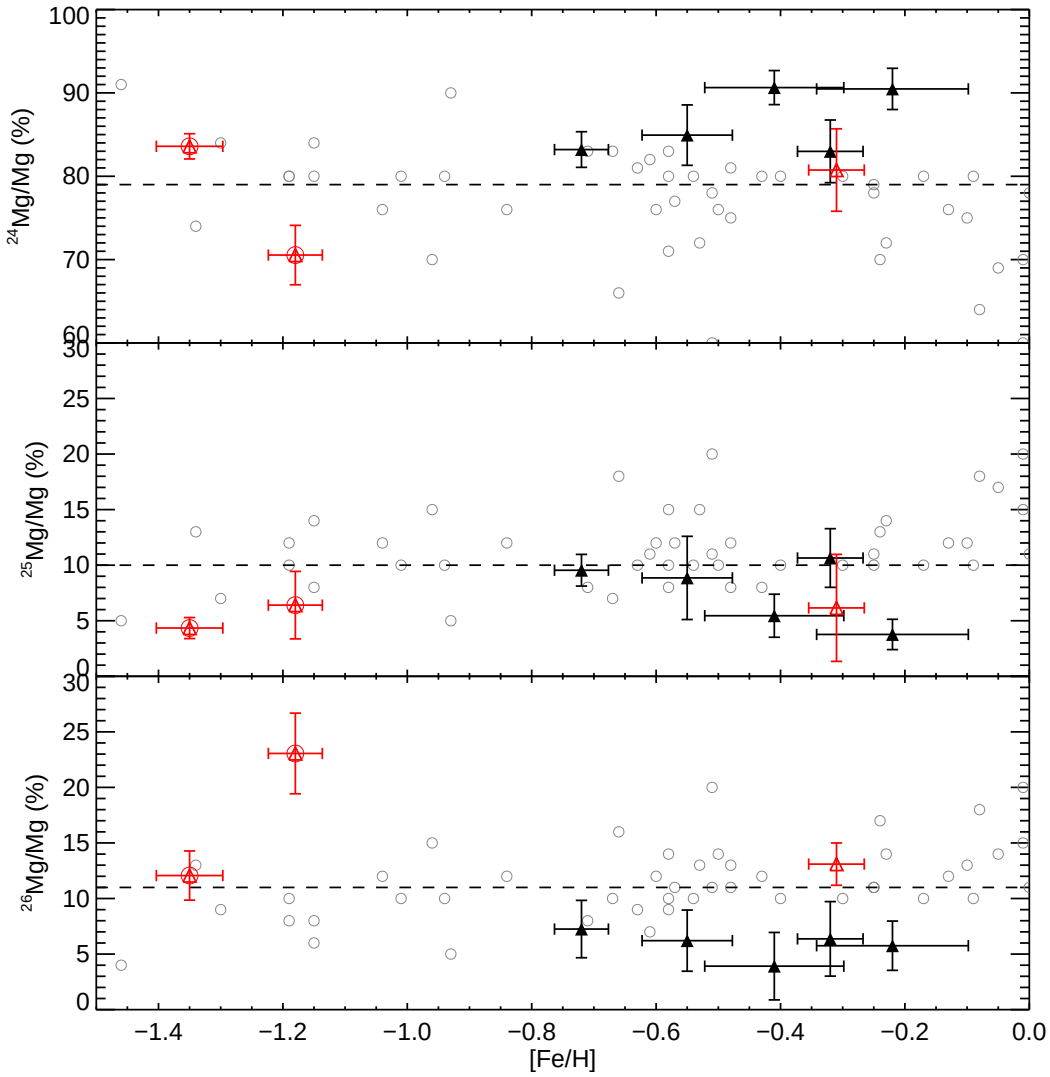

Figure 5.11: Mg isotopic ratios for our sample of stars. Symbols have the same meaning as in Fig 5.9. The dashed line indicate the solar isotopic fractions. Open, grey circles show the results from Yong et al. (2003b)

to the comparison sample. In addition, these two stars are the ones most strongly affected by molecular blends of TiO, further decreasing the derived abundance. Because the TiO bands are highly sensitive to temperature, an increase of only 100 K will significantly decrease the TiO band influence, which would result in a higher abundance of Al if we have a slight offset of our $T_{\rm eff}$ scale. The strong temperature sensitivity of TiO is also reflected in the large uncertainties on these measurements.

When looking at the total [α/Fe], it would appear that the two lowest metallicity disk stars are members of the Galactic thick disk, with relatively high α-enhancement, whereas I-322 and J05115688 have abundance patterns consistent with thin disk membership. The two remaining stars cannot reliably be assigned to either of the disks, since their α-

abundances fall more or less in-between, and there exists a significant overlap in [α/Fe] between these two MW components.

There is some evidence that the bulge may have had a more efficient star formation than the current disk (Bensby et al. 2013). In particular, their stars seem to have a higher [Mg/Fe] ratio compared to the local sample, with the knee in the [α/Fe] ratios appearing at slightly higher metallicity. On the other hand, the only detailed abundance study of giants in the inner disk (Bensby et al. 2010), shows that the α-elements in this part of the MW looks strikingly similar to the solar neighborhood. Thus, it is not obvious that the inner part of the disk should have had a more efficient star formation than our immediate surrounding, although the slightly elevated [Mg/Fe] found by (Bensby et al. 2013) may indicate this. However, their sample is too small to firmly establish this.

Looking now at our measured isotopic distribution of magnesium for the field sample (Fig. 5.11), they all appear to be less enhanced in ^{26}Mg isotopes than the Sun, whereas I-322 has a higher isotopic fraction of ^{26}Mg, relative to the rest of the field stars. Although the fraction of heavy isotopes is expected to decrease with decreasing metallicity, any significant decrease below Solar is only seen around [Fe/H] ≈ -1.0 (Yong et al. 2003b). It would thus appear that the high-metallicity stars in the inner part of the disk are less enhanced in ^{26}Mg, relative to the Solar neighborhood.

5.5.3 *Comparison with previous work*

The most comprehensive investigation of Mg isotopes in the disks is the study by Yong et al. 2003b (hereafter Y03), which we choose as the comparison work. Inspecting again Fig. 5.11, there does appear to be a small offset between our measurements and those of Y03. The reason for this discrepancy may be due to differences in the line lists used, where we use an updated list, compared to the Y03 study. To investigate this, we re-analyzed three stars from the Y03 sample (HIP36827, LP734-54, G 70-35), plus the sub-giant HIP34608, for which we also have preliminary measurements of the isotopic fractions (Yong, priv. comm. 2015). The stars were selected to have a similar metallicity to the field stars in this work, although none of them are giants. We use the same method for analysis as in the original study, also adopting their stellar parameters. For HIP34608 we adopt the parameters from Ramírez et al. (2013). The only difference is that we use our updated line list. We use the C_2 feature at 5136 Å to inform us about the upper limit on the carbon abundance, which was not provided by Y03. This feature is much more prominent in dwarfs than in giants, which is why this feature was discarded in the analysis of our original sample, whereas it was of use in the comparison stars.

Table 5.9: Comparison between the Mg isotopic fractions from our analysis of three dwarfs from Yong et al. (2003b), and the original values. Included are also preliminary results for HIP34608 (Yong, priv. comm. 2015). The resolution of the observations, R, is given in the last row.

	HIP36827	LP734-54	G 70-35	HIP34608
$T_{\rm eff}$	5000	4800	5000	4970
$\log g$	4.50	4.50	4.50	3.42
ξ_t	1.10	0.40	0.60	1.09
[Fe/H]	−0.25	−0.66	−0.67	−0.43
$[^{24}$Mg:^{25}Mg:^{26}Mg $]_{\rm own,all}$	78.8 : 13.2 : 08	72.5 : 16.5 : 11	83.8 : 9.5 : 6.7	80.8 : 11.2 : 8.0
$[^{24}$Mg:^{25}Mg:^{26}Mg $]_{\rm own}$	82 : 9.3 : 8.7	74 : 15.7 : 10.3	86 : 07 : 07	86.7 : 5.3 : 8.0
$[^{24}$Mg:^{25}Mg:^{26}Mg $]_{\rm Y03}$	79 : 10 : 11	66 : 18 : 16	83 : 07 : 10	81.6 : 8.7 : 9.7
R	60 000	60 000	120 000	120 000

In Table. 5.9, we present the results of this exercise. Since we use the MgH feature at 5135 Å, which Y03 had discarded from their analysis, we present two sets of isotopic fractions from our re-analysis. $X_{\rm own,all}$, which is the isotopic fractions we derive, when using the four features also used in the giants, with the same weights applied, and $X_{\rm own}$, which is the straight average when excluding the 5135 Å feature.

It is evident that with our updated line list, we find less ^{26}Mg and more ^{24}Mg, relative to the Y03 study, in particular when using only the same three features as Y03. On average, we find differences of 5.2% for ^{24}Mg, −1.7% for ^{25}Mg, and −3.3% for ^{26}Mg, in the sense *this work minus Y03*. Using all four features, as done in the present work, gives mean differences of 1.7%, 1.6% and −3.3% for ^{24}Mg, ^{25}Mg and ^{26}Mg respectively. Thus, the observed offsets can, in part, be attributed to differences between the line list used here, and by Y03. However, we note that the results are not directly comparable, as our sample is a set of evolved giants, where the conditions in the line-forming layers of the atmosphere are significantly different than in the dwarfs we use for this comparison test. Since the isotopic ratios themselves are relatively insensitive to changes in parameters, the differences are mostly due to different behaviour of the blending species.

The comparison suggests that the differences between the local sample of Y03 and the inner disk are due to different line lists, but a real difference in the amount of heavy isotopes would be expected if the inner disk and the bulge had different evolutionary histories than the Solar neighborhood (Fenner et al. 2003). If the inner part of the disk has had a more efficient star formation history, compared to the Solar neighborhood, this could result in an observable difference in the isotopic mixture. In this case, the inner disk would have been more enriched in ^{24}Mg at early times, because the vast majority of Mg produced

by type II supernovae is this isotope (Kobayashi et al. 2011). In addition, the necessary seed for producing the heavy isotopes in core-collapse supernovae through the $^{22}\mathrm{Ne}(\alpha, n)^{25}\mathrm{Mg}$ and $^{22}\mathrm{Ne}(\alpha, \gamma)^{26}\mathrm{Mg}$ processes would be available earlier. This implies that, for a given metallicity, one would expect both the [Mg/Fe] value and the amount of heavy Mg isotopes to be higher in a region with efficient star formation, compared to a less efficient population. At the high metallicities treated here ($[\mathrm{Fe/H}] > -1.0$ dex), the main contributor to the heavy isotope budget is indeed core-collapse supernovae, so although a region with less efficient star-formation would be younger, and thus have experienced a higher AGB contribution, the supernova production would still dominate. Thus, one would expect less heavy Mg isotopes in the Solar neighborhood than in the inner disk, somewhat contrary to what is observed here, at least for the inner disk sample.

Nevertheless, it would be possible to probe differences in the star formation history, even though the bulk Mg abundance would be very similar between the disk and the bulge. However, a much larger sample of stars with isotopic measurements of Mg would be required in both the inner part of the MW disk and in the bulge itself to investigate this.

5.5.4 *Chemical evolution models*

Two different groups have provided predictions of the chemical evolution of the Mg isotopes in different parts of the MW. Fenner et al. (2003) presented a model with a prescription of star formation that is inversely proportional with the galactocentric radius. Their model allows for an investigation of the behaviour of the isotopic ratios at different metallicities and positions in the Galaxy. Their model includes yields from type I and type II SNe, as well as AGB stars, and it predicts that the inner parts of the MW should have a higher $^{26}\mathrm{Mg}/^{24}\mathrm{Mg}$ ratio than the Solar neighborhood at high metallicities. This is due to the more efficient star formation, which will provide the necessary seed for type II SNe to become important for the Mg isotopes at an earlier time. In addition, since their model predicts rapid star formation at early times in the inner Galaxy, the metal-poor stars should show lower ratios, since AGB stars have not contributed, whereas this would be different for the solar neighborhood, as well as for the outer disk. Looking at their most extreme radii, their models predict a difference in $^{26}\mathrm{Mg}/^{24}\mathrm{Mg}$ of about 0.05, between stars at galactocentric radii of 4 kpc and 16kpc, at $[\mathrm{Fe/H}] \approx -0.3$ dex. This difference is larger than the uncertainties we find for our two stars at this metallicity, and should thus be detectable. Interestingly, the two stars we have observed at this metallicity are indeed the bulge star, I-322, and the outer disk star J05115688, which show a difference larger than what is predicted by Fenner et al. (2003).

On the other hand, J05115688 does not show a behaviour that is significantly different from the remaining inner disk sample, which would be expected from the predictions, but with only two stars, no conclusions can be drawn based on this.

The more sophisticated model presented by Kobayashi et al. (2011), provides predictions for a large number of isotopes for the MW halo, thick disk, bulge, and Solar neighborhood. For each of these components, they assume a Kroupa IMF, but different models are assumed for outflow and inflow of gas in the different MW components, as well as different MDFs, inclusion of Galactic winds and different star formation rates (see Kobayashi et al. (2006) for details).

Their work include yield contributions from type II SNe, hypernovae, type Ia SNe, spin-stars and AGB stars, so all potential sources of Mg isotopes, except the supermassive stars, should be accounted for. In Fig. 5.12 we compare our results for the Mg isotopes in the inner disk and bulge, with the predictions from the model of Kobayashi et al. (2011) for the Solar neighborhood and the MW bulge. The differences between the model predicitions for the bulge and the Solar neighborhood increases when going to higher metallicity. Similar to the predictions of Fenner et al. (2003), their model also predict a higher ^{26}Mg/^{24}Mg ratio in the bulge, relative to the Solar neighborhood for [Fe/H] > -0.6. A similar behaviour is predicted for ^{25}Mg. This is indeed what we observe for our single bulge star, for both ^{26}Mg/^{24}Mg, whereas the ^{25}Mg/^{24}Mg ratio essentially looks like the Solar neighborhood, but no firm conclusions can be drawn from just a single data point. Our results for the disk show a remarkable agreement with the model for the Solar neighborhood, especially for the ^{26}Mg/^{24}Mg ratio. If our measurements are taken at face value, the model of Kobayashi et al. (2011) is underproducing heavy isotopes at low metallicities. This was already pointed out as a problem by the authors of the original study. On the other hand, it is also clear that the typical precision of our isotopic ratios is sufficiently high that we would be able to distinguish between their predictions for the bulge and the Solar neighborhood at metallicities $\gtrsim -0.4$ dex. We here note that the chemical evolution model of Kobayashi et al. (2011) is not taking any dynamical effects into account and is thus not able to address the dynamical bulge-disk connection.

With the sample investigated here, and taking into account the uncertainties, and the potential offset discussed above, we cannot claim any robust differences between the stars in the inner disk and the bulge, nor between the inner disk and the Solar neighborhood. This would require a more dedicated survey of this part of the MW with more stars in both the inner disk and, in particular, the bulge. In addition, all the results presented here, have been derived using 1D stellar atmospheric models, whereas our results from Chapter 4 indicate that 3D effects in giants

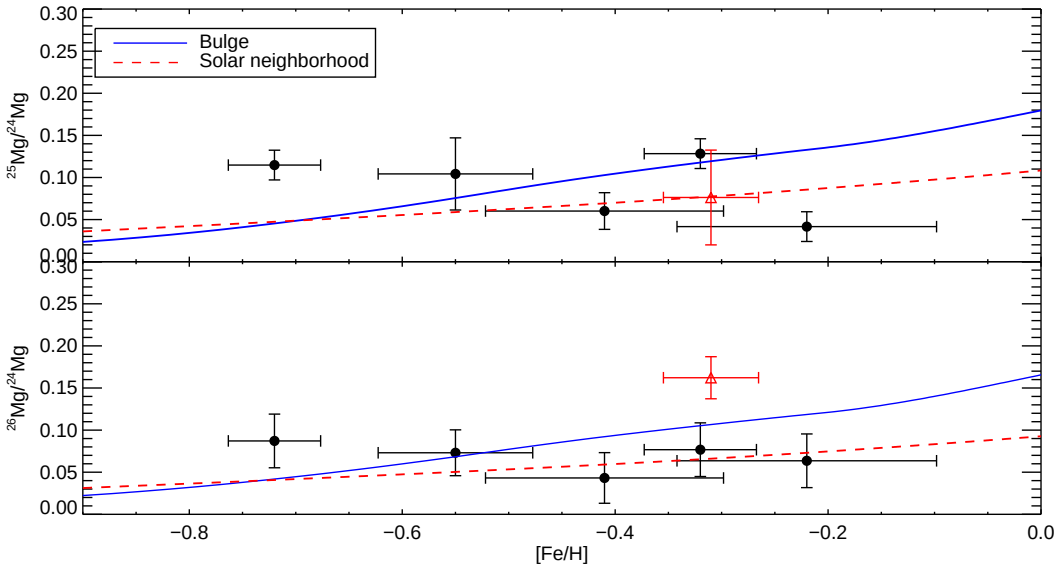

Figure 5.12: Comparison between our measured isotopic ratios and the predictions from Kobayashi et al. (2011) for the bulge (solid, blue line) and Solar neighborhood (dashed red line).

would serve to increase the fraction of ^{25}Mg, and decrease the amount of ^{24}Mg, bringing our results in closer agreement with what is seen in the local sample of Y03. An analysis of a larger sample of bulge stars would be interesting, to investigate if the star formation was indeed more efficient in this part of the MW

5.6 CONCLUSIONS

In this work we have presented measurements of a number of elements in three stars in the MW bulge as well as five stars in the inner part of the disk, from high resolution, high S/N optical spectra. Two of the bulge stars (I-264 and IV-203) are members of the GC NGC 6522. We find the abundance pattern of these two stars to be consistent with them belonging to the polluted population of stars in this cluster (enhanced in Na and Al and depleted in O, relative to field stars). Both these stars are also found to be enhanced in barium, consistent with the enhancement seen by earlier investigations of Ba in this cluster (Barbuy et al. 2009; Ness et al. 2014; Barbuy et al. 2014).

For the field stars, we find that two stars have α-element abundances consistent with the thin disk, two with thick disk membership, whereas for two stars, no population membership could be assigned. We note that the one field star in the bulge, I-322, has [α/Fe] consistent with thin disk membership.

We have performed the first ever NLTE analysis of aluminum in these stars and find that the NLTE corrections result in a lowering of the [Al/Fe] value, consistent with the results for the giants analyzed in Chapter 3. Our measurements of [Al/Fe], as well as [Na/Fe] and [Ni/Fe] are fully consistent with the results from large-scale surveys of stars in the MW disk.

Furthermore, we present the first measurement of the isotopic distribution of magnesium in the inner part of the MW disk, as well as in the MW bulge. We find that the two GC stars are enhanced in the heavy isotopes, reinforcing their status as members of the polluted population, and consistent with what has been observed in the few studies of Mg isotopes in GCs of comparable metallicity (Yong et al. 2003a, 2006).

Although the high metallicities of the field stars make the derivation of the Mg isotopes challenging, we were able to derive isotopic fractions with typical uncertainties of about 3%. We found no significant differences between the distribution of the isotopes in the inner disk stars and our single bulge star, although the latter does show an indication of a higher fraction of ^{26}Mg, relative to the disk stars. However, with only a single data point it would be premature to conclude that a real difference exists between the inner disk and the bulge.

The models of Fenner et al. (2003) and Kobayashi et al. (2011) suggest a higher fraction of heavy Mg isotopes in the bulge at high metallicity, relative to the thick disk and the Solar neighborhood, consistent with the measurement of ^{26}Mg/^{24}Mg in our single, high-metallicity bulge star. We find good agreement between our measurements and the predictions for the Solar neighborhood for our disk stars, although our results suggest that the models are underproducing heavy Mg isotopes at metallicities below [Fe/H] $= -0.8$ dex. Unfortunately, their models do not include the dynamical evolution of the MW. They are thus unable to address the effects that disk instabilities may have had on the present-day chemical composition of the bulge.

For the sample of stars in the inner disk, we find slightly lower abundances of the heavy Mg isotopes compared to the Solar neighborhood study of Yong et al. (2003b). This can largely be explained by different choices of line lists, in particular blending lines, and when taking this into account, we see no differences in the isotopic ratios between the inner disk and the local sample from the study of Yong et al. (2003b).

The results presented here, provide new constraints for the chemical evolution models concerned with the inner part of the Milky Way. In particular, the Mg isotopic ratios have the potential of investigating differences in the star formation timescale and chemical evolution, *even when the bulk Mg abundances are identical*. We have shown that it is possible, albeit challenging, to obtain Mg isotopic ratios with an accuracy that will allow to distinguish between currently available models. Al-

though these results are encouraging, a larger sample of stars with measurements of Mg isotopic fractions is required to make firm conclusions about any differences, or similarities, between stars in the inner disk and the bulge.

6 SUMMARY AND FUTURE PROSPECTS

"Congratulations. I am delighted that you could make it. Getting here wasn't easy, I know. In fact, I suspect it was a little tougher than you realize."

— Bill Bryson, A Short History of Nearly Everything, 2003

6.1 SUMMARY

The work presented in this thesis has been concerned with the chemical composition and Mg isotopic mixture in a number of different stellar populations; the metal-rich, massive globular cluster 47 Tucanae, and stars in the inner part of the Milky Way disk and in the bulge. In all cases, the goal has been to use the isotopic distribution together with elemental abundances to gain additional information about the chemical evolution history of these populations.

In the case of 47 Tucanae, we first performed a comprehensive elemental abundance analysis of our sample of 13 giant stars, presented in Chapter 3. We derived abundances of 27 elements, which, to the best of our knowledge, is the most comprehensive study to date of this cluster. Based on the abundance ratio [Na/Fe], we separated our sample in pristine stars and polluted stars, with seven and six stars in the two samples, respectively.

We performed the first ever NLTE analysis of aluminum in this cluster, which resulted in a reduction of the measured spread of [Al/Fe] by a factor of two, consistent with a constant value within the uncertainties. However, we stress that the apparent lack of spread is attributed to our samll sample size, since other authors have found significantly different [Al/Fe] values for stars with identical parameters. We also do not see any indication of an anti-correlation between Mg and Al, nor a correlation between Na and Al, as has previously been reported by Carretta et al. (2013). Cordero et al. (2014), on the other hand, did also not find any correlation between Na and Al, but merely a variation in Al for a given Na abundance, consistent with our results. In addition, an overall shift of the abundances to slightly lower values was found. Since variations in [Al/Fe] are observed in many clusters (often correlated with Na, and anti-correlated with Mg), this has been used as a strong constraint on the mass range of the earlier generation of stars, thought to be responsible for the observed spread in light elements. However, since most of these studies rely on traditional LTE analyses based on small

samples of bright stars, neglecting NLTE effects may result in systematic effects on the spread of aluminum, with consequences for the proposed models for light element variations.

In Chapter 4 we expand on the results from Chapter 3 and derive the isotopic mixture of Mg in the same sample of stars. This represents the first investigation of Mg isotopes in 47 Tucanae, and only the second globular cluster at this metallicity with measurements of these isotopes, the other being M71. 47 Tucanae is significantly more massive than M71, so its chemical evolution history could well be different, even though they have the same metallicity. With these measurements, we add a new data point to the sparse sample of GCs with Mg isotopic measurements (only measured in four other GCs). In clusters with a larger range of aluminum abundances than 47 Tucanae, the amount of ^{26}Mg is found to be correlated with the aluminum abundance, in particular visible for $[\mathrm{Al/Fe}] \gtrsim 0.5$. This suggests that the process responsible for the Al variations is linked to the production of the heavy Mg isotopes, likely through the Mg-Al burning chain. We see no indication of such a correlation in our sample, which is not surprising, since we do not see strong Al variations either. On the other hand, we do find a larger spread of the heavy isotopes in the polluted sample of stars, compared to the pristine sample. This could indicate a mild activation of the Mg-Al burning chain, but with too little Mg being converted to result in an anti-correlation between the two elements.

In addition, we presented the *first ever* investigation of the effects of using 3D hydrodynamical atmospheric models (whose characteristics are outlined in Chapter 2) in the derivation of Mg isotopes. This is important, since convection is known to cause asymmetries in spectral lines. This effect is not accounted for in 1D models, and therefore, systematic offsets in the isotopic ratios may arise because of this inadequate modeling of the stellar atmospheres. Due to issues with blending lines of C_2, which we suspect to have erroneous $\log(gf)$ values, we were only able to investigate 3D effects for two of the four MgH features that were used in 1D. We computed two 3D models, with parameters matching the least evolved giants in our sample, using the CO^{5}BOLD code, and computed a full 3D radiative transfer through this model atmospheres. Due to the limitations of the 3D hydrodynamical code, as well as the radiative transfer code, we were not able to compute models matching the parameters of our full sample of stars. The synthesis based on 3D radiative transfer provided a significantly improved fit to the asymmetries of the MgH features, compared to 1D. In addition, we found that the fraction of ^{25}Mg increased by up to a factor of 2.5, relative to the 1D results, whereas the fraction of ^{26}Mg stayed essentially unchanged. This increase in ^{25}Mg resulted in an improved agreement with the predicted yields from AGB models, where stark disagreement between the obser-

vations and model predictions have been observed in the past. However, although the agreement improved, the AGB models still predict a significant difference between the pristine and the polluted stars, which the 3D corrections would not alleviate.

In Chapter 5 we turned our attention to giant stars in the inner part of the MW disk and the bulge. The structure and formation of the MW bulge is currently a hotly debated topic. A large part of the discussion is focused on the extent to which the bulge is a result of a classical hierarchical collapse of smaller parts at a very early time (classical bulge), or a consequence of dynamical instabilities in the inner part of the disk (pseudo-bulge). Whereas there is accumulating evidence that the classical bulge is only a minor part of the overall bulge structure, it has also become clear that the bulge is a very complex component of the MW, with several stellar populations. By comparing elemental abundance patterns in the MW disk and bulge, it is possible to compare their chemical evolution history, and there is increasing evidence that a large fraction of the bulge stars share chemical properties with stars in the MW disk. To provide further clues to the connection between the disk and the bulge, we analyzed three giants in the bulge, and five giants in the inner disk, which were all selected from the literature. Two of the bulge stars were members of the GC NGC 6522, believed to be one of the oldest GCs in the MW. Our observations are of the highest quality in terms of combined S/N and resolution obtained for stars in this region of the MW.

We derived abundances for several elements in the entire sample of stars, and found that the light element abundances in the GC stars were consistent with them being members of the polluted population. This was further confirmed by the measurements of Mg isotopes, where both stars showed enhancement above what would be expected for field stars at the metallicity of the cluster. No previous measurements of Mg isotopes exist for this cluster. In addition, the star with the highest [Al/Fe] ratio was found to be most strongly enhanced in ^{26}Mg, consistent with other GCs at comparable metallicities. Further, we found the GC stars to be enhanced in barium.

For the field stars, which were all at higher metallicity than the cluster stars, the α-element abundances showed no differences from stars in the Solar neighborhood, but we note that two of the disk stars have abundances consistent with thick disk membership, whereas the bulge field star, together with an additional disk star, have abundances consistent with being members of the thin disk. For the remaining two disk stars, no clear membership could be assigned.

We successfully measured the Mg isotopic distribution in our full sample of field stars, which has never been done for any stars in this part of the Galaxy. We are able to get typical uncertainties of 3% on

the isotopic fractions. This level of precision is enough to distinguish between the model predictions of Kobayashi et al. (2011) for the Solar neighborhood and the bulge, although a larger sample of both bulge and inner disk stars should be analyzed before firm claims on the similarity, or difference, of the two populations can be claimed.

For the sample presented here, we do not detect any significant difference between the Solar neighborhood sample of Yong et al. (2003b) and what is seen in the inner part of the disk, when correcting for an offset due to different line lists between ours and the comparison study. This does not suggest a more efficient star formation in the inner disk, as this would have resulted in higher fractions of the heavy isotopes. Our single, high-metallicity bulge star has a higher $^{26}Mg/^{24}Mg$ ratio than the inner disk sample, suggesting that this star may have formed in a region with more efficient star formation than the inner disk sample, although the measurement would stay consistent with the local sample, even after the correction for different line lists. However, it would be premature to conclude that differences between the bulge and the inner disk exist, based on only a single data-point. But we have demonstrated that such a study would be feasible and that, even for metal-rich stars, we can reach a level of precision high enough for such comparisons to be meaningful.

6.2 FUTURE PROSPECTS

Although the results presented in this thesis have added new elements to the chemical inventory of three stellar populations in the MW, there is still much to learn about the overall chemical evolution of the MW. As already illustrated, accurate measurements of magnesium isotopes can help address this, as well as details in models of nucleosynthesis. Three possible uses of Mg isotopes come to mind, which I will outline below.

6.2.1 *Magnesium isotopes in halo sub-dwarfs*

The assembly of the MW halo is still a matter of active research and the determination of its formation timescale represents a key observation. This can be investigated from the abundance patterns of low-metallicity stars ($[Fe/H] \leq -1.0$), by which the fast enrichment from type II supernovae (SN II) can be disentangled from the slower enrichment from AGB stars (a few Myr vs. > 30 Myr). An unambiguous detection of the metallicity where AGB star enrichment appears will thus put stringent limits on the halo formation timescale.

Accurate measurements of magnesium isotopic ratios can be used as an indicator of the time of the onset of AGB enrichment in the Halo.

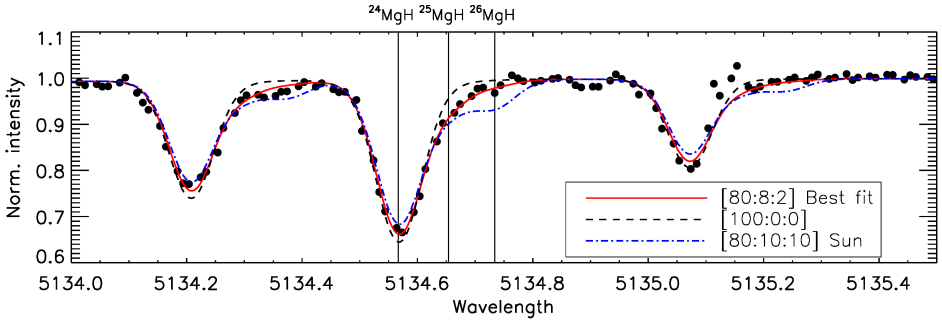

Figure 6.1: 1D synthesis of the MgH band of the Galactic halo star NLTT51106 ([Fe/H] $= -1.9$ dex) from our already obtained data. Shown is the best-fitting synthesis, as well as a pure ^{24}MgH and a solar mixture. Magnesium isotopic fractions are given as percentages [^{24}Mg:^{25}Mg:^{26}Mg]. Small variations in the heavy isotopes can easily be detected.

Previous estimates of the onset of AGB enrichment were based on ratios of s-process to r-process elements, such as Barium-to-Europium and Lanthanum-to-Europium ratios (e.g., Simmerer et al. 2004). Roederer et al. (2011) show that the rise in Lanthanum-to-Europium ratios with increasing metallicity is not accompanied by the expected rise in Lead-to-Europium ratios, thereby challenging prior interpretations of the halo chemical evolution. In the metal-poor regime, below [Fe/H] $= -1.0$, lead measurements are exceptionally difficult and often only upper limits are obtained.

Whereas the measurement of Mg isotopes become challenging in giants at low metallicity, they can still be readily measured in dwarf stars, even below [Fe/H] $= -1.5$ (Fig. 6.1). An increase in the ^{25}Mg/^{24}Mg and ^{26}Mg/^{24}Mg ratios at a very low metallicity would be a clear sign of AGB enrichment. This would constitute a more sensitive and less ambiguous measure of AGB enrichment than the elemental abundance ratios discussed above. Such an investigation will complement existing large scale spectroscopic surveys, which do not provide the required spectral quality to determine the abundances of magnesium isotopes.

Previous investigations of magnesium isotopic ratios in nearby field stars spanning a range in metallicities (Barbuy et al. 1987; Gay & Lambert 2000; Yong et al. 2003b; Meléndez & Cohen 2007) show a sharp increase in the ^{25}Mg/^{24}Mg and ^{26}Mg/^{24}Mg ratios at a metallicity of around [Fe/H]$= -1.0$ dex, mostly because of metallicity dependent SN II yields. At lower metallicities, the fraction of heavy isotopes become increasingly small and in this regime, AGB stars may become an important source of these isotopes. As a matter of fact, the scant data available below [Fe/H]$= -2.0$ dex suggests that some source of ^{25}Mg and ^{26}Mg exists in this regime aside the (vanishing) contribution from SN

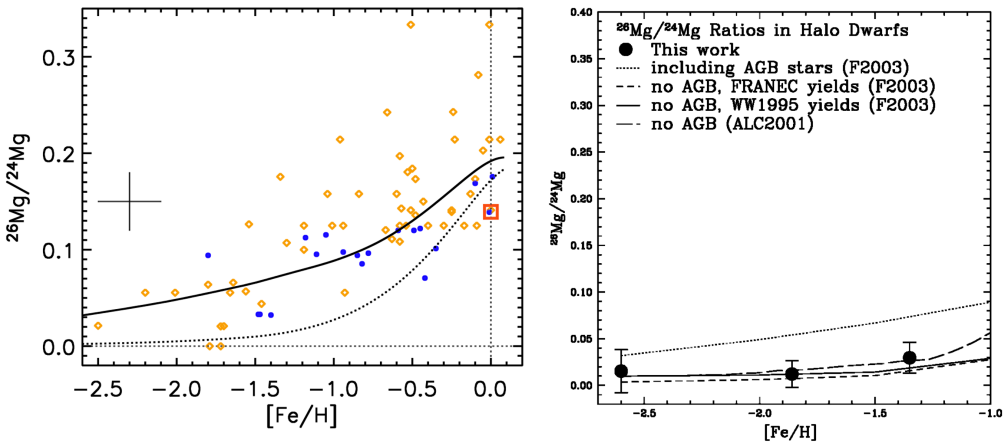

Figure 6.2: Left: Magnesium isotope measurements and model predictions from Fenner et al. (2003). The solid line includes AGB contribution whereas the dotted does not. Yellow diamonds from Yong et al. (2003b), blue dots from Gay & Lambert (2000). Right: Similar figure from Meléndez & Cohen (2007).

II. However, the presence or absence of a residual AGB contribution for [Fe/H] < -2.0 dex hinges on a small number (3) of observations (see Fenner et al. 2003). Indeed, the study of Meléndez & Cohen (2007) finds no evidence of an AGB contribution to the magnesium isotopic mixture below [Fe/H]$= -2.0$ dex, but this conclusion is based on only three new data points compared to Fenner et al. 2003 (Fig. 6.2).

We are in the process of securing observations sufficient to double the current sample available at metallicities below [Fe/H] $= -1.5$. We intend to perform a detailed analysis of these data, and in addition, re-analyse the existing archival data. This will make our study the largest homogeneously analyzed sample currently available.

While earlier analysis of the magnesium isotopic mixture provided contradicting conclusions (Yong et al. 2003b; Meléndez & Cohen 2007) and relied on standard 1D stellar atmospheres, I will continue my work with 3D model atmospheres and again use CO^{5}BOLD models to perform the analysis. Whereas the 3D effects were modest for the giants analyzed in this thesis, these are expect to increase when analyzing dwarf stars at lower metallicities, where significant differences are seen between the 1D and 3D model structures (e. g. Behara et al. 2010; Magic et al. 2013). As such, this project will yield important new clues about the formation of one of the oldest components of the MW and hopefully settle the debate whether any significant AGB contribution exists below a metallicity of [Fe/H] $= -2.0$ dex.

6.2.2 *Magnesium isotopes in post-AGB stars*

Our understanding of nucleosynthesis in AGB stars is still rather incomplete, although there has been a notable success in explaining a number of observed abundance trends in stars, in particular the observed s-process patterns. However, discrepancies between models and observations are still significant. For instance, the recent non-detection of lead enhancement in post-AGB stars (De Smedt et al. 2014) emphasizes that we do not yet have the full understanding of AGB star nucleosynthesis. Furthermore, there is still substantial disagreement among the yields presented by different research groups, as discussed in the Introduction.

Most of the information we possess about AGB nucleosynthesis is inferred from indirect measurements, combining models of AGB stars with abundances derived from stars in a later generation. These stars are born from pristine gas which has been mixed with ejecta from AGB stars. These inferences all rely on assumptions about e.g. convection in the AGB stars, internal mixing, mass loss, and mixing with interstellar matter. Very few direct measurements of AGB star abundances exist. Deriving abundances from atomic lines in AGB stars themselves is extremely challenging, because of their cool, extended atmospheres which results in spectra highly contaminated with molecular lines. This contamination also prevents direct measurements of the magnesium isotopes from the MgH features in AGB stars.

Post-AGB stars have ejected most of their cool envelope, exposing hotter regions of the star. The photosphere of these objects suffer from molecular line blends to a much lower degree, making abundance studies much easier. Measurements in such stars have the ability to probe AGB nucleosynthesis ***directly*** and provide important new constraints on the AGB models (Van Winckel & Reyniers 2000, Reyniers et al. 2004, and van Aarle et al. 2013). These studies have largely been confined to the study of s-process elements until now, but have already yielded new information on the neutron exposure and behaviour of the ^{13}C pocket during the thermally pulsating phase in these objects.

Another application of magnesium isotopic measurements is their use in investigating another aspect of AGB star nucleosynthesis directly. As discussed earlier, in the few cases where the distribution of magnesium isotopes has been measured, the results are in stark contrast with the predicted yields from AGB stars, although 3D effects may help to resolve part of the observed discrepancy (see Chapter 4). Discrepancies are also seen between the measured and predicted Mg isotopic ratios at low metallicities (Kobayashi et al. 2011).

The predicted strong increase in ^{25}Mg has so far not been observed in any of the five GCs for which such measurements exist. The fraction

of ^{25}Mg is found to be constant, both in stars belonging to the pristine population, and stars from the polluted population, which shows an enhancement in Al and Na not seen in field stars. Even taking mixing with pristine gas into account, based on the models, one would expect the polluted population to be enhanced in ^{25}Mg, which is not observed.

To investigate whether this is an observational issue or a modeling issue, we plan obtain high-resolution spectra of a number of post-AGB stars which are cool enough that the MgH features are still visible. From these spectra, we will derive the magnesium isotopic mixture. This project will represent the ***first direct observational test of this key nucleosynthesis process in AGB stars.*** The targets will be selected mainly from the Torun catalogue of post-AGB objects (Szczerba et al. 2007, 2012) but will be supplemented by additional targets from the literature.

Preferentially we will select targets also observed by both the Herschel and Spitzer Space Telescopes, which will provide additional information about these stars. In particular, information about mass loss rates in these intriguing objects (Groenewegen et al. 2011) will be important. Because mass loss rates are one of the important uncertainties in AGB stellar modeling, which also affects the final abundance yields, the combination of such data with the measurements of the magnesium isotopes will help to select the most representative AGB models. If significant discrepancies between the AGB predictions and the observations are found, this will also impact the interpretation of the results for the halo stars, as the AGB star models may require modification.

6.2.3 *Detailed abundances of giants in the Globular Clusters NGC 288 and NGC 362*

Since Searle & Zinn (1978) used GCs to establish the two-phase formation of the Milky Way, the study of GCs has been crucial to understand the MW formation. The lessons learned from local GCs have been used to also derive information about the formation of other galaxies (Brodie & Strader 2006), as GCs are some of the brightest sources that can be observed in these systems. Thus, a detailed understanding of the evolution of GCs is of importance to understand not only the formation of the MW, but also how external galaxies formed. This is especially true since in most cases only the integrated light of the extragalactic GC is observed, which then needs to be correctly interpreted. Such an interpretation requires a good understanding of GC systems.

Using already available high-resolution, high S/N spectra I intend to perform a detailed abundance analysis of red giants in the two GCs NGC 288 and NGC 362. Focus will again be the derivation of magnesium isotopes, but abundances of other important elements like Barium

and Europium will also be derived. The metallicity of these two clusters place them in between 47 Tucanae and the remaining sample of clusters where magnesium isotopes have been derived, closing the gap between low and high-metallicity clusters. This will form a natural extension of my thesis work on 47 Tucanae. I also intend to investigate the behaviour of magnesium and aluminum when performing a full NLTE spectral analysis. A significant change in the behaviour of aluminum in NLTE, compared to LTE was already demonstrated for 47 Tucanae by Thygesen et al. (2014). Since the Mg-Al anti-correlation seen in a number of GCs is used to constrain the mass-range of the intra-cluster polluter candidates, any change in this behaviour will have important consequences for the pollution scenarios.

The combination of NLTE analysis of the Mg-Al anti-correlation and the derivation of magnesium isotopes will provide new information on the mass-ranges of the proposed polluter candidates and help shed more light on the exciting topic of the internal chemical evolution of GCs.

These projects will combine nicely to provide new insights into the chemical evolution of the MW and contribute to our understanding of how the Galactic halo formed.

A

APPENDIX OF ADDITIONAL FIGURES AND TABLES

A.1 TABLES

Table A.1: The full line list for the elements without reported HFS. XX.0 refers to neutral species and XX.1 to the first ionization stage. All wavelengths are given in Å. The table is also available online through CDS.

Wavelength	Ion	$\log(gf)$	E_{low}
6300.304	8.0	-9.715	0.000
6363.776	8.0	-10.190	0.020
6154.226	11.0	-1.547	2.102
6160.747	11.0	-1.246	2.104
6318.717	12.0	-1.950	5.108
6319.237	12.0	-2.165	5.108
6319.495	12.0	-2.803	5.108
5690.425	14.0	-1.773	4.930
5701.104	14.0	-1.953	4.930
5948.541	14.0	-1.130	5.082
6131.573	14.0	-1.556	5.616
6131.852	14.0	-1.615	5.616
6142.483	14.0	-1.295	5.619
6155.134	14.0	-0.754	5.619
6155.693	14.0	-2.252	5.619
6195.433	14.0	-1.490	5.871
6244.466	14.0	-1.093	5.616
5260.387	20.0	-1.719	2.521
5512.980	20.0	-0.464	2.933
5867.562	20.0	-1.570	2.933
6455.598	20.0	-1.290	2.523
5223.620	22.0	-0.490	2.092
5340.666	22.0	-3.180	0.818

Continued on next page

Table A.1 Continued from previous page

Wavelength	Ion	$\log(gf)$	E_{low}
5384.630	22.0	-2.910	0.826
5648.565	22.0	-0.161	2.495
5689.460	22.0	-0.360	2.297
5702.656	22.0	-0.590	2.292
5903.315	22.0	-2.089	1.067
6092.792	22.0	-1.322	1.887
6098.658	22.0	-0.010	3.062
6303.756	22.0	-1.510	1.443
6312.236	22.0	-1.496	1.460
6336.099	22.0	-1.686	1.443
6395.472	22.0	-2.650	1.502
4874.009	22.1	-0.800	3.095
5013.677	22.1	-2.190	1.582
5336.771	22.1	-1.630	1.582
5418.751	22.1	-2.110	1.582
6219.940	22.1	-3.038	2.061
4885.953	24.0	-1.120	3.087
4936.336	24.0	-0.250	3.113
5238.961	24.0	-1.270	2.709
5340.447	24.0	-0.730	3.438
5628.643	24.0	-0.740	3.422
5642.358	24.0	-0.899	3.857
5719.816	24.0	-1.580	3.013
5844.595	24.0	-1.770	3.013
5982.874	24.0	-1.734	3.168
6630.011	24.0	-3.560	1.030
4808.148	26.0	-2.740	3.251
4873.751	26.0	-3.010	3.301
4918.013	26.0	-1.340	4.230
5058.496	26.0	-2.830	3.642
5253.021	26.0	-3.940	2.279
5279.650	26.0	-3.440	3.301
5285.127	26.0	-1.620	4.434

Continued on next page

Table A.1 Continued from previous page

Wavelength	Ion	$\log(gf)$	E_{low}
5294.547	26.0	-2.810	3.640
5295.312	26.0	-1.670	4.415
5320.036	26.0	-2.490	3.642
5379.574	26.0	-1.514	3.694
5386.333	26.0	-1.740	4.154
5398.279	26.0	-0.710	4.445
5436.295	26.0	-1.510	4.386
5441.339	26.0	-1.700	4.312
5491.832	26.0	-2.188	4.186
5522.446	26.0	-1.520	4.209
5560.211	26.0	-1.160	4.434
5587.574	26.0	-1.850	4.143
5618.632	26.0	-1.275	4.209
5633.946	26.0	-0.320	4.991
5652.318	26.0	-1.920	4.260
5698.020	26.0	-2.630	3.640
5732.296	26.0	-1.560	4.991
5760.344	26.0	-2.440	3.642
5837.701	26.0	-2.340	4.294
5853.148	26.0	-5.280	1.485
5881.280	26.0	-1.840	4.607
5883.817	26.0	-1.310	3.960
5902.473	26.0	-1.810	4.593
5952.718	26.0	-1.390	3.984
5976.777	26.0	-1.243	3.943
6012.210	26.0	-4.038	2.223
6019.366	26.0	-3.310	3.573
6027.051	26.0	-1.089	4.076
6034.035	26.0	-2.312	4.312
6056.005	26.0	-0.460	4.733
6078.491	26.0	-0.321	4.796
6093.643	26.0	-1.470	4.607
6096.664	26.0	-1.880	3.984

Continued on next page

Table A.1 Continued from previous page

Wavelength	Ion	$\log(gf)$	E_{low}
6120.246	26.0	-5.970	0.915
6165.360	26.0	-1.473	4.143
6226.734	26.0	-2.220	3.883
6353.836	26.0	-6.477	0.915
6608.025	26.0	-4.030	2.279
6648.080	26.0	-5.918	1.011
6699.141	26.0	-2.101	4.593
6704.480	26.0	-2.380	4.217
6713.743	26.0	-1.600	4.795
6733.150	26.0	-1.580	4.638
6746.954	26.0	-4.304	2.608
6793.258	26.0	-2.326	4.076
5197.580	26.1	-2.220	3.230
5234.625	26.1	-2.180	3.221
5264.812	26.1	-3.130	3.230
5284.109	26.1	-3.195	2.891
5325.553	26.1	-3.160	3.221
5414.073	26.1	-3.580	3.221
5425.257	26.1	-3.220	3.199
5991.380	26.1	-3.540	3.150
6084.110	26.1	-3.790	3.200
6113.322	26.1	-4.230	3.221
6149.260	26.1	-2.690	3.890
6247.560	26.1	-2.300	3.890
6369.462	26.1	-4.110	2.891
6432.680	26.1	-3.570	2.891
6456.383	26.1	-2.050	3.903
6516.080	26.1	-3.310	2.891
4829.016	28.0	-0.140	3.542
4873.438	28.0	-0.380	3.699
4913.968	28.0	-0.500	3.743
4935.831	28.0	-0.213	3.941
4946.029	28.0	-1.151	3.796

Continued on next page

Table A.1 Continued from previous page

Wavelength	Ion	$\log(gf)$	E_{low}
4976.130	28.0	-1.250	3.606
5084.089	28.0	-0.084	3.679
5157.976	28.0	-1.510	3.606
5392.327	28.0	-1.315	4.154
5589.357	28.0	-0.938	3.898
5593.733	28.0	-0.682	3.898
5625.312	28.0	-0.549	4.089
5638.745	28.0	-1.580	3.898
5682.198	28.0	-0.344	4.105
5694.977	28.0	-0.467	4.089
6086.276	28.0	-0.410	4.266
6111.066	28.0	-0.865	4.088
6175.360	28.0	-0.389	4.089
6176.807	28.0	-0.260	4.088
6378.247	28.0	-0.830	4.154
6598.593	28.0	-0.821	4.236
6772.313	28.0	-0.797	3.658
4810.528	30.0	-0.160	4.078
5289.810	39.1	-1.850	1.030
5544.611	39.1	-1.090	1.738
5728.887	39.1	-1.659	1.839
5506.490	42.0	0.060	1.330
5533.031	42.0	-0.069	1.335
5689.146	42.0	-1.002	1.382
5722.740	42.0	-1.500	1.420
5751.408	42.0	-1.014	1.420
6030.644	42.0	-0.523	1.531
5309.265	44.0	-1.390	0.928
5699.056	44.0	-1.470	1.087
5274.229	58.1	0.130	1.044
4914.380	60.1	-0.700	0.380
5293.160	60.1	0.100	0.823
5356.970	60.1	-0.280	1.264

Continued on next page

Table A.1 Continued from previous page

Wavelength	Ion	$\log(gf)$	E_{low}
5442.260	60.1	-0.910	0.680
5688.520	60.1	-0.310	0.986
5740.858	60.1	-0.530	1.160
5742.090	60.1	-0.830	1.090
6385.190	60.1	-0.360	1.600
6740.078	60.1	-2.100	0.064
6790.370	60.1	-2.110	0.180
4890.103	66.1	-2.314	0.103

Concluded

Table A.2: Line list of HFS-elements measured. XX.0 and XX.1 indicate neutral and ionized species respectively. The full table is also available online. With the exception of barium, all lines have been split into individual HFS components in this list. Oscillator strength given as reduced $\log(gf)$. All wavelengths given in Å.

Wavelength	Ion	$\log(gf)_{\text{red}}$	E_{low}
5356.087	21.0	-0.189	1.865
5356.097	21.0	-0.084	1.865
5671.775	21.0	-0.505	1.448
5671.790	21.0	-0.209	1.448
5671.803	21.0	-0.471	1.448
5671.816	21.0	-0.290	1.448
5671.827	21.0	-1.027	1.448
5671.844	21.0	-0.232	1.448
5671.864	21.0	-0.178	1.448
5686.825	21.0	-0.305	1.440
5686.838	21.0	-0.133	1.440
5686.854	21.0	-0.235	1.440
5686.866	21.0	-0.251	1.440
5686.879	21.0	-2.606	1.440
5717.307	21.0	-0.532	1.440

Continued on next page

Table A.2 Continued from previous page

Wavelength	Ion	$\log(gf)$	E_{low}
5724.107	21.0	-0.661	1.433
6193.666	21.0	-2.760	0.000
6193.678	21.0	-2.134	2.109
6193.678	21.0	-2.906	0.000
6210.604	21.0	-2.738	0.000
6210.617	21.0	-2.260	0.000
6210.645	21.0	-2.135	0.000
6210.660	21.0	-2.755	0.000
6210.681	21.0	-2.249	0.000
6210.700	21.0	-2.140	0.000
6239.408	21.0	-2.274	0.000
6276.295	21.0	-2.605	0.021
6344.805	21.0	-3.060	0.000
6378.807	21.0	-2.420	0.000
5526.790	21.1	0.024	1.768
5641.001	21.1	-1.131	1.500
5657.896	21.1	-0.603	1.507
5667.149	21.1	-1.309	1.500
5669.042	21.1	-1.200	1.500
5684.202	21.1	-1.074	1.507
6245.637	21.1	-1.022	1.507
6279.753	21.1	-1.252	1.500
6309.920	21.1	-1.618	1.497
6604.601	21.1	-1.309	1.357
4807.521	23.0	0.380	2.125
4875.454	23.0	-3.394	0.040
4875.468	23.0	-2.202	0.040
4875.481	23.0	-1.335	0.040
4875.493	23.0	-1.422	0.040
4875.508	23.0	-1.193	0.040
4881.498	23.0	-3.642	0.069
4881.511	23.0	-2.341	0.069
4881.523	23.0	-1.327	0.069

Continued on next page

Table A.2 Continued from previous page

Wavelength	Ion	$\log(gf)$	E_{low}
4881.542	23.0	-1.349	0.069
4881.558	23.0	-1.422	0.069
4881.569	23.0	-1.999	0.069
4881.582	23.0	-1.296	0.069
4881.596	23.0	-1.625	0.069
5240.830	23.0	-0.661	2.374
5240.841	23.0	-0.439	2.374
5240.855	23.0	-0.626	2.374
5240.865	23.0	-0.564	2.374
5240.877	23.0	-0.510	2.374
5240.891	23.0	-0.462	2.374
5507.682	23.0	-1.468	2.359
5507.700	23.0	-1.526	2.359
5507.716	23.0	-1.417	2.359
5507.735	23.0	-1.130	1.712
5507.736	23.0	-1.330	2.359
5507.760	23.0	-1.257	2.359
5507.788	23.0	-1.195	2.359
5507.820	23.0	-1.141	2.359
5557.456	23.0	-3.430	0.017
5592.921	23.0	-5.814	0.040
5592.939	23.0	-4.622	0.040
5592.957	23.0	-3.755	0.040
5592.975	23.0	-3.609	0.040
5592.994	23.0	-3.849	0.040
5604.901	23.0	-1.644	1.043
5604.955	23.0	-1.535	1.043
5624.872	23.0	-1.060	1.051
5626.017	23.0	-1.240	1.043
5627.613	23.0	-0.993	1.081
5627.624	23.0	-1.055	1.081
5627.634	23.0	-1.128	1.081
5627.647	23.0	-0.965	1.081

Continued on next page

Table A.2 Continued from previous page

Wavelength	Ion	$\log(gf)$	E_{low}
5627.658	23.0	-1.215	1.081
5632.397	23.0	-6.202	0.069
5632.417	23.0	-4.850	0.069
5632.438	23.0	-3.821	0.069
5632.456	23.0	-3.894	0.069
5632.471	23.0	-3.981	0.069
5632.485	23.0	-3.856	0.069
5632.500	23.0	-4.185	0.069
5646.108	23.0	-1.196	1.051
5657.421	23.0	-1.587	1.064
5657.436	23.0	-1.400	1.064
5657.450	23.0	-1.525	1.064
5668.340	23.0	-1.660	1.081
5668.352	23.0	-1.722	1.081
5668.362	23.0	-1.795	1.081
5668.375	23.0	-1.632	1.081
5668.386	23.0	-1.882	1.081
5670.832	23.0	-1.050	1.081
5670.844	23.0	-1.112	1.081
5670.854	23.0	-1.185	1.081
5670.868	23.0	-1.022	1.081
5670.879	23.0	-1.272	1.081
5703.555	23.0	-0.779	1.051
5703.568	23.0	-0.851	1.051
5703.586	23.0	-0.689	1.051
5703.599	23.0	-0.990	1.051
5727.016	23.0	-0.644	1.081
5727.032	23.0	-0.787	1.081
5727.041	23.0	-1.450	1.081
5727.052	23.0	-0.787	1.081
5727.065	23.0	-0.867	1.081
5727.078	23.0	-0.953	1.081
5727.090	23.0	-0.864	1.081

Continued on next page

Table A.2 Continued from previous page

Wavelength	Ion	$\log(gf)$	E_{low}
5727.616	23.0	-1.338	1.051
5727.650	23.0	-1.425	1.051
5727.678	23.0	-1.534	1.051
5727.699	23.0	-1.681	1.051
5737.031	23.0	-1.240	1.064
5737.055	23.0	-1.338	1.064
5737.074	23.0	-1.455	1.064
5737.089	23.0	-1.608	1.064
5737.102	23.0	-1.726	1.064
5743.447	23.0	-0.970	1.081
6002.282	23.0	-2.285	1.218
6002.294	23.0	-2.160	1.218
6002.307	23.0	-2.347	1.218
6039.707	23.0	-1.217	1.064
6039.723	23.0	-1.030	1.064
6039.739	23.0	-1.155	1.064
6081.441	23.0	-0.582	1.051
6090.190	23.0	-0.692	1.081
6090.204	23.0	-0.754	1.081
6090.215	23.0	-0.827	1.081
6090.231	23.0	-0.664	1.081
6090.243	23.0	-0.914	1.081
6111.609	23.0	-1.116	1.043
6111.673	23.0	-1.007	1.043
6119.507	23.0	-0.887	1.064
6119.524	23.0	-0.700	1.064
6119.541	23.0	-0.825	1.064
6150.118	23.0	-1.994	0.301
6150.133	23.0	-2.078	0.301
6150.147	23.0	-2.168	0.301
6150.160	23.0	-2.264	0.301
6150.171	23.0	-2.368	0.301
6150.181	23.0	-2.281	0.301

Continued on next page

Table A.2 Continued from previous page

Wavelength	Ion	$\log(gf)$	E_{low}
6150.198	23.0	-2.006	0.301
6150.210	23.0	-3.168	0.301
6150.227	23.0	-3.320	0.301
6199.156	23.0	-1.973	0.287
6199.173	23.0	-2.078	0.287
6199.188	23.0	-2.194	0.287
6199.203	23.0	-2.323	0.287
6199.214	23.0	-2.353	0.287
6199.225	23.0	-2.222	0.287
6199.242	23.0	-2.071	0.287
6199.259	23.0	-2.981	0.287
6213.812	23.0	-3.697	0.301
6213.823	23.0	-3.482	0.301
6213.834	23.0	-3.405	0.301
6213.853	23.0	-2.510	0.301
6213.866	23.0	-2.376	0.301
6213.879	23.0	-2.822	0.301
6213.895	23.0	-2.910	0.301
6213.902	23.0	-3.034	0.301
6216.315	23.0	-1.920	0.275
6216.333	23.0	-2.062	0.275
6216.348	23.0	-2.225	0.275
6216.362	23.0	-2.259	0.275
6216.374	23.0	-2.316	0.275
6216.386	23.0	-2.033	0.275
6216.404	23.0	-2.300	0.275
6251.771	23.0	-2.924	0.287
6251.788	23.0	-2.720	0.287
6251.805	23.0	-1.931	0.287
6251.817	23.0	-2.077	0.287
6251.830	23.0	-2.116	0.287
6251.847	23.0	-2.335	0.287
6251.860	23.0	-1.990	0.287

Continued on next page

Table A.2 Continued from previous page

Wavelength	Ion	$\log(gf)$	E_{low}
6256.839	23.0	-3.356	0.275
6256.857	23.0	-3.174	0.275
6256.871	23.0	-2.534	0.275
6256.884	23.0	-2.758	0.275
6256.896	23.0	-3.037	0.275
6256.914	23.0	-2.612	0.275
6256.921	23.0	-3.208	0.275
6268.798	23.0	-2.128	0.301
6274.607	23.0	-2.935	0.267
6274.629	23.0	-2.458	0.267
6274.641	23.0	-2.479	0.267
6274.656	23.0	-1.967	0.267
6274.678	23.0	-2.604	0.267
6285.098	23.0	-3.568	0.275
6285.120	23.0	-2.567	0.275
6285.135	23.0	-2.381	0.275
6285.149	23.0	-1.822	0.275
6285.162	23.0	-2.293	0.275
6285.170	23.0	-2.441	0.275
6292.759	23.0	-4.054	0.287
6292.776	23.0	-3.644	0.287
6292.791	23.0	-2.817	0.287
6292.806	23.0	-2.362	0.287
6292.826	23.0	-1.714	0.287
6292.839	23.0	-2.077	0.287
6349.432	23.0	-3.189	1.854
6349.449	23.0	-2.271	1.854
6349.461	23.0	-1.660	1.854
6349.477	23.0	-0.825	1.854
6357.288	23.0	-0.965	1.849
6357.297	23.0	-1.479	1.849
6452.341	23.0	-1.206	1.195
6452.345	23.0	-2.780	2.743

Continued on next page

Table A.2 Continued from previous page

Wavelength	Ion	$\log(gf)$	E_{low}
6504.164	23.0	-1.230	1.183
6531.399	23.0	-1.345	1.218
6531.414	23.0	-1.220	1.218
6531.429	23.0	-1.408	1.218
6543.500	23.0	-1.660	1.195
6565.878	23.0	-2.070	1.183
5377.594	25.0	-1.577	3.844
5377.609	25.0	-0.897	3.844
5377.624	25.0	-1.246	3.844
5377.631	25.0	-0.839	3.844
5377.652	25.0	-0.572	3.844
5377.667	25.0	-1.945	3.844
5377.684	25.0	-1.371	3.844
5377.708	25.0	-2.325	3.844
5399.499	25.0	-0.345	3.853
5413.668	25.0	-0.647	3.859
5420.261	25.0	-2.702	2.143
5420.276	25.0	-2.449	2.143
5420.298	25.0	-2.483	2.143
5420.312	25.0	-2.745	2.143
5420.332	25.0	-2.313	2.143
5420.351	25.0	-2.771	2.143
5420.376	25.0	-2.165	2.143
5420.400	25.0	-2.947	2.143
5420.428	25.0	-2.029	2.143
5457.380	25.0	-4.131	2.164
5457.393	25.0	-3.877	2.164
5457.411	25.0	-3.912	2.164
5457.424	25.0	-4.174	2.164
5457.439	25.0	-3.742	2.164
5457.457	25.0	-4.200	2.164
5457.476	25.0	-3.593	2.164
5457.498	25.0	-4.376	2.164

Continued on next page

Table A.2 Continued from previous page

Wavelength	Ion	$\log(gf)$	E_{low}
5457.521	25.0	-3.458	2.164
5516.701	25.0	-2.753	2.178
5516.717	25.0	-2.897	2.178
5516.741	25.0	-2.776	2.178
5516.756	25.0	-2.776	2.178
5516.771	25.0	-2.950	2.178
5516.790	25.0	-2.878	2.178
5516.810	25.0	-2.878	2.178
5516.829	25.0	-2.401	2.178
5537.692	25.0	-3.234	2.187
5537.712	25.0	-3.122	2.187
5537.741	25.0	-3.086	2.187
5537.769	25.0	-3.122	2.187
5537.809	25.0	-2.757	2.187
6013.478	25.0	-0.869	3.072
6013.499	25.0	-1.081	3.072
6013.518	25.0	-1.354	3.072
6013.533	25.0	-1.078	3.072
6013.547	25.0	-1.433	3.072
6013.561	25.0	-1.225	3.072
6021.746	25.0	-2.756	3.075
6021.773	25.0	-1.483	3.075
6021.800	25.0	-0.541	3.075
6021.818	25.0	-0.650	3.075
6021.830	25.0	-0.796	3.075
6021.845	25.0	-0.752	3.075
6440.947	25.0	-1.861	3.772
6440.959	25.0	-1.770	3.772
6440.969	25.0	-2.520	3.772
6440.981	25.0	-1.490	3.772
6440.995	25.0	-2.520	3.772
4813.389	27.0	-2.862	3.216
4813.407	27.0	-2.464	3.216

Continued on next page

Table A.2 Continued from previous page

Wavelength	Ion	$\log(gf)$	E_{low}
4813.423	27.0	-1.482	3.216
4813.437	27.0	-1.288	3.216
4813.448	27.0	-1.224	3.216
4813.462	27.0	-0.191	3.216
4813.480	27.0	-0.280	3.216
4813.945	27.0	-1.372	3.298
4813.961	27.0	-1.641	3.298
4813.974	27.0	-1.629	3.298
4813.988	27.0	-1.459	3.298
4899.513	27.0	-1.597	2.042
5230.208	27.0	-1.840	1.740
5247.920	27.0	-2.070	1.785
5280.535	27.0	-3.012	3.629
5280.565	27.0	-1.660	3.629
5280.588	27.0	-1.450	3.629
5280.607	27.0	-0.619	3.629
5280.624	27.0	-0.703	3.629
5280.638	27.0	-0.737	3.629
5280.649	27.0	-1.053	3.629
5280.660	27.0	-0.784	3.629
5359.135	27.0	-0.960	4.149
5359.145	27.0	-0.863	4.149
5359.156	27.0	-0.717	4.149
5359.171	27.0	-0.608	4.149
5359.189	27.0	-0.521	4.149
5359.211	27.0	-0.448	4.149
5359.237	27.0	-0.386	4.149
5369.567	27.0	-2.158	1.740
5369.578	27.0	-2.374	1.740
5369.598	27.0	-2.028	1.740
5369.618	27.0	-2.293	1.740
5483.301	27.0	-2.040	1.710
5483.324	27.0	-2.181	1.710

Continued on next page

Table A.2 Continued from previous page

Wavelength	Ion	$\log(gf)$	E_{low}
5483.342	27.0	-2.234	1.710
5483.358	27.0	-2.298	1.710
5483.372	27.0	-2.405	1.710
5483.385	27.0	-2.269	1.710
5483.398	27.0	-2.521	1.710
5483.877	27.0	-1.153	3.632
5483.911	27.0	-1.258	3.632
5483.941	27.0	-1.374	3.632
5483.968	27.0	-1.417	3.632
5483.991	27.0	-1.473	3.632
5484.011	27.0	-1.546	3.632
5484.027	27.0	-1.639	3.632
5484.044	27.0	-1.469	3.632
5484.066	27.0	-2.219	3.632
5523.234	27.0	-2.106	2.328
5523.274	27.0	-2.573	2.328
5523.298	27.0	-2.427	2.328
5523.325	27.0	-2.427	2.328
5523.350	27.0	-2.904	2.328
5523.364	27.0	-2.448	2.328
5530.733	27.0	-2.860	1.710
5530.755	27.0	-3.001	1.710
5530.772	27.0	-3.054	1.710
5530.787	27.0	-3.127	1.710
5530.800	27.0	-3.214	1.710
5530.812	27.0	-3.089	1.710
5530.824	27.0	-3.341	1.710
5590.645	27.0	-2.336	2.042
5590.716	27.0	-2.424	2.042
5590.774	27.0	-2.533	2.042
5590.817	27.0	-2.679	2.042
5647.208	27.0	-2.127	2.280
5647.220	27.0	-2.343	2.280

Continued on next page

Table A.2 Continued from previous page

Wavelength	Ion	$\log(gf)$	E_{low}
5647.232	27.0	-2.626	2.280
5647.243	27.0	-2.285	2.280
5647.257	27.0	-2.373	2.280
5647.269	27.0	-2.425	2.280
5659.115	27.0	-2.563	2.042
5915.499	27.0	-3.199	2.137
5915.509	27.0	-2.894	2.137
5915.523	27.0	-3.359	2.137
5915.546	27.0	-2.799	2.137
5915.556	27.0	-2.812	2.137
5915.566	27.0	-2.633	2.137
5915.580	27.0	-3.352	2.137
5915.595	27.0	-3.345	2.137
5915.610	27.0	-3.410	2.137
5915.626	27.0	-3.614	2.137
6004.976	27.0	-5.379	1.710
6004.986	27.0	-4.513	1.710
6004.999	27.0	-3.888	1.710
6005.013	27.0	-4.255	1.710
6005.036	27.0	-3.847	1.710
6005.058	27.0	-3.996	1.710
6005.069	27.0	-4.826	1.710
6093.097	27.0	-3.458	1.740
6093.123	27.0	-2.871	1.740
6093.147	27.0	-3.255	1.740
6093.162	27.0	-3.458	1.740
6093.176	27.0	-3.169	1.740
6093.187	27.0	-3.470	1.740
6116.962	27.0	-3.142	1.785
6117.000	27.0	-2.695	1.785
6117.039	27.0	-3.473	1.785
6188.924	27.0	-3.795	1.710
6188.938	27.0	-3.096	1.710

Continued on next page

Table A.2 Continued from previous page

Wavelength	Ion	$\log(gf)$	E_{low}
6188.966	27.0	-3.614	1.710
6188.978	27.0	-3.388	1.710
6188.991	27.0	-3.795	1.710
6189.004	27.0	-3.375	1.710
6189.028	27.0	-3.302	1.710
6189.050	27.0	-3.392	1.710
6189.069	27.0	-3.350	1.710
6429.771	27.0	-4.994	2.137
6429.800	27.0	-4.584	2.137
6429.826	27.0	-4.362	2.137
6429.850	27.0	-3.402	2.137
6429.870	27.0	-3.523	2.137
6429.887	27.0	-3.333	2.137
6429.897	27.0	-3.931	2.137
6429.923	27.0	-2.596	2.137
6632.400	27.0	-2.568	2.280
6632.415	27.0	-2.783	2.280
6632.430	27.0	-3.066	2.280
6632.444	27.0	-2.726	2.280
6632.461	27.0	-2.814	2.280
6632.477	27.0	-2.866	2.280
6770.940	27.0	-2.954	1.883
6770.950	27.0	-3.103	1.883
6770.962	27.0	-3.011	1.883
6770.973	27.0	-5.274	1.883
6770.992	27.0	-2.997	1.883
6771.022	27.0	-2.934	1.883
6771.057	27.0	-2.693	1.883
6771.090	27.0	-2.616	1.883
6771.104	27.0	-3.134	1.883
6771.154	27.0	-3.315	1.883
5105.496	29.0	-2.210	1.389
5105.506	29.0	-2.398	1.389

Continued on next page

Table A.2 Continued from previous page

Wavelength	Ion	$\log(gf)$	E_{low}
5105.519	29.0	-1.993	1.389
5105.521	29.0	-2.051	1.389
5105.541	29.0	-2.051	1.389
5105.546	29.0	-1.942	1.389
5105.564	29.0	-1.942	1.389
5153.227	29.0	-0.023	3.786
5153.228	29.0	-0.023	3.786
5119.1094	39.1	-2.9041	0.992
5119.1113	39.1	-1.6030	0.992
5119.1128	39.1	-1.7579	0.992
5289.8145	39.1	-2.2479	1.030
5289.8159	39.1	-3.3941	1.030
5289.8154	39.1	-2.0930	1.030
5728.8887	39.1	-2.5179	1.030
5728.8892	39.1	-1.5637	1.030
5728.8906	39.1	-1.3718	1.030
5728.8911	39.1	-2.5179	1.030
6127.4413	40.0	-3.7424	0.154
6127.4437	40.0	-3.2653	0.154
6127.4465	40.0	-3.5461	0.154
6127.4498	40.0	-3.2073	0.154
6127.4521	40.0	-3.7424	0.154
6127.4542	40.0	-3.4871	0.154
6127.4585	40.0	-3.0770	0.154
6127.4618	40.0	-3.5461	0.154
6127.4642	40.0	-3.5237	0.154
6127.4696	40.0	-2.9265	0.154
6127.4733	40.0	-1.3486	0.154
6127.4739	40.0	-3.4871	0.154
6127.4762	40.0	-1.8257	0.154
6127.4766	40.0	-3.7102	0.154
6127.4783	40.0	-1.8200	0.154
6127.4799	40.0	-2.6128	0.154

Continued on next page

Table A.2 Continued from previous page

Wavelength	Ion	$\log(gf)$	E_{low}
6127.4832	40.0	-2.7754	0.154
6127.4885	40.0	-3.5237	0.154
6127.4992	40.0	-2.6310	0.154
6127.5057	40.0	-3.7102	0.154
6134.5741	40.0	-2.7961	0.000
6134.5738	40.0	-3.4395	0.000
6134.5834	40.0	-3.2970	0.000
6134.5834	40.0	-1.5686	0.000
6134.5836	40.0	-3.1536	0.000
6134.5839	40.0	-3.4395	0.000
6134.5861	40.0	-2.0457	0.000
6134.5881	40.0	-2.0400	0.000
6134.5897	40.0	-2.8328	0.000
6134.5908	40.0	-3.3269	0.000
6134.5909	40.0	-3.6949	0.000
6134.5911	40.0	-3.2970	0.000
6134.5959	40.0	-3.5152	0.000
6134.5960	40.0	-5.0593	0.000
6134.5961	40.0	-3.3269	0.000
6134.5990	40.0	-4.0593	0.000
6134.5991	40.0	-3.5152	0.000
6143.2359	40.0	-3.6275	0.071
6143.2367	40.0	-3.4180	0.071
6143.2378	40.0	-3.7244	0.071
6143.2389	40.0	-3.3423	0.071
6143.2399	40.0	-3.6363	0.071
6143.2418	40.0	-3.6275	0.071
6143.2423	40.0	-3.3643	0.071
6143.2434	40.0	-3.3600	0.071
6143.2466	40.0	-3.4180	0.071
6143.2469	40.0	-3.5386	0.071
6143.2482	40.0	-3.0912	0.071
6143.2503	40.0	-1.3886	0.071

Continued on next page

Table A.2 Continued from previous page

Wavelength	Ion	$\log(gf)$	E_{low}
6143.2527	40.0	-3.3423	0.071
6143.2532	40.0	-1.8657	0.071
6143.2543	40.0	-2.8538	0.071
6143.2553	40.0	-1.8600	0.071
6143.2568	40.0	-2.6528	0.071
6143.2602	40.0	-3.3643	0.071
6143.2616	40.0	-2.6465	0.071
6143.2690	40.0	-3.5386	0.071
5853.668	56.1	-1.000	0.604
6141.713	56.1	-0.080	0.704
6496.897	56.1	-0.380	0.604
6390.458	57.1	-2.012	0.321
6390.471	57.1	-2.183	0.321
6390.472	57.1	-2.752	0.321
6390.482	57.1	-3.752	0.321
6390.482	57.1	-2.570	0.321
6390.483	57.1	-2.390	0.321
6390.491	57.1	-3.334	0.321
6390.492	57.1	-2.536	0.321
6390.493	57.1	-2.661	0.321
6390.499	57.1	-3.100	0.321
6390.500	57.1	-2.595	0.321
6390.501	57.1	-3.079	0.321
6390.505	57.1	-2.954	0.321
6390.506	57.1	-2.778	0.321
6390.509	57.1	-2.857	0.321
5259.6113	59.1	-3.729	0.633
5259.6294	59.1	-3.419	0.633
5259.6465	59.1	-3.357	0.633
5259.6626	59.1	-1.950	0.633
5259.6758	59.1	-1.764	0.633
5259.6865	59.1	-1.717	0.633
5259.7007	59.1	-1.555	0.633

Continued on next page

Table A.2 Continued from previous page

Wavelength	Ion	$\log(gf)$	E_{low}
5259.7217	59.1	-0.539	0.633
5259.7354	59.1	-0.029	0.633
5322.6729	59.1	-2.870	0.483
5322.7080	59.1	-1.682	0.483
5322.7188	59.1	-1.844	0.483
5322.7314	59.1	-1.061	0.483
5322.7446	59.1	-1.100	0.483
5322.7588	59.1	-1.016	0.483
5322.7744	59.1	-0.933	0.483
5322.7915	59.1	-0.854	0.483
5322.8096	59.1	-0.778	0.483
5276.8691	60.1	-0.440	0.859
5276.8940	60.1	-1.144	0.859
5276.9043	60.1	-1.144	0.859
5276.9053	60.1	-0.440	0.859
5276.9062	60.1	-1.192	0.859
5276.9165	60.1	-0.917	0.859
5276.9175	60.1	-1.246	0.859
5276.9209	60.1	-0.440	0.859
5276.9209	60.1	-0.440	0.859
5276.9209	60.1	-0.440	0.859
5276.9282	60.1	-1.042	0.859
5276.9331	60.1	-1.042	0.859
5276.9385	60.1	-1.100	0.859
5276.9497	60.1	-1.100	0.859
5319.8101	60.1	-0.140	0.550
5319.8237	60.1	-0.844	0.550
5319.8335	60.1	-0.844	0.550
5319.8354	60.1	-0.892	0.550
5319.8384	60.1	-0.140	0.550
5319.8452	60.1	-0.617	0.550
5319.8462	60.1	-0.946	0.550
5319.8496	60.1	-0.140	0.550

Continued on next page

Table A.2 Continued from previous page

Wavelength	Ion	$\log(gf)$	E_{low}
5319.8496	60.1	-0.140	0.550
5319.8496	60.1	-0.140	0.550
5319.8569	60.1	-0.742	0.550
5319.8613	60.1	-0.742	0.550
5319.8667	60.1	-0.800	0.550
5319.8770	60.1	-0.800	0.550
5548.3989	60.1	-1.974	0.550
5548.4097	60.1	-1.974	0.550
5548.4121	60.1	-2.022	0.550
5548.4224	60.1	-1.747	0.550
5548.4238	60.1	-2.076	0.550
5548.4268	60.1	-1.270	0.550
5548.4268	60.1	-1.270	0.550
5548.4268	60.1	-1.270	0.550
5548.4268	60.1	-1.270	0.550
5548.4268	60.1	-1.270	0.550
5548.4336	60.1	-2.138	0.550
5548.4351	60.1	-1.872	0.550
5548.4458	60.1	-1.930	0.550
5548.4473	60.1	-1.951	0.550
5548.4585	60.1	-2.173	0.550
6645.021	63.1	-0.517	1.380
6645.024	63.1	-0.495	1.380
6645.032	63.1	-1.814	1.380
6645.039	63.1	-0.555	1.380
6645.047	63.1	-0.593	1.380
6645.050	63.1	-0.621	1.380
6645.062	63.1	-0.319	1.380
6645.064	63.1	-0.625	1.380
6645.084	63.1	-0.693	1.380
6645.101	63.1	-0.773	1.380
6645.113	63.1	-0.871	1.380

Concluded

Table A.3: Abundance ratios for red giants in 47 Tucanae. Boldface IDs indicate the polluted population. Fe to Mg.

ID	[FeI/H]	σ_{tot}	N	[FeII/H]	σ_{tot}	N	[O/Fe]	$\sigma_{[X/Fe]}$	N	[Na/Fe]	$\sigma_{[X/Fe]}$	N	[Mg/Fe]	$\sigma_{[X/Fe]}$	N
4794	−0.66	0.06	44	−0.66	0.22	10	0.38	0.10	2	0.15	0.14	2	0.40	0.09	2
5968	−0.79	0.06	49	−0.79	0.23	7	0.41	0.10	2	0.08	0.14	2	0.49	0.08	2
6798	−0.69	0.06	44	−0.67	0.22	14	0.37	–	2	0.01	0.13	2	0.44	0.09	2
10237	−0.83	0.06	42	−0.83	0.22	13	0.57	0.10	2	0.04	0.13	2	0.32	0.09	2
13396	−0.83	0.06	47	−0.86	0.22	11	0.48	0.10	1	0.07	0.13	2	0.44	0.07	3
20885	−0.84	0.06	37	−0.86	0.22	14	–	–	0	0.11	0.13	2	0.47	0.09	3
29861	−0.84	0.06	40	−0.82	0.22	12	0.47	0.10	2	0.10	0.13	2	0.40	0.11	1
1062	−0.78	0.06	44	−0.80	0.22	10	0.23	0.10	2	0.24	0.14	2	0.46	0.07	2
5265	−0.69	0.06	43	−0.69	0.22	11	0.00	–	2	0.31	0.16	2	0.40	0.07	3
27678	−0.76	0.06	47	−0.76	0.22	12	0.13	0.10	2	0.50	0.14	2	0.45	0.10	2
28956	−0.86	0.06	46	−0.82	0.22	13	0.06	0.12	2	0.41	0.13	2	0.46	0.07	3
38916	−0.83	0.06	48	−0.85	0.22	14	–	–	0	0.42	0.14	2	0.52	0.07	3
40394	−0.71	0.06	43	−0.67	0.22	10	0.23	0.10	2	0.26	0.14	2	0.43	0.08	3

Table A.4: Abundance ratios for red giants in 47 Tucanae. Boldface IDs indicate the polluted population. Al to Sc.

ID	[Al/Fe]	$\sigma_{[X/Fe]}$	N	[Si/Fe]	$\sigma_{[X/Fe]}$	N	[Ca/Fe]	$\sigma_{[X/Fe]}$	N	[ScI/Fe]	$\sigma_{[X/Fe]}$	N	[ScII/Fe]	$\sigma_{[X/Fe]}$	N
4794	0.15	0.08	3	0.31	0.10	9	0.17	0.13	4	−0.10	0.15	8	0.25	0.18	5
5968	0.17	0.08	3	0.31	0.09	9	0.22	0.12	4	−0.08	0.15	5	0.22	0.18	10
6798	0.12	0.08	3	0.23	0.10	6	0.30	0.13	4	−0.13	0.15	7	0.19	0.18	6
10237	0.18	0.08	3	0.29	0.09	9	0.19	0.13	4	−0.12	0.15	9	0.19	0.17	7
13396	0.25	0.08	3	0.33	0.09	8	0.21	0.13	4	−0.02	0.14	7	0.28	0.17	6
20885	0.23	0.08	3	0.34	0.09	7	0.05	0.14	2	0.03	0.17	3	0.22	0.17	6
29861	0.27	0.08	3	0.34	0.09	7	0.18	0.12	4	0.09	0.16	6	0.19	0.18	8
1062	0.16	0.08	3	0.29	0.10	8	0.25	0.12	4	0.14	0.16	4	0.22	0.17	7
5265	0.19	0.08	3	0.41	0.10	8	0.35	0.12	4	−0.15	0.15	6	0.15	0.19	5
27678	0.29	0.08	3	0.42	0.10	6	0.28	0.13	3	0.17	0.15	4	0.18	0.18	8
28956	0.29	0.08	3	0.35	0.10	7	0.17	0.12	4	0.00	0.15	7	0.09	0.17	9
38916	0.29	0.08	3	0.30	0.09	9	0.30	0.13	4	0.07	0.15	9	0.28	0.17	9
40394	0.12	0.08	3	0.23	0.09	6	0.43	0.14	3	0.23	0.15	6	0.25	0.17	8

Table A.5: Abundance ratios for red giants in 47 Tucanae. Boldface IDs indicate the polluted population. Ti to Mn.

ID	[TiI/Fe]	$\sigma_{[X/Fe]}$	N	[TiII/Fe]	$\sigma_{[X/Fe]}$	N	[V/Fe]	$\sigma_{[X/Fe]}$	N	[Cr/Fe]	$\sigma_{[X/Fe]}$	N	[Mn/Fe]	$\sigma_{[X/Fe]}$	N
4794	0.20	0.15	12	0.34	0.14	3	0.08	0.14	34	−0.10	0.11	8	−0.20	0.12	8
5968	0.32	0.15	12	0.33	0.15	4	0.14	0.14	28	−0.04	0.11	9	−0.25	0.14	5
6798	0.24	0.15	10	0.39	0.15	3	0.08	0.14	30	−0.20	0.11	6	−0.30	0.16	5
10237	0.21	0.14	13	0.26	0.14	4	0.13	0.14	35	−0.10	0.11	8	−0.14	0.13	7
13396	0.24	0.14	11	0.35	0.14	4	0.10	0.14	36	−0.05	0.11	7	−0.15	0.13	5
20885	0.16	0.15	10	0.23	0.15	1	0.05	0.14	34	−0.07	0.11	4	−0.16	0.15	6
29861	0.26	0.14	9	0.31	0.14	2	0.14	0.14	36	−0.02	0.11	8	−0.15	0.14	7
1062	0.28	0.15	12	0.49	0.14	4	0.28	0.14	26	0.04	0.11	8	−0.22	0.15	5
5265	0.29	0.15	13	0.68	0.18	3	0.13	0.14	27	−0.02	0.11	8	−0.23	0.20	3
27678	0.40	0.16	13	0.61	0.15	4	0.32	0.15	26	0.03	0.11	8	−0.23	0.13	7
28956	0.31	0.15	12	0.46	0.14	5	0.20	0.14	22	0.00	0.11	8	−0.17	0.13	9
38916	0.34	0.14	10	0.39	0.15	4	0.22	0.14	31	0.01	0.11	8	−0.13	0.13	7
40394	0.44	0.15	11	0.49	0.16	4	0.35	0.15	24	0.07	0.12	8	−0.22	0.13	8

Table A.6: Abundance ratios for red giants in 47 Tucanae. Boldface IDs indicate the polluted population. Co to Y.

ID	[Co/Fe]	$\sigma_{[X/Fe]}$	N	[Ni/Fe]	$\sigma_{[X/Fe]}$	N	[Cu/Fe]	$\sigma_{[X/Fe]}$	N	[Zn/Fe]	$\sigma_{[X/Fe]}$	N	[Y/Fe]	$\sigma_{[X/Fe]}$	N
4794	0.01	0.07	15	−0.17	0.05	17	−0.16	0.35	1	0.27	0.13	1	0.13	0.19	3
5968	−0.02	0.07	12	−0.13	0.04	18	−0.30	0.35	1	0.22	0.13	1	0.11	0.21	1
6798	−0.05	0.07	12	−0.12	0.04	19	−0.31	0.35	1	0.27	0.13	1	−0.05	0.21	1
10237	0.01	0.07	14	−0.11	0.04	18	0.03	0.35	1	0.29	0.11	1	−0.04	0.19	2
13396	0.05	0.07	11	−0.11	0.04	19	−0.21	0.35	1	0.24	0.11	1	0.26	0.19	2
20885	0.07	0.06	11	−0.19	0.05	17	−0.27	0.35	1	0.16	0.13	1	0.17	0.21	1
29861	0.06	0.07	14	−0.11	0.04	17	−0.05	0.35	1	0.26	0.13	1	0.16	0.18	2
1062	−0.05	0.07	13	−0.15	0.05	19	−0.10	0.35	1	0.25	0.13	1	0.01	0.19	3
5265	−0.14	0.07	13	−0.06	0.05	20	−0.17	0.35	1	0.25	0.17	1	−0.09	0.18	2
27678	−0.01	0.08	11	−0.11	0.05	19	−0.23	0.35	1	0.33	0.13	1	0.13	0.18	2
28956	0.10	0.07	14	−0.05	0.04	20	−0.09	0.35	1	0.29	0.13	1	−0.09	0.18	2
38916	−0.02	0.07	14	−0.09	0.05	10	0.01	0.35	1	0.21	0.13	1	0.16	0.18	3
40394	−0.05	0.07	13	−0.10	0.04	20	0.07	0.35	1	0.30	0.13	1	0.07	0.18	2

Table A.7: Abundance ratios for red giants in 47 Tucanae. Boldface IDs indicate the polluted population. Zr to La.

ID	[Zr/Fe]	$\sigma_{[X/Fe]}$	N	[Mo/Fe]	$\sigma_{[X/Fe]}$	N	[Ru/Fe]	$\sigma_{[X/Fe]}$	N	[Ba/Fe]	$\sigma_{[X/Fe]}$	N	[La/Fe]	$\sigma_{[X/Fe]}$	N
4794	0.35	0.18	3	0.41	0.13	6	0.47	0.13	2	0.22	0.24	3	0.10	0.20	5
5968	0.45	0.17	3	0.53	0.13	6	0.51	0.13	2	0.14	0.25	3	0.12	0.20	2
6798	0.32	0.17	3	0.45	0.13	5	0.43	0.13	2	0.33	0.26	3	−0.04	0.22	2
10237	0.22	0.17	2	0.53	0.14	4	0.46	0.13	2	0.24	0.25	3	0.17	0.20	3
13396	0.29	0.17	3	0.54	0.13	5	0.47	0.13	2	0.23	0.24	3	0.23	0.20	3
20885	0.22	0.18	2	0.50	0.14	4	0.56	0.15	1	0.18	0.24	3	0.22	0.22	1
29861	0.27	0.17	3	0.57	0.13	4	0.62	0.13	2	0.16	0.24	3	0.23	0.19	3
1062	0.52	0.17	3	0.53	0.13	5	0.50	0.14	2	0.27	0.25	3	0.06	0.19	3
5265	0.37	0.17	3	0.48	0.14	6	0.36	0.12	2	0.24	0.25	3	−0.15	0.21	3
27678	0.67	0.17	3	0.72	0.13	7	0.52	0.13	2	0.40	0.25	3	0.05	0.21	3
28956	0.41	0.17	3	0.57	0.13	6	0.57	0.13	2	0.33	0.24	3	−0.13	0.21	2
38916	0.38	0.17	3	0.59	0.13	5	0.55	0.15	1	0.22	0.24	3	0.10	0.22	3
40394	0.92	0.18	3	0.69	0.13	7	0.56	0.16	2	0.31	0.24	3	−0.07	0.22	2

Table A.8: Abundance ratios for red giants in 47 Tucanae. Boldface IDs indicate the polluted population. Ce to Dy.

ID	[Ce/Fe]	$\sigma_{[X/Fe]}$	N	[Pr/Fe]	$\sigma_{[X/Fe]}$	N	[Nd/Fe]	$\sigma_{[X/Fe]}$	N	[Eu/Fe]	$\sigma_{[X/Fe]}$	N	[Dy/Fe]	$\sigma_{[X/Fe]}$	N
4794	−0.04	0.32	1	−0.02	0.22	7	0.10	0.24	1	0.36	0.19	1	0.64	0.27	2
5968	−0.11	0.32	1	−0.00	0.22	6	0.03	0.24	1	0.38	0.19	1	0.76	0.27	2
6798	–	–	0	−0.02	0.24	4	0.03	0.25	1	0.17	0.18	1	0.60	0.27	1
10237	0.04	0.32	1	0.01	0.21	7	0.04	0.23	1	0.43	0.18	1	0.77	0.27	2
13396	0.10	0.32	1	0.11	0.21	4	0.09	0.23	1	0.44	0.18	1	0.85	0.27	2
20885	0.08	0.32	1	−0.02	0.24	7	0.17	0.24	1	0.44	0.19	1	0.80	0.27	1
29861	0.00	0.32	1	0.07	0.21	8	0.17	0.23	1	0.43	0.18	1	0.81	0.27	2
1062	−0.13	0.32	1	−0.08	0.24	9	0.09	0.24	1	0.31	0.19	1	0.71	0.27	1
5265	−0.20	0.32	1	−0.21	0.24	8	−0.16	0.24	1	0.17	0.19	1	0.53	0.27	2
27678	−0.03	0.32	1	0.01	0.26	6	−0.04	0.25	1	0.26	0.19	1	0.70	0.27	2
28956	−0.13	0.32	1	−0.13	0.25	6	−0.06	0.24	1	0.15	0.18	1	0.62	0.27	2
38916	−0.03	0.32	1	−0.04	0.22	9	0.10	0.23	1	0.39	0.18	1	0.73	0.27	2
40394	–	–	0	−0.23	0.24	6	−0.05	0.25	1	0.21	0.19	1	0.60	0.27	1

A.2 LIGHT ELEMENT CORRELATIONS

We here present plots of [X/Fe] vs. [Na/Fe] to trace elements that vary in step with the light element variations.

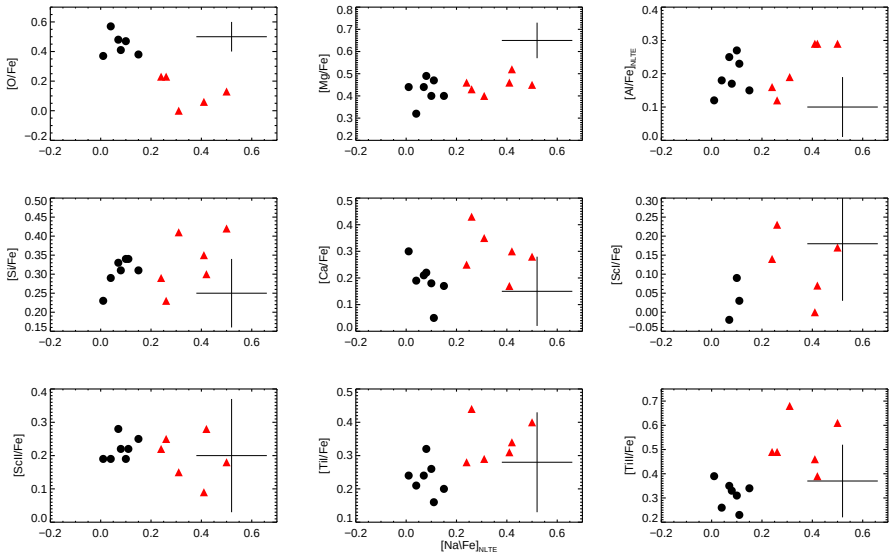

Figure A.1: [X/Fe] vs. [Na/Fe] from O to Ti. In each plot is shown representative uncertainties. Symbols the same as in Fig. 3.11

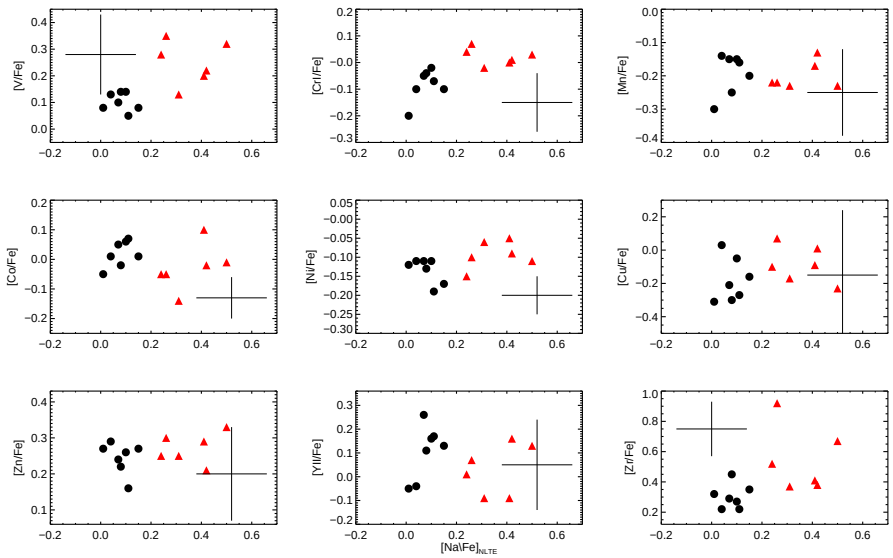

Figure A.2: [X/Fe] vs. [Na/Fe] from V to Zr. In each plot is shown representative uncertainties. Symbols the same as in Fig. 3.11

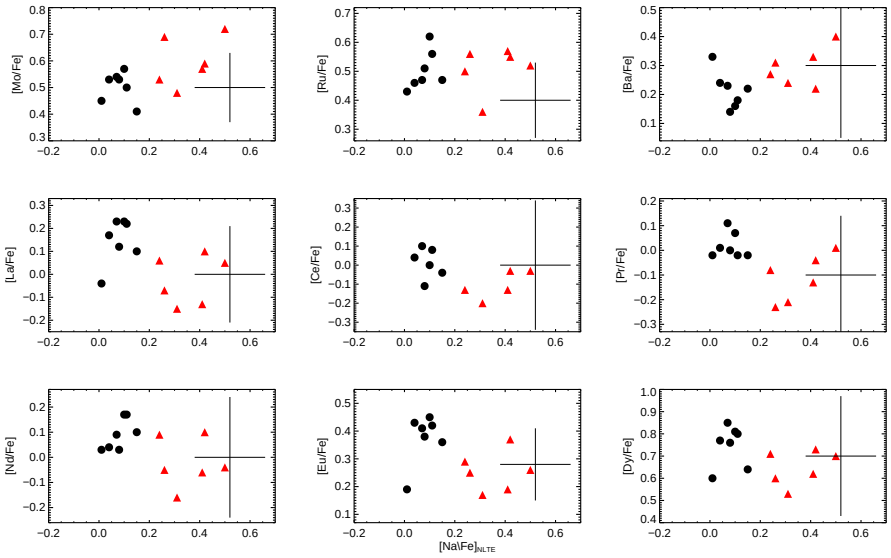

Figure A.3: [X/Fe] vs. [Na/Fe] from Mo to Dy. In each plot is shown representative uncertainties. Symbols the same as in Fig. 3.11

A.3 KURUCZ MOLECULAR LINE FORMAT

When modifying line lists for the use with `SYNTHE` or when needing to extract data from the already compiled line lists that comes with the software, an accurate description of the line list format is essential. The current documentation on Robert Kurucz webpage[1] for the molecular line lists provided with `SYNTHE/ATLAS12` is unfortunately somewhat outdated. Below follows a full description of the current format, together with some fine-print comments.

An example of the input format in tabular form is as follows:

Table A.9: Kurucz molecular line list input format.

wl(nm)	log(gf)	J	E(cm^{-1})	J′	E′(cm^{-1})	code	V	V′	iso	lifetime
433.0318	-3.524	19.5	-10563.271	20.5	-33649.772	106	X02F2	A02F1	13	627.0
513.4647	-1.912	11.5	751.215	11.5	20221.325	112	X00E1	A00F2	24	739.0

Most of the items above should be self-explanatory but a few comments to the above format are needed:

- The non-primed quantities refer to the lower energy level *for V=0 only.* For higher V-V′ transitions, this is not always the case and should be checked.
- The energy levels will sometimes have a negative value. This is used to indicate levels that are *extrapolated* to J and V values beyond what has measured in the lab, so when porting, always use

1 http://kurucz.harvard.edu/linelists.html

absolute values. Thus, the first example has extrapolated energies, whereas the second example has laboratory data.

- The `code` for the diatomic molecules is two 2-digit element numbers in ascending order (106 = CH, 112 = MgH).
- Following this are the labels for the two levels in the transition. The labels consist of the electronic states (X and A above), the vibrational levels (02 and 02 for CH, 00 and 00 for MgH), the lambda-doubling component (F and F for CH, E and F for MgH). E is positive parity, F is negative. Finally is the spin state (1 and 2 for CH, 1 and 2 for MgH).
- 'iso' refers to the isotope of the heavier atom. So the above is a ^{13}CH and a ^{24}MgH transition.
- lietime: The lifetime of the electronic state. The inverse of this quantity is the radiative damping constant.

BIBLIOGRAPHY

Aguerri, J. A. L., Balcells, M., & Peletier, R. F. 2001, A&A., 367, 428
Alibés, A., Labay, J., & Canal, R. 2001, A&A., 370, 1103
Allende Prieto, C., Majewski, S. R., Schiavon, R., et al. 2008, Astronomische Nachrichten, 329, 1018
Alves-Brito, A., Barbuy, B., Ortolani, S., et al. 2005, A&A., 435, 657
Alves-Brito, A., Meléndez, J., Asplund, M., Ramírez, I., & Yong, D. 2010, A&A., 513, A35
Anderson, J., Piotto, G., King, I. R., Bedin, L. R., & Guhathakurta, P. 2009, ApJ Lett., 697, L58
Andrievsky, S. M., Spite, M., Korotin, S. A., et al. 2008, A&A., 481, 481
Andrievsky, S. M., Spite, M., Korotin, S. A., et al. 2009, A&A., 494, 1083
Arlandini, C., Käppeler, F., Wisshak, K., et al. 1999, ApJ, 525, 886
Arnett, W. D. & Thielemann, F.-K. 1985, ApJ, 295, 589
Asplund, M., Grevesse, N., Sauval, A. J., & Scott, P. 2009, Ann. Rev. Astron. Astrophys., 47, 481
Asplund, M., Lambert, D. L., Nissen, P. E., Primas, F., & Smith, V. V. 2006a, ApJ, 644, 229
Asplund, M., Lambert, D. L., Nissen, P. E., Primas, F., & Smith, V. V. 2006b, ApJ, 644, 229
Barbuy, B., Chiappini, C., Cantelli, E., et al. 2014, A&A., 570, A76
Barbuy, B., Spite, F., & Spite, M. 1987, A&A., 178, 199
Barbuy, B., Zoccali, M., Ortolani, S., et al. 2009, A&A., 507, 405
Bastian, N., Cabrera-Ziri, I., & Salaris, M. 2015, MNRAS, 449, 3333
Bastian, N., Lamers, H. J. G. L. M., de Mink, S. E., et al. 2013, MNRAS, 436, 2398
Behara, N. T., Bonifacio, P., Ludwig, H.-G., et al. 2010, A&A., 513, A72
Bekki, K., Campbell, S. W., Lattanzio, J. C., & Norris, J. E. 2007, MNRAS, 377, 335
Bensby, T., Adén, D., Meléndez, J., et al. 2011a, A&A., 533, A134
Bensby, T., Alves-Brito, A., Oey, M. S., Yong, D., & Meléndez, J. 2010, A&A., 516, L13
Bensby, T., Alves-Brito, A., Oey, M. S., Yong, D., & Meléndez, J. 2011b, ApJ Lett., 735, L46
Bensby, T., Feltzing, S., & Oey, M. S. 2014, A&A., 562, A71
Bensby, T., Yee, J. C., Feltzing, S., et al. 2013, A&A., 549, A147
Bergemann, M. 2011, MNRAS, 413, 2184
Bergemann, M., Lind, K., Collet, R., Magic, Z., & Asplund, M. 2012, MNRAS, 427, 27
Bernath, P. F., Black, J. H., & Brault, J. W. 1985, ApJ, 298, 375

Binney, J. 2009, in IAU Symposium, Vol. 254, IAU Symposium, ed. J. Andersen, Nordströara, B. m, & J. Bland-Hawthorn, 145–152
Bisterzo, S., Travaglio, C., Gallino, R., Wiescher, M., & Käppeler, F. 2014, ApJ, 787, 10
Boesgaard, A. M., King, J. R., Cody, A. M., Stephens, A., & Deliyannis, C. P. 2005, ApJ, 629, 832
Bond, H. E. & Neff, J. S. 1969, ApJ, 158, 1235
Boyles, J., Lorimer, D. R., Turk, P. J., et al. 2011, ApJ, 742, 51
Briley, M. M., Hesser, J. E., Bell, R. A., Bolte, M., & Smith, G. H. 1994, AJ, 108, 2183
Briley, M. M., Smith, V. V., Suntzeff, N. B., et al. 1996, Nature, 383, 604
Brodie, J. P. & Strader, J. 2006, Ann. Rev. Astron. Astrophys., 44, 193
Brooke, J. S. A., Bernath, P. F., Schmidt, T. W., & Bacskay, G. B. 2013, J. Quant. Spec. Radiat. Transf., 124, 11
Brooke, J. S. A., Ram, R. S., Western, C. M., et al. 2014, ApJS, 210, 23
Brown, J. A. & Wallerstein, G. 1992a, AJ, 104, 1818
Brown, J. A. & Wallerstein, G. 1992b, AJ, 104, 1818
Brown, T. M., Sahu, K., Anderson, J., et al. 2010, ApJ Lett., 725, L19
Buurman, E. P., Donszelmann, A., Hansen, J. E., & Snoek, C. 1986, A&A., 164, 224
Caffau, E., Bonifacio, P., Sbordone, L., et al. 2013a, A&A., 560, A71
Caffau, E. & Ludwig, H.-G. 2007, A&A., 467, L11
Caffau, E., Ludwig, H.-G., Malherbe, J.-M., et al. 2013b, A&A., 554, A126
Caffau, E., Ludwig, H.-G., Steffen, M., et al. 2008, A&A., 488, 1031
Caffau, E., Steffen, M., Bonifacio, P., et al. 2014, Astronomische Nachrichten, 335, 59
Canuto, V. M. & Mazzitelli, I. 1991, ApJ, 370, 295
Carlsson, M. 1986, Uppsala Astronomical Observatory Reports, 33
Carollo, D., Beers, T. C., Lee, Y. S., et al. 2007, Nature, 450, 1020
Carollo, D., Martell, S. L., Beers, T. C., & Freeman, K. C. 2013, ApJ, 769, 87
Carretta, E., Bragaglia, A., Gratton, R., D'Orazi, V., & Lucatello, S. 2011a, A&A., 535, A121
Carretta, E., Bragaglia, A., Gratton, R., & Lucatello, S. 2009a, A&A., 505, 139
Carretta, E., Bragaglia, A., Gratton, R. G., et al. 2010, A&A., 520, A95
Carretta, E., Bragaglia, A., Gratton, R. G., et al. 2009b, A&A., 505, 117
Carretta, E. & Gratton, R. G. 1997, A&AS, 121, 95
Carretta, E., Gratton, R. G., Bragaglia, A., Bonifacio, P., & Pasquini, L. 2004, A&A., 416, 925
Carretta, E., Gratton, R. G., Bragaglia, A., D'Orazi, V., & Lucatello, S. 2013, A&A., 550, A34
Carretta, E., Gratton, R. G., Lucatello, S., Bragaglia, A., & Bonifacio, P. 2005, A&A., 433, 597

Carretta, E., Lucatello, S., Gratton, R. G., Bragaglia, A., & D'Orazi, V. 2011b, A&A., 533, A69
Casagrande, L., Schönrich, R., Asplund, M., et al. 2011, A&A., 530, A138
Castelli, F. & Kurucz, R. L. 2004, arXiv astro-ph/0405087
Cayrel, R., Depagne, E., Spite, M., et al. 2004, A&A., 416, 1117
Cayrel, R., Steffen, M., Chand, H., et al. 2007, A&A., 473, L37
Cescutti, G. & Chiappini, C. 2010, A&A., 515, A102
Cescutti, G. & Chiappini, C. 2014, A&A., 565, A51
Cescutti, G., Chiappini, C., Hirschi, R., Meynet, G., & Frischknecht, U. 2013, A&A., 553, A51
Chavez, J. & Lambert, D. L. 2009, ApJ, 699, 1906
Chiappini, C., Frischknecht, U., Meynet, G., et al. 2011, Nature, 472, 454
Chiappini, C., Matteucci, F., & Romano, D. 2001, ApJ, 554, 1044
Chieffi, A. & Limongi, M. 2013, ApJ, 764, 21
Cohen, J. G. & Meléndez, J. 2005, AJ, 129, 303
Collet, R., Asplund, M., & Trampedach, R. 2007, A&A., 469, 687
Colucci, J. E., Bernstein, R. A., Cameron, S. A., & McWilliam, A. 2012, ApJ, 746, 29
Combes, F. & Sanders, R. H. 1981, A&A., 96, 164
Cordero, M. J., Pilachowski, C. A., Johnson, C. I., et al. 2014, ApJ, 780, 94
Cordero, M. J., Pilachowski, C. A., Johnson, C. I., & Vesperini, E. 2015, ApJ, 800, 3
Cottrell, P. L. & Da Costa, G. S. 1981, ApJ Lett., 245, L79
Da Costa, G. S., Held, E. V., Saviane, I., & Gullieuszik, M. 2009, ApJ, 705, 1481
Da Costa, G. S., Norris, J. E., & Yong, D. 2013, ApJ, 769, 8
Dalessandro, E., Salaris, M., Ferraro, F. R., Mucciarelli, A., & Cassisi, S. 2013, MNRAS, 430, 459
Dalessandro, E., Schiavon, R. P., Rood, R. T., et al. 2012, AJ, 144, 126
Dalton, G., Trager, S. C., Abrams, D. C., et al. 2012, in SPIE Conference Series, Vol. 8446, SPIE Conference Series, 0
D'Antona, F. & Ventura, P. 2007, MNRAS, 379, 1431
de Jong, R. S., Barden, S., Bellido-Tirado, O., et al. 2014, in SPIE Conference Series, Vol. 9147, SPIE Conference Series, 0
de Mink, S. E., Langer, N., Izzard, R. G., Sana, H., & de Koter, A. 2013, ApJ, 764, 166
de Mink, S. E., Pols, O. R., Langer, N., & Izzard, R. G. 2009, A&A., 507, L1
De Smedt, K., Van Winckel, H., Kamath, D., et al. 2014, A&A., 563, L5
Decressin, T., Meynet, G., Charbonnel, C., Prantzos, N., & Ekström, S. 2007, A&A., 464, 1029
Dékány, I., Minniti, D., Catelan, M., et al. 2013, ApJ Lett., 776, L19
Dekker, H., D'Odorico, S., Kaufer, A., Delabre, B., & Kotzlowski, H.

2000, in SPIE Conference Series, Vol. 4008, SPIE Conference Series, ed. M. Iye & A. F. Moorwood, 534–545
Denisenkov, P. A. & Denisenkova, S. N. 1990, Soviet Astronomy Letters, 16, 275
Denissenkov, P. A. & Hartwick, F. D. A. 2014, MNRAS, 437, L21
Denissenkov, P. A. & Herwig, F. 2003, ApJ Lett., 590, L99
Denissenkov, P. A., VandenBerg, D. A., Hartwick, F. D. A., et al. 2015, MNRAS, 448, 3314
D'Ercole, A., D'Antona, F., Carini, R., Vesperini, E., & Ventura, P. 2012, MNRAS, 423, 1521
D'Ercole, A., Vesperini, E., D'Antona, F., McMillan, S. L. W., & Recchi, S. 2008, MNRAS, 391, 825
di Criscienzo, M., Ventura, P., D'Antona, F., Milone, A., & Piotto, G. 2010, MNRAS, 408, 999
Dickens, R. J., Bell, R. A., & Gustafsson, B. 1979, ApJ, 232, 428
Dickens, R. J., Croke, B. F. W., Cannon, R. D., & Bell, R. A. 1991, Nature, 351, 212
Dinescu, D. I., Girard, T. M., van Altena, W. F., & López, C. E. 2003, AJ, 125, 1373
Dobrovolskas, V., Kučinskas, A., Bonifacio, P., et al. 2014, A&A., 565, A121
Doherty, C. L., Gil-Pons, P., Lau, H. H. B., Lattanzio, J. C., & Siess, L. 2014, MNRAS, 437, 195
D'Orazi, V., Lugaro, M., Campbell, S. W., et al. 2013, ApJ, 776, 59
Drake, G. W. F. 2006, Springer Handbook of Atomic, Molecular, and Optical Physics
Dravins, D. 1982, Ann. Rev. Astron. Astrophys., 20, 61
Eggen, O. J., Lynden-Bell, D., & Sandage, A. R. 1962, ApJ, 136, 748
Fabbian, D., Asplund, M., Barklem, P. S., Carlsson, M., & Kiselman, D. 2009, A&A., 500, 1221
Fenner, Y., Campbell, S., Karakas, A. I., Lattanzio, J. C., & Gibson, B. K. 2004, MNRAS, 353, 789
Fenner, Y., Gibson, B. K., Lee, H.-c., et al. 2003, PASA, 20, 340
Fishlock, C. K., Karakas, A. I., Lugaro, M., & Yong, D. 2014, ApJ, 797, 44
François, P., Depagne, E., Hill, V., et al. 2007, A&A., 476, 935
Freeman, K. & Bland-Hawthorn, J. 2002, Ann. Rev. Astron. Astrophys., 40, 487
Freeman, K., Ness, M., Wylie-de-Boer, E., et al. 2013, MNRAS, 428, 3660
Freytag, B., Steffen, M., Ludwig, H.-G., et al. 2012, Journal of Computational Physics, 231, 919
Frischknecht, U., Hirschi, R., & Thielemann, F.-K. 2012, A&A., 538, L2
Fulbright, J. P., McWilliam, A., & Rich, R. M. 2006, ApJ, 636, 821
Fulbright, J. P., McWilliam, A., & Rich, R. M. 2007, ApJ, 661, 1152
Gallagher, A. J., Ryan, S. G., García Pérez, A. E., & Aoki, W. 2010, A&A.,

523, A24
García-Hernández, D. A., Lambert, D. L., Kameswara Rao, N., Hinkle, K. H., & Eriksson, K. 2010, ApJ, 714, 144
Gay, P. L. & Lambert, D. L. 2000, ApJ, 533, 260
Gehren, T., Liang, Y. C., Shi, J. R., Zhang, H. W., & Zhao, G. 2004, A&A., 413, 1045
Gehren, T., Shi, J. R., Zhang, H. W., Zhao, G., & Korn, A. J. 2006, A&A., 451, 1065
Gilmore, G., Randich, S., Asplund, M., et al. 2012, The Messenger, 147, 25
Gilmore, G. & Reid, N. 1983, MNRAS, 202, 1025
Gonzalez, O. A., Rejkuba, M., Zoccali, M., et al. 2011, A&A., 530, A54
González Hernández, J. I. & Bonifacio, P. 2009, A&A., 497, 497
Gratton, R. G., Carretta, E., & Bragaglia, A. 2012, A&A Rev., 20, 50
Gratton, R. G., Sneden, C., Carretta, E., & Bragaglia, A. 2000, A&A., 354, 169
Gray, D. F. 2008, The Observation and Analysis of Stellar Photospheres
Groenewegen, M. A. T., Waelkens, C., Barlow, M. J., et al. 2011, A&A., 526, A162
Grundahl, F., Briley, M., Nissen, P. E., & Feltzing, S. 2002a, A&A., 385, L14
Grundahl, F., Stetson, P. B., & Andersen, M. I. 2002b, A&A., 395, 481
Grupp, F., Kurucz, R. L., & Tan, K. 2009, A&A., 503, 177
Gustafsson, B., Edvardsson, B., Eriksson, K., et al. 2008, A&A., 486, 951
Hansen, C. J., Andersen, A. C., & Christlieb, N. 2014, A&A., 568, A47
Harris, M. J., Lambert, D. L., & Smith, V. V. 1988, ApJ, 325, 768
Harris, W. E. 1996, AJ, 112, 1487
Haywood, M., Di Matteo, P., Lehnert, M. D., Katz, D., & Gómez, A. 2013, A&A., 560, A109
Hedrosa, R. P., Abia, C., Busso, M., et al. 2013, ApJ Lett., 768, L11
Heger, A. & Langer, N. 2000, ApJ, 544, 1016
Herzberg, G. & Mrozowski, S. 1951, American Journal of Physics, 19, 390
Hesser, J. E. & Bell, R. A. 1980, ApJ Lett., 238, L149
Hill, V., Lecureur, A., Gómez, A., et al. 2011, A&A., 534, A80
Hinkel, N. R., Timmes, F. X., Young, P. A., Pagano, M. D., & Turnbull, M. C. 2014, AJ, 148, 54
Hinkle, K. H., Wallace, L., Ram, R. S., et al. 2013, ApJS, 207, 26
Hirschi, R., Meynet, G., & Maeder, A. 2005, A&A., 433, 1013
Howes, L. M., Asplund, M., Casey, A. R., et al. 2014, MNRAS, 445, 4241
Husser, T.-O., Wende-von Berg, S., Dreizler, S., et al. 2013, A&A., 553, A6
Ivans, I. I., Kraft, R. P., Sneden, C., et al. 2001, AJ, 122, 1438
Ivans, I. I., Sneden, C., Kraft, R. P., et al. 1999a, AJ, 118, 1273

Ivans, I. I., Sneden, C., Kraft, R. P., et al. 1999b, AJ, 118, 1273
James, F. & Roos, M. 1975, Computer Physics Communications, 10, 343
James, G., François, P., Bonifacio, P., et al. 2004, A&A., 427, 825
Johansson, S., Litzén, U., Lundberg, H., & Zhang, Z. 2003, ApJ Lett., 584, L107
Johnson, C. I., Pilachowski, C. A., Simmerer, J., & Schwenk, D. 2008, ApJ, 681, 1505
Kacharov, N., Koch, A., & McWilliam, A. 2013, A&A., 554, A81
Karakas, A. I. 2010, in IAU Symposium, Vol. 266, IAU Symposium, ed. R. de Grijs & J. R. D. Lépine, 161–168
Karakas, A. I. & Lattanzio, J. C. 2003, PASA, 20, 279
Karakas, A. I. & Lattanzio, J. C. 2014, PASA, 31, 30
Karakas, A. I., Lugaro, M. A., Wiescher, M., Görres, J., & Ugalde, C. 2006, ApJ, 643, 471
Keller, L. D., Pilachowski, C. A., & Sneden, C. 2001, AJ, 122, 2554
Kippenhahn, R. & Weigert, A. 1990, Stellar Structure and Evolution
Kiselman, D. 1993, A&A., 275, 269
Kobayashi, C., Karakas, A. I., & Umeda, H. 2011, MNRAS, 414, 3231
Kobayashi, C. & Nakasato, N. 2011, ApJ, 729, 16
Kobayashi, C., Umeda, H., Nomoto, K., Tominaga, N., & Ohkubo, T. 2006, ApJ, 653, 1145
Koch, A. & McWilliam, A. 2008, AJ, 135, 1551
Kormendy, J. & Kennicutt, Jr., R. C. 2004, Ann. Rev. Astron. Astrophys., 42, 603
Korotin, S. A., Andrievsky, S. M., & Luck, R. E. 1999, A&A., 351, 168
Kupka, F. G., Ryabchikova, T. A., Piskunov, N. E., Stempels, H. C., & Weiss, W. W. 2000, Baltic Astronomy, 9, 590
Kurucz, R. L. 1993, SYNTHE spectrum synthesis programs and line data
Kurucz, R. L. 2005, Memorie della Societa Astronomica Italiana Supplementi, 8, 14
Lacey, C. G. & Fall, S. M. 1985, ApJ, 290, 154
Langer, G. E., Hoffman, R., & Sneden, C. 1993, PASP, 105, 301
Lardo, C., Bellazzini, M., Pancino, E., et al. 2011, A&A., 525, A114
Lardo, C., Pancino, E., Mucciarelli, A., et al. 2013, MNRAS, 433, 1941
Larsen, S. S., Strader, J., & Brodie, J. P. 2012, A&A., 544, L14
Lawler, J. E., Guzman, A., Wood, M. P., Sneden, C., & Cowan, J. J. 2013, ApJS, 205, 11
Lazzaro, A. & Moneta, L. 2010, Journal of Physics Conference Series, 219, 042044
Leaman, R., VandenBerg, D. A., & Mendel, J. T. 2013, MNRAS, 436, 122
Lind, K., Asplund, M., Barklem, P. S., & Belyaev, A. K. 2011, A&A., 528, A103
Lind, K., Bergemann, M., & Asplund, M. 2012, MNRAS, 427, 50
Lind, K., Melendez, J., Asplund, M., Collet, R., & Magic, Z. 2013, A&A.,

554, A96
Longland, R., Iliadis, C., Champagne, A., et al. 2010, Nuclear Physics A, 841, 1 , the 2010 Evaluation of Monte Carlo based Thermonuclear Reaction Rates
Lundqvist, M., Wahlgren, G. M., & Hill, V. 2007, A&A., 463, 693
Magic, Z., Collet, R., Asplund, M., et al. 2013, A&A., 557, A26
Marcolini, A., Gibson, B. K., Karakas, A. I., & Sánchez-Blázquez, P. 2009, MNRAS, 395, 719
Marino, A. F., Milone, A. P., Piotto, G., et al. 2009, A&A., 505, 1099
Marino, A. F., Villanova, S., Piotto, G., et al. 2008, A&A., 490, 625
Marks, M. & Kroupa, P. 2010, MNRAS, 406, 2000
Markwardt, C. B. 2009, in Astronomical Society of the Pacific Conference Series, Vol. 411, Astronomical Data Analysis Software and Systems XVIII, ed. D. A. Bohlender, D. Durand, & P. Dowler, 251
Martell, S. L. & Grebel, E. K. 2010, A&A., 519, A14
Martell, S. L., Smolinski, J. P., Beers, T. C., & Grebel, E. K. 2011, A&A., 534, A136
Masseron, T., Plez, B., Van Eck, S., et al. 2014, A&A., 571, A47
Matteucci, F. & Francois, P. 1989, MNRAS, 239, 885
McCarthy, I. G., Font, A. S., Crain, R. A., et al. 2012, MNRAS, 420, 2245
McWilliam, A. & Bernstein, R. A. 2008, ApJ, 684, 326
McWilliam, A. & Lambert, D. L. 1988, MNRAS, 230, 573
McWilliam, A. & Rich, R. M. 1994, ApJS, 91, 749
McWilliam, A., Wallerstein, G., & Mottini, M. 2013, ApJ, 778, 149
McWilliam, A. & Zoccali, M. 2010, ApJ, 724, 1491
Meléndez, J. & Barbuy, B. 2009, A&A., 497, 611
Meléndez, J., Bergemann, M., Cohen, J. G., et al. 2012, A&A., 543, A29
Meléndez, J. & Cohen, J. G. 2007, ApJ Lett., 659, L25
Meléndez, J. & Cohen, J. G. 2009, ApJ, 699, 2017
Meléndez, J., Dodds-Eden, K., & Robles, J. A. 2006, ApJ Lett., 641, L133
Melendez, J. L. & Ramirez, I. 2007, in Bulletin of the American Astronomical Society, Vol. 39, American Astronomical Society Meeting Abstracts, 103.05
Meynet, G. & Maeder, A. 2002, A&A., 390, 561
Milone, A. P., Marino, A. F., Cassisi, S., et al. 2012a, ApJ Lett., 754, L34
Milone, A. P., Marino, A. F., Piotto, G., et al. 2013, ApJ, 767, 120
Milone, A. P., Piotto, G., Bedin, L. R., et al. 2012b, ApJ, 744, 58
Minchev, I., Chiappini, C., & Martig, M. 2013, A&A., 558, A9
Monelli, M., Milone, A. P., Stetson, P. B., et al. 2013, MNRAS, 431, 2126
Mucciarelli, A., Bellazzini, M., Ibata, R., et al. 2012, MNRAS, 426, 2889
Mucciarelli, A., Lapenna, E., Massari, D., et al. 2015, ArXiv e-prints:1507.01596
Ness, M., Asplund, M., & Casey, A. R. 2014, MNRAS, 445, 2994
Ness, M., Freeman, K., Athanassoula, E., et al. 2013, MNRAS, 430, 836

Nomoto, K., Kobayashi, C., & Tominaga, N. 2013, Ann. Rev. Astron. Astrophys., 51, 457
Nomoto, K., Tominaga, N., Umeda, H., Kobayashi, C., & Maeda, K. 2006, Nuclear Physics A, 777, 424
Norris, J. & Freeman, K. C. 1979, ApJ Lett., 230, L179
Norris, J. E. & Da Costa, G. S. 1995, ApJ, 447, 680
Odenkirchen, M., Grebel, E. K., Rockosi, C. M., et al. 2001, ApJ Lett., 548, L165
Pietrukowicz, P., Kozlowski, S., Skowron, J., et al. 2014, ArXiv e-prints
Pietrukowicz, P., Udalski, A., Soszyński, I., et al. 2012, ApJ, 750, 169
Piotto, G., Bedin, L. R., Anderson, J., et al. 2007, ApJ Lett., 661, L53
Piotto, G., Milone, A. P., Anderson, J., et al. 2012, ApJ, 760, 39
Piotto, G., Milone, A. P., Marino, A. F., et al. 2013, ApJ, 775, 15
Plez, B. 1998, A&A., 337, 495
Portail, M., Wegg, C., & Gerhard, O. 2015a, MNRAS, 450, L66
Portail, M., Wegg, C., Gerhard, O., & Martinez-Valpuesta, I. 2015b, MNRAS, 448, 713
Prantzos, N., Charbonnel, C., & Iliadis, C. 2007, A&A., 470, 179
Prantzos, N. & Goswami, A. 2001, Nuclear Physics A, 688, 37
Prantzos, N. & Silk, J. 1998, ApJ, 507, 229
Ramírez, I., Allende Prieto, C., & Lambert, D. L. 2013, ApJ, 764, 78
Ramírez, I., Allende Prieto, C., Lambert, D. L., & Asplund, M. 2008, in ASPCS, Vol. 393, New Horizons in Astronomy, ed. A. Frebel, J. R. Maund, J. Shen, & M. H. Siegel, 255
Ramírez, I. & Meléndez, J. 2005, ApJ, 626, 465
Ramírez, S. V. & Cohen, J. G. 2002, AJ, 123, 3277
Ramírez, S. V., Cohen, J. G., Buss, J., & Briley, M. M. 2001, AJ, 122, 1429
Renzini, A. & Voli, M. 1981, A&A., 94, 175
Reyniers, M., Van Winckel, H., Gallino, R., & Straniero, O. 2004, A&A., 417, 269
Rich, R. M., Reitzel, D. B., Howard, C. D., & Zhao, H. 2007, ApJ Lett., 658, L29
Richer, H. B., Heyl, J., Anderson, J., et al. 2013, ApJ Lett., 771, L15
Roederer, I. U., Cowan, J. J., Karakas, A. I., et al. 2010, ApJ, 724, 975
Roederer, I. U., Marino, A. F., & Sneden, C. 2011, ApJ, 742, 37
Roediger, J. C., Courteau, S., Graves, G., & Schiavon, R. P. 2014, ApJS, 210, 10
Rossi, L. J., Ortolani, S., Barbuy, B., Bica, E., & Bonfanti, A. 2015, MNRAS, 450, 3270
Ruchti, G. R., Bergemann, M., Serenelli, A., Casagrande, L., & Lind, K. 2013, MNRAS, 429, 126
Saha, K., Martinez-Valpuesta, I., & Gerhard, O. 2012, MNRAS, 421, 333
Saito, R. K., Zoccali, M., McWilliam, A., et al. 2011, AJ, 142, 76

Sbordone, L. 2005, Memorie della Societa Astronomica Italiana Supplementi, 8, 61
Sbordone, L., Bonifacio, P., Castelli, F., & Kurucz, R. L. 2004, Memorie della Societa Astronomica Italiana Supplementi, 5, 93
Sbordone, L., Caffau, E., Bonifacio, P., & Duffau, S. 2014, A&A., 564, A109
Sbordone, L., Limongi, M., Chieffi, A., et al. 2009, A&A., 503, 121
Sbordone, L., Salaris, M., Weiss, A., & Cassisi, S. 2011, A&A., 534, A9
Searle, L. & Zinn, R. 1978, ApJ, 225, 357
Shayesteh, A. & Bernath, P. F. 2011, J. Chem. Phys., 135, 094308
Shetrone, M. D. 1996, AJ, 112, 2639
Short, C. I. & Hauschildt, P. H. 2006, ApJ, 641, 494
Silva, D. R. & M. Peron, M. 2004, ESO Messenger, 118, 2
Simmerer, J., Sneden, C., Cowan, J. J., et al. 2004, ApJ, 617, 1091
Smith, V. V., Lambert, D. L., & Nissen, P. E. 1998, ApJ, 506, 405
Smith, V. V., Suntzeff, N. B., Cunha, K., et al. 2000, AJ, 119, 1239
Sneden, C., Bean, J., Ivans, I., Lucatello, S., & Sobeck, J. 2012, MOOG: LTE line analysis and spectrum synthesis, astrophysics Source Code Library
Sneden, C., Cowan, J. J., Lawler, J. E., et al. 2002, ApJ Lett., 566, L25
Sneden, C., Lucatello, S., Ram, R. S., Brooke, J. S. A., & Bernath, P. 2014, ApJS, 214, 26
Sneden, C., Pilachowski, C. A., & Vandenberg, D. A. 1986, ApJ, 311, 826
Sneden, C. A. 1973, PhD thesis, The University of Texaz at Austin.
Sobeck, J. S., Kraft, R. P., Sneden, C., et al. 2011, AJ, 141, 175
Stasińska, G., Prantzos, N., Meynet, G., et al., eds. 2012, EAS Publications Series, Vol. 54, Oxygen in the Universe
Steffen, M., Cayrel, R., Caffau, E., et al. 2012, Memorie della Societa Astronomica Italiana Supplementi, 22, 152
Stetson, P. B. 1987, PASP, 99, 191
Straniero, O., Cristallo, S., & Piersanti, L. 2014, ApJ, 785, 77
Suntzeff, N. B. & Smith, V. V. 1991, ApJ, 381, 160
Szczerba, R., Siódmiak, N., Stasińska, G., & Borkowski, J. 2007, A&A., 469, 799
Szczerba, R., Siódmiak, N., Stasińska, G., et al. 2012, in IAU Symposium, Vol. 283, IAU Symposium, 506–507
Taylor, B. J. 1986, ApJS, 60, 577
Terndrup, D. M., Popowski, P., Gould, A., Rich, R. M., & Sadler, E. M. 1998, AJ, 115, 1476
Thielemann, F. K. & Arnett, W. D. 1985, ApJ, 295, 604
Thygesen, A. O., Sbordone, L., Andrievsky, S., et al. 2014, A&A., 572, A108
Tody, D. 1986, in SPIE Conference Series, Vol. 627, SPIE Conference Series, ed. D. L. Crawford, 733

Tody, D. 1993, in Astronomical Society of the Pacific Conference Series, Vol. 52, Astronomical Data Analysis Software and Systems II, ed. R. J. Hanisch, R. J. V. Brissenden, & J. Barnes, 173
Tominaga, N., Umeda, H., & Nomoto, K. 2007, ApJ, 660, 516
Tsymbal, V. 1996, in Astronomical Society of the Pacific Conference Series, Vol. 108, M.A.S.S., Model Atmospheres and Spectrum Synthesis, ed. S. J. Adelman, F. Kupka, & W. W. Weiss, 198
Uttenthaler, S., Schultheis, M., Nataf, D. M., et al. 2012, A&A., 546, A57
van Aarle, E., Van Winckel, H., De Smedt, K., Kamath, D., & Wood, P. R. 2013, A&A., 554, A106
Van Winckel, H. & Reyniers, M. 2000, A&A., 354, 135
Vandame, B. 2002, in SPIE Conference Series, Vol. 4847, Astronomical Data Analysis II, ed. J.-L. Starck & F. D. Murtagh, 123–134
Velichko, A. B., Mashonkina, L. I., & Nilsson, H. 2010, Astronomy Letters, 36, 664
Venn, K. A., Irwin, M., Shetrone, M. D., et al. 2004, AJ, 128, 1177
Ventura, P., Carini, R., & D'Antona, F. 2011, MNRAS, 415, 3865
Ventura, P., Criscienzo, M. D., D'Antona, F., et al. 2014, MNRAS, 437, 3274
Ventura, P. & D'Antona, F. 2008, MNRAS, 385, 2034
Ventura, P. & D'Antona, F. 2009, A&A., 499, 835
Ventura, P. & D'Antona, F. 2011, MNRAS, 410, 2760
Visscher, C., Lodders, K., & Fegley, Jr., B. 2010, ApJ, 716, 1060
Wall, J. V. & Jenkins, C. R. 2012, Practical Statistics for Astronomers
Wallerstein, G., Iben, Jr., I., Parker, P., et al. 1997, Reviews of Modern Physics, 69, 995
Wegg, C. & Gerhard, O. 2013, MNRAS, 435, 1874
Williams, M. J., Bureau, M., & Cappellari, M. 2010, MNRAS, 409, 1330
Wood, M. P., Lawler, J. E., Sneden, C., & Cowan, J. J. 2013, ApJS, 208, 27
Woosley, S. E. & Weaver, T. A. 1995, ApJS, 101, 181
Wylie, E. C., Cottrell, P. L., Sneden, C. A., & Lattanzio, J. C. 2006, ApJ, 649, 248
Yong, D., Aoki, W., & Lambert, D. L. 2006, ApJ, 638, 1018
Yong, D., Grundahl, F., D'Antona, F., et al. 2009, ApJ Lett., 695, L62
Yong, D., Grundahl, F., Johnson, J. A., & Asplund, M. 2008a, ApJ, 684, 1159
Yong, D., Grundahl, F., Lambert, D. L., Nissen, P. E., & Shetrone, M. D. 2003a, A&A., 402, 985
Yong, D., Karakas, A. I., Lambert, D. L., Chieffi, A., & Limongi, M. 2008b, ApJ, 689, 1031
Yong, D., Lambert, D. L., Allende Prieto, C., & Paulson, D. B. 2004, ApJ, 603, 697
Yong, D., Lambert, D. L., & Ivans, I. I. 2003b, ApJ, 599, 1357
Zhang, H. W., Gehren, T., & Zhao, G. 2008, A&A., 481, 489

Zoccali, M., Hill, V., Lecureur, A., et al. 2008, A&A., 486, 177
Zoccali, M., Lecureur, A., Barbuy, B., et al. 2006, A&A., 457, L1
Zoccali, M., Renzini, A., Ortolani, S., et al. 2003, A&A., 399, 931
Zucker, D. B., de Silva, G., Freeman, K., Bland-Hawthorn, J., & Hermes Team. 2012, in Astronomical Society of the Pacific Conference Series, Vol. 458, Galactic Archaeology: Near-Field Cosmology and the Formation of the Milky Way, ed. W. Aoki, M. Ishigaki, T. Suda, T. Tsujimoto, & N. Arimoto, 421